SYNTHETIC APERTURE RADAR IMAGING WITH DEEP NEURAL NETWORKS

by
MUHAMMED BURAK ALVER

Submitted to the Graduate School of Engineering and Natural Sciences
in partial fulfilment of
the requirements for the degree of Doctor of Philosophy

Sabancı University
December 2020

SYNTHETIC APERTURE RADAR IMAGING WITH DEEP NEURAL NETWORKS

Approved by:

Prof. Müjdat Çetin .....
(Dissertation Supervisor)

Prof. Selim Balcısoy .....
(Dissertation Co-Supervisor)

Prof. Özgür Gürbüz .....

Assoc. Prof. İlker Hamzaoğlu .....

Assoc. Prof. Koray Kayabol .....

Asst. Prof. N. Özben Önhon .....

Date of Approval: Dec 22, 2020

ABSTRACT

SYNTHETIC APERTURE RADAR IMAGING WITH DEEP NEURAL NETWORKS

MUHAMMED BURAK ALVER

ELECTRONICS ENGINEERING Ph.D DISSERTATION, December 2020

Dissertation Supervisor: Prof. Müjdat Çetin

Dissertation Co-Supervisor: Prof. Selim Balcısoy

Keywords: Synthetic aperture radar, inverse problems, computational imaging, deep learning, convolutional neural networks, plug-and-play priors, automatic target recognition.

Synthetic aperture radar (SAR) is a remote sensing imaging modality that has been in use since the 1960s. Conventional image formation in SAR is based on 2D inverse Fourier transform of the reflectivity field of the scene to be imaged. This conventional image formation technique is developed for a clean and complete data collection scenario. However, in reality, the collected data are only a reduced representation of the underlying scene due to hardware limitations and uncertainties in the data collection geometry, and hence suffer from reduction and phase errors. Therefore, many SAR image formation frameworks using regularization have been proposed over the years, in order to account for these limitations.

In this dissertation, we have focused on the SAR imaging problem, particularly image formation, phase error correction, and automatic target recognition (ATR), and developed three frameworks. The first framework tackles the SAR image formation problem. In this framework, SAR image formation is formulated as a regularized optimization problem, and using the plug-and-play (PnP) priors framework, we have incorporated deep learning-based priors into our formulation. Our second framework is an extension of the first one, which aims at joint image formation and phase error correction. Experimental results show the effectiveness of these two frameworks and

our proposed methods exceed the state-of-the-art image formation and phase error correction performances in the majority of the scenarios considered. The third proposed framework focuses on the ATR problem, and within this framework two ATR approaches are presented which perform the ATR task in the data domain rather than image domain. We have experimentally shown that the ATR task can be successfully performed in the data domain, and with further development, it might be possible to reach state-of-the-art performance.

Overall, we have shown that the performance in various SAR imaging tasks can be improved significantly using deep learning tools.

ÖZET

DERİN SİNİR AĞLARI İLE SENTETİK AÇIKLIKLI RADAR GÖRÜNTÜLEME

MUHAMMED BURAK ALVER

ELEKTRONİK MÜHENDİSLİĞİ DOKTORA TEZİ, Aralık 2020

Tez Danışmanı: Prof. Dr. Müjdat Çetin

Tez Eş Danışmanı: Prof. Dr. Selim Balcısoy

Anahtar Kelimeler: Sentetik açıklıklı radar, ters problemler, hesaplamalı görüntüleme, derin öğrenme, evrişimsel sinir ağları, tak-çalıştır önseller, özdevimli hedef tanılama.

Sentetik açıklıklı radar (SAR), 1960'lardan beri kullanımda olan bir uzaktan görüntüleme yaklaşımıdır. Geleneksel SAR görüntü oluşturma yöntemi, görüntülenecek sahnenin yansıtma alanının 2B Fourier dönüşümü tabanlıdır. Bu geleneksel görüntü oluşturma yöntemi, temiz ve tam veri toplama senaryosu için geliştirilmiştir. Ancak, gerçekte toplanan veri, donanım kısıtları ve veri toplama geometrisindeki belirsizliklerden ötürü, altta yatan sahnenin ancak indirgenmiş bir temsilidir ve bunlar veri azaltımı ve faz hatalarına sebep olmaktadır. Bundan dolayı, bu kısıtları denkleştirme adına yıllar içinde düzenlileştirme kullanan birçok SAR görüntü oluşturma çerçeveleri önerilmiştir.

Bu tezde, SAR görüntüleme problemine odaklanılmıştır ve görüntü oluşturma, faz hatası düzeltimi ve özdevimli hedef tanılama (ATR) için üç çerçeve geliştirilmiştir. İlk çerçeve, SAR görüntüleme problemi odaklıdır. Bu çerçevede SAR görüntüleme, düzenlileştirmeli bir eniyileme problemi olarak kurgulanmıştır ve tak-çalıştır (PnP) önseller çerçevesi kullanılarak, derin öğrenme tabanlı önseller kurgulamaya dahil edilmiştir. İkinci çerçeve, önerilen ilk çerçevenin görüntü oluşturmanın yanında faz hatalarını da gidermeyi amaçlayan bir uzantısıdır. Deneysel sonuçlar, önerilen iki çerçevenin görüntü oluşturma ve faz hatası gidermede, düşünülen betiklerin çoğunluğunda en iyi başarımları elde ettiğini göstermektedir. Önerilen üçüncü

çerçeve ATR problemine odaklanmaktadır ve bu çerçevede ATR görevini görüntü uzayı yerine veri uzayında gerçekleştiren iki ATR yaklaşımı sunulmuştur. Deneysel sonuçlarla, ATR görevinin veri uzayında da başarılı bir şekilde gerçekleştirilebileceği gösterilmiş ve bu çerçevenin daha fazla geliştirilmesiyle, en iyi başarımlara ulaşılabilmesinin mümkün olduğu vurgulanmıştır.

Sonuç olarak bu tezdeki çalışmalar, farklı SAR görüntüleme görevlerinde, derin öğrenme teknikleri kullanılarak sonuçların önemli ölçüde iyileştirilebileceğini göstermektedir.

ACKNOWLEDGEMENTS

The accomplishments in this dissertation would not have been possible without the help and support of many individuals. First, and foremost, I would like to express my earnest and heartfelt gratitude to my supervisor, Prof. Müjdat Çetin, for his continuous guidance, support, encouragement, patience, and most importantly being an excellent example as an academician. I consider myself very fortunate to have worked with him and I have learned a lot from him, including how to be a great instructor, how to have the perfect student-advisor relationship, and how to approach research problems and ask the right questions. I am also grateful to my dissertation jury members Prof. Selim Balcısoy, Prof. Özgür Gürbüz, Assoc. Prof. İlker Hamzaoğlu, Assoc. Prof. Koray Kayabol, and Asst. Prof. N. Özben Önhon for their careful evaluation of my work. They helped in improving the quality of this dissertation with their valuable suggestions and feedback.

I am thankful to my friends at the SPIS lab. I am profoundly indebted to Ammar Saleem who has contributed all parts of this dissertation either in the form of direct collaboration or through fruitful discussions. Ammar is, without a doubt, the most selfless person I have ever met, and has helped more people during the last four years than I could have in a lifetime. I was very fortunate to have the chance to work with him, and I have learned a lot from him during our many technical and non-technical discussions. I am also thankful to him for introducing me many delicious Pakistani food, to which I am getting addicted. I am thankful to Majed Elwardy for being a great friend, and also being a great neighbor for nearly two years. I will always remember those crazy minibus rides we had together. I thank Sara Atito for helping me getting familiar with the deep learning terminology, as well as numerous cups of coffee. I thank Mastaneh Torkamani for her help during the semesters we have taught Signals together. I am thankful to Muhammad Usman Ghani and Abdullahi Adamu with whom I have shared great moments in the first two years of my Ph.D. journey. I would also like the appreciate the help of the SPIS lab administrator Osman Rahmi Fıçıcı, for his continuous support in terms of computing facilities.

I would like to acknowledge The Scientific and Technological Research Council of Turkey (TÜBİTAK), for providing financial support for my Ph.D. through the BİDEB 2011 scholarship, and the German Aerospace Center (DLR) for providing the TerraSAR-X data.

I have been working as a research assistant at the Maltepe University during the

last two years of my Ph.D., and I would like to express my gratitude to my fellow research assistants, especially to my (current and former) office mates and table tennis (and occasionally "Age of Empires II") partners Muhammet Cihat Mumcu, Uğur Osman Yücel, Mehmet Cüneyt Özbalcı, and Ebubekir Ceyhan. I am also thankful to our former head of department Asst. Prof. Burhan Demir Öner for his help during my time at Maltepe University.

I would like to thank my longtime friends Muhammet Alperen Karaçeşme, Cüneyt Koç, and Mohamed Camara, with whom I could not have spend much time during my Ph.D., yet we have managed to stay close to each other.

I am grateful to my parents, my sister, and my wife's parents for their everlasting trust, encouragement, emotional support, and pure love. I am thankful to my son Yusuf Erdem for bringing great enjoyment to our home with his smiles and kindly reminding me that I should graduate already! Finally, I would like to express my sincere appreciation of my beloved wife, Özlem. She has always had more trust in my work than I had, which could not have been completed without her unconditional love and support. I am very fortunate to have her by my side to face many challenges of life together.

to my wife and my son

Contents

List of Tables

List of Figures

List of Abbreviations

ADMM Alternating Direction Method of Multipliers . xi, 4, 5, 33, 34, 35, 36, 37, 38, 39, 41, 43, 44, 51, 71, 72, 73

AE Autoencoder ..... xi, 29, 30

AI Artificial Intelligence 29

AMP Approximate Message Passing 34

ATR Automatic Target Recognition .. iii, iv, v, vi, x, xi, 1, 5, 6, 7, 27, 28, 33, 84, 85, 89, 91, 92

BM3D Block-Matching and 3D Filtering 33, 39, 43, 44, 55, 91

CNN Convolutional Neural Network . xi, xviii, xix, 4, 5, 28, 29, 30, 32, 36, 39, 42, 43, 44, 47, 52, 73, 84, 85, 91, 92, 94

CT Computed Tomography 16

DL Dictionary Learning ..... xix, xxi, 33, 39, 43, 44, 52, 55, 62, 67, 68, 91

DNN Deep Neural Network 5, 7, 31

FBP Filtered Backprojection 15, 16

FFT Fast Fourier Transform ..... xiv, 15, 39, 41, 43, 55, 63, 73, 75, 83

FIR Finite Impulse Response 31

GMM Gaussian Mixture Model 34

GMTI Ground Moving Target Indication 4

GPU Graphics Processing Unit 42, 86

GRU Gated Recurrent Unit 31

HQS Half Quadratic Splitting 18, 34

IIR Infinite Impulse Response 31

ILSVRC ImageNet Large Scale Visual Recognition Challange 31

IMU Inertial Measurement Unit 20

IPRPHC Image-Phase Removed Phase History Classification xi, xii, xiv, xxii, 5, 85, 86, 87, 88, 90, 92

ISTA Iterative Shrinkage-Thresholding Algorithm 33, 34

JPL Jet Propulsion Laboratory 2

LSTM Long Short-Term Memory 31

MCA Multi-Channel Autofocus ..... x, 26

MLP Multilayer Perceptron ..... xi, 29, 30

MSTAR Moving and Stationary Target Acquisition and Recognition .. xiv, xviii, 27, 28, 85, 87, 89, 90

NASA National Aeronautics and Space Administration 2, 3

NCSR Nonlocally Constrained Sparse Representation 34

NLM Non-Local Means 34

NQR Non-Quadratic Regularization 33, 39, 43, 55, 62, 91, 93

PFA Polar Format Algorithm 15

PGA Phase Gradient Autofocus ..... x, 25

PHDC Phase History Domain Classification xi, xiv, xxii, 5, 84, 85, 86, 87, 88, 90, 92, 94

PnP Plug-and-Play ..... iii, v, xi, 4, 5, 7, 33, 34, 35, 36, 39, 41, 43, 44, 55, 69, 91

ReLU Rectified Linear Unit ..... xviii, 41

RNN Recurrent Neural Network ..... xi, xviii, 29, 31, 32

ROI Region-of-interest 27

SAR Synthetic Aperture Radar iii, iv, v, vi, x, xi, xviii, 1, 2, 3, 4, 5, 6, 7, 8, 9, 11, 13, 14, 15, 16, 18, 19, 20, 21, 22, 24, 27, 28, 31, 33, 36, 37, 39, 40, 41, 47, 69, 70, 73, 84, 91, 92

SDA Sparsity-driven Autofocus ..... x, xiv, 26, 27, 73, 75, 83, 92

SNR Signal-to-Noise Ratio xiv, xviii, xix, xx, 26, 43, 44, 45, 46, 48, 51, 54, 55, 58, 61, 75, 83, 91, 92, 93

SSIM Structural Similarity xiv, xviii, xix, xx, 43, 44, 45, 46, 48, 51, 54, 55, 58, 61, 75, 83, 91, 92, 93

UWB Ultra-Wide Band 22

Chapter 1

Introduction

This dissertation presents new approaches to the problems of synthetic aperture radar (SAR) image reconstruction, phase error correction, and automatic target recognition (ATR). The purpose of this chapter is to: 1) introduce the problems addressed in this dissertation; 2) summarize the current state of SAR technology; 3) provide a concise description of the approach taken in this work by pointing out the main contributions; 4) present the outline of the dissertation.

1.1 Synthetic Aperture Radar (SAR) Imaging

Synthetic aperture radar (SAR) imaging is a remote sensing imaging modality that has been widely used in a variety of applications since 1960s. Its advantages over other remote sensing modalities, such as optical imaging, include; day and night capability, all-weather operation, ability of discriminating among different materials, penetrating through different covers and vegetation layers. Specifically, SAR is an active sensor which has its own illumination, i.e., it transmits a chirp signal and collects the returned signal from the area of interest, and hence can work at day or night, whereas optical imaging modalities require an external illumination, e.g., sunlight, which limits the operational time. Moreover, SAR works in the microwave regime, which allows its transmitted signals to penetrate through cloud or rain, as well as light foliage, hence it can work in any weather conditions and detect underground structures if they are buried shallowly in dry environments [4].

SAR sensors are carried on a platform (aircraft or satellite) which travels along a path transmitting microwave pulses towards the ground. Figure 1.1 shows an illustration of SAR data collection using an airborne platform. Some of the transmitted microwave energy is reflected from the ground back to the SAR sensor and received

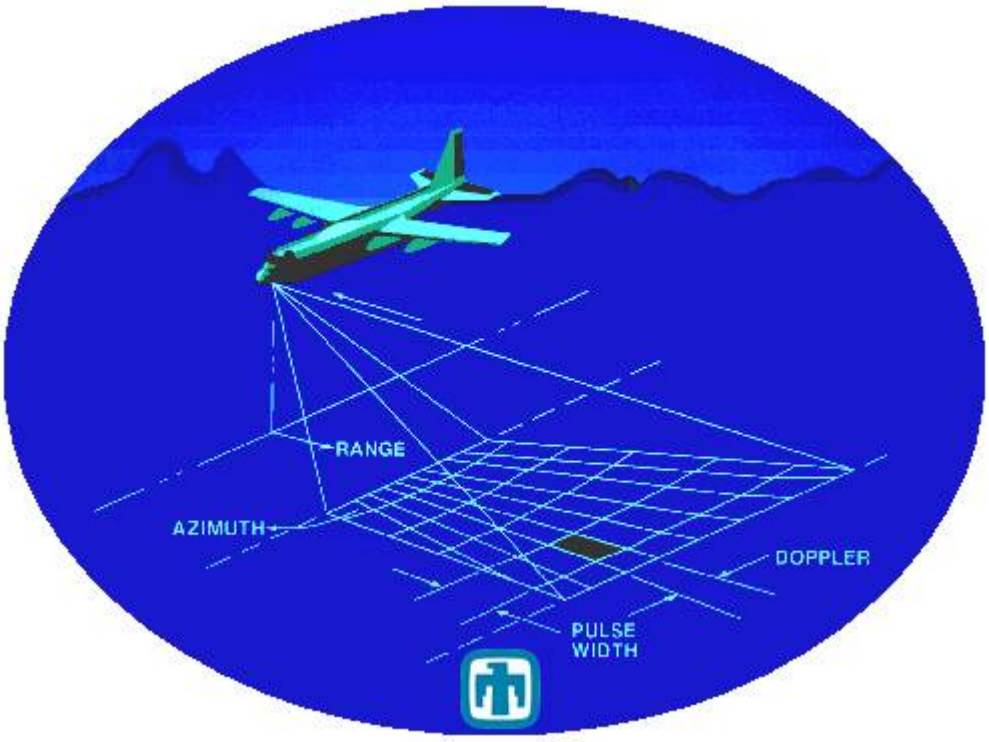

Figure 1.1 Simple illustration of SAR data collection. (Image obtained from the web site of Sandia National Laboratories.)

as a signal. This process is repeated for many aperture positions as the platform moves. The data used for imaging are obtained after a preprocessing of the received signal, involving mixing and filtering steps [5]. The SAR image formation problem is the problem of reconstruction of a spatial reflectivity field of the area of interest from the preprocessed SAR signals.

1.2 Current State of SAR Technology

The use of radar as an imaging sensor dates back as early as the 1940s. However, these early imaging radars, which are nowadays usually referred to as *real aperture radars*, had an important limitation: the poor resolution achievable with the operating wavelength, as the resolution is inversely proportional to the antenna or aperture size of the sensor. To overcome this limitation, the idea of synthesizing a very long antenna by moving a small one along a convenient path, which is generally attributed to Carl Wiley of Goodyear Aircraft Corporation, is developed in the 1950s [6]. Subsequently, a group of researchers at the University of Illinois carried out the experimental validation of the SAR concept [7]. The first operational airborne SAR system is considered to be the one developed at the University of Michigan, in 1957, which operated at the X-band. Over the following decades, many more SAR systems were built. JPL developed an L-band SAR sensor for NASA, which is

Figure 1.2 A TerraSAR-X image.

installed on a rocket in 1962, and on an airplane in 1966. NASA also upgraded the system developed at the University of Michigan, by adding L-band channel in 1973. SAR sensors have continued to be used in many more NASA missions, including the Apollo 17 lunar mission, SEASAT satellite, spaceborne imaging radar (SIR), and Magellan mission to image the planet Venus [8]. SEASAT is considered to be the first civilian application of SAR, which was oriented to oceanographic investigations. Although its operational lifetime was only a few months due to a short circuit in its power system, obtained results clearly demonstrated how impactful SAR systems were going to be for the area of remote sensing [6]. 1990s and onwards, many satellites with SAR sensors have been built: ALMAZ-1 (1991) from the Soviet Union (and later Russia); ERS-1 (1991), ERS-2 (1995), ENVISAT (2002), Sentinel-1A (2014) and Sentinel-1B (2016) from the European Space Agency (ESA); JERS-1 (1992), ALOS-1 (2006) and ALOS-2 (2014) from the Japan Aerospace Exploration Agency (JAXA); RADARSAT-1 (1995) and RADARSAT-2 (2007) from the Canadian Space Agency (CSA); TerraSAR-X (2007) and TanDEM-X (2010) from the German Space Agency (DLR). Figure 1.2 shows an image from the TerraSAR-X satellite.

Early developments in SAR research were mostly targeting the hardware-related issues and limitations, and considerable improvements were achieved. Back then, this research field was dominated by those working in physics, electromagnetics, and radar engineering. Only in the 1980s, a signal processing view of SAR has emerged [9–11]. Over the years, studies are geared towards imperfections of the collected data, e.g., noisy and/or incomplete data due to the limited observation time, or the environment not being very structured and cooperating. As a result,

the collected data would be a reduced representation of the underlying scene [12].

For many years (and still today, to a large extent), the standard approach for SAR image formation has been through a Fourier transform-based algorithm. This technique, however, is not designed with the limitations such as noisy or incomplete data in mind, and hence cannot overcome such limitations. Furthermore, within this approach, the knowledge about the underlying scene cannot be exploited, and the imaging cannot be reoriented to address the final objective better. The overall output quality is limited by the quality of the collected data.

Improvements in SAR imaging systems draw attention from many different research fields and SAR has started to find use in many applications including reconnaissance [13–15], change detection [16–18], oceanography [19–22], glaciology [23, 24], forestry [25, 26], earthquake monitoring [27–29] and ground moving target indication (GMTI) [15, 30–32]. Most of these applications, if not all, can benefit from automated processing techniques in extracting information from a SAR image for an accurate and efficient interpretation of the scene. Therefore, new processing techniques which are geared towards the final objectives of the mission, and which are robust to reduced data domains are required for the SAR systems [12].

1.3 Contributions of this Dissertation

The first contribution of this dissertation is the formulation of a SAR image reconstruction algorithm using the Plug-and-Play (PnP) priors framework [33], namely, PnP-CNN-SAR. This is the first SAR image formation approach that combines a physics-based forward model with a learning-based prior in a principled and computationally feasible way within the PnP framework. In this framework, the image formation problem is solved through minimization of a regularization-based objective function. In particular, the minimization problem is divided into sub-problems using the Alternating Direction Method of Multipliers (ADMM) algorithm [34], resulting in separating the data-fidelity term and the regularization term of the objective function, to solve sub-problems iteratively. PnP priors framework [33] has shown that, after this separation, optimization of the regularization term, i.e., the prior term, is equivalent to a simple denoising of an intermediate solution under white Gaussian noise. Hence, the regularizer can be replaced with an off-the-shelf denoiser. In our framework, we have replaced the regularizer with a convolutional neural network (CNN) denoiser. We have demonstrated the effectiveness of our framework, i.e., PnP-CNN-SAR, in a variety of scenarios, i.e., for different levels of data limitations and noise for both synthetic and real SAR scenes.

The second contribution of this dissertation is the extension of our first contribution to jointly address phase errors along with image reconstruction, namely, PnP-CNN-SAR-AF. This framework also utilizes the PnP priors using the ADMM algorithm and deep priors, however there are two additional steps in each ADMM iteration, namely, phase error estimation and phase error correction. We have demonstrated the effectiveness of PnP-CNN-SAR-AF in a variety of scenarios, i.e., for different phase error levels for real SAR scenes, improving upon the performance of existing methods.

The third contribution of this dissertation is a new SAR ATR framework that works in the phase history domain. Within this framework, we have introduced two methodologies, namely, phase history domain classification (PHDC) and image-phase removed phase history classification (IPRPHC). PHDC purely works in the phase history domain, i.e., the classification task is performed without image reconstruction. IPRPHC, on the other hand, involves certain steps, particularly, image reconstruction, image-phase removal, and phase history generation from the phase-removed image, before the classification task is performed. Two well-known CNNs, i.e., AlexNet [35] and VGG16 [36], are used for the classification task for both methodologies. IPRPHC has reached a performance level similar to that of state-of-the-art SAR ATR methods while the performance of the PHDC was not competitive enough. Nevertheless, our results suggests that SAR ATR in the phase history domain can be an important research direction.

Overall, this dissertation proposes several ways to utilize deep neural networks (DNNs), particularly CNNs, in order to improve the performance of SAR image reconstruction and automatic target recognition. The ideas proposed here can be extended to build fully-automated end-to-end SAR image reconstruction and ATR frameworks utilizing CNNs.

1.4 Organization

This dissertation is organized as follows. Chapter 2 includes the review of the background knowledge that the ideas proposed here are built upon, i.e., Section 2.1 presents a review of SAR imaging and describes the problems to be addressed in detail, the deep learning background is provided in Section 2.2 along with a brief survey of its utilization in the SAR imaging literature, and Section 2.3 is dedicated to the PnP priors framework. PnP-CNN-SAR is introduced in Chapter 3 and experimental results on both synthetic and real SAR scenes are provided. In Chapter 4, the framework for joint image reconstruction and phase error correction, i.e., PnP-CNN-SAR-AF, is described and its experimental results for real SAR scenes are

presented. Two methodologies proposed for SAR ATR in the phase history domain and their experimental results are presented in Chapter 5. Chapter 6 includes the summary of the contributions and obtained results, as well as potential future work suggestions.

Chapter 2

Preliminaries

In this chapter, we provide background information on three topics, namely, SAR imaging, deep learning, and PnP priors. The discussion on SAR imaging includes the basic principles, mathematical formulation of the data collection and preprocessing in SAR, the autofocus problem and phase errors in SAR imaging, and a review of SAR ATR. The deep learning discussion gives the required background knowledge, and then the use of DNNs for the various SAR tasks is presented. The final part of this chapter is dedicated to the PnP priors framework, which is utilized in our first two contributions.

2.1 SAR Background

Radars use a basic principle known as echo ranging. Echo ranging is the concept that is used to measure the distance of an object by transmitting an echo signal to the object and *listening* the reflection of the echo signal. As the echo signal's reflection will travel twice the distance of the object, one can easily estimate the distance if the propagation speed of the echo signal is known. The distance then will be half of the round trip flight time of the echo signal multiplied by its propagation speed. This principle is implemented in radar systems by transmitting high-bandwidth pulses and using pulse compression techniques [5, 37]. Hence, radars can distinguish objects that are at different distances. Imaging radars, however, have to be able to distinguish objects that are at the same distance but at different directions as well, in order to produce a 2D visualization of the scene, i.e., having resolving power only in the range direction is not sufficient. In theory, this can be achieved by transmitting a narrow beam to illuminate a narrow strip of the ground. However, this is not as easy as it sounds, since how narrow the transmitted beam can be, or analogously how small the cross-range resolution can be depends on the antenna aperture size

through the following equation:

$$\rho = \frac{\lambda_w R}{w} \tag{2.1}$$

where λ_w is the wavelength of the illuminating source, R is the target range, and w is the width of the antenna aperture. Consider the case where the wavelength of the source and the distance of the target are 0.03 m and 50 km, respectively. This is a typical wavelength for an X-band radar. Suppose that we want to reconstruct a radar image for which the resolution is 1 meter. In order to achieve this resolution level, we would need a physical antenna with the width of 1500 m, which is of course impractical to carry on an aircraft or a satellite.

SAR solves this problem by sending multiple pulses from a number of observation points, and then focusing the received information coherently to obtain a high-resolution 2-D description of the scene. Hence it synthesizes the effect of a large antenna, using multiple observations from a small antenna [12].

SAR imaging systems can operate in two modes, namely, stripmap-mode SAR, and spotlight-mode SAR. In stripmap-mode SAR, the antenna remains fixed with respect to the radar platform so that the antenna beam sweeps out a strip on the ground. In spotlight-mode, the antenna is steered to continuously illuminate a single spot of terrain. This study focuses on the spotlight-mode SAR. Spotlight-mode SAR is able to provide higher resolution at the expense of spatial coverage, as by steering the antenna, the same terrain portion can be observed through a wider range of angles while other areas within a given accessibility swath of the SAR cannot be illuminated. Figure 2.1 shows the geometry for data collection in a spotlight-mode SAR.

2.1.1 Spotlight-Mode SAR Observation Model

This section provides the preprocessing of the received signals in the spotlight-mode SAR, based on the tomographic derivation in [10], and very closely follows the development in [12]. Let $f(x, y)$ be the complex reflectivity density of the ground patch, and assume that it is constant over the range of frequencies and the range of viewing angles θ employed by the radar. Note that this is an approximation, and there are cases where the dependence of the reflectivity on frequency or aspect angle is important and must be taken into account [38].

In most SAR applications, the transmitted signal is a linear FM chirp signal, which

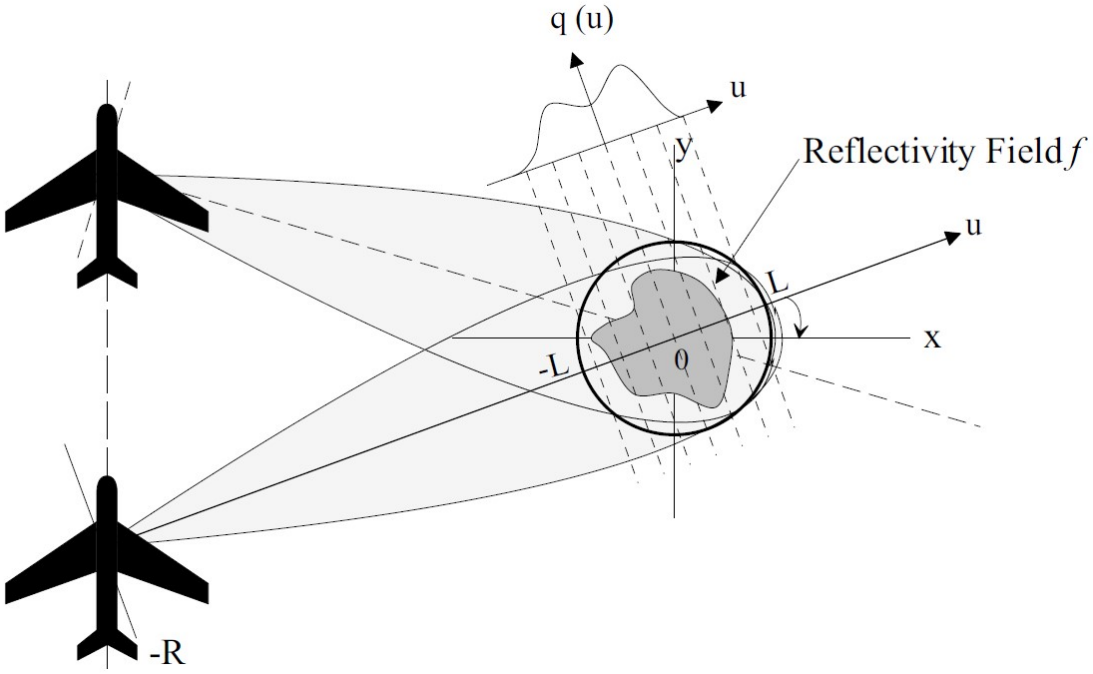

Figure 2.1 Spotlight-mode SAR imaging geometry [1].

has the following form:

$$s(t) = \begin{cases} e^{j(\omega_0 t + \alpha t^2)}, & |t| \leq \frac{T_p}{2} \\ 0, & \text{otherwise} \end{cases} \tag{2.2}$$

where ω_0 is the carrier frequency and 2α is the chirp rate. Assume the radar transmits the real part of such a signal, $\Re\{s(t)\}$. The return signal $\nu_{(\theta,x_0,y_0)}(t)$ from a differential area centered on the point (x_0, y_0) at a distance R_0 will be:

$$\nu_{(\theta,x_0,y_0)}(t) = |f(x_0,y_0)| cos\left(\omega_0\left(t - \frac{2R_0}{c}\right) + \alpha\left(t - \frac{2R_0}{c}\right)^2 + \angle f(x_0,y_0)\right) dx\ dy \tag{2.3}$$

where c is the speed of the light, and $2R_0/c$ accounts for the two-way travel time from radar to target. Here, the effect of propagation attenuation is neglected, as it can be compensated for later. The complex-valued nature of $f(x, y)$ captures both amplitude scaling and phase shifting of the transmitted waveform by the scatterers. The amplitude scaling is due to that only a fraction of the radiated energy is reflected back to the receiver. The phase shift of the reflected signal, however, could be the result of various factors, the most prominent being the shift at the air/target interface due to the difference between the dielectric constants of air and the target material. The phase shift is also due to the tendency of the RF radiation to creep around target surfaces and its ability to penetrate soft objects and be reflected from within [10]. For most SAR scenes the phase of the reflectivity at a certain location

can be modeled to be random, with a uniform probability density, and uncorrelated with the phase at other locations [11].

The return signal can be more simply written as

$$\nu_{(\theta,x_0,y_0)}(t) = \Re\left\{ f(x_0,y_0) s\left(t - \frac{2R_0}{c}\right)\right\} dx\ dy. \tag{2.4}$$

Now let us consider the return from a continuum of scatterers which are at the same distance to the radar. The return from such scatterers will be received by the radar at the same time. Let R be the distance from the radar to the center of the scene, and L be the radius of the ground region of interest, as shown in Figure 2.1. Points in the ground patch equidistant from the radar lie on an arc, but for a typical system $R \gg L$, so that this arc is nearly a straight line. This inequality is related to two conditions that must be satisfied, so that we can assume points at the same range lie on a line (i.e. so that curvature of the wavefront can be neglected). First, the range error due to this assumption for any point in the ground patch must be less than a resolution cell:

$$\frac{L^2}{2R} < \frac{c}{2B} = \rho_x, \tag{2.5}$$

where ρ_x is the range resolution, and B is the bandwidth of the transmitted waveform. Second, the range error due to this assumption at a particular point must not vary much through the aperture:

$$\frac{L^2 sin(2\theta_{max})}{R} \ll \frac{c}{2\omega_0}, \tag{2.6}$$

where θ_{max} is the maximum look angle. The derivations of these conditions can be found in [10]. We will assume that the combined return from such an "equidistant" set of scatterers is the sum of the returns that would be received from each individual scatterer. This is a common and reasonable assumption, as discussed in [39]. Let us take $q_\theta(u)$ to be such a sum of reflectivities (i.e. a line integral) at distance $R+u$ to the radar, from observation angle θ. Then, we can write the relationship between the projection $q_\theta(u)$ and $f(x,y)$ as [40]:

$$q_\theta(u) = \iint\limits_{x^2+y^2 \le L^2} \delta(u - x\cos\theta - y\sin\theta) f(x,y) dx\ dy \tag{2.7}$$

This is the standard Radon transform. With this definition, the return signal from a differential line of scatterers normal to the u axis at $u = u_0$ is given by

$$\nu_{\theta,u_0}(t) = \Re\left\{ q_\theta(u_0) s\left(t - \frac{2(R+u_0)}{c}\right)\right\} du. \tag{2.8}$$

This is the contribution to the received signal of all scatterers at range $R+u_0$. Then the return from the entire ground patch (which is what the sensor actually receives) at observation angle θ is given by the integral of ν_{θ,u_0} over u

$$\nu_\theta(t) = \Re\left\{\int_{-L}^{L} q_\theta(u) s\left(t - \frac{2(R+u_0)}{c}\right) du\right\}. \tag{2.9}$$

Taking into account that $s(\cdot)$ is a chirp pulse, we have

$$\nu_\theta(t) = \Re\left\{\int_{-L}^{L} q_\theta(u) \exp\left\{j\left[\omega_0\left(t - \frac{2(R+u)}{c}\right) + \alpha\left(t - \frac{2(R+u)}{c}\right)^2\right]\right\} du\right\} \tag{2.10}$$

on the interval

$$-\frac{T_p}{2} + \frac{2(R+L)}{c} \le t \le \frac{T_p}{2} + \frac{2(R-L)}{c}. \tag{2.11}$$

Letting $\tau_0 = 2R/c$ be the round-trip delay to the center of the ground patch and mixing with $\nu_\theta(t)$ with the reference chirp

$$\exp\left[-j(\omega_0(t-\tau_0) + \alpha(t-\tau_0)^2)\right] \tag{2.12}$$

and then low-pass filtering yields the complex signal[1]

$$\bar{r}_\theta(t) = \int_{-L}^{L} q_\theta(u) \exp\left\{j\frac{4\alpha u^2}{c^2}\right\} \cdot \exp\left\{-j\frac{2}{c}(\omega_0 + 2\alpha(t-\tau_0))u\right\} du. \tag{2.13}$$

So $\bar{r}_\theta(t)$ is the demodulated observation signal at platform position θ, as a function of time. In practice, the mixing operation described above is carried out by multiplying $\nu_\theta(t)$ with the in phase and quadrature components of the reference chirp signal, i.e.,

$$s_I(t) = \cos(\omega(t-\tau_0) + \alpha(t-\tau_0)^2) \tag{2.14}$$

$$s_Q(t) = -\sin(\omega(t-\tau_0) + \alpha(t-\tau_0)^2), \tag{2.15}$$

separately. Also note, we assume here that τ_0 is known. In practice it is only known imperfectly and this makes it necessary to have a post-processing technique in SARs known as autofocus or automatic phase-error correction [5]. The autofocus problem will be discussed in Section 2.1.4.

We will assume that the effect of the quadratic phase term $\exp\{j4\alpha u^2/c^2\}$ in (2.13) can be neglected. This is a reasonable approximation for most situations, since usually it is true that $4\alpha u^2 \ll c^2$. A more detailed analysis of this approximation

[1] Note that a constant factor of 1/2 is neglected here.

can be found in [5]. After this approximation, the observed signal is given by:

$$\begin{aligned} r_\theta(t) &= \int_{-L}^{L} q_\theta(u) \exp\left\{-j\frac{2}{c}(\omega_0 + 2\alpha(t-\tau_0))u\right\} du \\ &= \int_{-L}^{L} \exp\{-j\Omega(t)u\} du. \end{aligned} \tag{2.16}$$

This signal can be identified as the Fourier transform of the projection $q_\theta(u)$ where the spatial frequency variable is $\Omega(t) = \frac{2}{c}(\omega_0 + 2\alpha(t-\tau_0))$. Note $\Omega(t)$ is limited to a finite spatial frequency interval, because the observation duration t is limited, and the chirp rate α is finite (equivalently $s(t)$ is narrow-band). Also $\Omega(t)$ is offset from the origin of the spatial frequency plane due to ω_0. In summary, at least within the time interval considered, the processed return signal $r_\theta(t)$ carries band-pass information related to a particular line integral of the reflectivity field.

To derive the relationship between the field $f(x,y)$ and the demodulated observed signal $r_\theta(t)$, let us substitute (2.7) in the observation relationship (2.16), to obtain

$$\begin{aligned} r_\theta(t) &= \int\limits_{|u|\le L} \iint\limits_{x^2+y^2\le L^2} \delta(u - x\cos\theta - y\sin\theta) f(x,y) \exp\{-j\Omega(t)\} dx\ dy\ du \\ &= \iint\limits_{x^2+y^2\le L^2} f(x,y) \exp\{-j\Omega(t)(x\cos\theta + y\sin\theta)\} dx\ dy \end{aligned} \tag{2.17}$$

Hence, $r_\theta(t)$ is a finite (i.e. band-limited) slice at angle θ from the 2D Fourier transform of the filed $f(x,y)$. Here $\Omega(t)$ serves as the radial spatial frequency. So, there are two interpretations of $r_\theta(t)$: a 1D Fourier transform of the projections (based on (2.16)), and a slice through the 2D Fourier transform of the field (based on (2.17)). This equivalence is essentially a band-limited version of the projection slice theorem [40] from computed tomography (CT). The data $r_\theta(t)$ from all observation angles are usually called the phase histories and lie on a polar grid in the 2D frequency domain as shown in Figure 2.2.

Now let us derive the discrete observation model. (2.17) can be compactly written as $r_\theta(t) = (\mathcal{H}_\theta f(x,y))(t)$, where $\mathcal{H}_\theta$ is the continuous observation kernel. In practice, the observations at the i-th observation angle θ_i are samples $r_{\theta_i}(t_j)$ of the continuous received signal $r_{\theta_i}(t)$ at sampling times t_j. This sampling in the time domain results in sampling of the spectrum of the underlying reflectivity field. Sampling places a limit on the maximum allowable scene size that can be imaged without aliasing (in the spatial domain) [12].

Let $\mathbf{r}_{\theta_i}$ be the vector of these observed samples, $\mathbf{H}_{\theta_i}$ be a discretized approximation to the continuous observation kernel $\mathcal{H}_{\theta_i}$ and $\mathbf{f}$ be a complex-valued vector representing

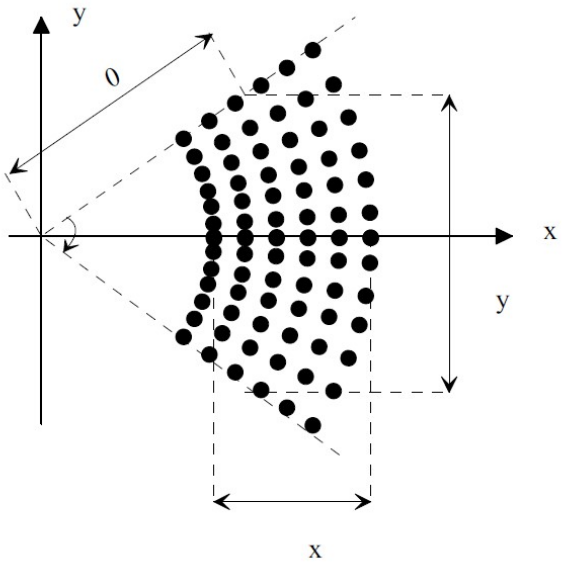

Figure 2.2 Graphical representation of an annulus segment containing known samples of the Fourier transform of the reflectivity density.

the unknown sampled reflectivity image. Then, overall, we can write:

$$\underbrace{\begin{bmatrix} \mathbf{r}_{\theta_1} \\ \mathbf{r}_{\theta_2} \\ \vdots \\ \mathbf{r}_{\theta_M} \end{bmatrix}}_{\mathbf{r}} = \underbrace{\begin{bmatrix} \mathbf{H}_{\theta_1} \\ \mathbf{H}_{\theta_2} \\ \vdots \\ \mathbf{H}_{\theta_M} \end{bmatrix}}_{\mathbf{H}} \mathbf{f} \tag{2.18}$$

where M is the total number of angular observation points. The data $\mathbf{r} \in \mathbb{C}^{KM \times 1}$ are the column-stacked sampled phase histories where K is the number of range positions. If we consider the presence of measurement noise, the observation model becomes

$$\mathbf{y} = \mathbf{H}\mathbf{f} + \mathbf{n} \tag{2.19}$$

where $\mathbf{n}$ stands for measurement noise and $\mathbf{y}$ is the noisy observations.

2.1.2 Range and Azimuth Resolution

Now, let us try to find the relationship between the achievable resolution of the SAR image and the dimensions of the annular region shown in Figure 2.2, which is specified by system parameters. We can motivate a definition of resolution in the image domain with the assumption that this annulus can be approximated by a rectangle of width $\Delta\Omega_x$ and height $\Delta\Omega_y$. Let us consider a point reflector in the scene. If we compute the Fourier transform of the scene limited to this rectangular region, and then compute an inverse Fourier transform, we would obtain a two

dimensional sinc function. The resolution of the formed image gets better as the mainlobe of this sinc gets narrower, which can be achieved by a wider the support of the rectangular region. More precisely, the first zero crossings of the sinc occur at $2\pi/\Delta\Omega_x$ and $2\pi/\Delta\Omega_y$. Hence, the resolution of two point reflectors having equal reflectivity requires that the reflectors be separated by more than $\rho_x = 2\pi/\Delta\Omega_x$ in the x (range) dimension and $\rho_y = 2\pi/\Delta\Omega_y$ in the y (cross-range or azimuth) dimension.

Let us first consider the range resolution. Assume that the width of the rectangle $2\pi/\Delta\Omega_x$ is equal to the radial width of the annular region, which is essentially the spatial frequency bandwidth of each return. We can determine the lower and upper limits of the radial extent by substituting the limits for the observation time t from (2.11) into the definition of $\Omega(t)$ to find the lowest and highest spatial frequencies:

$$\begin{aligned}\Omega_{x_l} &= \frac{2}{c}\left(\omega_0 - \alpha T_p + \frac{4\alpha L}{c}\right) \\ \Omega_{x_h} &= \frac{2}{c}\left(\omega_0 + \alpha T_p - \frac{4\alpha L}{c}\right).\end{aligned} \tag{2.20}$$

For a typical SAR, we can assume $T_p \gg 4L/c$. Hence, we can conclude that

$$\Delta\Omega_x = \Omega_{x_h} - \Omega_{x_l} \approx \frac{4\alpha T_p}{c} = \frac{4\pi B}{c} \tag{2.21}$$

where we have used the fact that the bandwidth of the transmitted pulse (in Hz) is given by $B = \alpha T_p/\pi$.

Now let us consider the cross-range (azimuth) resolution, which will be determined by $\Delta\Omega_y$. From Figure 2.2:

$$\sin\left(\frac{\Delta\theta}{2}\right) \approx \frac{\Delta\Omega_y/2}{\Omega_0} \tag{2.22}$$

where, in our case $\Omega_0 = 2\omega_0/c$. Hence, for $\Delta\theta \ll 1$ we have

$$\Delta\Omega_y \approx \frac{2\omega_0\Delta\theta}{c}. \tag{2.23}$$

Lastly, since the wavelength of the transmitted pulse is given by $\lambda = 2\pi c/\omega_0$, we can deduce the following range and cross-range resolution relationships for the system:

$$\rho_x \approx \frac{c}{2B} \tag{2.24}$$

$$\rho_y \approx \frac{\pi c}{\omega_0\Delta\theta} = \frac{\lambda}{2\Delta\theta}. \tag{2.25}$$

In conclusion, the range resolution ρ_x depends on the bandwidth of the transmitted pulse, while the cross-range resolution is determined by angular diversity of the observations and carrier frequency (and therefore equivalently wavelength) of the transmitted chirp signal.

2.1.3 SAR Image Reconstruction Methods

The problem of SAR image reconstruction is to obtain an estimate of the reflectivity density $f(x, y)$ based on the observed, pre-processed SAR data. Since the phase history data constitute a band-limited two dimensional spatial Fourier transform of the reflectivity density, the standard approach to tackle the SAR image reconstruction problem has been based on two-dimensional fast Fourier transform (FFT). These 2D FFT based methods are therefore termed as *conventional* methods. However, these 2D FFT-based reconstruction methods are ideal only when perfect data are available throughout the spatial frequency domain, which is not the case in a practical measurement scenario, primarily due to finite bandwidth of the transmitted signal and the finite range of look angles. Therefore, the problem in (2.19) is ill-posed [41], and can be considered as ill-conditioned to a certain extent depending on the specifics of the observation scenario. Consequently, (2.19) can only be solved satisfactorily by incorporating some sort of regularization into the inversion process. In this section, we will describe two well-known conventional methods, namely, polar format algorithm (PFA) and filtered backprojection (FBP), as well as regularization-based image reconstruction methods.

2.1.3.1 Conventional Reconstruction Methods

Conventional methods are based on the inverse operator for the case when perfect data are available throughout the spatial frequency domain. These methods have no explicit mechanism to counter any imperfection in the data. Although there are algorithmic differences between the two methods, the reconstructions they produce are similar.

Polar Format Algorithm In polar format algorithm (PFA), the known data samples are first interpolated to a Cartesian grid, assuming unknown samples to be zero. Then, an inverse 2-D FFT is employed and the magnitude of the reconstructed complex image is displayed for viewing. To reduce sidelobe levels, the data can be windowed before FFT processing. This is the most common SAR image reconstruction algorithm.

Filtered Backprojection Filtered backprojection algorithm (FBP) [10, 40, 42] is suggested by the tomographic formulation of SAR [10]. The derivation of FBP is through the 2D inverse Fourier transform in polar coordinates. The radial slices in the frequency domain are then recognized as 1-D Fourier transforms of the projections of the field at the corresponding angle, by virtue of the projection slice theorem [40]. This way the double Fourier integral is reduced to two sequential operations: first the data at each observation angle are filtered by a ramp filter, and then the results are backprojected to obtain a reconstruction. FBP is the algorithm that is currently used in commercial CT scanners.

2.1.3.2 Regularization-Based Reconstruction Methods

In image reconstruction and restoration problems, the goal is to find an estimate of a 2D field from its indirect observations. Hence, we can view image reconstruction and restoration problems as general observation problems which we meet in most situations of engineering interest. We will concentrate on problems where the mathematical relationship between the measurements and the field is governed by a linear integral equation, i.e., as in (2.19). This simple observation model that we derived for SAR imaging is analogous to those of many other engineering problems. At first look, it might seem easy to find an estimate $\hat{\mathbf{f}}$ of $\mathbf{f}$ with a simple matrix inversion, however that certainly is not possible in general, e.g., the matrix may not even be square. There are four main issues that this approach can not handle [43]:

1. Due to the observation noise, there may not exist any $\mathbf{f}$ which solves this equation exactly.

2. There may be more than one $\mathbf{f}$ which satisfy these equations, hence the solution may not be unique.

3. The estimate $\hat{\mathbf{f}}$ is desired to remain stable despite the perturbations in the observations.

4. It is desirable to include any *a priori* information about $\mathbf{f}$ in the inversion process, however this approach is only data-driven.

Least-squares solution can overcome the first problem mentioned above. The solution is the best fit to the observed data in the least-squares sense:

$$\hat{\mathbf{f}}_{\mathsf{LS}} = \underset{\mathbf{f}}{\operatorname{argmin}} \|\mathbf{y} - \mathbf{H}\mathbf{f}\|_2^2 \tag{2.26}$$

where $\|\cdot\|_2$ denotes the ℓ_2 norm. If $\mathbf{H}$ has full column rank, the estimate is unique

and is obtained as

$$(\mathbf{H}^H\mathbf{H})\hat{\mathbf{f}}_{\mathsf{LS}} = \mathbf{H}^H\mathbf{y}. \tag{2.27}$$

However, when the null-space of $\mathbf{H}$ is not empty, the least-squares solution is not unique. A common approach to address this problem is to choose the field with minimum norm, among the set of least-squares solutions, as the estimate of the true field $\mathbf{f}$:

$$\hat{\mathbf{f}}^{+} = \underset{\hat{\mathbf{f}}_{\mathsf{LS}}}{\operatorname{argmin}} \left\|\hat{\mathbf{f}}_{\mathsf{LS}}\right\|_2 \tag{2.28}$$

which is called as the generalized solution. Although generalized solution provides, a simple, reasonable way to deal with the first two issues mentioned in the list above, it does not directly address the third and fourth issues. Particularly, if the model matrix $\mathbf{H}$ is ill-conditioned, i.e., the ratio of the largest eigenvalue to the smallest is very large, small changes in the data lead to large changes in the solution.

These issues, which cannot be resolved by the generalized solution, can be addressed using regularization. Regularization allows us to include any prior information to stabilize the solution in the presence of noisy data, and allow reasonable estimates.

Tikhonov Regularization One of the most common regularization methods is Tikhonov regularization [44, 45]. In this method, the prior information on the field is incorporated by including an additional term to the least-squares cost function:

$$\hat{\mathbf{f}}_{\mathsf{Tik}} = \underset{\mathbf{f}}{\operatorname{argmin}} \|\mathbf{y} - \mathbf{H}\mathbf{f}\|_2^2 + \lambda^2 \|\mathbf{P}\mathbf{f}\|_2^2 \tag{2.29}$$

where $\mathbf{P}$ is a matrix, and λ is a scalar. The first term in (2.29) is a data-fidelity term. The second term, through which the prior information about $\mathbf{f}$ is incorporated, is called the regularizer. The parameter λ determines the weight of the prior knowledge in the estimation process.

The choice of the matrix $\mathbf{P}$ is determined by which information about the field we want to incorporate and the simplest choice would be an identity matrix. In this case, large values in the reconstruction would be penalized by the regularizer. If $\mathbf{P}$ is chosen as 2D derivative (gradient) operator, then its effect will be to penalize roughness on the solution, which essentially enforces the final reconstruction to be smooth.

By taking the gradient of (2.29) with respect to $\mathbf{f}$ and equate it to zero, we reach the following set of linear equations as the solution for the Tikhonov regularization:

$$(\mathbf{H}^H\mathbf{H} + \lambda^2\mathbf{P}^H\mathbf{P})\hat{\mathbf{f}}_{\mathsf{Tik}} = \mathbf{H}^H\mathbf{y} \tag{2.30}$$

When the null spaces of $\mathbf{H}$ and $\mathbf{P}$ are distinct, there exists a unique, closed-form solution to (2.30).

Non-Quadratic Regularization The cost function of Tikhonov regularization (2.29) is a quadratic function of $\mathbf{f}$. Hence, (2.30) leads to a linear function of $\mathbf{f}$, which in turn corresponds to a linear processing of the data $\mathbf{y}$ for image restoration or reconstruction. Although it is desirable to have such a linear processing as it ensures computational efficiency, it fails to obtain more powerful results that are only possible if nonlinear methods are allowed [43], e.g., in many imaging applications the data are expected to be sparse as themselves, or in a transform domain, and sparsity cannot be effectively enforced within a linear framework. Thus, let us consider more general problems of the following form:

$$\hat{\mathbf{f}}_{\mathsf{NQ}} = \underset{\mathbf{f}}{\operatorname{argmin}} \|\mathbf{y} - \mathbf{H}\mathbf{f}\|_2^2 + \lambda^2 \sum_{i=1}^{M} \psi((\mathbf{P}\mathbf{f})_i) \tag{2.31}$$

where M is the length of the vector $\mathbf{P}\mathbf{f}$, and $(\mathbf{P}\mathbf{f})_i$ denotes its i-th element. Note that when $\psi(x) = x^2$, (2.31) reduces to the Tikhonov cost function in (2.29), however $\psi(x)$ is in general non-quadratic. Many well-known regularization approaches fall into the category of non-quadratic regularization, e.g., maximum entropy [46], and the total variation [47,48] methods. Note that unlike Tikhonov regularization, (2.31) does not lead to a closed-form solution in general, hence numerical methods must be used to find $\hat{\mathbf{f}}_{\mathsf{NQ}}$. Half quadratic splitting (HQS) [49,50] is one such method that can be used to solve (2.31).

The sparsity-promoting formulation for the case that the field $\mathbf{f}$ is expected to be sparse would be in the form

$$\hat{\mathbf{f}}_{\mathsf{Sparse}} = \underset{\mathbf{f}}{\operatorname{argmin}} \|\mathbf{y} - \mathbf{H}\mathbf{f}\|_2^2 + \lambda^2 \|\mathbf{f}\|_p^p \tag{2.32}$$

with $p \leq 1$ being a common choice. See Figure 2.3 for an illustration for the case of a scalar, real-valued version of $\|\mathbf{f}\|_p^p$, i.e., $|f|^p$ for various choices of p. When we view these plots as penalty functions, we deduce that as the value of p gets smaller, the relative penalty on large values of f reduces. In the SAR imaging problem, this effect helps the preservation and enhancement of strong scatterers in the scene, while still suppressing artifacts. On the other hand, small p values are more punishing for the smaller values of f, hence enforcing sparsity. However, for the values of $p < 1$, the penalty functions become concave, thus minimization of objective functions containing such terms can be challenging. Therefore the choice of $p = 1$ has become quite popular as it can enforce sparsity while also generating a

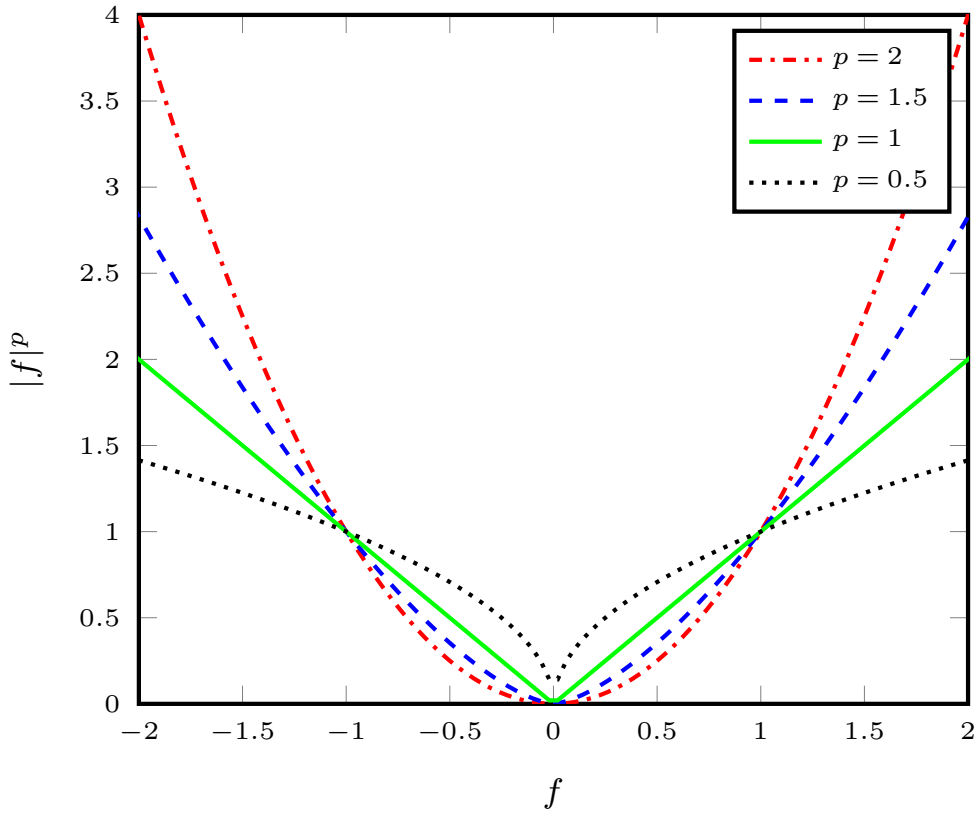

Figure 2.3 Behavior of the function $|f|^p$ for various choices of p.

convex penalty function.

The formulation for the total variation regularization is given as:

$$\hat{\mathbf{f}}_{\mathsf{TV}} = \underset{\mathbf{f}}{\operatorname{argmin}} \|\mathbf{y} - \mathbf{H}\mathbf{f}\|_2^2 + \lambda^2 \|\nabla \mathbf{f}\|_1 \tag{2.33}$$

where ∇ is the discrete gradient operator. The regularizer in (2.33) preserves strong edges and produces improved reconstruction quality in piece-wise smooth regions.

Feature-Enhanced SAR Imaging A feature-enhanced SAR image reconstruction approach based on non-quadratic regularization was proposed in [1, 12]. The overall SAR image formation in this case is modeled by the following optimization problem:

$$\hat{\mathbf{f}}_{\mathsf{FE}} = \underset{\mathbf{f}}{\operatorname{argmin}} \|\mathbf{y} - \mathbf{H}\mathbf{f}\|_2^2 + \lambda_1 \|\mathbf{f}\|_p^p + \lambda_2 \|\nabla |\mathbf{f}|\|_p^p \tag{2.34}$$

where ∇ is the 2D discrete gradient operator. $|\mathbf{f}|$ denotes the vector of magnitudes of the complex-valued vector $\mathbf{f}$. The scalar parameters λ_1 and λ_2 determine the weights of the corresponding terms in the estimation process. The first term in (2.34) is the data-fidelity term that ensures the estimate $\hat{\mathbf{f}}_{\mathsf{FE}}$ is consistent with the data. The second and third terms in (2.34) incorporate prior information regarding

both the behavior of the field $\mathbf{f}$, and the nature of the features of interest in the resulting reconstructions. These terms are aimed at enhancing point-based and region-based features respectively. The relative magnitudes of the parameters λ_1 and λ_2 determine the relative emphasis on these two types of features. Note for the region-based feature enhancement that the smoothness is imposed on the magnitude of the reflectivity field, as the correlation in a homogeneous region of $\mathbf{f}$ in SAR is due to the similarity of backscatter power, which is better represented in the magnitude of $\mathbf{f}$ than its real and imaginary parts [12].

2.1.4 SAR Autofocus Problem & Phase Errors

In SAR systems, the demodulation time τ_0 at every aperture position[2], which is the time required for the signal transmitted by the SAR sensor to propagate from the SAR platform to the field and return, is required to be known precisely, in order to obtain the data used for imaging from the returned signals. The inexact knowledge of the demodulation time causes phase errors in the SAR data which result in defocusing of the reconstructed images [5]. The inexact measurement of the distance between the SAR platform and the scene due to SAR platform position uncertainties, or random delays in the signal due to propagation in atmospheric turbulence are among the most common causes of demodulation time errors. As these errors cause defocusing in the reconstructed image, this problem is known as SAR autofocus problem, and phase error correction methods are also called autofocus methods. In addition to the uncertainties related to the SAR platform, moving targets on the ground can also cause phase errors. However, this kind of phase errors would affect the reconstructed image locally, i.e., only around the moving target, hence these phase errors cause space-variant defocusing.

In current SAR systems, inertial measurement units (IMUs) are used to measure the distance R between the SAR platform and the patch center. However, even with high quality IMUs, the measurement of R might not be within the maximum tolerated error margin. Inexact measurements of R cause demodulation time errors, which in turn results in phase errors in the SAR data obtained after the preprocessing of the returned signal. Conventional approaches to tackle this problem have been to increase the accuracy of IMUs and postprocessing the reconstructed SAR image to remove phase errors. These postprocessing methods are generally termed as autofocusing techniques, and they have advantages over improving IMUs' accuracy. Improving accuracy of the IMU systems can only help reducing the effects of demodulation time errors caused by platform position uncertainties, however it

[2]Recall that in Section 2.1.1, the demodulation time was defined as $\tau_0 = 2R/c$ where R is the distance from the SAR platform to the patch center.

would be of no help against phase errors caused by atmospheric turbulence. Autofocusing techniques can remove the effects of demodulation errors independent of the error source, while also eliminating the significant hardware costs associated with ultra-high-accuracy navigation systems [5].

In Section 2.1.1, we have derived the SAR observation model without considering demodulation time errors, i.e., with the assumption that the demodulation time at each aperture position is known exactly. Demodulation time errors can be modeled as constant phase errors on each range compressed pulse. Hence, if we let ϵ denote the demodulation time error, during preprocessing, the received signals are multiplied with

$$s_I(t) = \cos(\omega(t-\tau_0+\epsilon)+\alpha(t-\tau_0+\epsilon)^2) \tag{2.35}$$

$$s_Q(t) = -\sin(\omega(t-\tau_0+\epsilon)+\alpha(t-\tau_0+\epsilon)^2), \tag{2.36}$$

instead of the expressions in (2.14) and (2.15)[3]. Then, the output of the preprocessing step becomes

$$Z_\epsilon(\Omega(t)) = r_{\theta_\epsilon}(t) = \exp\{(-j\epsilon^2\alpha)(j\frac{\epsilon c}{2}\Omega(t))\} \int\limits_{|u|\leq L} q_\theta(u)\exp\{-j\Omega(t)u\}du. \tag{2.37}$$

Thus, the corrupted and error-free phase history expressions are related as

$$Z_\epsilon(\Omega(t)) = \exp\{(-j\epsilon^2\alpha)(j\frac{\epsilon c}{2}\Omega(t))\}Z(\Omega(t)). \tag{2.38}$$

$\epsilon^2\alpha \ll 1$, and hence we can assume $\exp\{-j\epsilon^2\alpha\} \approx 1$. Then (2.38) becomes

$$Z_\epsilon(\Omega(t)) = \exp\{j\frac{\epsilon c}{2}\Omega(t)\}Z(\Omega(t)). \tag{2.39}$$

Hence, $Z_\epsilon(\Omega(t))$ is simply $Z(\Omega(t))$ altered by a linear phase term. Substituting $\Omega(t) = \frac{2}{c}(\omega_0 + 2\alpha(t-\tau_0))$ into (2.39), we get

$$Z_\epsilon(\Omega(t)) = \exp\{(j\epsilon\omega_0)(j\epsilon(2\alpha(t-\tau_0)))\}Z(\Omega(t)). \tag{2.40}$$

The value of the term $2\alpha(t-\tau_0)$ is in general much smaller compared to the value of ω_0, and hence can be neglected. Thus we would obtain

$$Z_\epsilon(\Omega(t)) = \exp\{j\phi\}Z(\Omega(t)) \tag{2.41}$$

where $\phi = \epsilon\omega_0$ is the phase error. Note that ϕ is different at every aperture position,

[3]Note that the development in this section closely follows the one in [51].

therefore its effect on the reconstructed image is along the cross-range. The implication of such an error in the image domain is the convolution of each range line of the image with a 1D blurring kernel in the cross-range direction. Hence, such phase errors cause defocusing of the image in the cross-range direction [52].

Although most phase errors encountered are 1D cross-range varying functions, it is also possible to encounter both range and cross-range varying 2D phase errors. For example, low frequency UWB SAR systems may suffer from severe propagation effects that can appear through the ionosphere, including Faraday rotation, dispersion, and scintillation. Dispersion imposes an unknown phase error on the transmitted chirp. On a single pulse basis, dispersion would cause the ideal impulse response function to defocus in the range direction. Furthermore, pulse-to-pulse variations in the dispersion and propagation delay lead to defocus in the cross-range direction. Because these unknown phase errors change over the synthetic aperture, the 2D phase history becomes corrupted by a fully coupled 2D phase error [53]. In principle, 2D phase errors can be handled in two sub-categories, namely, separable and non-separable errors, nevertheless 2D separable phase errors are not common in practice.

2.1.4.1 2D Non-separable Phase Errors

In the presence of 2D non-separable phase errors, all sample points of the phase history data are perturbed with different and potentially independent phase errors. Let $\mathbf{R} \in \mathbb{C}^{K \times M}$ denote the sampled phase history data[4], and $\mathbf{\Phi}_{2D-ns}$ be a 2D non-separable phase error function. The relationship between the phase-corrupted and error-free phase histories are as follows:

$$\mathbf{R}_{\epsilon}(k,m) = e^{j\mathbf{\Phi}_{2D-ns}(k,m)}\mathbf{R}(k,m) \tag{2.42}$$

where $\mathbf{R}_{\epsilon}$ denotes the phase-corrupted phase history data, and $k \in 1,2,\ldots,K$ and $m \in 1,2,\ldots,M$ denote range and cross-range sample positions, respectively. To express this relationship in terms of the observation model, first we define the vector ϕ_{2D-ns} as

$$\boldsymbol{\phi}_{2D-ns} = [\boldsymbol{\phi}_{2D-ns}(1), \boldsymbol{\phi}_{2D-ns}(2), \ldots, \boldsymbol{\phi}_{2D-ns}(KM)]^T \tag{2.43}$$

which is created by concatenating the columns of the phase error matrix $\mathbf{\Phi}_{2D-ns}$ under each other. Using the corresponding vector forms, the relationship in (2.42)

[4]Recall that the column-stacked vector version of sampled phase histories were denoted by $\mathbf{r} \in \mathbb{C}^{KM \times 1}$, in Section 2.1.1.

becomes

$$\mathbf{r}_\epsilon = \mathbf{D}_{2D-ns}\mathbf{r} \tag{2.44}$$

where $\mathbf{D}_{2D-ns} \in \mathbb{C}^{KM\times KM}$ is a diagonal matrix in the form:

$$\mathbf{D}_{2D-ns} = \text{diag}\{e^{\phi_{2D-ns}}\} \tag{2.45}$$

In terms of observation model matrices, the relationship in (2.44) is as follows:

$$\mathbf{H}(\boldsymbol{\phi}_{2D-ns})\mathbf{f} = \mathbf{D}_{2D-ns}\mathbf{H}\mathbf{f} \tag{2.46}$$

where $\mathbf{H}$ is the initially assumed model matrix by the imaging system, and $\mathbf{H}(\boldsymbol{\phi}_{2D-ns})$ is the model matrix that takes the phase errors into account.

2.1.4.2 2D Separable Phase Errors

A 2D separable phase error function is composed of range varying and cross-range varying 1D phase error functions as follows:

$$\boldsymbol{\Phi}_{2D-s}(k,m) = \boldsymbol{\xi}(k) + \boldsymbol{\gamma}(m). \tag{2.47}$$

Here, $\boldsymbol{\xi} \in \mathbb{C}^{K\times 1}$ represents the range varying phase error, and $\boldsymbol{\gamma} \in \mathbb{C}^{M\times 1}$ represents the cross-range varying phase error. The vector $\boldsymbol{\phi}_{2D-s} \in \mathbb{C}^{KM\times 1}$ for 2D separable phase errors is obtained by concatenating the columns of $\boldsymbol{\Phi}_{2D-s}$ as follows:

$$\boldsymbol{\phi}_{2D-s} = \Bigg[\underbrace{\boldsymbol{\xi}(1)+\boldsymbol{\gamma}(1)}_{\boldsymbol{\phi}_{2D-s}(1)}, \ldots, \underbrace{\boldsymbol{\xi}(K)+\boldsymbol{\gamma}(1)}_{\boldsymbol{\phi}_{2D-s}(K)}, \underbrace{\boldsymbol{\xi}(2)+\boldsymbol{\gamma}(1)}_{\boldsymbol{\phi}_{2D-s}(K+1)}, \ldots, \underbrace{\boldsymbol{\xi}(1)+\boldsymbol{\gamma}(M)}_{\boldsymbol{\phi}_{2D-s}((M-1)K+1)}, \ldots, \underbrace{\boldsymbol{\xi}(K)+\boldsymbol{\gamma}(M)}_{\boldsymbol{\phi}_{2D-s}(KM)} \Bigg]^T \tag{2.48}$$

A 2D separable phase error function affects the observation model matrix in the as follows:

$$\mathbf{H}(\boldsymbol{\phi}_{2D-s})\mathbf{f} = \mathbf{D}_{2D-s}\mathbf{H}\mathbf{f} \tag{2.49}$$

where $\mathbf{D}_{2D-s}$ is given as

$$\boldsymbol{\phi}_{2D-s} = [\boldsymbol{\phi}_{2D-s}(1), \boldsymbol{\phi}_{2D-s}(2), \ldots, \boldsymbol{\phi}_{2D-s}(KM)]^T. \tag{2.50}$$

2.1.4.3 1D Phase Errors

In the case of 1D phase errors, for a particular cross-range position the phase error is the same at all range positions. Let $\boldsymbol{\phi}_{1D} \in \mathbb{C}^M$ be a vector whose elements are cross-range varying phase errors for every aperture position $m = 1, 2, \ldots, M$:

$$\boldsymbol{\phi}_{1D} = [\boldsymbol{\phi}_{1D}(1), \boldsymbol{\phi}_{1D}(2), \ldots, \boldsymbol{\phi}_{1D}(M)]^T . \tag{2.51}$$

Then, the relationship between the error-free and the phase-corrupted data can be expressed as:

$$\mathbf{H}(\boldsymbol{\phi}_{1D})\mathbf{f} = \mathbf{D}_{1D}\mathbf{H}\mathbf{f} \tag{2.52}$$

where $\mathbf{D}_{1D}$ is given as

$$\mathbf{D}_{1D} = \operatorname{diag}\left\{ \left[\underbrace{e^{j\boldsymbol{\phi}_{1D}(1)}, \ldots, e^{j\boldsymbol{\phi}_{1D}(1)}}_{K}, \underbrace{e^{j\boldsymbol{\phi}_{1D}(2)}, \ldots, e^{j\boldsymbol{\phi}_{1D}(2)}}_{K}, \ldots, \underbrace{e^{j\boldsymbol{\phi}_{1D}(M)}, \ldots, e^{j\boldsymbol{\phi}_{1D}(M)}}_{K} \right] \right\}. \tag{2.53}$$

Note that, in the case of 1D phase errors, there are M unknowns, while in 2D separable and non-separable phase error cases, there are $M+K$ and MK unknowns, respectively. Hence, 2D non-separable phase error correction is a more challenging task compared to the others.

2.1.5 Existing Autofocus Methods

SAR autofocus has been an active area of research over the years [52, 54–104]. In early studies, researchers have focused on 1D phase errors, and tackling 2D separable and non-separable phase errors is a relatively recent research area [52, 75–77, 79, 96]. Most of the existing autofocusing algorithms perform postprocessing, i.e., they try to eliminate the effects of phase errors from conventionally reconstructed images. Recently, algorithms for joint image reconstruction and phase error correction have also been proposed [52, 75, 76, 79, 81].

2.1.5.1 Conventional Methods

Two methods, namely, inverse filtering and subaperture-based methods, are considered as conventional methods, as they are the earliest attempts to tackle phase errors, and have simple formulations with easy implementations.

Inverse Filtering In inverse filtering, the amount of defocus on a single point target is used to estimate phase errors. As mentioned before, the effect of 1D phase errors in the image domain can be viewed as convolution of each range line of the image with a 1D blurring kernel in the cross-range direction. This effect can be expressed as

$$\tilde{\mathbf{F}}(a,b) = \tilde{\mathbf{h}}(b) \circledast \mathbf{F}(a,b) \tag{2.54}$$

where

$$\tilde{\mathbf{h}}(b) = \mathfrak{F}_m^{-1} e^{j\phi(m)}. \tag{2.55}$$

Here, $\tilde{\mathbf{F}}$ denotes the defocused version of the image $\mathbf{F}$[5], $\mathfrak{F}^{-1}$ denotes inverse Fourier transform, a and b are range and cross-range image domain indices, respectively, $\circledast$ denotes circular convolution operation and, m is the cross-range index in the frequency domain. In inverse filtering approach, it is assumed that a single point target can be isolated in the defocused image. This technique estimates phase errors by finding such an isolated strong point target in the defocused image and then using the defocus information on that point target.

Subaperture-based Methods In these methods, the data from subapertures are used to estimate phase errors. The main assumption of these methods is that the phase error function is a polynomial function of the aperture position. For example, in case of quadratic phase error, the aperture is divided into two subapertures, then in each subaperture, the phase error is approximated by a linear function. Since a linear phase error function only shifts the image proportional to its slope, the two low-resolution defocused images reconstructed from the two subaperture data are shifted versions of the original image in reverse directions [51].

2.1.5.2 Phase Gradient Autofocus (PGA)

In phase gradient autofocus (PGA) [57, 61], the phase error function is estimated by averaging across many range lines, as every target in the image is corrupted by the same blur function. This averaging operation is performed using maximum likelihood estimation formulation. Unlike subaperture-based methods, PGA is a non-parametric algorithm. The algorithm aims to isolate a number of single targets in the image to estimate phase error from those targets. Single targets are isolated via center shifting and windowing operations. PGA selects the strongest target on each range line and circularly shifts it to the scene center, as using the targets with strong reflectivities provides a much better phase error estimation than using the targets with weak reflectivities. This shifting operation produces a new image. In

[5] $\mathbf{F}$ is the matrix version of $\mathbf{f}$, i.e., another interpretation is that $\mathbf{f}$ is a column-stacked vector generated from $\mathbf{F}$.

this new image, all of the targets which will be used in the estimation process, lie in the center of the cross-range dimension. In the next step, a windowing operation is performed to preserve the information contained in the blur footprints of the center-shifted targets and reject information from all other surrounding targets with weak reflectivities. After center-shifting, the necessary information, contained in the support of the blur footprint, is extracted through windowing. In this stage, determining the window width is crucial, as choosing a width smaller than the blur footstep would prohibit capturing all of the necessary information, while choosing the width larger than the blur footprint would increase noise levels.

2.1.5.3 Multi-Channel Autofocus (MCA)

Multi-channel autofocus MCA [74] employs a non-iterative algorithm which finds the focused image using a basis formed from the defocused image, relying on a condition on the image support to obtain a unique solution. In particular, MCA estimates 1D phase error functions by directly solving a set of linear equations obtained through an assumption that there are zero-reflectivity regions in the scene to be imaged. When this is not precisely satisfied, presence of a low-return region is exploited, and the phase error is estimated by minimizing the energy of the low-return region. When the desired conditions are satisfied, MCA performs very well. However, in scenarios involving low-quality data, e.g., due to low SNR, the performance of MCA degrades. A number of modifications to MCA have been proposed, including the incorporation of sharpness metric optimization into the framework [74], and the use of a semi-definite relaxation based optimization procedure [83] for better phase error estimation performance [51].

2.1.5.4 Sparsity-driven Autofocus (SDA)

In sparsity-driven autofocus (SDA) [52], phase error correction is performed jointly with image reconstruction, rather than as a postprocessing step. The overall process is formulated as a regularized optimization with the cost function

$$J(\mathbf{f}, \boldsymbol{\phi}) = \|\mathbf{y} - \mathbf{H}(\boldsymbol{\phi})\mathbf{f}\|_2^2 + \lambda \|\mathbf{f}\|_1 \tag{2.56}$$

where λ is the regularization parameter, which determines the emphasis on the sparsity-promoting ℓ_1-norm prior, and $\boldsymbol{\phi}$ is the correct phase of the phase history data. Note that, unlike (2.19), in SDA the model matrix $\mathbf{H}$ depends on $\boldsymbol{\phi}$, rather than being constant. This optimization problem is solved through a coordinate descent based numerical iterative algorithm. This algorithm jointly minimizes the cost function with respect to $\mathbf{f}$ and $\boldsymbol{\phi}$. Particularly in each iteration, there are image formation, phase error estimation, and phase error correction steps. In image

formation step, $\boldsymbol{\phi}$ is kept constant and $\mathbf{f}$ is estimated, then in the phase error estimation step, $\boldsymbol{\phi}$ is updated using the new estimate of $\mathbf{f}$, and finally in the phase error correction step, the model matrix $\mathbf{H}$ is updated according to the updated $\boldsymbol{\phi}$. These three steps are performed iteratively until convergence, or stopping criteria are satisfied. Algorithm 1 summarizes the SDA process. The success of SDA is partially attributed to the use of non-quadratic regularization, as it helps overall algorithm to exhibit robustness to small perturbations on the observation model matrix [105]. In SDA, separate algorithms have been proposed for the cases of 1D phase errors, 2D separable phase errors, and 2D non-separable phase errors.

Algorithm 1: Sparsity-driven autofocus algorithm.

Require: $\mathbf{H}(\boldsymbol{\phi}^{(0)})$, ϵ, N.
  $\mathbf{f}^{(0)} \leftarrow \mathbf{H}(\boldsymbol{\phi}^{(0)})^H \mathbf{y}$
  while $\frac{\|\mathbf{f}^{(n+1)} - \mathbf{f}^{(n)}\|}{\|\mathbf{f}^{(n)}\|} \geq \epsilon$ and $n \leq N$ **do**
    $\hat{\mathbf{f}}^{(n+1)} = \text{argmin}_{\mathbf{f}} J(\mathbf{f}, \boldsymbol{\phi}^{(n)})$
    $\hat{\boldsymbol{\phi}}^{(n+1)} = \text{argmin}_{\boldsymbol{\phi}} J(\mathbf{f}^{(n+1)}, \boldsymbol{\phi})$
    Update $\mathbf{H}(\boldsymbol{\phi}^{(n+1)})$ using $\boldsymbol{\phi}^{(n+1)}$ and $\mathbf{H}(\boldsymbol{\phi}^{(n)})$.
    $n \leftarrow n+1$
  end while

2.1.6 SAR ATR

Automatic target recognition (ATR) is an important application of SAR imaging. In ATR, the task is to automatically identify the regions-of-interest (ROIs) that contain targets and then to determine which classes targets belong to. ATR tasks are considered as highly challenging, as SAR images are extremely sensitive to target orientation. Figure 2.4 shows the conventionally reconstructed images of T72 tank in the MSTAR dataset [2] for different orientations relative to the imaging platform.

SAR ATR has been an active and popular research area for decades [106–126]. The process of SAR ATR generally includes four steps; detection, discrimination, feature extraction, and classification [119]. In the detection step, potential ROIs are located, and then falsely detected ROIs are discarded in the discrimination step. In the feature extraction step, distinctive features are extracted from the detected ROIs, and then finally classification task is performed using these extracted features in the last step. In SAR ATR literature, the emphasis is mostly on last two steps with the assumption that the ROIs including targets are already detected and discriminated. In early works, the classification task was done without feature extraction, i.e., by directly using reconstructed images, with pre-defined classifiers. Later studies first introduced feature extraction with hand-picked features, and then learned classi-

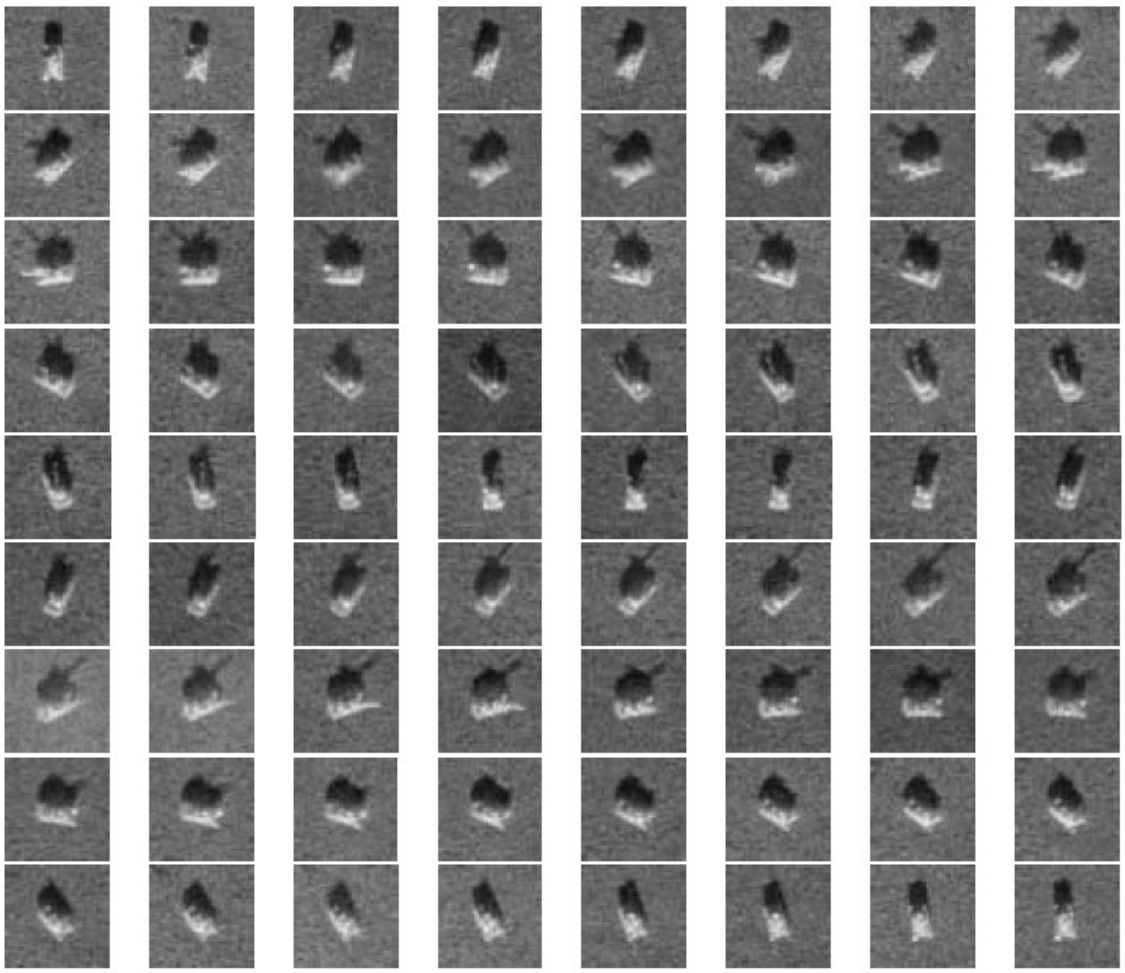

Figure 2.4 SAR images of T72 tank in the MSTAR dataset [2] for different orientations relative to the radar platform. From top left to bottom right, each image corresponds to an orientation angle from 0° to 355°, with 5° increments.

fiers, e.g., using dictionary learning, rather than pre-defined ones. Recent studies combined these two steps using convolutional neural networks (CNNs). The main advantage of using a CNN to learn features rather than using hand-picked features is that the CNN can learn more useful patterns whose existences are not necessarily apparent in the image.

2.2 Deep Learning Background

This section provides background information on deep learning and presents a brief review on the use of deep learning tools within SAR imaging and SAR ATR frameworks.

2.2.1 Brief History of Deep Learning

Deep learning can be considered as one of the solutions to a variety of artificial intelligence (AI) problems. Although it has become extremely popular only in the last decade, deep learning has a long history that dates back to 1940s. However, it has been called with different names at different time windows, i.e., cybernetics in 1940s-1960s, connectionism in the 1980s to early 1990s, artificial neural networks in the 1990s-200s, and only recently, the name 'deep learning' has become widespread [127].

The idea of building a machine that can think is at least over two millennia old and is usually attributed to ancient Greeks [127]. The earliest primitive attempts to build such machines dates around the medieval times, e.g., polymaths such as al-Jazari [128] and Leonardo da Vinci [129] designed machines that are regarded as the ancestors of modern robots.

Although the ideas that evolved into deep learning has emerged around the time that first computers were built, these ideas did not draw much attention until recently due to two main reasons: 1) Computers did not have enough computational resources that would satisfy the needs to train deep neural networks; and 2) deep neural networks need large amounts of data to train, which has only been available after the recent digitization of the society [127].

2.2.2 Deep Neural Network Layout Types

In this section, we will describe four common deep neural network layouts, namely, multilayer perceptron (MLP), autoencoder (AE), convolutional neural network (CNN), and recurrent neural network (RNN).

2.2.2.1 Multilayer Perceptron (MLP)

The perceptron, which was capable of binary classification, was introduced in 1958 [130]. MLPs are extensions of perceptrons which are designed for more complicated tasks. An MLP consists of an input layer, one or more hidden layers, and an output layer. The nodes in the layers of MLPs, apart from the input layer, are made of perceptrons with nonlinear activation functions, and are often called as neurons. Figure 2.5 shows an MLP with an input layer with dimension of 3, an output layer with dimension of 2, and two hidden layers with 4 and 3 neurons, respectively. MLPs are also called as feedforward neural networks, as information only flows from input layer to output layer, i.e., there are no feedback connections in which the output is fed back into the network. MLPs are considered to be main or 'vanilla' neural

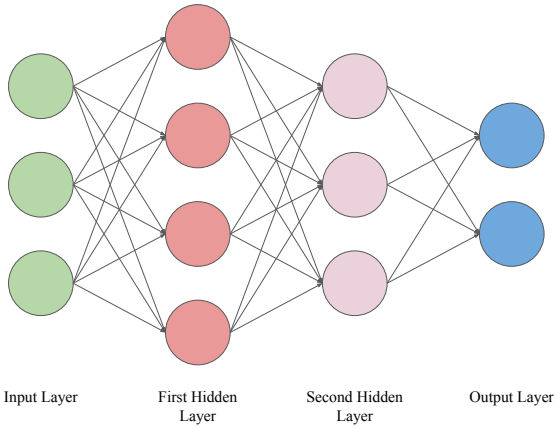

Figure 2.5 An illustration of a multilayer perceptron with two hidden layers.

network as other layouts are derived from MLPs.

2.2.2.2 Autoencoder (AE)

Autoencoders (AE)s are neural networks that try to mimic their input at their output. AEs can be considered as consisting of two parts, i.e., encoder and decoder. The encoder aims to learn a mapping from the input to a transform domain, which typically has a lower dimensionality than the input, and the task of the decoder is to reconstruct the input at the output from the transformed version of the input. However, AEs are not generally used to copy the input at the output, rather they are designed to be unable to learn to copy perfectly. They are usually restricted in ways to ensure that they will only copy approximately, and only copy those inputs which resembles the training data [127]. These restrictions usually lead AEs to learn useful properties of the data. Figure 2.6 shows an illustration of an AE with one hidden layer. AEs can be used in many tasks, e.g., dimensionality reduction, feature learning, manifold learning, information retrieval, and denoising.

2.2.2.3 Convolutional Neural Network (CNN)

Convolutional neural networks (CNNs) are a special kind of MLPs which are suitable for data that has grid-like topology, e.g., images. The earliest CNN-like design was Neocognitron [131] which was built for shift-invariant pattern recognition in 1980s. CNNs are neural networks in which at least in one layer, the matrix multiplication is replaced with the convolution operation. Unlike MLPs, in CNNs, nodes in a layer are only connected to a subset of nodes from the previous and the next layers, hence CNNs have sparse connectivity. Also, within convolutional layers, same parameters are used for each node. Sparse interactions and parameter sharing help with both efficient memory use and translational and shift-invariance. Figure 2.7 shows a CNN

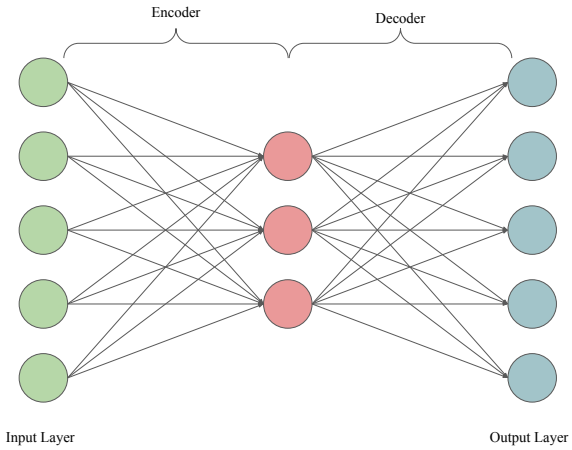

Figure 2.6 An illustration of an autoencoder with a single hidden layer.

with the convolutional kernel size of 3 at every layer. Note that each node is only connected to 3 nodes from the previous layer and 3 nodes from the next layer (except those at the edges) rather than all nodes.

2.2.2.4 Recurrent Neural Network (RNN)

Recurrent neural networks (RNNs) [132] are neural networks that are designed for processing sequential data, e.g., speech signals, videos, stock market values, texts, DNA sequences etc. Unlike previous layouts, RNNs have feedback connections from one or more layers to other (same or previous) layer(s). Figure 2.8 shows an illustration of an RNN in which the value of the hidden node is fed back to itself. RNNs can have finite impulse response (FIR) or infinite impulse response (IIR). FIR RNNs are in the form of directed acyclic graph while IIR RNNs are in the form of directed cyclic graphs. Finite impulse RNNs can be unrolled and replaced with a feedforward neural network [133]. Long short-term memory (LSTM) networks [134] and gated recurrent units (GRUs) [135] are two common layouts of RNNs, both of which can be FIR or IIR.

2.2.3 Deep Learning in SAR Literature

After the resurgence of deep learning in 2006 [136], and especially since the success of AlexNet [35] in ILSVRC 2012, DNNs have enjoyed a growing amount of attention coming from many different research areas, most notably, computer vision and signal processing. DNNs have been used for many image processing tasks in the last decade, including classification, reconstruction, restoration, denoising, deblurring, and super-resolution. Naturally, SAR imaging has also received its share

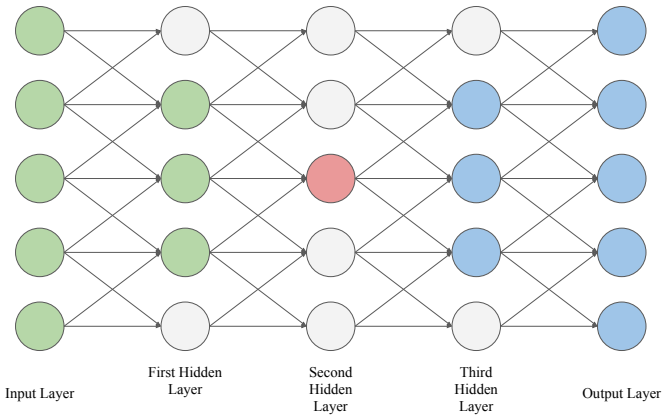

Figure 2.7 An illustration of a CNN with the convolutional kernel size of 3. All the nodes whose values are used to determine the value of the red node in the second hidden layer are shown in green, while all the nodes whose values are determined using the value of the red node are shown in blue.

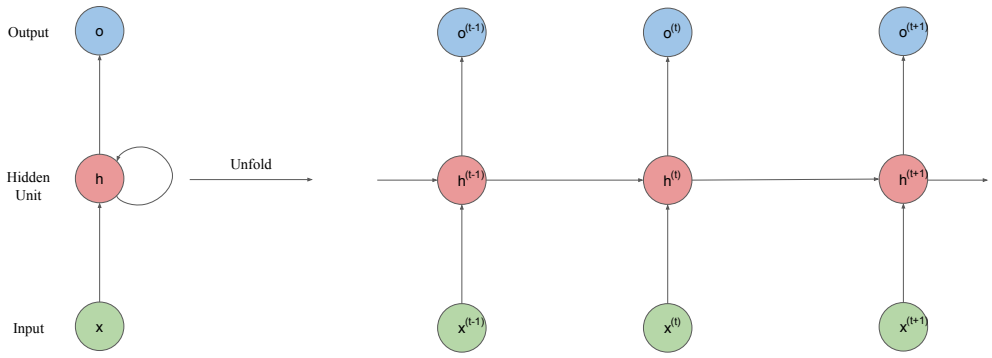

Figure 2.8 An illustration of an RNN with a single input, a single hidden unit and a single output.

from this ever-growing interest. Much like early[6] deep learning works were mostly concentrated on image classification tasks, initial works on SAR imaging using deep learning tools were on ATR [117, 121–123, 125, 126, 137–140] and other classification or detection applications [141–145]. However, only a few works focused on image formation [146–149].

2.3 Plug-and-Play (PnP) Priors

As we have discussed before, the discrete observation model given in (2.19), like many inverse problems in imaging, is ill-posed, and can only be solved satisfactorily by incorporating regularization into the inversion process. Regularized cost functions typically involve two terms: a data fidelity term to ensure the final image is consistent with the measured data, and a regularizer (prior) term that promotes solutions with desirable properties [150, 151]. Regularization-based image reconstruction methods can alleviate problems caused by incomplete data or sparse apertures. Also, they produce images with increased resolution, reduced sidelobes, and reduced speckle by incorporating prior information about the scene. In the past, many regularization-based image reconstruction methods have been proposed including non-quadratic regularization (NQR) based [1, 75], sparsity-driven [87, 152–154] and dictionary learning (DL) based [3] SAR imaging.

It is not an easy task to minimize a regularized cost function, as the two terms are usually quite different, and it is unlikely to find a single optimization approach that will be appropriate for both. Using a proximal algorithm [155] such as iterative shrinkage thresholding algorithm (ISTA) [156] and alternative direction method of multipliers (ADMM) [34,157] is the natural choice to tackle this issue, as they convert the original optimization problem into a series of smaller optimization problems, hence each term can be minimized separately using an appropriate minimization method. Proximal methods have also found use in SAR imaging tasks [89, 158–160]. The key ingredient in these methods is the proximal operator which involves an optimization problem that is shown to be equivalent to a simple denoising of intermediate solutions under Gaussian white noise [33, 151].

Recently, a new framework, called plug-and-play (PnP) priors has been introduced [33] which replaces the proximal operator by a suitable denoising method. This framework has gained great attention from the computational imaging community [151,161–185] since its emergence. Different denoisers have been adopted within the PnP framework, such as BM3D [186] (as in [33, 151, 162–164, 167, 168, 170, 179]),

[6] Early within this last resurgence.

non-local means (NLM, as in [162, 164, 173, 176, 182]), NCSR [187] (as in [161]), Gaussian mixture models (GMM, as in [165, 169, 172]), and deep learning based ones [166, 174, 175, 178, 181, 183, 185]. Along with ADMM, and ISTA, various other proximal algorithms, including approximate message passing (AMP) [188], half quadratic splitting (HQS) [49, 50], primal-dual splitting [189], and consensus equilibrium [171] have been used within PnP. This framework has been applied to many imaging problems including reconstruction [33, 151, 164, 174, 175, 179, 180, 183, 185], denoising [166,176], restoration [162,165,167,170,172,173], deblurring [165,166,181], super-resolution [161,162,173,181,182], phase retrieval [163,185], and hyperspectral sharpening [169].

PnP priors with a variable splitting algorithm such as ADMM enables the integration of data fidelity based on a physical observation model with any explicit or implicit regularizing prior. Next, we will first describe the ADMM algorithm, and then formulate the PnP framework using ADMM.

2.3.1 Alternating Direction Method of Multipliers (ADMM)

Consider the unconstrained optimization problem

$$\hat{\mathbf{x}} = \underset{\mathbf{x}}{\operatorname{argmin}}\, f(\mathbf{x}) + \lambda g(\mathbf{x}) \tag{2.57}$$

The idea of ADMM is to convert (2.57) into the following constrained problem by variable splitting:

$$\{\hat{\mathbf{x}}, \hat{\mathbf{v}}\} = \underset{\mathbf{x},\mathbf{v}}{\operatorname{argmin}}\, f(\mathbf{x}) + \lambda g(\mathbf{v}) \;\; \textit{subject to} \;\; \mathbf{x} = \mathbf{v} \tag{2.58}$$

Next, consider the augmented Lagrangian function corresponding to (2.58):

$$\mathcal{L}(\mathbf{x}, \mathbf{v}, \mathbf{u}) = f(\mathbf{x}) + \lambda g(\mathbf{v}) + \mathbf{u}^T(\mathbf{x} - \mathbf{v}) + \frac{\rho}{2} \|\mathbf{x} - \mathbf{v}\|_2^2 \tag{2.59}$$

where ρ is the penalty parameter of the ADMM.

The minimizer of (2.58) is the saddle point of $\mathcal{L}$, which can be found by solving a sequence of sub-problems, i.e., the ADMM iterations, which, in *scaled form*, are

given by [34]:

$$\mathbf{x}^{(k+1)} = \underset{\mathbf{x}\in\mathbb{R}^n}{\operatorname{argmin}} f(\mathbf{x}) + \frac{\rho}{2}\left\|\mathbf{x} - \tilde{\mathbf{x}}^{(k)}\right\|_2^2 \tag{2.60}$$

$$\mathbf{v}^{(k+1)} = \underset{\mathbf{v}\in\mathbb{R}^n}{\operatorname{argmin}} \lambda g(\mathbf{v}) + \frac{\rho}{2}\left\|\mathbf{v} - \tilde{\mathbf{v}}^{(k)}\right\|_2^2 \tag{2.61}$$

$$\bar{\mathbf{u}}^{(k+1)} = \bar{\mathbf{u}}^{(k)} + (\mathbf{x}^{(k+1)} - \mathbf{v}^{(k+1)}) \tag{2.62}$$

where $\bar{\mathbf{u}}^{(k)} \triangleq (1/\rho)\mathbf{u}^{(k)}$ is the scaled Lagrange multiplier, $\tilde{\mathbf{x}}^{(k)} \triangleq \mathbf{v}^{(k)} - \bar{\mathbf{u}}^{(k)}$ and $\tilde{\mathbf{v}}^{(k)} \triangleq \mathbf{x}^{(k+1)} + \bar{\mathbf{u}}^{(k)}$. Under mild conditions, e.g., when both f and g are closed, proper and convex, and if a saddle point of $\mathcal{L}$ exists, it can be shown that the iterates (2.60)-(2.62) converge to the solution of (2.58).

2.3.2 PnP ADMM

Note that ADMM iterations (2.60)-(2.62) have a modular structure. (2.60) can be regarded as an inversion step as it involves the forward imaging model $f(\mathbf{x})$ whereas (2.61) can be considered as a denoising step as it is an image domain operation involving the prior $g(\mathbf{v})$. To show that, let us define $\sigma \triangleq \sqrt{\lambda/\rho}$, then (2.61) becomes

$$\mathbf{v}^{(k+1)} = \underset{\mathbf{v}\in\mathbb{R}^n}{\operatorname{argmin}} g(\mathbf{v}) + \frac{1}{2\sigma^2}\left\|\mathbf{v} - \tilde{\mathbf{v}}^{(k)}\right\|_2^2 \tag{2.63}$$

Treating $\tilde{\mathbf{v}}^{(k)}$ as the noisy image, (2.63) minimizes the residue between $\tilde{\mathbf{v}}^{(k)}$ and clean image $\mathbf{v}$ using the prior $g(\mathbf{v})$. For example, if $g(\mathbf{v}) = \|\mathbf{v}\|_{\mathsf{TV}}$, i.e., the total variation norm, then (2.63) is the standard total variation denoising problem.

Venkatakrishnan *et al.* [33] proposed a variant of the ADMM algorithm by suggesting that one does not need to specify g before running the ADMM. Instead, they replaced (2.61) by an off-the-shelf image denoising algorithm, denoted by $\mathcal{D}_\sigma$, to yield

$$\mathbf{v}^{(k+1)} = \mathcal{D}_\sigma(\tilde{\mathbf{v}}^{(k)}) \tag{2.64}$$

which they called Plug-and-Play (PnP) ADMM. The convergence guarantee of the ADMM does not necessarily hold in general, for the PnP-ADMM. Accordingly, convergence is a topic of ongoing research [162, 177, 178, 184].

Chapter 3

PnP-CNN-SAR for Image Reconstruction

Previously, we have discussed that the discrete observation model given in (2.19) is ill-posed [41], and can be considered as ill-conditioned to a certain extent depending on the specifics of the observation scenario. Hence, we have concluded that it can only be solved satisfactorily using regularization. In this chapter, we introduce the PnP-CNN-SAR framework for SAR image reconstruction. In this framework, the problem of SAR image reconstruction is formulated as a regularized optimization problem, then using the PnP priors framework with ADMM, the objective function is divided into subproblems and the proximal operator is replaced with a CNN-based prior. The final portion of this chapter contains experimental results, demonstrating the effectiveness of the proposed PnP-CNN-SAR framework. This is a joint work with Ammar Saleem, another Ph.D. student in our group.

3.1 Objective Function

Consider the discrete observation model introduced in (2.19):

$$\mathbf{y} = \mathbf{H}\mathbf{f} + \mathbf{n} \tag{3.1}$$

where $\mathbf{y} \in \mathbb{C}^{M\times 1}$ is the complex valued column-stacked observation vector from which we desire to estimate the underlying column-stacked SAR image $\mathbf{f} \in \mathbb{C}^{N\times 1}$ where $M \leq N$[1], and $\mathbf{H} \in \mathbb{C}^{M\times N}$ is the Fourier transform-based forward model. Let

[1]Note that, in Chapter 2, we have used K and M to denote numbers of sampled observation points in range and cross-range directions, respectively. However, in this chapter, we only use column-stacked vectors for both phase histories and underlying SAR image, i.e., $\mathbf{y}$ and $\mathbf{f}$, throughout the formulation of the proposed

$\mathcal{R}$ denote the regularization function we impose on the reflectivity field. Then the regularized objective function becomes

$$\hat{\mathbf{f}} = \underset{\mathbf{f}}{\operatorname{argmin}} \|\mathbf{y} - \mathbf{H}\mathbf{f}\|_2^2 + \lambda \mathcal{R}(|\mathbf{f}|) \tag{3.2}$$

Note that regularization is performed on the magnitude of the reflectivity field $\mathbf{f}$. For most SAR scenes, reflectivity phase at a certain location can be modeled as a uniformly distributed random variable uncorrelated with the phase at other locations [11]. Nevertheless, we need to estimate the complex-valued field $\mathbf{f}$ in the process of ensuring good data fidelity. We can write $\mathbf{f} = \boldsymbol{\Theta}\mathbf{f}_m$ where $\boldsymbol{\Theta}$ is a diagonal matrix containing the phases of $\mathbf{f}$ at each pixel in exponentiated form, i.e., $\boldsymbol{\Theta} = \operatorname{diag}(e^{j\varphi(\mathbf{f})})$ where $\varphi(\cdot)$ denotes the phase, and $\mathbf{f}_m$ denotes the magnitude of $\mathbf{f}$. Then, replacing $\mathbf{f}$ with $\boldsymbol{\Theta}\mathbf{f}_m$ in (3.2), we get:

$$\{\hat{\mathbf{f}}_m, \hat{\boldsymbol{\Theta}}\} = \underset{\mathbf{f}_m, \boldsymbol{\Theta}}{\operatorname{argmin}} ||\mathbf{y} - \mathbf{H}\boldsymbol{\Theta}\mathbf{f}_m||_2^2 + \lambda \mathcal{R}(\mathbf{f}_m) \tag{3.3}$$

It is pertinent to mention that, up to this point, the explicit definition of a regularizer has not been formulated. The regularization will be explained in Section 3.2 after we formulate ADMM iterations for (3.3) and decouple the data-fidelity term and the regularization term. By doing so, we will be able to plug-in any regularizer into the objective function without affecting the data-fidelity.

3.2 Variable Splitting and ADMM

Rewriting (3.3) in a suitable form by introducing an auxiliary variable with a constraint, we have

$$\begin{aligned} \{\hat{\mathbf{f}}_m, \hat{\boldsymbol{\Theta}}, \hat{\mathbf{h}}\} = &\underset{\mathbf{f}_m, \boldsymbol{\Theta}, \mathbf{h}}{\operatorname{argmin}} ||\mathbf{y} - \mathbf{H}\boldsymbol{\Theta}\mathbf{f}_m||_2^2 + \lambda \mathcal{R}(\mathbf{h}) \\ &\text{s.t. } \mathbf{f}_m - \mathbf{h} = 0 \end{aligned} \tag{3.4}$$

The augmented Lagrangian for (3.4) is given by

$$\mathcal{L}\left(\hat{\mathbf{f}}_m, \hat{\boldsymbol{\Theta}}, \hat{\mathbf{h}}, \hat{\mathbf{u}}\right) = ||\mathbf{y} - \mathbf{H}\boldsymbol{\Theta}\mathbf{f}_m||_2^2 + \lambda \mathcal{R}(\mathbf{h}) + \frac{\rho}{2}||\mathbf{f}_m - \mathbf{h} + \mathbf{u}||_2^2 + \frac{\rho}{2}||\mathbf{u}||_2^2 \tag{3.5}$$

Let $\tilde{\mathbf{f}}^{(k)} = \mathbf{h}^{(k)} - \mathbf{u}^{(k)}$ and $\tilde{\mathbf{h}}^{(k)} = \mathbf{f}_m^{(k+1)} + \mathbf{u}^{(k)}$. Also, let us introduce a vector $\boldsymbol{\theta} \in \mathbb{C}^{N\times 1}$ that contains the diagonal elements of the phase matrix $\boldsymbol{\Theta}$, and the matrix $\mathbf{B}$ whose diagonal elements are the reflectivity magnitudes $\mathbf{f}_m$. Finally, let us invoke

---

method. Hence, for notational simplicity, we use M and N to denote sizes of $\mathbf{y}$ and $\mathbf{f}$, respectively.

the constraint that the magnitudes of the elements of $\boldsymbol{\theta}$ denoted as $|\theta_i|$ should be 1, simply because they contain phases of $\mathbf{f}$ at each pixel in exponentiated vector form $e^{j\varphi(\mathbf{f})}$. Then, each iteration of the ADMM algorithm will perform the following steps:

$$\boldsymbol{\theta}^{(k+1)} = \underset{\boldsymbol{\theta}}{\operatorname{argmin}} \, ||\mathbf{y} - \mathbf{H}\mathbf{B}^{(k)}\boldsymbol{\theta}||_2^2 + \lambda_{\boldsymbol{\theta}} \sum_{i=1}^{N} (|\theta_i| - 1)^2 \tag{3.6}$$

$$\mathbf{f}_m^{(k+1)} = \underset{\mathbf{f}_m}{\operatorname{argmin}} \, ||\mathbf{y} - \mathbf{H}\boldsymbol{\Theta}^{(k)}\mathbf{f}_m||_2^2 + \frac{\rho}{2}||\mathbf{f}_m - \tilde{\mathbf{f}}^{(k)}||_2^2 \tag{3.7}$$

$$\mathbf{h}^{(k+1)} = \underset{\mathbf{h}}{\operatorname{argmin}} \, \lambda\mathcal{R}(\mathbf{h}) + \frac{\rho}{2}||\tilde{\mathbf{h}}^{(k)} - \mathbf{h}||_2^2 \tag{3.8}$$

$$\mathbf{u}^{(k+1)} = \mathbf{u}^{(k)} + \mathbf{f}_m^{(k+1)} - \mathbf{h}^{(k+1)} \tag{3.9}$$

where $\lambda_{\boldsymbol{\theta}}$ and ρ are hyper-parameters.

The first two steps only depend on the choice of the forward model while the third step only depends on the choice of the regularizer. Therefore, using this plug-and-play framework, we can now write the minimization as two independent modules. Thus, this framework can be used to mix and match different prior models with forward models.

Sub-problem (3.6) is solved through a fixed point algorithm, which can also be shown to be equivalent to a particular quasi-Newton iterative minimization algorithm:

$$\mathbf{G}\boldsymbol{\theta}^{(n+1)} = (\mathbf{H}\mathbf{B})^H\mathbf{y} + \lambda_{\boldsymbol{\theta}} e^{j\varphi(\boldsymbol{\theta}^{(n)})} \tag{3.10}$$

where

$$\mathbf{G} = (\mathbf{H}\mathbf{B})^H(\mathbf{H}\mathbf{B}) + \lambda_{\boldsymbol{\theta}}\mathbf{I} \tag{3.11}$$

Each iteration in (3.10) involves solving a set of linear equations. This is an indication that the approach here solves the non-quadratic optimization problem in (3.6) by turning it into a series of quadratic problems. This linear set of equations can efficiently be solved by the conjugate gradient algorithm with the convergence criterion $\frac{\left\|\boldsymbol{\theta}^{(n+1)} - \boldsymbol{\theta}^{(n)}\right\|}{\left\|\boldsymbol{\theta}^{(n)}\right\|} < 10^{-14}$. For this sub-problem, it is possible that one can come up with a more efficient algorithm than ours.

Sub-problem (3.7) has a closed form solution, i.e., taking the derivative with respect to $\mathbf{f}_m$ and equating it to zero results in the following:

$$(\frac{\rho}{2}\mathbf{I} + \boldsymbol{\Theta}^H\mathbf{H}^H\mathbf{H}\boldsymbol{\Theta})\hat{\mathbf{f}}_m = \boldsymbol{\Theta}^H\mathbf{H}^H\mathbf{y} + \frac{\rho}{2}\tilde{\mathbf{f}} \tag{3.12}$$

We solve this complex-valued linear system using the conjugate gradient algorithm. This produces a complex solution. Therefore, we address it by considering its real part only and equating any negative value to zero, as in practice the imaginary part of this solution has values close to zero which can easily be ignored, and the real part usually has only a small number of negative values at most (which are also very close to zero). Note that within each iteration of ADMM, sub-problems (3.6) and (3.7) are solved iteratively until the convergence criterion is satisfied, before moving to the sub-problem (3.8). This process is called the model update.

Sub-problem (3.8) can be rewritten as

$$\mathbf{h}^{(k+1)} = \underset{\mathbf{h}}{\operatorname{argmin}} \frac{1}{2(\sqrt{\lambda/\rho})^2} ||\tilde{\mathbf{h}}^{(k)} - \mathbf{h}||_2^2 + \mathcal{R}(\mathbf{h}) \tag{3.13}$$

which is equivalent to denoising the image $\tilde{\mathbf{h}}^{(k)}$ with a Gaussian denoiser with a noise level $\sqrt{\lambda/\rho}$ [190]. Hence, any Gaussian denoiser can act as a modular component of the overall algorithm to solve (3.8). In the work we present here, denoising is achieved through a trained CNN. Note that the parameter λ is not explicitly defined as it depends on ρ and the network settings. The details about the architecture and training will be discussed in Section 3.3.1.

Note that (3.9) is not an optimization problem, rather it is a direct update on the Lagrange multiplier $\mathbf{u}$. Algorithm 2 shows the summary of the PnP-CNN-SAR. Note that $\mathbf{f}_m^{[t]}$ stands for the outputs of the inner loop, i.e., the model update, while $\mathbf{f}_m^{(k)}$ stands for the outputs of the outer loop, i.e., the overall ADMM algorithm. Typical values for K and T are 20 and 100, respectively.

3.3 Experimental Results

In this section, we demonstrate the effectiveness of PnP-CNN-SAR on synthetic and real SAR scenes. We also tabulate results for various scenarios and compare them with FFT-based, NQR-based [1], and DL-based [3] SAR image reconstructions as well as a PnP framework with BM3D [186] regularizer. Finally, we give an analysis on the effect of training different networks for different scenarios, in case of synthetic scene experiments.

3.3.1 Setup

The experiments are conducted with variation in two major aspects, first is the type of observation SAR scene, second is the parameters of SAR observation phenomenon. The observation SAR scenes are further bifurcated to synthetic and real scenes. The

Algorithm 2: PnP-CNN-SAR for image reconstruction.

Require: $\mathbf{y}$, $\mathbf{H}$, ϵ, $\mathcal{D}_\sigma(x)$, K, T.

$\mathbf{f}^{(0)} \leftarrow \mathbf{H}^H\mathbf{y}$ {Conventional reconstruction}
$\mathbf{B}^{(0)} \leftarrow \text{diag}\{\mathbf{f}_m^{(0)}\}$
$\boldsymbol{\theta}^{(0)} \leftarrow \angle\mathbf{f}^{(0)}$
$\mathbf{h}^{(0)} \leftarrow \mathbf{f}_m^{(0)}$
$\mathbf{u}^{(0)} \leftarrow 0$
$k \leftarrow 0$
$n \leftarrow 0$
while $\frac{\left\|\mathbf{u}^{(k+1)}-\mathbf{u}^{(k)}\right\|}{\left\|\mathbf{u}^{(k)}\right\|} \geq \epsilon$ and $k \leq K$ **do**
  $\tilde{\mathbf{f}}^{(k)} \leftarrow \mathbf{h}^{(k)} - \mathbf{u}^{(k)}$
  $\mathbf{f}_m^{[0]} \leftarrow \mathbf{f}_m^{(k)}$
  while $\frac{\left\|\mathbf{f}_m^{[t+1]}-\mathbf{f}_m^{[t]}\right\|}{\left\|\mathbf{f}_m^{[t]}\right\|} \geq 10^{-4}$ and $t \leq T$ **do**
    Calculate $\boldsymbol{\theta}^{(t)}$ using (3.6) {Phase alignment}
    Solve for $\mathbf{f}_m^{(t)}$ using (3.7) {Magnitude update}
    $t \leftarrow t+1$
  end while
  $\mathbf{f}_m^{(k+1)} \leftarrow \mathbf{f}_m^{[t]}$
  $\tilde{\mathbf{h}}^{(k)} \leftarrow \mathbf{f}_m^{(k+1)} + \mathbf{u}^{(k)}$
  $\mathbf{h}^{(k+1)} \leftarrow \mathcal{D}_\sigma(\tilde{\mathbf{h}}^{(k)})$ {Prior update}
  $\mathbf{u}^{(k+1)} \leftarrow \mathbf{u}^{(k)} + \mathbf{f}_m^{(k+1)} - \mathbf{h}^{(k+1)}$
  $k \leftarrow k+1$
end while
return $\mathbf{f}_m^{(k+1)}$

details of the real scenes are given in Section 3.3.3. It is pertinent to mention that, SAR scenes are complex valued but the synthetic scenes are real-valued and we only have access to the reflectivity magnitudes of the real scenes. Therefore, we add uniform random phase distributed over $[-\pi, \pi]$ to these real-valued (synthetic and real) SAR scenes to generate/simulate complex valued SAR reflectivities of a SAR scene.

The secondary segregation of the experiments brings SAR observation phenomenon into account. It is based on parameters of forward model $\mathbf{H}$ and noise $\mathbf{n}$. The forward model $\mathbf{H}$ consists of band-limited 2D Fourier transform where the band-limitation is denoted in terms of data availability percentage L. In particular $L = N_a/N_d$ where N_a is the number of available phase history samples and N_d is the number of phase history samples in full band-width data. In case of real SAR scene, full band-width data is not available, therefore, the existing bandwidth of the reference SAR scene is assumed to be full or 100%. The phase histories are acquired from the complex

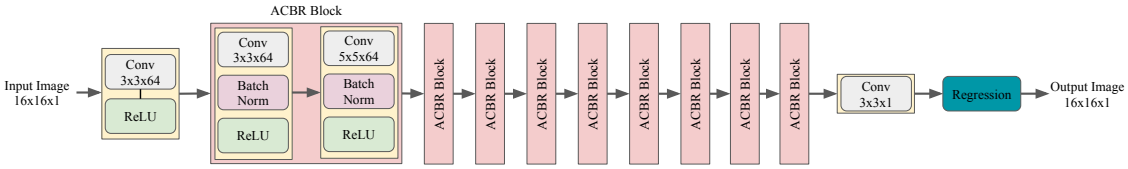

Figure 3.1 Network architecture for synthetic scene experiments. ACBR stands for Alternating Convolutional-Batch normalization-ReLU layers.

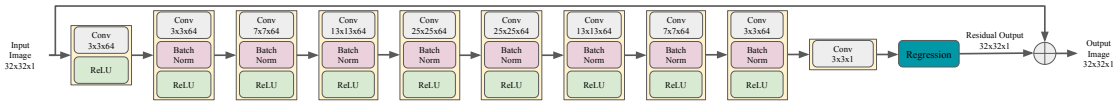

Figure 3.2 Network architecture for real scene experiments.

valued SAR reflectivities using the approach described in [12, 191]. For the implementation of different data availability levels, we crop the appropriate amount of phase history data with equal band-limitation in the range and azimuth directions. In the Fourier perspective, its a low-pass square box filter where the box is located in the center of the 2D Fourier spectrum, essentially eliminating high frequency complex-valued frequency components. The area of the box is calculated from the data availability level L. The box filtering effect is essentially limiting the transmitted signal bandwidth and the range of look angles, leading to reductions in nominal range and cross-range resolution, respectively. Note that in spotlight-mode SAR, phase history data (after pre-processing steps) consist of samples of the band-limited spatial Fourier transform of the reflectivity field on a polar grid (see Eq. (2.16) and Refs. [12, 191]). Conventional polar format imaging interpolates the data to a rectangular grid and then performs a 2D FFT. We use a slightly simplified forward model and generate band-limited data on a rectangular, rather than polar, grid. In practice, this would correspond to adding one more data preprocessing step, namely polar to rectangular interpolation, and then posing the image formation problem based on such interpolated data on the rectangular grid. The other parameter involved in SAR observation process is noise $\mathbf{n}$, which is assumed to be i.i.d. in each pixel and circularly-symmetric complex Gaussian, whose real and imaginary parts are normally distributed with zero mean and $\sigma_{\mathbf{n}}$ standard deviation.

In both synthetic and real scene experiments, we have considered various scenarios, i.e., two different noise levels ($\sigma_{\mathbf{n}} \in \{0.1, 1\} \times \sigma_{\mathbf{y}}$, where $\sigma_{\mathbf{y}}$ is the standard deviation of the magnitude of the phase history data) and 6 different data availability levels in the phase history domain (100%, 90%, 80%, 70%, 50%, and 30%), hence, in total 12 types of experiments are conducted.

Our experimental procedure is composed of two phases, namely, network training and image reconstruction using the PnP-ADMM algorithm. The network training

is performed on two different architectures, one each for synthetic and real scene experiments. The network architecture for the synthetic scene experiments is shown in Figure 3.1. The architecture used for real scene experiments is inspired from U-Net [192] and is shown in Figure 3.2[2]. It is worth noting that the network architectures we used for the synthetic and real scene experiments are different. These selections were made based on empirical exploration of several architectures for each scenario. These choices were driven by the types of features and the sizes of the scenes. While the architectures used here provide good results, we do not claim to have found the best ones. It would also be of interest to find architectures that perform well over all scenarios. The architecture we have proposed for our real scene experiments should be appropriate for generic real SAR imaging tasks. For the synthetic scene experiments, we have trained 12 different networks of the same architecture, i.e., one for each type of experiments considered, while for the real scene experiments, a single network is trained, which corresponds to the case of 100% data availability and $\sigma_{\mathbf{n}} = \sigma_{\mathbf{y}}$.

In training, we perform conventional reconstruction from the noisy phase histories to get noisy images. We then extract overlapping patches using the magnitudes of the conventionally reconstructed images, (16×16 for the synthetic scene experiments, and 32×32 for the real scene experiments), and finally augment the patches by rotation, with angles $[90°, 180°, 270°]$. We train CNNs to learn a mapping from these noisy patches to their clean counterparts in the case of synthetic scene experiments, and we perform residual learning for the real scene experiments. Note that as we do not have ground truth for the real scene experiments, we start our experiments with high-resolution TerraSAR-X reconstructions, which we call reference images. In the context of our experiments, these reference images can be viewed as conventionally reconstructed images from 'full-bandwidth' noiseless data, i.e., without any bandwidth reduction we impose, and without any noise we add on the phase history data. Based on these reference images, we then generate simulated data for various scenarios by appropriate Fourier transformation, band limitation, and noise addition operations. The training of the networks for the synthetic scene experiments took around 3 hours each, while the network for the real scene experiments is trained roughly in 3 days, on MATLAB R2019b, using NVIDIA TITAN Xp GPU. Networks used in the synthetic scene experiments are trained with RMSProp [193] solver, 10^{-3} learning rate, 0.9 learning rate drop factor with the period of one epoch, mini-batch size of 1500 for 100 epochs, while the network used in the real scene experiments is trained with RMSProp [193], 10^{-4} learning rate, 0.9 learning rate drop factor with

[2]We acknowledge that the architecture we propose is inspired from the U-Net architecture, however it is not precisely U-Net.

the period of one epoch, mini-batch size of 500 for 20 epochs.

In image reconstruction, we follow the steps mentioned in Algorithm 2. We initialize the solution with the conventional FFT-based reconstruction. Then we solve equations (3.6) and (3.7) iteratively (within each iteration of ADMM), as mentioned in Section 3.2. Then we solve (3.8) by a denoising procedure using our trained CNN. The procedure include, first extracting overlapping patches from the input image (16×16 patches for the synthetic, and 32×32 patches for the real scene cases), and feeding the patches to the CNN to get denoised patches. Then we combine the overlapping patches to obtain the overall denoised image. These steps are repeated iteratively until the stopping criteria is satisfied. The stopping criterion is chosen as $\frac{\|\mathbf{u}^{(k+1)}-\mathbf{u}^{(k)}\|}{N} < \epsilon$. Since the data availability and noise levels have a great impact on the performance, various ϵ values are employed for different experiments. We observed that as the data availability reduces or the noise increases, i.e., as the problem at hand gets more challenging, a higher value of ϵ yields better results, while for the less challenging cases, a smaller ϵ is preferred. For synthetic experiments, we used ϵ values ranging from 5×10^{-5} to 5×10^{-3}, while for the real case, the range was from 1×10^{-3} to 1×10^{-1}. The value of ρ is chosen as 12 throughout the experiments and the value of $\lambda_{\boldsymbol{\theta}}$ is calculated from the data availability level, i.e., $\lambda_{\boldsymbol{\theta}} = \frac{2}{L^2}$ where L is the data availability level.

We compare our proposed framework with FFT-based, NQR-based [1], DL-based [3] reconstructions, and a PnP framework with BM3D [186] regularizer (PnP-BM3D) in terms of signal-to-noise ratio (SNR) and structural similarity (SSIM) index [194] values of the reconstructed images. The formula of SSIM is given as:

$$SSIM(\mathbf{x},\mathbf{y}) = \frac{(2\mu_{\mathbf{x}}\mu_{\mathbf{y}} + c_1)(2\sigma_{\mathbf{xy}} + c_2)}{(\mu_{\mathbf{x}}^2 + \mu_{\mathbf{y}}^2 + c_1)(\sigma_{\mathbf{x}}^2 + \sigma_{\mathbf{y}}^2 + c_2)} \tag{3.14}$$

where $\mu_{\mathbf{x}}$, $\mu_{\mathbf{y}}$, $\sigma_{\mathbf{x}}$, $\sigma_{\mathbf{y}}$, and $\sigma_{\mathbf{xy}}$ are the local means, standard deviations, and cross-covariance for images $\mathbf{x}$ and $\mathbf{y}$. $c_1 = (k_1 l)^2$ and $c_2 = (k_2 l)^2$ are constants to maintain formula validity, avoiding the denominator being zero. l represents the dynamic range of the pixel value. $k_1 = 0.01$ and $k_2 = 0.03$ are default values. A larger SSIM value indicates a better similarity of the two images.

The problem formulation for the NQR-based [1] reconstruction is given as:

$$\hat{\mathbf{f}} = \underset{\mathbf{f}}{\operatorname{argmin}} \|\mathbf{y} - \mathbf{H}\mathbf{f}\|_2^2 + \lambda_1 \|\mathbf{f}\|_p^p + \lambda_2 \|\mathbf{D}\mathbf{f}_m\|_p^p \tag{3.15}$$

where $\mathbf{D}$ is a discrete approximation to the 2D derivative operator (gradient). Here, the first term is the data-fidelity term while second and third terms are aimed at enhancing point-based and region-based features respectively. The parameters λ_1

and λ_2 are optimized to obtain the highest SNR for each image in each scenario while $p = 0.9$ is used for all the considered scenarios.

The problem formulation for the DL-based [3] reconstruction is given as:

$$\begin{aligned}\{|\hat{\mathbf{f}}|, \hat{\boldsymbol{\Theta}}, \hat{\mathbf{D}}, \hat{\alpha_i}\} = \underset{\mathbf{f}_m, \boldsymbol{\Theta}, \mathbf{D}, \alpha_i}{\operatorname{argmin}} \; & \lambda \|\mathbf{y} - \mathbf{H}\boldsymbol{\Theta}\mathbf{f}_m\|_2^2 \\ & + \sum_i \|\mathbf{E}_i|\mathbf{f}| - \mathbf{D}\alpha_i\|_2^2 + \sum_i \mu_i \|\alpha_i\|_0 \\ & \text{s.t. } |\boldsymbol{\Theta}_{jj}| = 1 \; \forall j \end{aligned} \tag{3.16}$$

where $\mathbf{D}$ and α_i are the dictionary and the sparse coefficients to be learned, respectively, and $\mathbf{E}_i$ are the patch extraction operators. See [3] for details.

For PnP-BM3D experiments, the steps in the Algorithm 2 are followed, and in the prior update step, the BM3D prior is used instead of the CNN-based prior. The MATLAB implementation of BM3D is downloaded from the authors' website[3].

3.3.2 Synthetic Scene Experiments

The training and the test images for the synthetic scene experiments are shown in Figures 3.3a and 3.3b, respectively. Note that training is not performed using the training images themselves, rather 16×16 overlapping patches that are extracted from the training images. Consequently, in every ADMM iteration, during the prior update step, overlapping patches are extracted, each patch is passed through the network, and then patches are combined to get the reconstructed image.

Although we have trained a network for each scenario, we have compared the performances of all networks in each scenario. Table 3.1 shows the average SNR and SSIM values for different experiments using different networks, respectively. Note that, the network that gives the best result for a particular scenario is not always the one that is trained for that scenario.

The best results from Table 3.1 are also presented in Table 3.2 for comparison with other methods. Table 3.2 shows that our framework outperforms other methods in terms of both SNR and SSIM in 11 out of 12 scenarios. Figure 3.4 shows the effects of the noise level and data availability on the SNR and SSIM values.

Figures 3.5 and 3.6 show reconstruction results for *Image 7* with noise $\sigma_{\mathbf{n}} = 0.1\,\sigma_{\mathbf{y}}$, and *Image 2* with noise $\sigma_{\mathbf{n}} = \sigma_{\mathbf{y}}$, respectively, for qualitative analysis. It appears that our proposed framework is better at preserving the details and more robust to

[3] http://www.cs.tut.fi/~foi/GCF-BM3D/index.html#ref_software

Table 3.1 Average [SNR/SSIM] values for synthetic scene experiments using different networks. Each row represents a network trained with a particular scenario considered, and each column represents a test scenario.

		$0.1\sigma_{\mathbf{y}}$						$\sigma_{\mathbf{y}}$					
		100%	90%	80%	70%	50%	30%	100%	90%	80%	70%	50%	30%
$0.1\sigma_{\mathbf{y}}$	100%	**32.170/0.905**	19.074/**0.869**	11.447/0.699	4.146/0.504	0.217/0.317	-2.008/0.198	1.623/0.347	0.629/0.282	0.273/0.258	-0.051/0.230	-0.551/0.184	-1.632/0.139
	90%	21.282/0.861	**19.574**/0.848	**16.552/0.816**	9.931/0.689	2.975/0.406	-1.074/0.240	2.585/0.439	1.625/0.360	1.518/0.341	1.611/0.297	1.176/0.217	-0.452/0.166
	80%	17.571/0.840	16.839/0.828	15.254/0.802	**11.417/0.726**	3.754/0.465	-0.956/0.237	2.055/0.413	0.648/0.305	0.571/0.286	1.107/0.300	1.543/0.265	-0.266/**0.178**
	70%	14.088/0.804	12.741/0.766	11.820/0.747	9.103/0.660	**5.480/0.490**	1.043/**0.278**	1.160/0.385	-1.008/0.197	-0.836/0.191	-0.089/0.230	1.065/0.208	0.706/0.139
	50%	8.948/0.716	5.414/0.567	4.404/0.521	3.781/0.458	3.748/0.392	**2.041**/0.276	-0.891/0.270	-3.000/0.087	-2.928/0.080	-2.903/0.074	-1.479/0.115	0.197/0.128
	30%	2.352/0.517	-2.459/0.119	-2.378/0.111	-2.366/0.104	-1.896/0.133	-1.349/0.164	-2.386/0.190	-4.032/0.054	-4.070/0.040	-3.996/0.026	-3.578/0.026	-3.350/0.028
$\sigma_{\mathbf{y}}$	100%	13.572/0.800	10.773/0.743	8.767/0.701	4.791/0.590	0.381/0.383	-3.082/0.171	**8.242/0.610**	**6.425/0.539**	5.015/**0.484**	3.182/**0.420**	0.752/0.276	-2.433/0.150
	90%	12.913/0.780	11.295/0.731	10.229/0.700	6.662/0.605	1.584/0.407	-2.542/0.183	6.749/0.541	5.444/0.468	5.034/0.437	4.356/0.388	2.062/**0.293**	-1.443/0.164
	80%	11.849/0.759	10.197/0.712	8.353/0.668	5.468/0.570	1.652/0.394	-2.187/0.205	6.710/0.549	5.312/0.470	**5.279**/0.458	**4.614**/0.401	2.285/0.291	-1.307/0.167
	70%	8.647/0.716	7.952/0.665	7.090/0.636	5.308/0.550	1.981/0.406	-2.147/0.217	4.383/0.461	3.588/0.378	3.689/0.368	3.871/0.358	**2.660**/0.287	-1.244/0.177
	50%	8.294/0.649	6.647/0.537	6.167/0.502	5.482/0.454	4.152/0.363	0.184/0.241	1.335/0.346	-0.786/0.182	-0.481/0.174	0.340/0.174	1.868/0.180	**1.027**/0.142
	30%	4.764/0.536	0.900/0.253	0.560/0.216	1.176/0.205	2.303/0.212	1.713/0.172	-1.651/0.212	-3.390/0.063	-3.163/0.061	-2.022/0.077	-0.209/0.072	0.351/0.039

Table 3.2 Average SNR and SSIM values for different noise and data availability levels for the synthetic scene experiments. Best results are shown in bold, second best results are shown in red.

Available Data	Method	SNR (dB)		SSIM	
		$0.1\sigma_{\mathbf{y}}$	$\sigma_{\mathbf{y}}$	$0.1\sigma_{\mathbf{y}}$	$\sigma_{\mathbf{y}}$
100%	FFT-based	25.55	5.84	0.906	0.449
	NQR-based [1]	27.31	12.36	0.985	0.631
	DL-based [3]	26.31	6.13	0.877	0.343
	PnP-BM3D	25.95	5.98	0.869	0.351
	PnP-CNN-SAR	**37.92**	**13.99**	**0.996**	**0.687**
90%	FFT-based	11.29	5.62	0.539	0.366
	NQR-based [1]	17.84	11.03	0.845	0.549
	DL-based [3]	24.76	4.81	0.869	0.269
	PnP-BM3D	17.77	5.88	0.737	0.289
	PnP-CNN-SAR	**25.33**	**12.18**	**0.954**	**0.591**
80%	FFT-based	9.65	5.64	0.474	0.336
	NQR-based [1]	15.55	10.02	0.809	0.486
	DL-based [3]	22.20	5.42	0.852	0.272
	PnP-BM3D	12.14	5.89	0.544	0.254
	PnP-CNN-SAR	**22.30**	**11.03**	**0.921**	**0.488**
70%	FFT-based	7.94	5.47	0.390	0.294
	NQR-based [1]	10.83	8.97	0.596	0.431
	DL-based [3]	12.22	6.02	0.566	0.254
	PnP-BM3D	8.68	5.84	0.409	0.229
	PnP-CNN-SAR	**17.17**	**10.37**	**0.831**	**0.433**
50%	FFT-based	6.00	5.26	0.289	0.227
	NQR-based [1]	8.97	8.02	0.432	0.316
	DL-based [3]	7.44	6.55	0.344	0.209
	PnP-BM3D	7.09	5.44	0.293	0.186
	PnP-CNN-SAR	**11.23**	**8.41**	**0.596**	**0.335**
30%	FFT-based	4.41	4.52	0.191	0.158
	NQR-based [1]	7.70	**7.32**	0.296	**0.263**
	DL-based [3]	5.71	6.31	0.216	0.156
	PnP-BM3D	5.36	5.15	0.188	0.131
	PnP-CNN-SAR	**7.79**	6.78	**0.390**	0.216

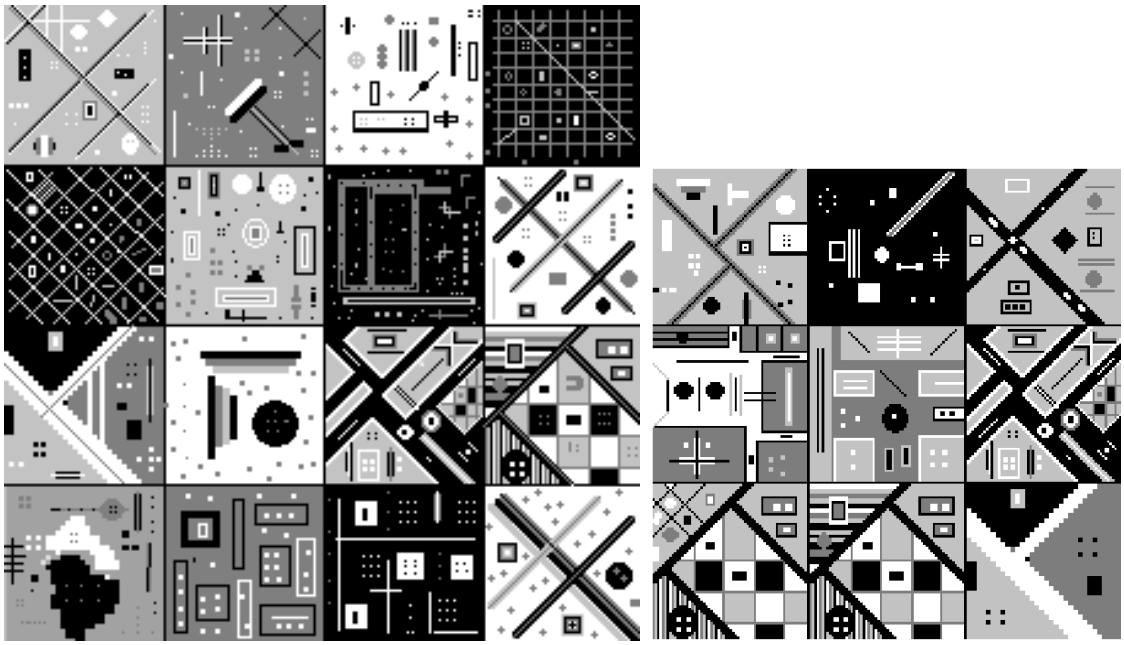

(a) (b)

Figure 3.3 Synthetic SAR scenes used for (a) training the CNN and learning the dictionary, and (b) performance evaluation.

data limitations, and gives the best visual quality in the majority of scenarios.

3.3.3 Real Scene Experiments

For the real scene experiments, TerraSAR-X [195] images are used and we designed two types of experimental settings in which we considered the following scenarios: 1) When the training and testing are performed on non-overlapping windows extracted from the same scene that are randomly split into training and test data sets, and 2) when the training is done using non-overlapping windows extracted from one scene, and testing is performed on non-overlapping windows extracted from a different scene. These two experimental settings will be called same scene experiments, and different scene experiments, respectively. For these experiments, two TerraSAR-X images are used to form the data set. The first image, shown in Figure 3.7, contains the view of the city of Wonsan in Democratic People's Republic of Korea and, the second image, shown in Figure 3.8, contains the view of the Kapıkule Border Crossing near the Turkey-Bulgaria-Greece border tripoint. These images will be referred as Wonsan and Kapıkule, respectively. The data collected for the Wonsan image has the incidence angle of 42.88° while the incidence angle for Kapıkule is 44.77°. After post-processing, both images have the pixel resolution of 1.60 m $\times$ 1.60 m.

158 non-overlapping 170×170 windows are extracted from the Wonsan image, and

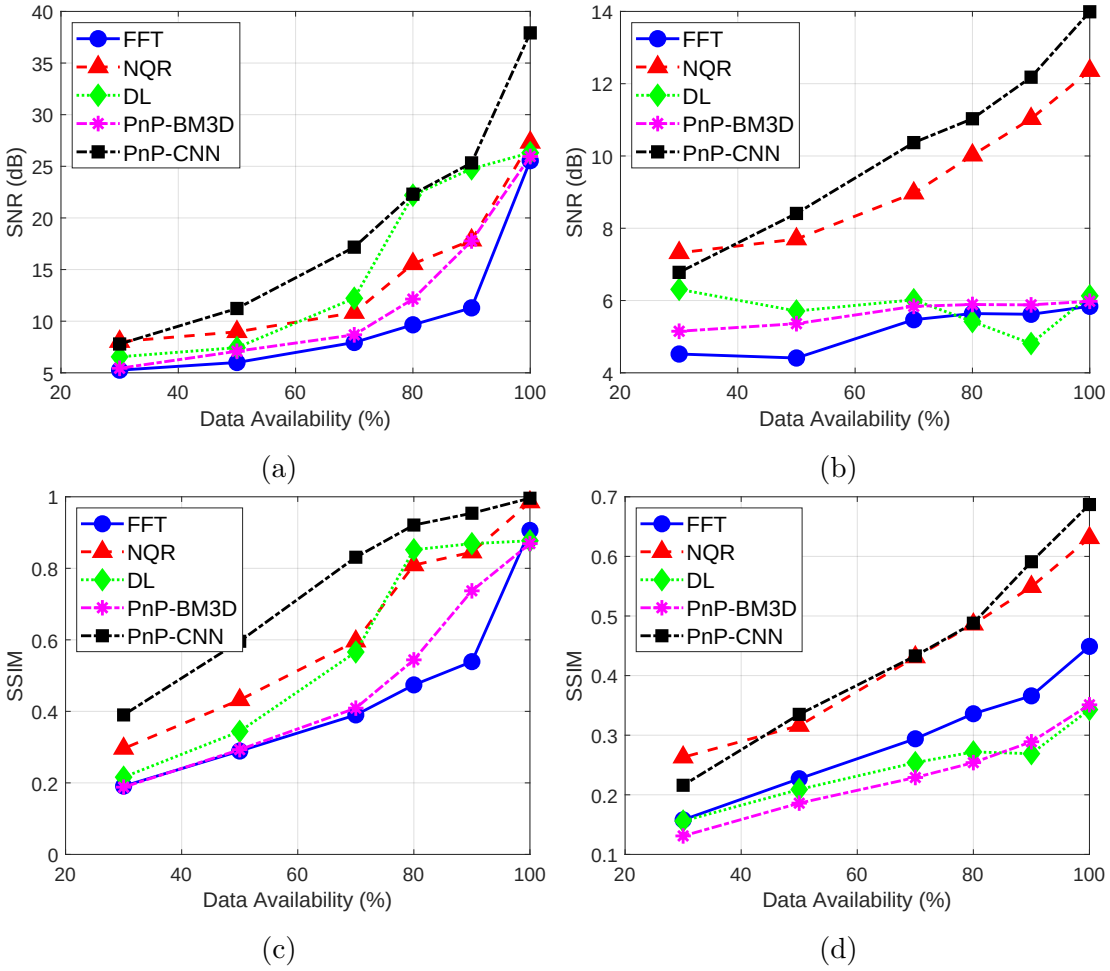

Figure 3.4 Average SNR values for synthetic scene experiments for (a) $\sigma_{\mathbf{n}} = 0.1\,\sigma_{\mathbf{y}}$, and (b) $\sigma_{\mathbf{n}} = \sigma_{\mathbf{y}}$. Average SSIM values for synthetic scene experiments for (c) $\sigma_{\mathbf{n}} = 0.1\,\sigma_{\mathbf{y}}$, and (d) $\sigma_{\mathbf{n}} = \sigma_{\mathbf{y}}$.

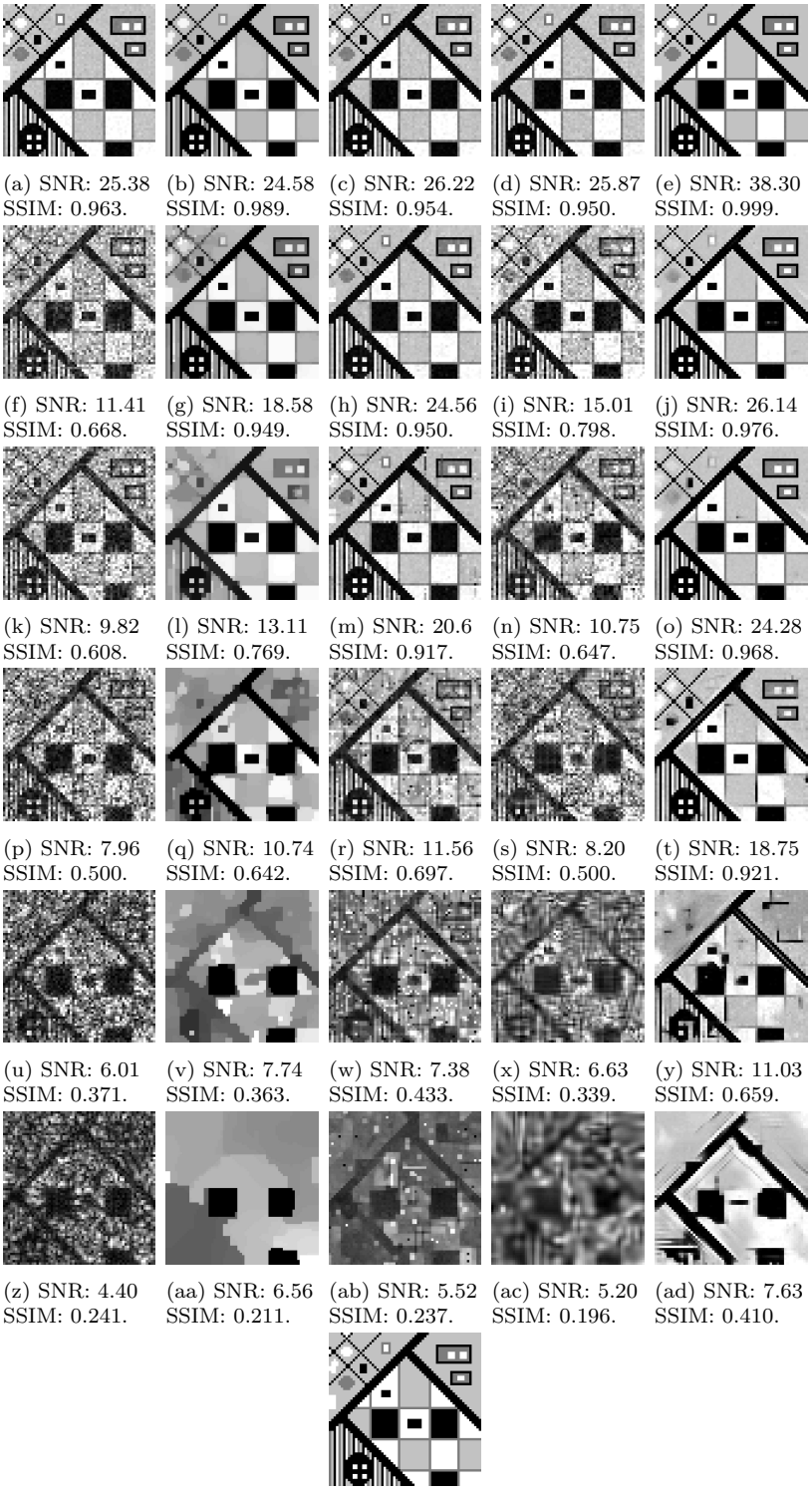

(a) SNR: 25.38 SSIM: 0.963. (b) SNR: 24.58 SSIM: 0.989. (c) SNR: 26.22 SSIM: 0.954. (d) SNR: 25.87 SSIM: 0.950. (e) SNR: 38.30 SSIM: 0.999.

(f) SNR: 11.41 SSIM: 0.668. (g) SNR: 18.58 SSIM: 0.949. (h) SNR: 24.56 SSIM: 0.950. (i) SNR: 15.01 SSIM: 0.798. (j) SNR: 26.14 SSIM: 0.976.

(k) SNR: 9.82 SSIM: 0.608. (l) SNR: 13.11 SSIM: 0.769. (m) SNR: 20.6 SSIM: 0.917. (n) SNR: 10.75 SSIM: 0.647. (o) SNR: 24.28 SSIM: 0.968.

(p) SNR: 7.96 SSIM: 0.500. (q) SNR: 10.74 SSIM: 0.642. (r) SNR: 11.56 SSIM: 0.697. (s) SNR: 8.20 SSIM: 0.500. (t) SNR: 18.75 SSIM: 0.921.

(u) SNR: 6.01 SSIM: 0.371. (v) SNR: 7.74 SSIM: 0.363. (w) SNR: 7.38 SSIM: 0.433. (x) SNR: 6.63 SSIM: 0.339. (y) SNR: 11.03 SSIM: 0.659.

(z) SNR: 4.40 SSIM: 0.241. (aa) SNR: 6.56 SSIM: 0.211. (ab) SNR: 5.52 SSIM: 0.237. (ac) SNR: 5.20 SSIM: 0.196. (ad) SNR: 7.63 SSIM: 0.410.

(ae)

Figure 3.5 Reconstruction results for *Image 7* of the synthetic scenes with noise $\sigma_{\mathbf{n}} = 0.1\,\sigma_{\mathbf{y}}$. First row, full data, second row, 90% data, third row, 80% data, fourth row, 70% data, fifth row, 50% data, sixth row, 30% data. First column, FFT-based reconstruction, second column, NQR-based reconstruction, third column, DL-based reconstruction, fourth column, PnP-BM3D based reconstruction, fifth column, PnP-CNN-SAR based reconstruction. (ae) Ground truth.

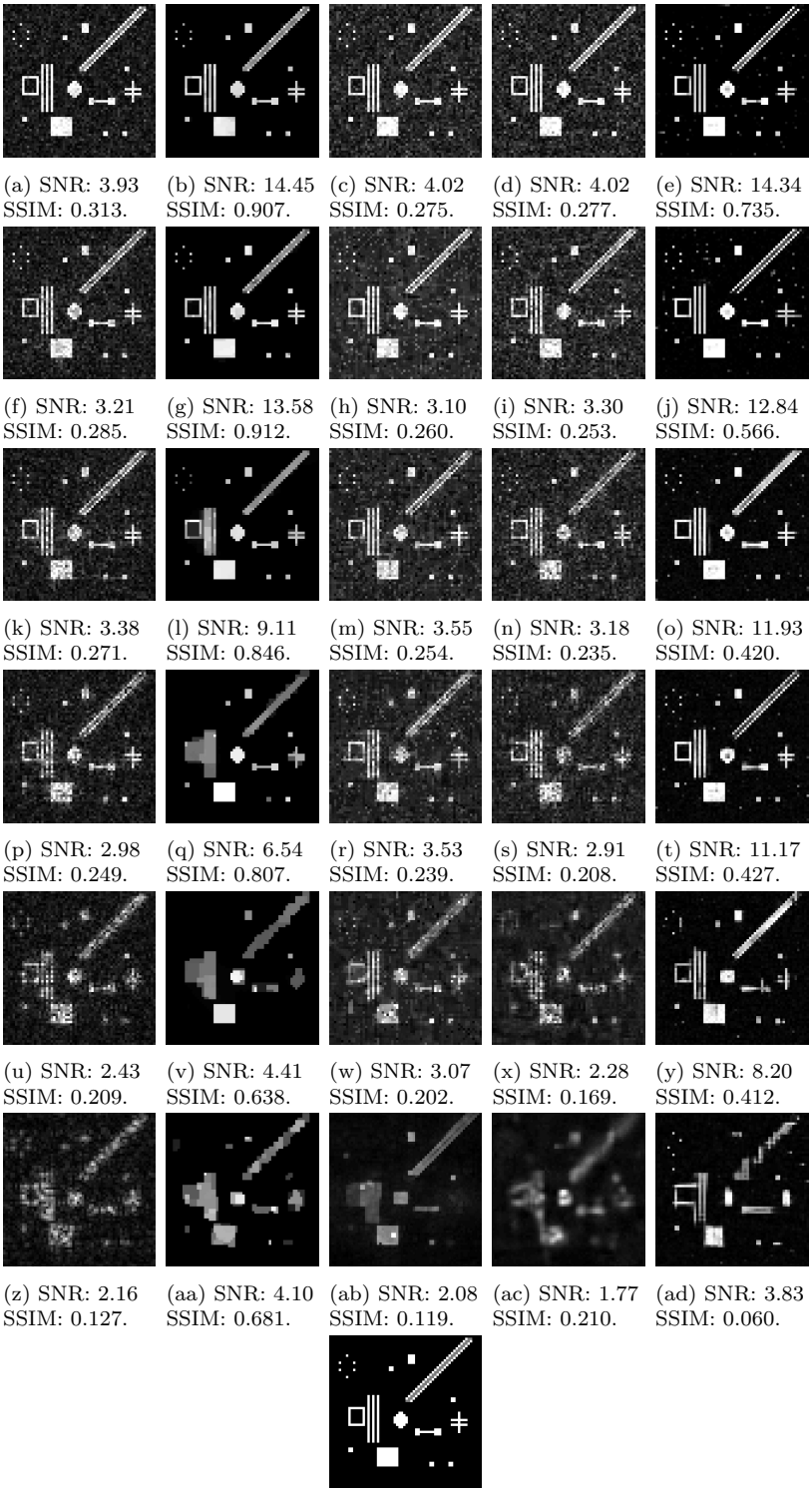

(a) SNR: 3.93 SSIM: 0.313. (b) SNR: 14.45 SSIM: 0.907. (c) SNR: 4.02 SSIM: 0.275. (d) SNR: 4.02 SSIM: 0.277. (e) SNR: 14.34 SSIM: 0.735.

(f) SNR: 3.21 SSIM: 0.285. (g) SNR: 13.58 SSIM: 0.912. (h) SNR: 3.10 SSIM: 0.260. (i) SNR: 3.30 SSIM: 0.253. (j) SNR: 12.84 SSIM: 0.566.

(k) SNR: 3.38 SSIM: 0.271. (l) SNR: 9.11 SSIM: 0.846. (m) SNR: 3.55 SSIM: 0.254. (n) SNR: 3.18 SSIM: 0.235. (o) SNR: 11.93 SSIM: 0.420.

(p) SNR: 2.98 SSIM: 0.249. (q) SNR: 6.54 SSIM: 0.807. (r) SNR: 3.53 SSIM: 0.239. (s) SNR: 2.91 SSIM: 0.208. (t) SNR: 11.17 SSIM: 0.427.

(u) SNR: 2.43 SSIM: 0.209. (v) SNR: 4.41 SSIM: 0.638. (w) SNR: 3.07 SSIM: 0.202. (x) SNR: 2.28 SSIM: 0.169. (y) SNR: 8.20 SSIM: 0.412.

(z) SNR: 2.16 SSIM: 0.127. (aa) SNR: 4.10 SSIM: 0.681. (ab) SNR: 2.08 SSIM: 0.119. (ac) SNR: 1.77 SSIM: 0.210. (ad) SNR: 3.83 SSIM: 0.060.

(ae)

Figure 3.6 Reconstruction results for *Image 2* of the synthetic scenes with noise $\sigma_{\mathbf{n}} = \sigma_{\mathbf{y}}$. First row, full data, second row, 90% data, third row, 80% data, fourth row, 70% data, fifth row, 50% data, sixth row, 30% data. First column, FFT-based reconstruction, second column, NQR-based reconstruction, third column, DL-based reconstruction, fourth column, PnP-BM3D based reconstruction, fifth column, PnP-CNN-SAR based reconstruction. (ae) Ground truth.

Figure 3.7 Wonsan image.

110 non-overlapping windows with the same size are extracted from the Kapıkule image. Randomly selected 127 windows from the Wonsan image are used for training the network that is to be used for both scenarios. Remaining 31 windows from the Wonsan image constitute the test set for the same scene experiments, while all windows from the Kapıkule image are used as the test set for the different scene experiments. Figures 3.9, 3.10, and 3.11 show the training windows, test windows for the same scene experiments, and the test windows for the different scene experiments, respectively. Note that the number of training windows are not enough to train the network and therefore the training is performed using 32×32 overlapping patches that are extracted from the training windows. Hence, the prior update step of the ADMM iteration is performed the same way as described in Section 3.3.2.

3.3.3.1 Same Scene Experiments

Columns under "Wonsan" in Table 3.3 show the average SNR and SSIM values for the same scene experiments. Figure 3.12 shows the effects of the noise level and data availability on the SNR and SSIM values. Results show that our framework outperforms other methods in 10 scenarios in terms of SNR, and in all scenarios in terms of SSIM. More detailed results can be found in the supplementary material.

Figures 3.13 and 3.14 show the reconstruction results for *Image 26* with noise $\sigma_{\mathbf{n}} = 0.1\,\sigma_{\mathbf{y}}$ and *Image 12* with noise $\sigma_{\mathbf{n}} = \sigma_{\mathbf{y}}$, respectively. It appears that the perceptual quality of the images produced by PnP-CNN-SAR is better, and our framework shows its value especially in the case of higher noise, where other methods tend to produce blurry and/or noisy images. It is worth noting that, as the amount

Figure 3.8 Kapıkule image.

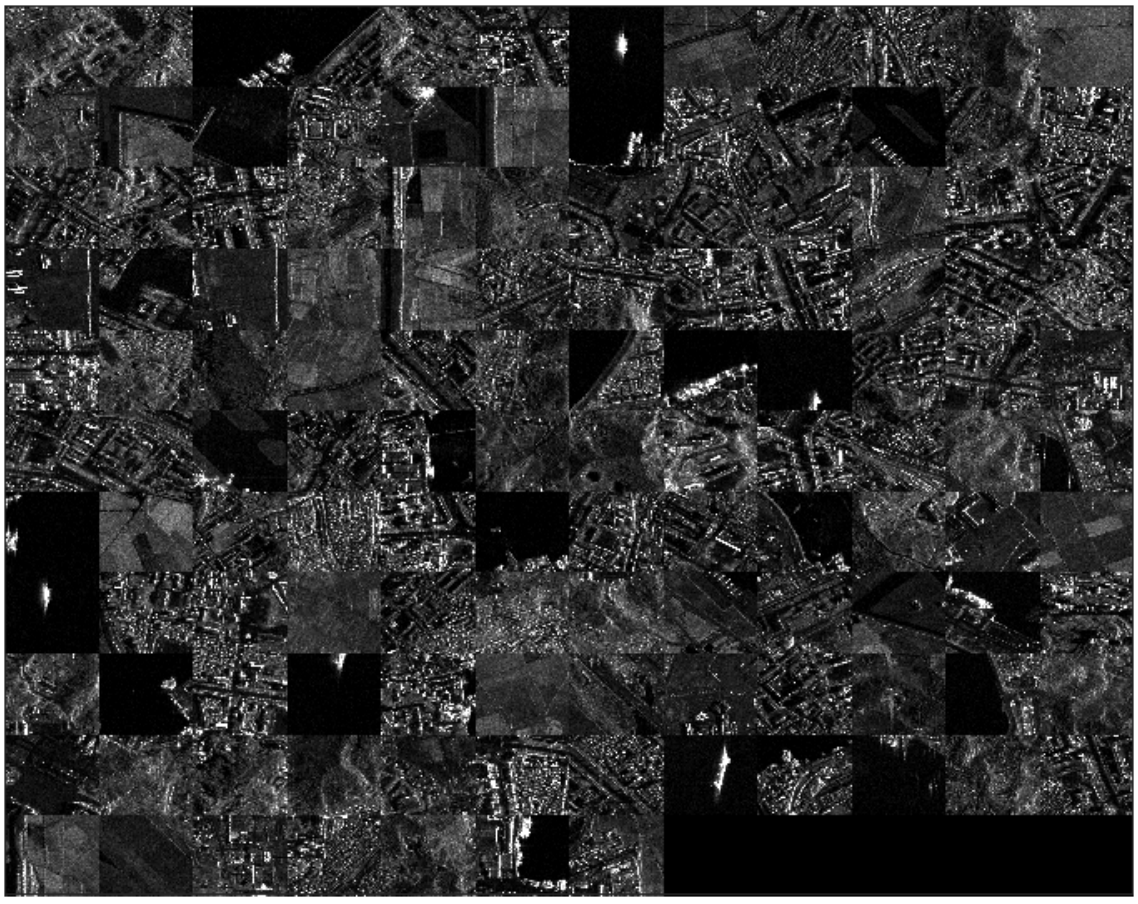

Figure 3.9 Windows extracted from the Wonsan image that are used for training the CNN for PnP-CNN-SAR and learning the dictionary for DL-based reconstruction.

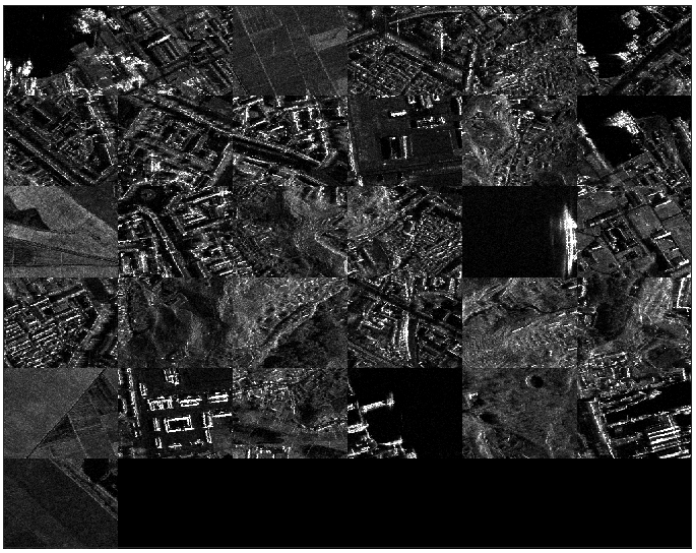

Figure 3.10 Windows extracted from the Wonsan image that are used for performance evaluation in the same scene experiments.

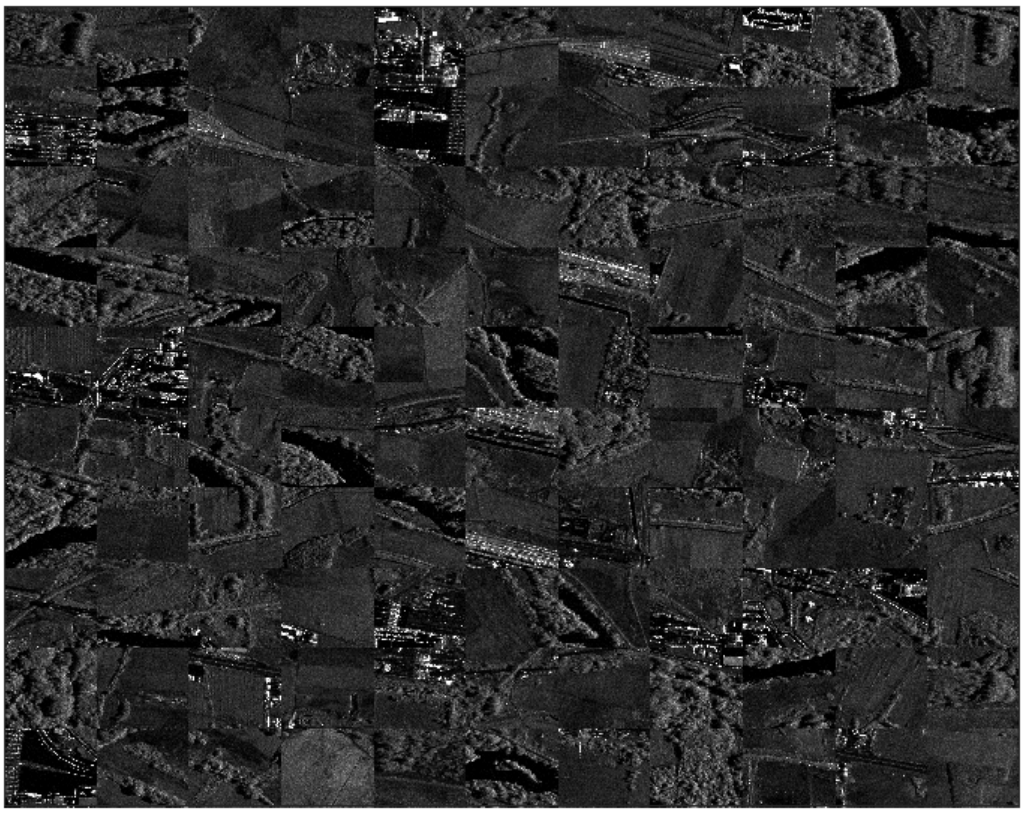

Figure 3.11 Windows extracted from the Kapıkule image that are used for performance evaluation in the different scene experiments.

Table 3.3 Average SNR and SSIM values for different noise and data availability levels for the real scene experiments. Best results are shown in bold, second best results are shown in red.

Available Data	Method	Wonsan				Kapıkule			
		SNR (dB)		SSIM		SNR (dB)		SSIM	
		$0.1\sigma_{\mathbf{y}}$	$\sigma_{\mathbf{y}}$	$0.1\sigma_{\mathbf{y}}$	$\sigma_{\mathbf{y}}$	$0.1\sigma_{\mathbf{y}}$	$\sigma_{\mathbf{y}}$	$0.1\sigma_{\mathbf{y}}$	$\sigma_{\mathbf{y}}$
100%	FFT-based	26.65	6.33	0.973	0.457	26.63	6.62	0.989	0.597
	NQR-based [1]	23.56	9.70	0.963	0.535	23.11	10.28	0.964	0.537
	DL-based [3]	22.95	16.13	0.976	0.924	24.66	11.08	0.981	0.647
	PnP-BM3D	26.65	6.42	0.973	0.462	26.63	6.75	0.979	0.459
	PnP-CNN-SAR	**40.03**	**36.82**	**0.998**	**0.997**	**38.52**	**36.27**	**0.998**	**0.997**
90%	FFT-based	13.23	6.16	0.802	0.423	13.21	6.49	0.758	0.516
	NQR-based [1]	11.64	9.09	0.683	0.486	11.70	9.65	0.705	0.492
	DL-based [3]	12.71	8.90	0.783	0.538	14.22	10.21	0.822	0.584
	PnP-BM3D	14.89	6.10	0.838	0.418	15.27	6.71	0.844	0.422
	PnP-CNN-SAR	**16.78**	**15.85**	**0.900**	**0.857**	**16.87**	**15.43**	**0.892**	**0.851**
80%	FFT-based	10.02	6.01	0.704	0.390	10.07	6.39	0.662	0.471
	NQR-based [1]	8.83	8.07	0.506	0.409	9.47	8.79	0.518	0.434
	DL-based [3]	9.97	8.07	0.671	0.470	11.22	9.50	0.699	0.520
	PnP-BM3D	11.65	6.18	0.731	0.400	12.36	6.82	0.729	0.401
	PnP-CNN-SAR	**13.29**	**12.55**	**0.830**	**0.781**	**13.60**	**12.98**	**0.796**	**0.749**
70%	FFT-based	8.41	5.84	0.632	0.362	8.41	6.28	0.576	0.426
	NQR-based [1]	7.49	7.19	0.427	0.355	8.22	8.29	0.439	0.391
	DL-based [3]	8.65	7.54	0.587	0.419	9.65	8.94	0.601	0.467
	PnP-BM3D	9.53	6.19	0.632	0.379	10.49	7.03	0.608	0.384
	PnP-CNN-SAR	**10.75**	**10.34**	**0.736**	**0.693**	**11.20**	**10.99**	**0.688**	**0.649**
50%	FFT-based	6.22	5.42	0.510	0.315	6.33	5.86	0.358	0.275
	NQR-based [1]	5.86	6.60	0.295	0.301	7.78	7.59	0.393	0.355
	DL-based [3]	6.85	6.51	0.450	0.333	7.63	7.70	0.455	0.380
	PnP-BM3D	7.68	6.15	0.452	0.334	**8.81**	7.39	0.419	0.348
	PnP-CNN-SAR	**8.11**	**8.09**	**0.580**	**0.562**	8.62	**8.81**	**0.527**	**0.516**
30%	FFT-based	4.53	4.57	0.394	0.267	4.67	4.94	0.220	0.182
	NQR-based [1]	5.71	**6.14**	0.270	0.284	**7.01**	6.84	0.346	0.323
	DL-based [3]	5.14	5.06	0.334	0.258	5.67	5.89	0.339	0.298
	PnP-BM3D	**5.98**	5.87	0.336	0.277	6.77	**7.14**	0.330	0.312
	PnP-CNN-SAR	5.56	5.89	**0.406**	**0.363**	5.98	6.48	**0.384**	**0.339**

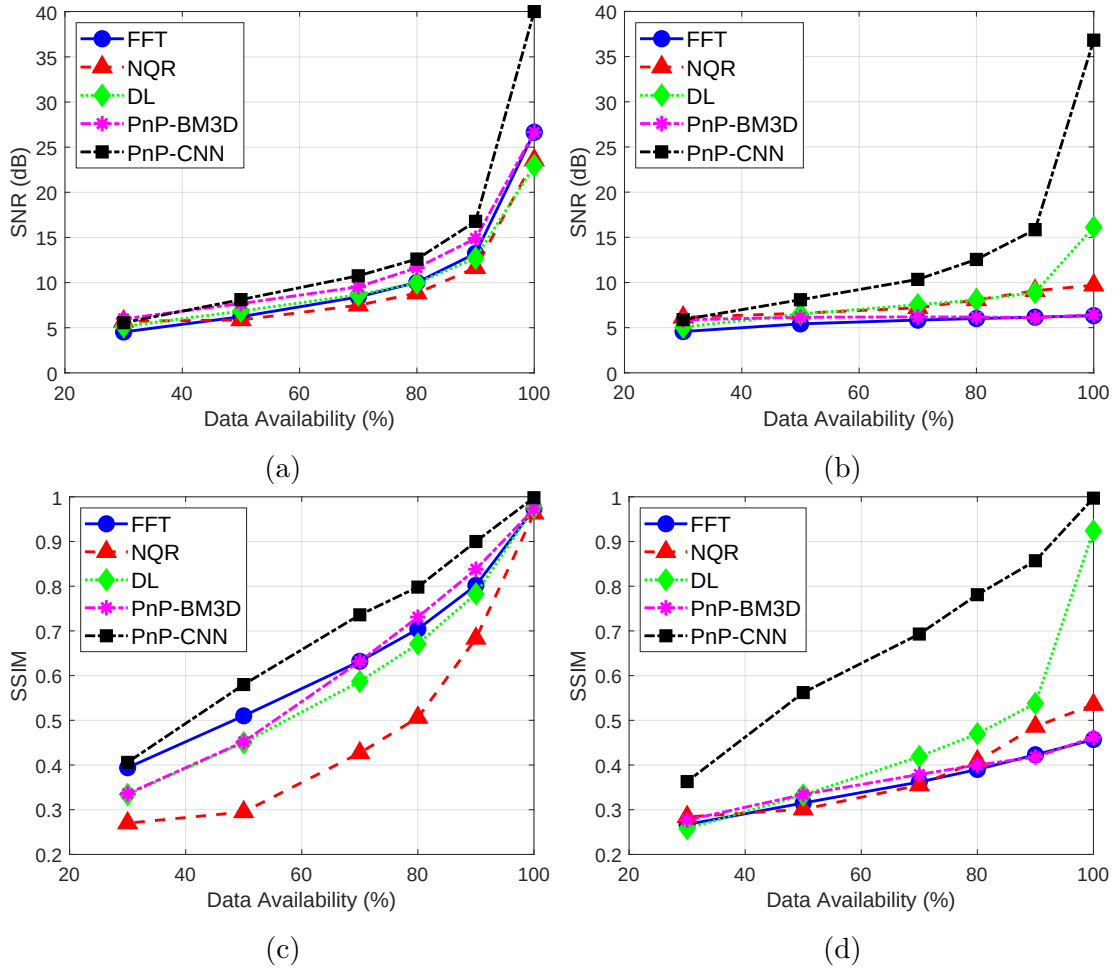

Figure 3.12 Average SNR values for same scene experiments for (a) $\sigma_{\mathbf{n}} = 0.1\,\sigma_{\mathbf{y}}$, and (b) $\sigma_{\mathbf{n}} = \sigma_{\mathbf{y}}$. Average SSIM values for same scene experiments for (c) $\sigma_{\mathbf{n}} = 0.1\,\sigma_{\mathbf{y}}$, and (d) $\sigma_{\mathbf{n}} = \sigma_{\mathbf{y}}$.

of available data reduces, the degradation of the reconstruction quality is more prominent in real case, compared to the synthetic case. This is most likely due to that in real case, all experiments are performed using the same network, i.e., trained with 100% data and $\sigma_{\mathbf{n}} = \sigma_{\mathbf{y}}$ noise, while in synthetic case, networks trained for all scenarios considered and results of the network that performed the best in each scenario are presented. A similar degradation scheme is also visible in case of different scene experiments, which will be discussed next.

3.3.3.2 Different Scene Experiments

Columns under "Kapıkule" in Table 3.3 show the average SNR and SSIM values for different scene experiments. Figure 3.15 shows the effects of the noise level and data availability on the SNR and SSIM values. Note that since FFT-based, NQR-based [1], and PnP-BM3D methods are not learning-based, the issue of training and testing on different scenes is only relevant to DL-based [3] and PnP-CNN-SAR.

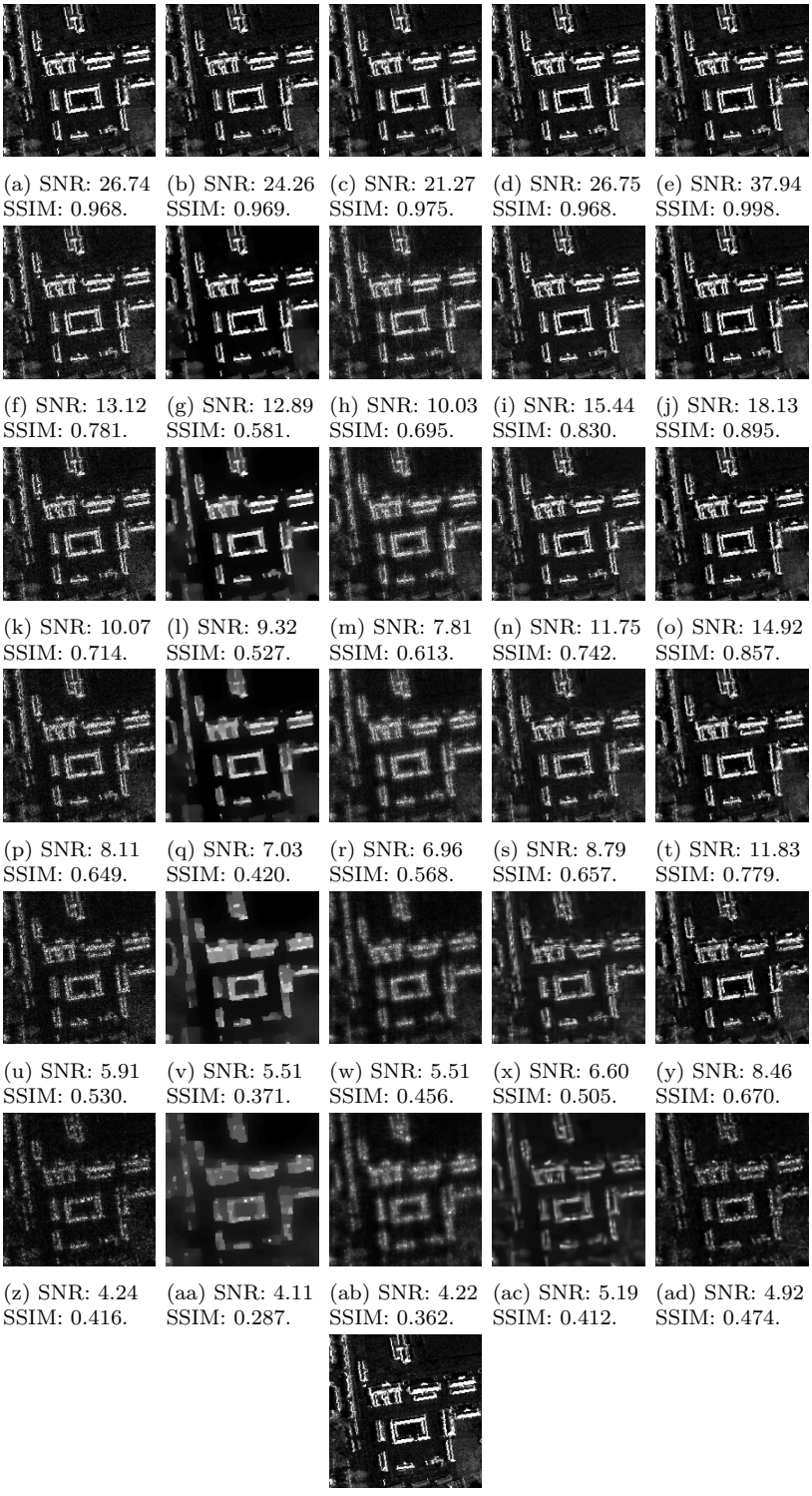

(a) SNR: 26.74 SSIM: 0.968. (b) SNR: 24.26 SSIM: 0.969. (c) SNR: 21.27 SSIM: 0.975. (d) SNR: 26.75 SSIM: 0.968. (e) SNR: 37.94 SSIM: 0.998.

(f) SNR: 13.12 SSIM: 0.781. (g) SNR: 12.89 SSIM: 0.581. (h) SNR: 10.03 SSIM: 0.695. (i) SNR: 15.44 SSIM: 0.830. (j) SNR: 18.13 SSIM: 0.895.

(k) SNR: 10.07 SSIM: 0.714. (l) SNR: 9.32 SSIM: 0.527. (m) SNR: 7.81 SSIM: 0.613. (n) SNR: 11.75 SSIM: 0.742. (o) SNR: 14.92 SSIM: 0.857.

(p) SNR: 8.11 SSIM: 0.649. (q) SNR: 7.03 SSIM: 0.420. (r) SNR: 6.96 SSIM: 0.568. (s) SNR: 8.79 SSIM: 0.657. (t) SNR: 11.83 SSIM: 0.779.

(u) SNR: 5.91 SSIM: 0.530. (v) SNR: 5.51 SSIM: 0.371. (w) SNR: 5.51 SSIM: 0.456. (x) SNR: 6.60 SSIM: 0.505. (y) SNR: 8.46 SSIM: 0.670.

(z) SNR: 4.24 SSIM: 0.416. (aa) SNR: 4.11 SSIM: 0.287. (ab) SNR: 4.22 SSIM: 0.362. (ac) SNR: 5.19 SSIM: 0.412. (ad) SNR: 4.92 SSIM: 0.474.

(ae)

Figure 3.13 Reconstruction results for *Image 26* of the Wonsan test set with noise $\sigma_{\mathbf{n}} = 0.1\,\sigma_{\mathbf{y}}$. First row, full data, second row, 90% data, third row, 80% data, fourth row, 70% data, fifth row, 50% data, sixth row, 30% data. First column, FFT-based reconstruction, second column, NQR-based reconstruction, third column, DL-based reconstruction, fourth column, PnP-BM3D based reconstruction, fifth column, PnP-CNN-SAR based reconstruction. (ae) Reference image.

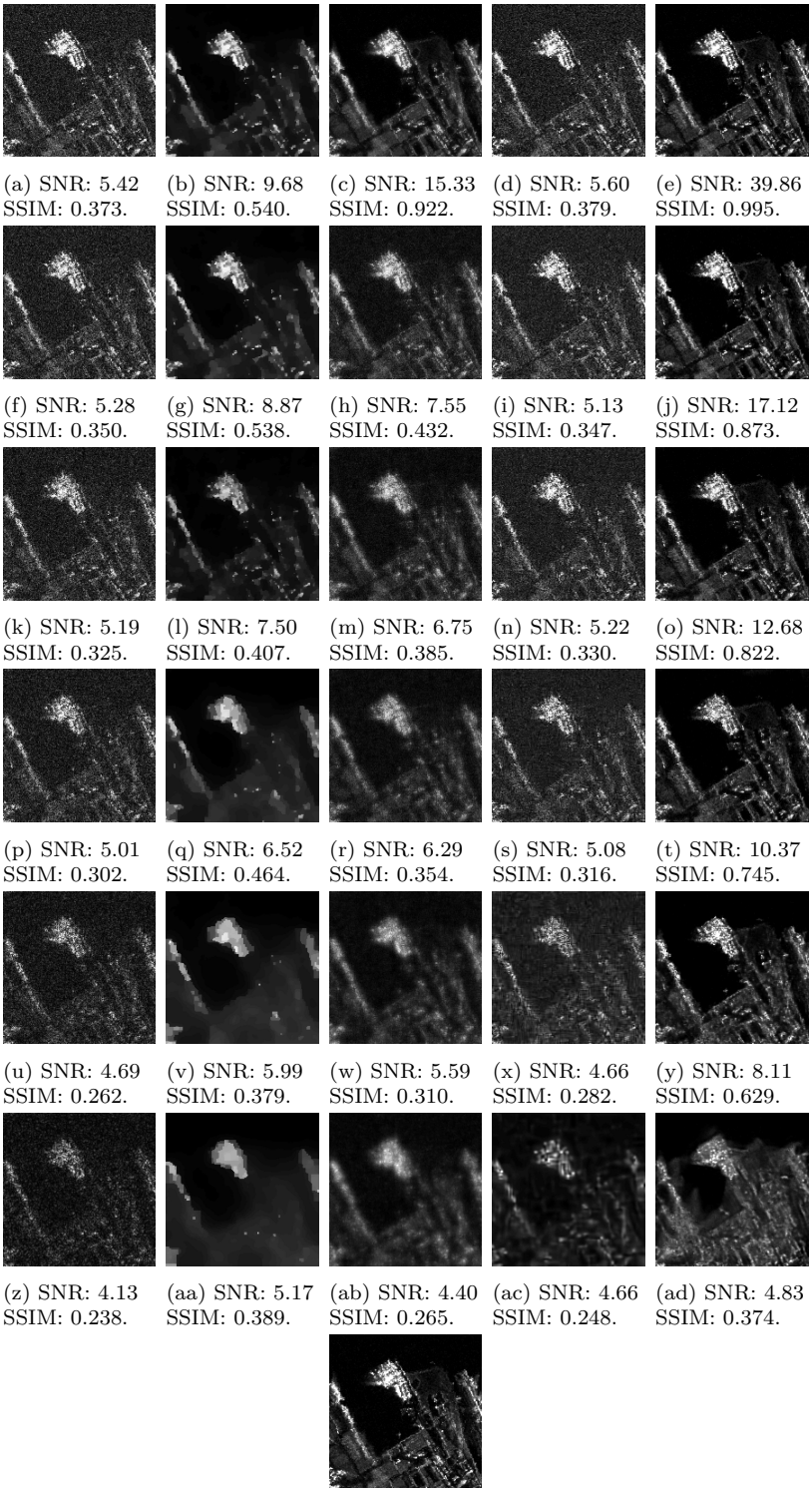

(a) SNR: 5.42 SSIM: 0.373. (b) SNR: 9.68 SSIM: 0.540. (c) SNR: 15.33 SSIM: 0.922. (d) SNR: 5.60 SSIM: 0.379. (e) SNR: 39.86 SSIM: 0.995.

(f) SNR: 5.28 SSIM: 0.350. (g) SNR: 8.87 SSIM: 0.538. (h) SNR: 7.55 SSIM: 0.432. (i) SNR: 5.13 SSIM: 0.347. (j) SNR: 17.12 SSIM: 0.873.

(k) SNR: 5.19 SSIM: 0.325. (l) SNR: 7.50 SSIM: 0.407. (m) SNR: 6.75 SSIM: 0.385. (n) SNR: 5.22 SSIM: 0.330. (o) SNR: 12.68 SSIM: 0.822.

(p) SNR: 5.01 SSIM: 0.302. (q) SNR: 6.52 SSIM: 0.464. (r) SNR: 6.29 SSIM: 0.354. (s) SNR: 5.08 SSIM: 0.316. (t) SNR: 10.37 SSIM: 0.745.

(u) SNR: 4.69 SSIM: 0.262. (v) SNR: 5.99 SSIM: 0.379. (w) SNR: 5.59 SSIM: 0.310. (x) SNR: 4.66 SSIM: 0.282. (y) SNR: 8.11 SSIM: 0.629.

(z) SNR: 4.13 SSIM: 0.238. (aa) SNR: 5.17 SSIM: 0.389. (ab) SNR: 4.40 SSIM: 0.265. (ac) SNR: 4.66 SSIM: 0.248. (ad) SNR: 4.83 SSIM: 0.374.

(ae)

Figure 3.14 Reconstruction results for *Image 12* of the Wonsan test set with noise $\sigma_{\mathbf{n}} = \sigma_{\mathbf{y}}$. First row, full data, second row, 90% data, third row, 80% data, fourth row, 70% data, fifth row, 50% data, sixth row, 30% data. First column, FFT-based reconstruction, second column, NQR-based reconstruction, third column, DL-based reconstruction, fourth column, PnP-BM3D based reconstruction, fifth column, PnP-CNN-SAR based reconstruction. (ae) Reference image.

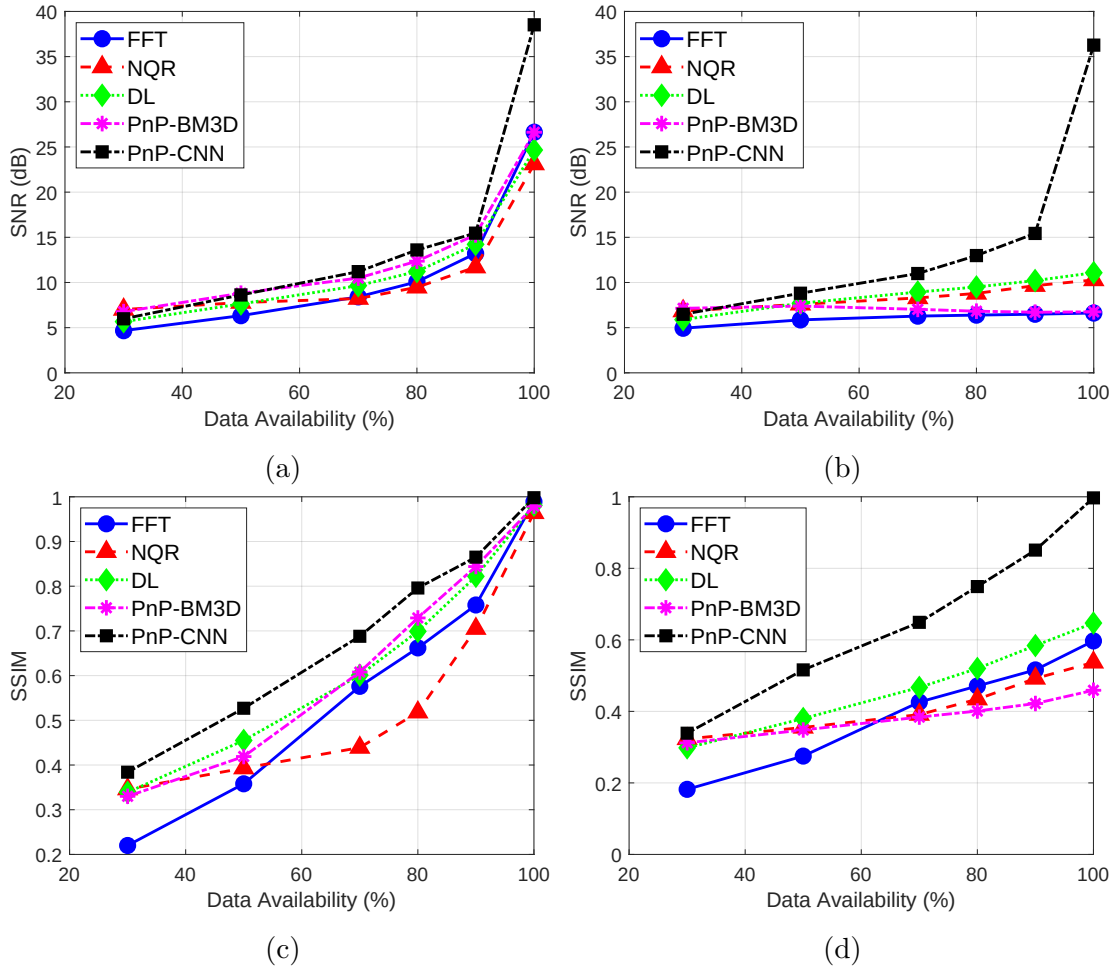

Figure 3.15 Average SNR values for different scene experiments for (a) $\sigma_{\mathbf{n}} = 0.1\,\sigma_{\mathbf{y}}$, and (b) $\sigma_{\mathbf{n}} = \sigma_{\mathbf{y}}$. Average SSIM values for different scene experiments for (c) $\sigma_{\mathbf{n}} = 0.1\,\sigma_{\mathbf{y}}$, and (d) $\sigma_{\mathbf{n}} = \sigma_{\mathbf{y}}$.

Nevertheless, we show results from all methods. Results show that our framework outperforms other methods in 9 scenarios in terms of SNR and, in all scenarios in terms of SSIM. More detailed results can be found in the supplementary material.

Figures 3.16 and 3.17 show the reconstruction results for *Image 16* with noise $\sigma_{\mathbf{n}} = 0.1\,\sigma_{\mathbf{y}}$ and *Image 78* with noise $\sigma_{\mathbf{n}} = \sigma_{\mathbf{y}}$, respectively. Once again, PnP-CNN-SAR produces visually better reconstructions, and is able to capture/preserve more features and details compared to other methods. The performance of our approach on the different scene experiments suggests that it offers good generalization capability.

3.3.4 Training Different Networks for Different Scenarios

In Table 3.1 we have shown the average SNR and SSIM values that are achieved using different networks in each scenario. Our first observation is that, the network that gives the best result for a particular scenario in terms of SNR, is not necessarily

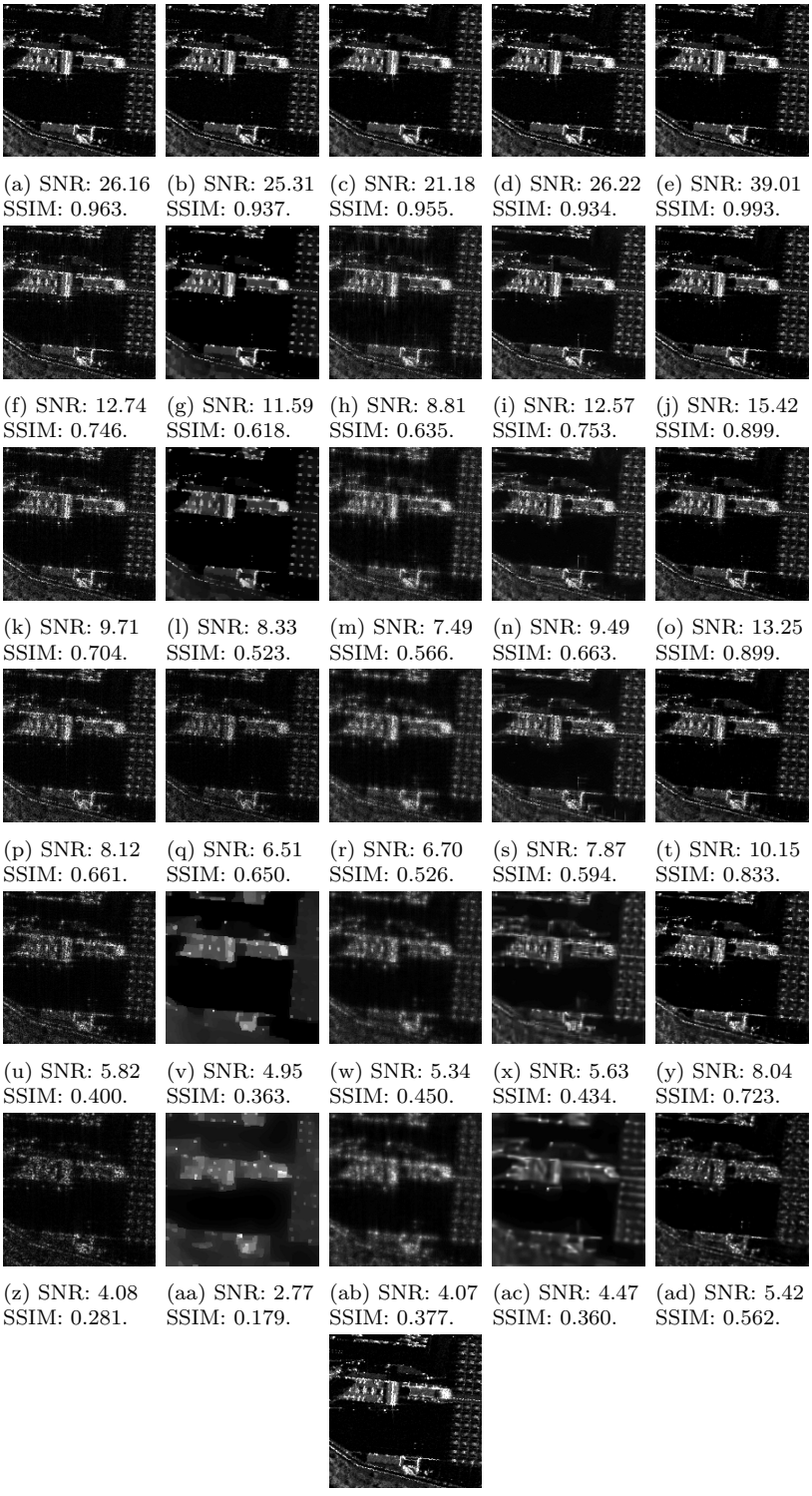

(a) SNR: 26.16 SSIM: 0.963. (b) SNR: 25.31 SSIM: 0.937. (c) SNR: 21.18 SSIM: 0.955. (d) SNR: 26.22 SSIM: 0.934. (e) SNR: 39.01 SSIM: 0.993.

(f) SNR: 12.74 SSIM: 0.746. (g) SNR: 11.59 SSIM: 0.618. (h) SNR: 8.81 SSIM: 0.635. (i) SNR: 12.57 SSIM: 0.753. (j) SNR: 15.42 SSIM: 0.899.

(k) SNR: 9.71 SSIM: 0.704. (l) SNR: 8.33 SSIM: 0.523. (m) SNR: 7.49 SSIM: 0.566. (n) SNR: 9.49 SSIM: 0.663. (o) SNR: 13.25 SSIM: 0.899.

(p) SNR: 8.12 SSIM: 0.661. (q) SNR: 6.51 SSIM: 0.650. (r) SNR: 6.70 SSIM: 0.526. (s) SNR: 7.87 SSIM: 0.594. (t) SNR: 10.15 SSIM: 0.833.

(u) SNR: 5.82 SSIM: 0.400. (v) SNR: 4.95 SSIM: 0.363. (w) SNR: 5.34 SSIM: 0.450. (x) SNR: 5.63 SSIM: 0.434. (y) SNR: 8.04 SSIM: 0.723.

(z) SNR: 4.08 SSIM: 0.281. (aa) SNR: 2.77 SSIM: 0.179. (ab) SNR: 4.07 SSIM: 0.377. (ac) SNR: 4.47 SSIM: 0.360. (ad) SNR: 5.42 SSIM: 0.562.

(ae)

Figure 3.16 Reconstruction results for *Image 16* of the Kapıkule test set with noise $\sigma_{\mathbf{n}} = 0.1\,\sigma_{\mathbf{y}}$. First row, full data, second row, 90% data, third row, 80% data, fourth row, 70% data, fifth row, 50% data, sixth row, 30% data. First column, FFT-based reconstruction, second column, NQR-based reconstruction, third column, DL-based reconstruction, fourth column, PnP-BM3D based reconstruction, fifth column, PnP-CNN-SAR based reconstruction. (ae) Reference image.

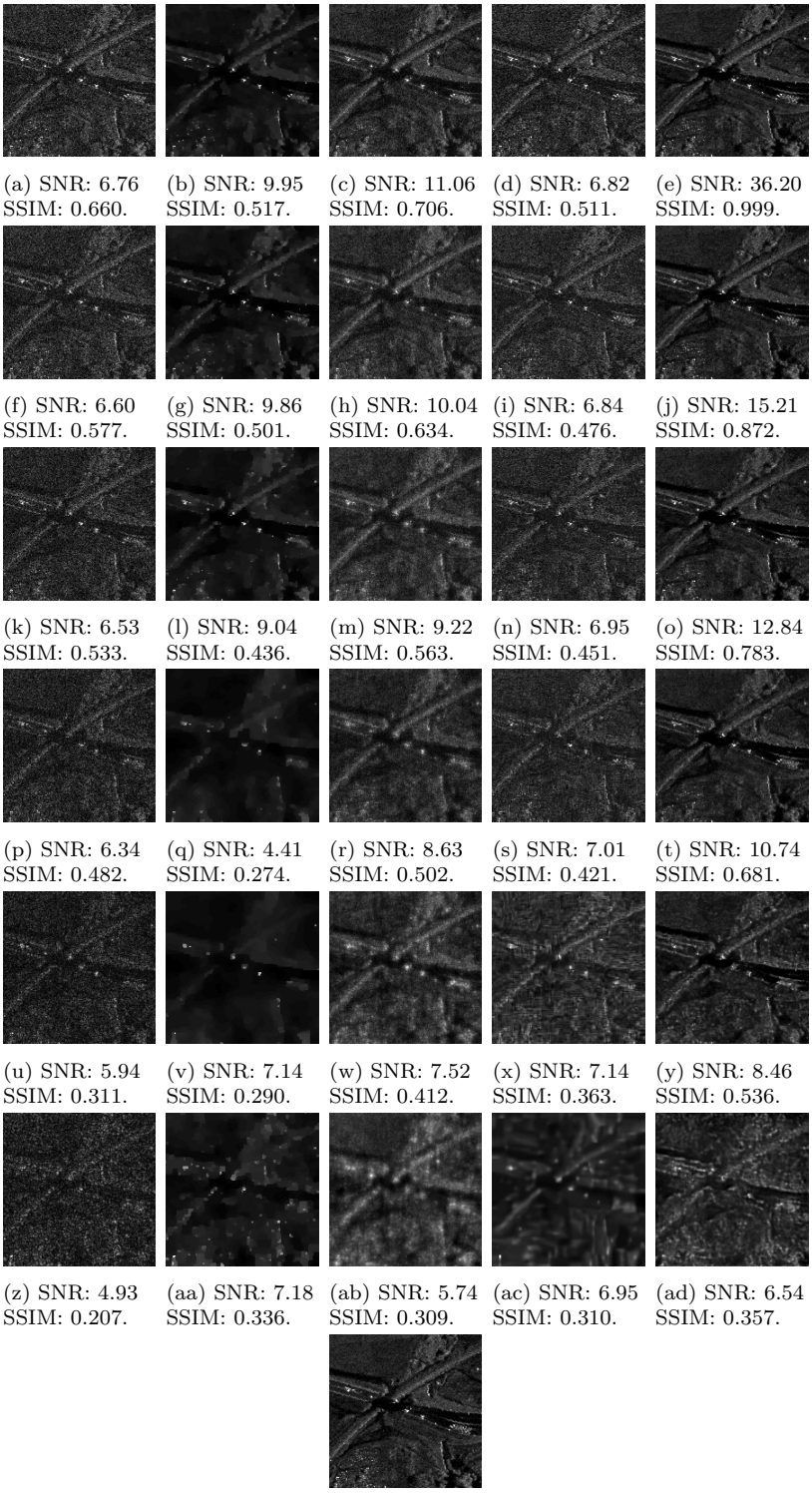

(a) SNR: 6.76 SSIM: 0.660. (b) SNR: 9.95 SSIM: 0.517. (c) SNR: 11.06 SSIM: 0.706. (d) SNR: 6.82 SSIM: 0.511. (e) SNR: 36.20 SSIM: 0.999.

(f) SNR: 6.60 SSIM: 0.577. (g) SNR: 9.86 SSIM: 0.501. (h) SNR: 10.04 SSIM: 0.634. (i) SNR: 6.84 SSIM: 0.476. (j) SNR: 15.21 SSIM: 0.872.

(k) SNR: 6.53 SSIM: 0.533. (l) SNR: 9.04 SSIM: 0.436. (m) SNR: 9.22 SSIM: 0.563. (n) SNR: 6.95 SSIM: 0.451. (o) SNR: 12.84 SSIM: 0.783.

(p) SNR: 6.34 SSIM: 0.482. (q) SNR: 4.41 SSIM: 0.274. (r) SNR: 8.63 SSIM: 0.502. (s) SNR: 7.01 SSIM: 0.421. (t) SNR: 10.74 SSIM: 0.681.

(u) SNR: 5.94 SSIM: 0.311. (v) SNR: 7.14 SSIM: 0.290. (w) SNR: 7.52 SSIM: 0.412. (x) SNR: 7.14 SSIM: 0.363. (y) SNR: 8.46 SSIM: 0.536.

(z) SNR: 4.93 SSIM: 0.207. (aa) SNR: 7.18 SSIM: 0.336. (ab) SNR: 5.74 SSIM: 0.309. (ac) SNR: 6.95 SSIM: 0.310. (ad) SNR: 6.54 SSIM: 0.357.

(ae)

Figure 3.17 Reconstruction results for *Image 78* of the Kapıkule test set with noise $\sigma_{\mathbf{n}} = \sigma_{\mathbf{y}}$. First row, full data, second row, 90% data, third row, 80% data, fourth row, 70% data, fifth row, 50% data, sixth row, 30% data. First column, FFT-based reconstruction, second column, NQR-based reconstruction, third column, DL-based reconstruction, fourth column, PnP-BM3D based reconstruction, fifth column, PnP-CNN-SAR based reconstruction. (ae) Reference image.

Table 3.4 Decision process of which network to use in which case.

	Data availability is known	Data availability is unknown
Noise level is known	Use a network trained with same amount of noise and higher data availability	Use a network trained with the same noise level and 70-90% data availability
Noise level is unknown	Use a network trained with high noise and higher data availability	Use a network trained with high noise and 70-90% data availability

the one trained for that scenario, rather, in most cases, the one that is trained with slightly higher data availability and same noise level. Another important observation is that, in each 6×6 block of the Table 3.1, the SNR values almost always decrease from left to right, which shows that regardless of for which case the network is trained, it is always easier for the network to reconstruct images from higher data availability levels. One last thing to note is that the performance of the networks trained with higher noise on the scenarios with lower noise is much better than the performance of the networks trained with lower noise on the scenarios with higher noise. These observations tell us that, when deciding for what kind of network one should train and use, a good rule of thumb would be; if both the data availability and the noise levels are known for the test scenario at hand, use a network trained with the same amount of noise and a slightly higher data; if only noise level is known, using a network trained with 70-90% data and same noise level would be a reasonable approach; if only data availability is known, safest approach would be to train with slightly higher data and high noise; and if neither is known, training with 70-90% data availability and high noise would be preferred approach. Table 3.4 shows the summary of the suggested decision process.

Reconstruction results in Figures 3.5 and 3.6 show that SNR and SSIM do not measure the performance of the methods well, especially in the case of lower data availability levels, i.e., 50% and 30%. To further elaborate that, in Figure 3.18, we show the reconstruction results of all 12 networks for *Image 7* of the synthetic test set for the case of 30% data availability and noise $\sigma_{\mathbf{n}} = 0.1\sigma_{\mathbf{y}}$. While the network trained with 50% data availability and noise $\sigma_{\mathbf{n}} = 0.1\sigma_{\mathbf{y}}$ performs the best in terms of both SNR and SSIM, it is not entirely clear that this is the best reconstruction in terms of visual quality. It seem that each network was able capture some features from the original scene and missing many others. There also seems to be a trend that networks trained with lower data availability tend to generate smoother reconstructions, compared to networks trained with higher data availability levels.

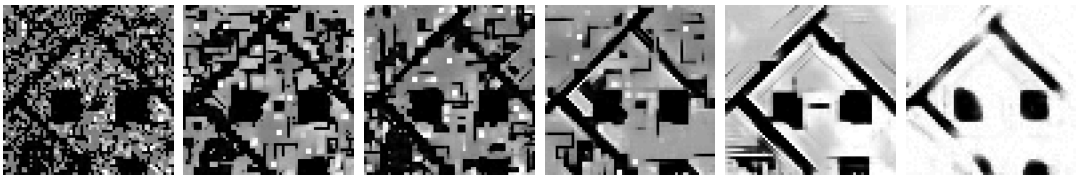

(a) SNR: 3.96 SSIM: 0.284. (b) SNR: 4.87 SSIM: 0.321. (c) SNR: 4.79 SSIM: 0.299. (d) SNR: 6.89 SSIM: 0.404. (e) SNR: 7.63 SSIM: 0.410. (f) SNR: 4.07 SSIM: 0.278.

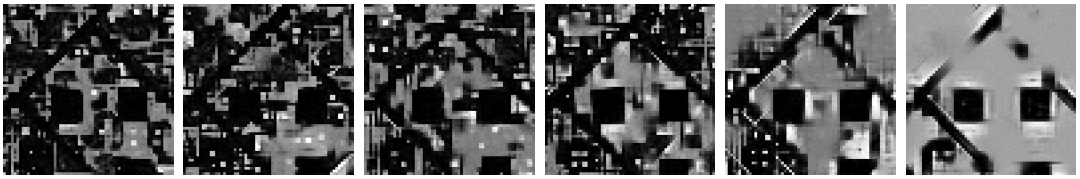

(g) SNR: 2.94 SSIM: 0.225. (h) SNR: 3.23 SSIM: 0.234. (i) SNR: 3.61 SSIM: 0.269. (j) SNR: 3.71 SSIM: 0.290. (k) SNR: 5.49 SSIM: 0.330. (l) SNR: 7.31 SSIM: 0.323.

Figure 3.18 Reconstruction results of *Image 7* of the synthetic test set in the case of 30% data availability and $\sigma_{\mathbf{n}} = 0.1\sigma_{\mathbf{y}}$ using different networks. First row, results of the networks trained with noise $\sigma_{\mathbf{n}} = 0.1\sigma_{\mathbf{y}}$. Second row, results of the networks trained with noise $\sigma_{\mathbf{n}} = \sigma_{\mathbf{y}}$. Each column represents a data availability level, in a decreasing order from left to right, i.e., (a) is the result of the network trained with full data and $\sigma_{\mathbf{n}} = 0.1\sigma_{\mathbf{y}}$, (b) is the result of the network trained with 90% data and $\sigma_{\mathbf{n}} = 0.1\sigma_{\mathbf{y}}$ etc. Note that (e) has the highest SNR among all reconstructions and hence, is the one presented in Figure 3.5ad.

3.3.5 Runtime Analysis

Table 3.5 shows the comparison of runtimes across different methods for the same scene experiments. PnP-CNN-SAR works faster than the NQR-based method in all scenarios, and PnP-BM3D in two scenarios. It is also worth noting that PnP-CNN-SAR works considerably slower in lower data availability scenarios, compared to the scenarios with higher data availability.

Figures 3.19 and 3.20 show the percentage shares of various steps within the overall algorithm time for the same scene experiments, for PnP-CNN-SAR. These results show that the prior update step dominates the overall procedure and takes around $60 - 90\%$ of the computation time, while the phase alignment step never exceeds 30%. Magnitude update and other steps do not contribute as much to the computational expense, compared to these two steps. Reconstructing the entire image at once, instead of using a patch-based approach, would likely reduce the computation time of the prior update step. However this would be at the expense of increasing the computation time of the phase alignment step, which is observed in the PnP-BM3D experiments, for which the results are shown in Figures 3.21 and 3.22. Note however that abandoning the patch-based approach would likely result in performance degradation. For comparison, we also show the percentage shares of various steps within the overall algorithm time for the same scene experiments, for DL-based reconstruction [3], in Figures 3.23 and 3.24.

Table 3.5 Average reconstruction time for one image for the same scene experiments. FFT-based reconstruction is not shown as it practically works in real time.

Scenario	NQR-based [1]	DL-based [3]	PnP-BM3D	PnP-CNN-SAR
Full Data, $\sigma_{\mathbf{n}} = 0.1\sigma_{\mathbf{y}}$	206.8 s	12.0 s	13.6 s	16.7 s
90% Data, $\sigma_{\mathbf{n}} = 0.1\sigma_{\mathbf{y}}$	223.1 s	15.6 s	19.3 s	23.0 s
80% Data, $\sigma_{\mathbf{n}} = 0.1\sigma_{\mathbf{y}}$	229.7 s	17.9 s	31.8 s	22.1 s
70% Data, $\sigma_{\mathbf{n}} = 0.1\sigma_{\mathbf{y}}$	232.8 s	19.7 s	27.6 s	24.5 s
50% Data, $\sigma_{\mathbf{n}} = 0.1\sigma_{\mathbf{y}}$	236.5 s	22.4 s	34.8 s	102.8 s
30% Data, $\sigma_{\mathbf{n}} = 0.1\sigma_{\mathbf{y}}$	232.1 s	27.0 s	25.2 s	91.4 s
Full Data, $\sigma_{\mathbf{n}} = \sigma_{\mathbf{y}}$	209.9 s	15.1 s	19.1 s	25.7 s
90% Data, $\sigma_{\mathbf{n}} = \sigma_{\mathbf{y}}$	229.4 s	16.9 s	17.6 s	27.4 s
80% Data, $\sigma_{\mathbf{n}} = \sigma_{\mathbf{y}}$	235.7 s	17.8 s	10.9 s	27.1 s
70% Data, $\sigma_{\mathbf{n}} = \sigma_{\mathbf{y}}$	230.2 s	21.6 s	11.3 s	26.5 s
50% Data, $\sigma_{\mathbf{n}} = \sigma_{\mathbf{y}}$	225.3 s	27.3 s	16.0 s	113.8 s
30% Data, $\sigma_{\mathbf{n}} = \sigma_{\mathbf{y}}$	218.5 s	32.0 s	18.6 s	84.8 s

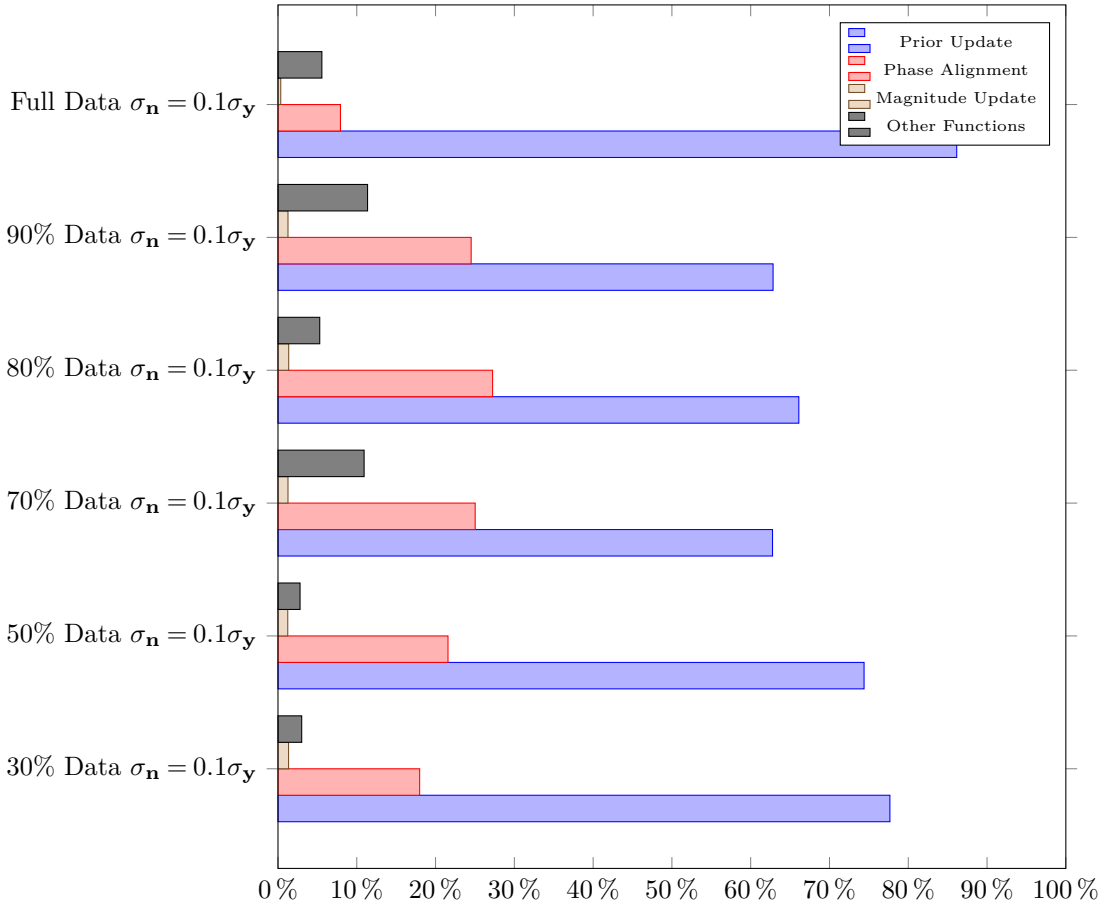

Figure 3.19 Percentage shares of various steps within the overall algorithm time for the same scene experiment scenarios with $\sigma_{\mathbf{n}} = 0.1\sigma_{\mathbf{y}}$, for PnP-CNN-SAR.

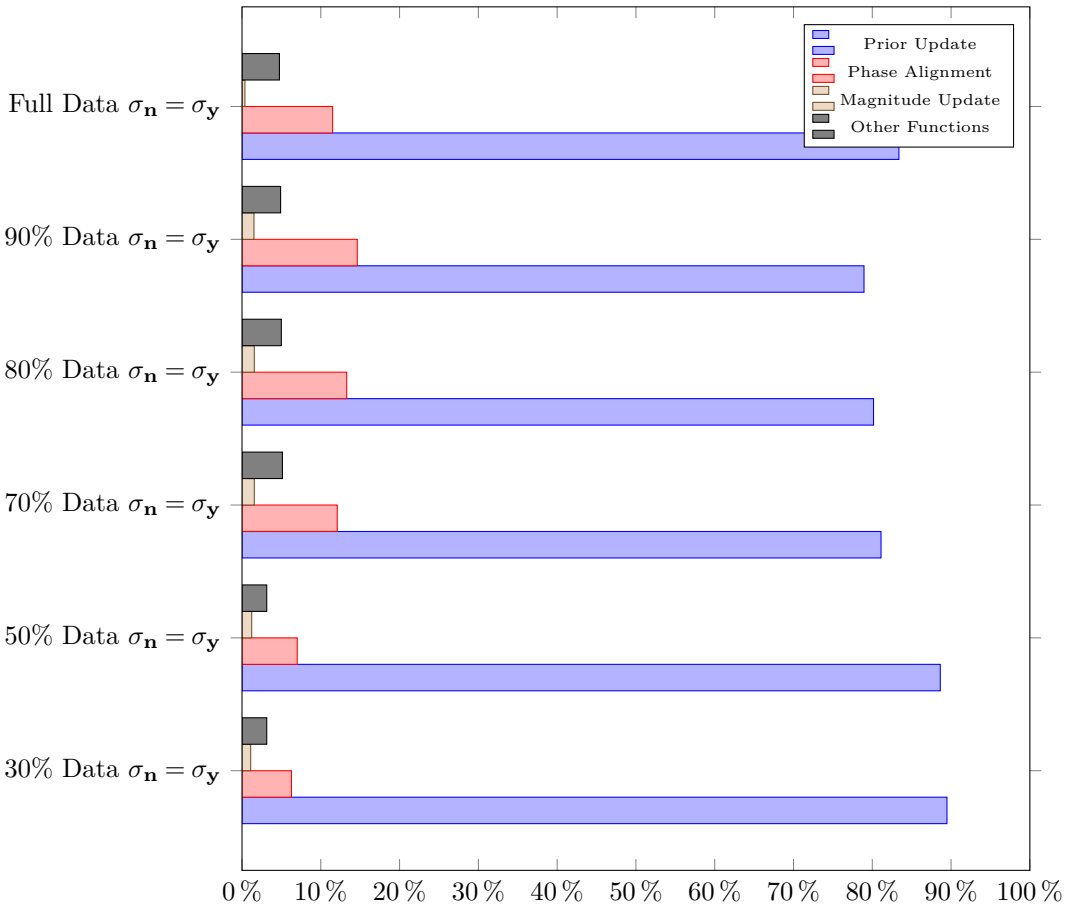

Figure 3.20 Percentage shares of various steps within the overall algorithm time for the same scene experiment scenarios with $\sigma_{\mathbf{n}} = \sigma_{\mathbf{y}}$, for PnP-CNN-SAR.

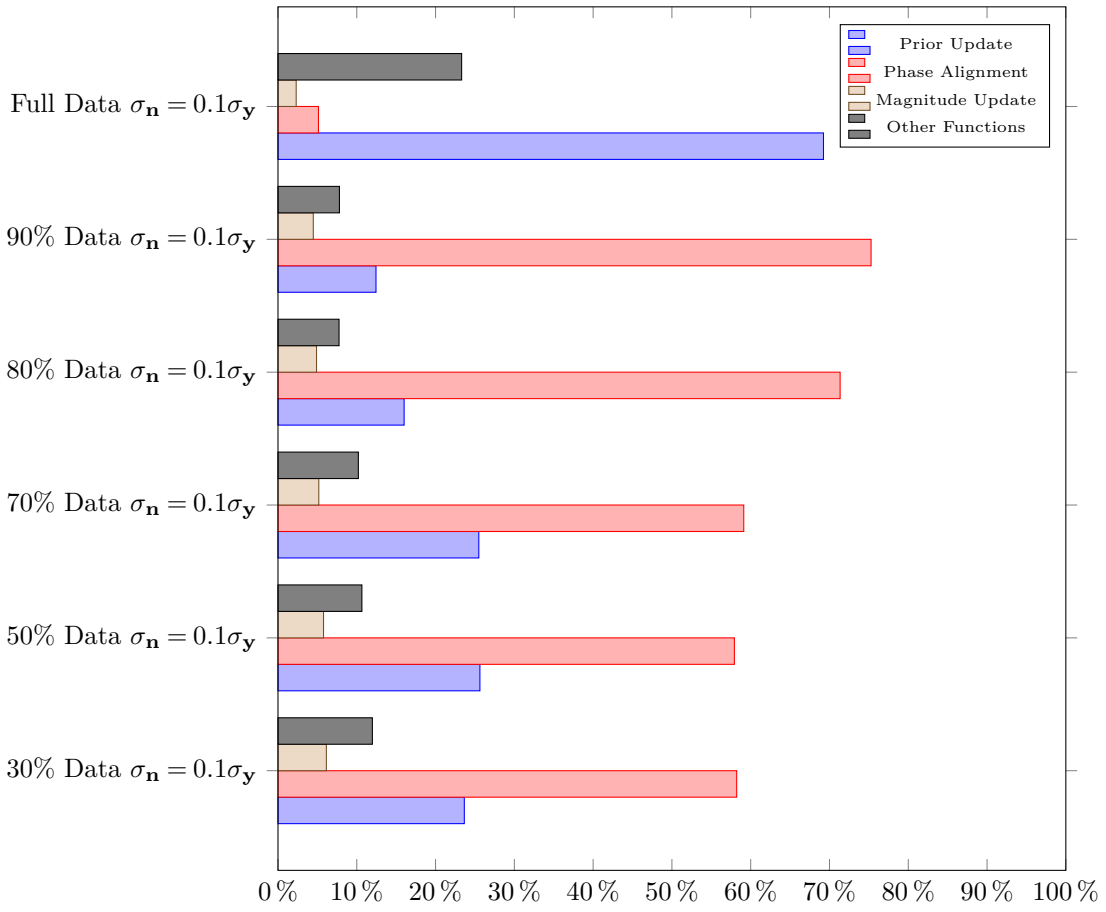

Figure 3.21 Percentage shares of various steps within the overall algorithm time for the same scene experiment scenarios with $\sigma_{\mathbf{n}} = 0.1\sigma_{\mathbf{y}}$, for PnP-BM3D.

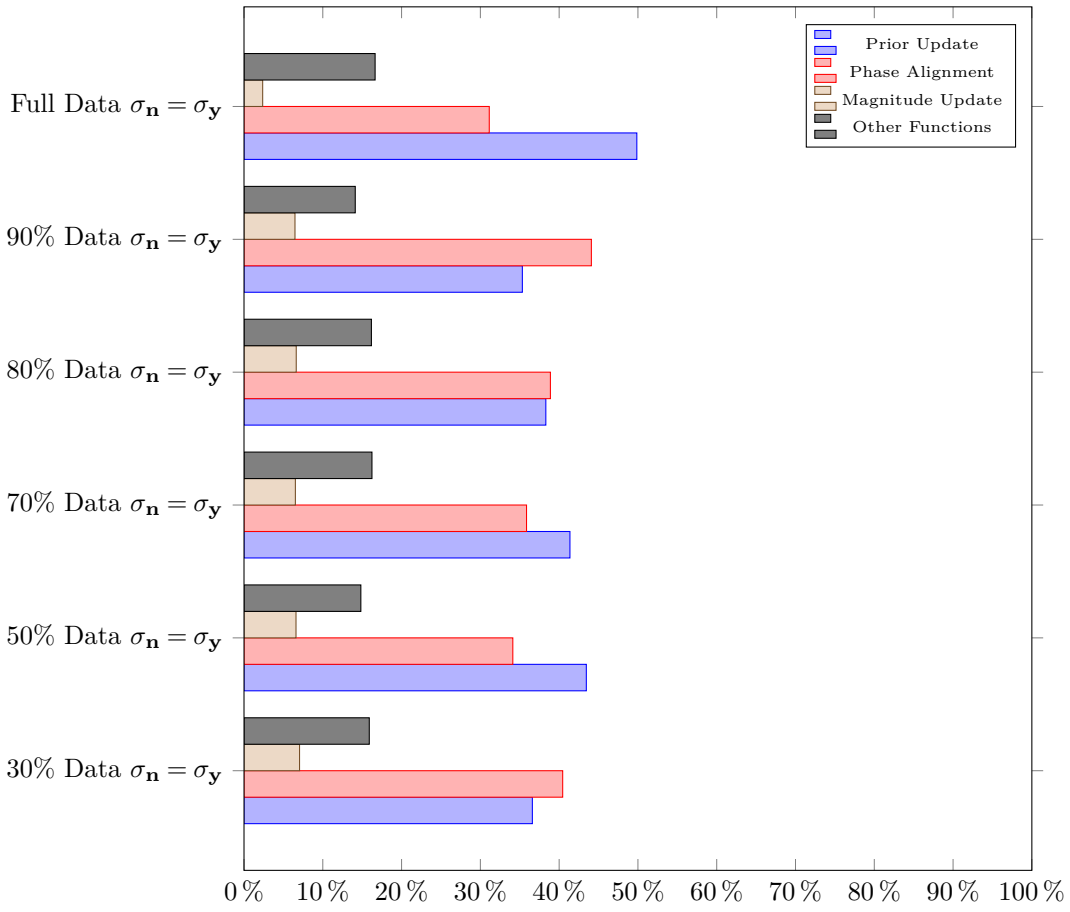

Figure 3.22 Percentage shares of various steps within the overall algorithm time for the same scene experiment scenarios with $\sigma_{\mathbf{n}} = \sigma_{\mathbf{y}}$, for PnP-BM3D.

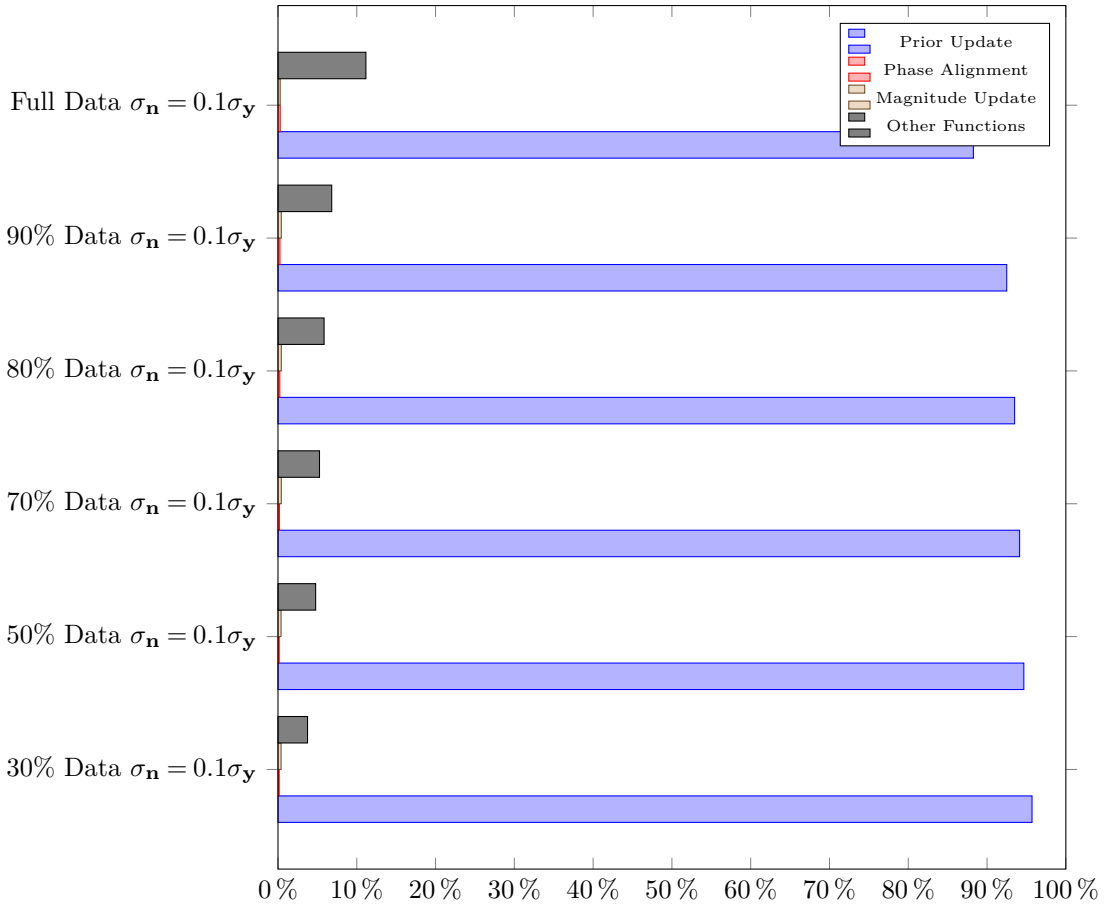

Figure 3.23 Percentage shares of various steps within the overall algorithm time for the same scene experiment scenarios with $\sigma_{\mathbf{n}} = 0.1\sigma_{\mathbf{y}}$, for DL-based reconstruction [3].

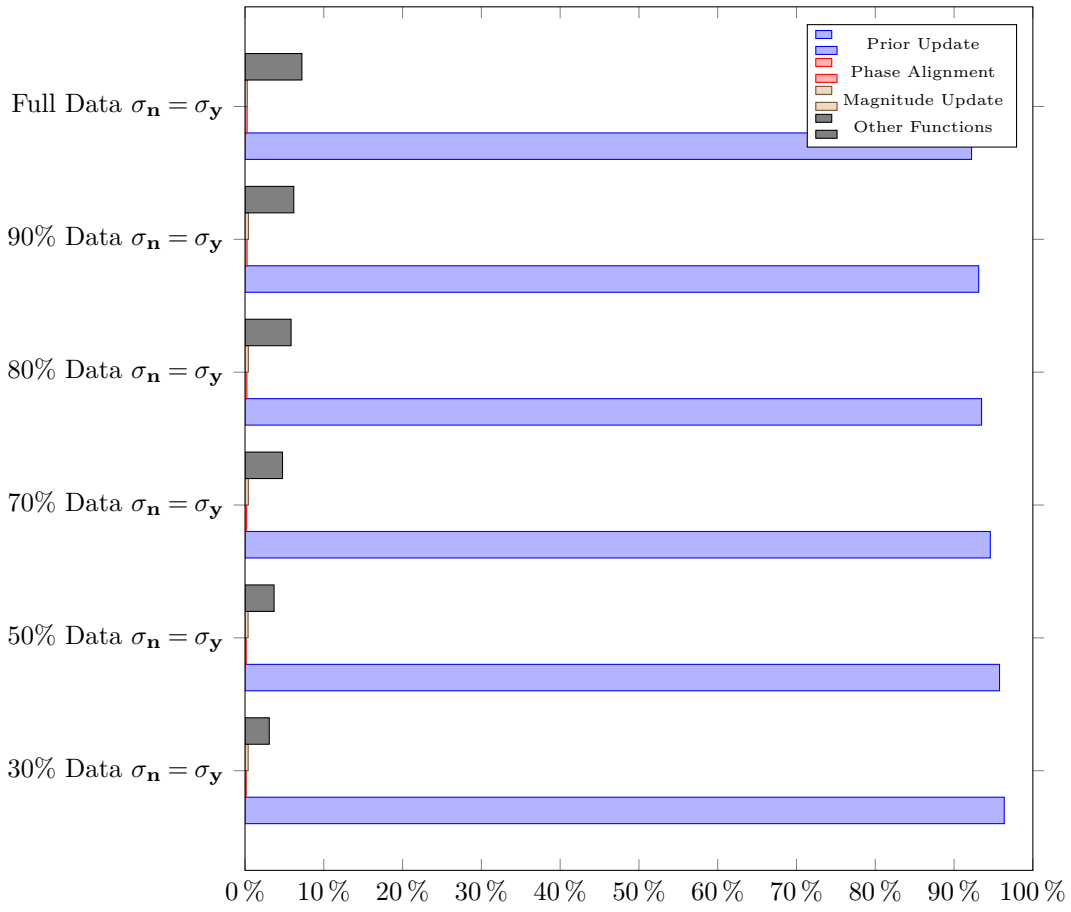

Figure 3.24 Percentage shares of various steps within the overall algorithm time for the same scene experiment scenarios with $\sigma_{\mathbf{n}} = \sigma_{\mathbf{y}}$, for DL-based reconstruction [3].

3.4 Summary

The results in this chapter show that performing regularization using deep priors with the help of PnP priors framework can produce better reconstructions in terms of visual quality compared to conventional as well as state-of-the-art SAR image reconstruction methods, especially in the more challenging, lower data availability and higher noise scenarios, and even when the performance metrics fail to fully reflect the performance of our proposed framework. Overall, these results suggest that deep learning methods may have the potential to learn complicated spatial patterns and enable their incorporation as priors into computational radar imaging.

In this chapter, we have only focused on image reconstruction, and did not account for possible phase errors. In Chapter 4, we extend the PnP-CNN-SAR framework to jointly address image reconstruction and phase error correction.

Chapter 4

PnP-CNN-SAR-AF for Joint Image Reconstruction and Phase Error Correction

In Chapter 3, we have introduced the PnP-CNN-SAR framework for SAR image reconstruction and demonstrated its effectiveness in various scenarios. However, in this framework, we did not account for phase errors. Although PnP-CNN-SAR can be combined with a postprocessing autofocus algorithm to eliminate phase errors, previous studies have shown that joint image reconstruction and phase error correction can produce better results than performing these two tasks sequentially [52,75,78,79,84,92,93]. Hence, in this chapter, we extend the PnP-CNN-SAR framework to address phase errors along with image reconstruction and introduce the PnP-CNN-SAR-AF framework (where AF stands for autofocus). This chapter includes the formulation and preliminary results of PnP-CNN-SAR-AF for 1D phase errors, and the formulation and implementation for 2D separable and non-separable phase errors are left for future work.

4.1 Objective Function

Consider the modified discrete observation model:

$$\mathbf{y} = \mathbf{H}(\boldsymbol{\phi})\mathbf{f} + \mathbf{n} \tag{4.1}$$

where $\boldsymbol{\phi}$ stands for the 1D phase error. Note that the observation model matrix $\mathbf{H}$ is no longer constant, rather it is a function of $\boldsymbol{\phi}$. Now let us introduce the regularized

objective function to solve (4.1):

$$\hat{\mathbf{f}}, \hat{\boldsymbol{\phi}} = \underset{\mathbf{f},\boldsymbol{\phi}}{\operatorname{argmin}} \|\mathbf{y} - \mathbf{H}(\boldsymbol{\phi})\mathbf{f}\|_2^2 + \lambda \mathcal{R}(\mathbf{f}_m) \tag{4.2}$$

where $\mathbf{f}_m = |\mathbf{f}|$. As we have already discussed in Chapter 3, for most SAR scenes, reflectivity phase at a certain location can be modeled as a uniformly distributed random variable uncorrelated with the phase at other locations [11]. Nevertheless, we need to estimate the complex-valued field $\mathbf{f}$ in the process of ensuring good data fidelity. Again, we can write $\mathbf{f} = \boldsymbol{\Theta}\mathbf{f}_m$ where $\boldsymbol{\Theta}$ is a diagonal matrix containing the phases of $\mathbf{f}$ at each pixel in exponentiated form, i.e., $\boldsymbol{\Theta} = \operatorname{diag}(e^{j\varphi(\mathbf{f})})$ where $\varphi(\cdot)$ denotes the phase. Then we get:

$$\hat{\mathbf{f}}_m, \hat{\boldsymbol{\theta}}, \hat{\boldsymbol{\phi}} = \underset{\mathbf{f}_m,\boldsymbol{\theta},\boldsymbol{\phi}}{\operatorname{argmin}} \|\mathbf{y} - \mathbf{H}(\boldsymbol{\phi})\boldsymbol{\Theta}\mathbf{f}_m\|_2^2 + \lambda \mathcal{R}(\mathbf{f}_m). \tag{4.3}$$

Once again, we do not explicitly define the regularizer until we formulate ADMM iterations for (4.3), and decouple the data-fidelity term and the regularization term.

4.2 Variable Splitting and ADMM

Rewriting (4.3) in a suitable form by introducing an auxiliary variable with a constraint, we have

$$\hat{\mathbf{f}}_m, \hat{\boldsymbol{\theta}}, \hat{\boldsymbol{\phi}}, \hat{\mathbf{h}} = \underset{\mathbf{f}_m,\boldsymbol{\theta},\boldsymbol{\phi},\mathbf{h}}{\operatorname{argmin}} \|\mathbf{y} - \mathbf{H}(\boldsymbol{\phi})\boldsymbol{\Theta}\mathbf{f}_m\|_2^2 + \lambda \mathcal{R}(\mathbf{h}) \text{ s.t. } \mathbf{f}_m - \mathbf{h} = 0. \tag{4.4}$$

The augmented Lagrangian for (4.4) is given by

$$\mathcal{L}(\hat{\mathbf{f}}_m, \hat{\boldsymbol{\theta}}, \hat{\boldsymbol{\phi}}, \hat{\mathbf{h}}, \hat{\mathbf{u}}) = \|\mathbf{y} - \mathbf{H}(\boldsymbol{\phi})\boldsymbol{\Theta}\mathbf{f}_m\|_2^2 + \lambda \mathcal{R}(\mathbf{h}) + \frac{\rho}{2}\|\mathbf{f}_m - \mathbf{h} + \mathbf{u}\|_2^2 + \frac{\rho}{2}\|\mathbf{u}\|_2^2. \tag{4.5}$$

Let $\tilde{\mathbf{f}}^{(k)} = \mathbf{h}^{(k)} - \mathbf{u}^{(k)}$, $\tilde{\mathbf{h}}^{(k)} = \mathbf{f}_m^{(k+1)} + \mathbf{u}^{(k)}$. Also, let us introduce a vector $\boldsymbol{\theta} \in \mathbb{C}^{N\times 1}$ that contains the diagonal elements of the phase matrix $\boldsymbol{\Theta}$, and the matrix $\mathbf{B}$ whose diagonal elements are the reflectivity magnitudes $\mathbf{f}_m$. Finally, let us invoke the constraint that the magnitudes of the elements of $\boldsymbol{\theta}$ denoted as $|\theta_i|$ should be 1, simply because they contain phases of $\mathbf{f}$ at each pixel in exponentiated vector form $e^{j\varphi(\mathbf{f})}$. Then, each iteration of the ADMM algorithm will perform model update, phase error estimation and correction, prior update, and Lagrange multiplier update steps.

Model update:

$$\boldsymbol{\theta}^{(k+1)} = \underset{\boldsymbol{\theta}}{\operatorname{argmin}} \left\| \mathbf{y} - \mathbf{H}(\boldsymbol{\phi}^{(k)})^{(k)} \mathbf{B}^{(k)} \boldsymbol{\theta} \right\|_2^2 + \lambda_{\boldsymbol{\theta}} \sum_{i=1}^{N} (|\theta_i| - 1)^2 \tag{4.6}$$

$$\mathbf{f}_m^{(k+1)} = \underset{\mathbf{f}_m}{\operatorname{argmin}} \left\| \mathbf{y} - \mathbf{H}(\boldsymbol{\phi}^{(k)})^{(k)} \boldsymbol{\Theta}^{(k)} \mathbf{f}_m \right\|_2^2 + \frac{\rho}{2} \left\| \mathbf{f}_m - \tilde{\mathbf{f}}^{(k)} \right\|_2^2. \tag{4.7}$$

Phase error estimation and correction:

For every cross-range position $p = 1 \dots P$

$$\Delta\phi_p^{(k+1)} = -\arctan(-\frac{I}{R}) \tag{4.8}$$

where

$$R = \Re\{(\mathbf{f}^{(k+1)})^H \mathbf{H}_p(\phi_p^{(k)})^H \mathbf{y}_p\} \tag{4.9}$$

and

$$I = \Im\{(\mathbf{f}^{(k+1)})^H \mathbf{H}_p(\phi_p^{(k)})^H \mathbf{y}_p\} \tag{4.10}$$

$$\phi_p^{(k+1)} = \phi_p^{(k)} + \Delta\phi_p^{(k+1)} \tag{4.11}$$

$$\mathbf{H}_p(\phi_p^{(k+1)}) = \exp\{j\Delta\phi_p^{(k+1)}\} \mathbf{H}_p(\phi_p^{(k)}). \tag{4.12}$$

Prior update:

$$\mathbf{h}^{(k+1)} = \underset{\mathbf{h}}{\operatorname{argmin}}\, \lambda\mathcal{R}(\mathbf{h}) + \frac{\rho}{2} \left\| \tilde{\mathbf{h}}^{(k)} - \mathbf{h} \right\|_2^2. \tag{4.13}$$

Lagrange multiplier update:

$$\mathbf{u}^{(k+1)} = \mathbf{u}^{(k)} + \mathbf{f}_m^{(k+1)} - \mathbf{h}^{(k+1)}. \tag{4.14}$$

$\lambda_{\boldsymbol{\theta}}$ and ρ are hyper-parameters.

The model update and phase error estimation and correction steps only depend on the forward model, while the prior update step only depends on the regularizer. ADMM first iteratively solves for $\boldsymbol{\theta}$ and $\mathbf{f}_m$ using (4.6) and (4.7) until the phase is aligned. Then for each cross-range position p, corresponding phase error is estimated using (4.8), and the model matrix is updated using (4.11) and (4.12). Note that

(4.6), (4.7), and (4.13) are optimization problems, while (4.8)-(4.12) and (4.14) are direct updates on the corresponding variables.

As is done in Chapter 3, sub-problems (4.6) and (4.7) are solved with conjugate gradient algorithm using (3.10) and (3.12), respectively. Sub-problem (4.13) is once again replaced with a CNN. However, in contrast to PnP-CNN-SAR, in PnP-CNN-SAR-AF, we investigate training the CNN using images corrupted only with noise, as well as using noisy and phase error-corrupted images. Algorithm 3 summarizes the PnP-CNN-SAR-AF framework. Note that $\mathbf{f}_m^{[t]}$ stands for the outputs of the inner loop, i.e., the model update, while $\mathbf{f}_m^{(k)}$ stands for the outputs of the outer loop, i.e., the overall ADMM algorithm. Typical value for T is 100, while the value of K depends on the amount of phase error in the data, and can be as low as 20, and as high as 1000.

4.3 Experimental Results

In this section, we demonstrate the effectiveness of PnP-CNN-SAR-AF on real SAR scenes. We also tabulate results for various scenarios, and compare them with FFT-based image reconstruction and sparsity driven autofocus (SDA) [52].

4.3.1 Setup

In both synthetic and real scene experiments, we have considered various scenarios, i.e., a single data availability level (100%) and 7 different 1D phase error levels (0; $[-\pi/6, \pi/6]$; $[-\pi/4, \pi/4]$; $[-\pi/3, \pi/3]$; $[-3\pi/8, 3\pi/8]$; $[-\pi/2, \pi/2]$; $[-2\pi/3, 2\pi/3]$) in the phase history domain, and a single noise level ($\sigma_{\mathbf{n}} = 0.1\sigma_{\mathbf{y}}$, where $\sigma_{\mathbf{y}}$ is the standard deviation of the magnitude of the phase history data), hence a total of 7 different scenarios. Note that the case of 0 phase error is equivalent to the scenario considered in Chapter 3.

The experimental procedure is the same as the procedure described in Chapter 3, i.e., same network architecture, same patch-based approach, same data augmentation procedure, etc., except that we trained a new network with the setting of 100% data availability, $\sigma_{\mathbf{n}} = 0.1\sigma_{\mathbf{y}}$ noise, and $[-\pi/6, \pi/6]$ phase error, and also, the algorithm has additional steps for phase error estimation and correction, as well as model matrix update, as described in the previous section. We have only performed same scene experiments, using the training and test windows from the Wonsan image.

Algorithm 3: PnP-CNN-SAR-AF for joint image reconstruction and 1D phase error correction.

Require: $\mathbf{y}$, $\mathbf{H}(\boldsymbol{\phi}^{(0)})$, ϵ, $\mathcal{D}_\sigma(x)$, K, T.

$\mathbf{f}^{(0)} \leftarrow \mathbf{H}(\boldsymbol{\phi}^{(0)})^H \mathbf{y}$ {Conventional reconstruction}

$\mathbf{B}^{(0)} \leftarrow \text{diag}\{\mathbf{f}_m^{(0)}\}$

$\boldsymbol{\theta}^{(0)} \leftarrow \angle \mathbf{f}^{(0)}$

$\mathbf{h}^{(0)} \leftarrow \mathbf{f}_m^{(0)}$

$\mathbf{u}^{(0)} \leftarrow 0$

$k \leftarrow 0$

$n \leftarrow 0$

while $\frac{\left\|\mathbf{u}^{(k+1)} - \mathbf{u}^{(k)}\right\|}{\left\|\mathbf{u}^{(k)}\right\|} \geq \epsilon$ and $k \leq K$ **do**

  $\tilde{\mathbf{f}}^{(k)} \leftarrow \mathbf{h}^{(k)} - \mathbf{u}^{(k)}$

  $\mathbf{f}_m^{[0]} \leftarrow \mathbf{f}_m^{(k)}$

  while $\frac{\left\|\mathbf{f}_m^{[t+1]} - \mathbf{f}_m^{[t]}\right\|}{\left\|\mathbf{f}_m^{[t]}\right\|} \geq 10^{-4}$ and $t \leq T$ **do**

    Calculate $\boldsymbol{\theta}^{(t)}$ using (4.6) {Phase alignment}

    Solve for $\mathbf{f}_m^{(t)}$ using (4.7) {Magnitude update}

    $t \leftarrow t+1$

  end while

  for Every cross-range position $p = 1 \ldots P$ **do**

    Calculate $\Delta\phi_p^{(k+1)}$ using (4.8) {Phase error estimation}

    Calculate $\phi_p^{(k+1)}$ using (4.11) {Phase error correction}

    Calculate $\mathbf{H}_p(\phi_p^{(k+1)})$ using (4.13) {Model matrix update}

  end for

  $\mathbf{f}_m^{(k+1)} \leftarrow \mathbf{f}_m^{[t]}$

  $\tilde{\mathbf{h}}^{(k)} \leftarrow \mathbf{f}_m^{(k+1)} + \mathbf{u}^{(k)}$

  $\mathbf{h}^{(k+1)} \leftarrow \mathcal{D}_\sigma(\tilde{\mathbf{h}}^{(k)})$ {Prior update}

  $\mathbf{u}^{(k+1)} \leftarrow \mathbf{u}^{(k)} + \mathbf{f}_m^{(k+1)} - \mathbf{h}^{(k+1)}$ {Lagrange multiplier update}

  $k \leftarrow k+1$

end while

return $\mathbf{f}_m^{(k+1)}$

Table 4.1 Experimental settings.

	PnP-CNN-SAR Algorithm	PnP-CNN-SAR-AF Algorithm
Network trained without phase error	PnP	PnP-AF
Network trained with phase error	PnP-pe	PnP-pe-AF

Table 4.2 Average SNR and SSIM values for different phase error levels and for PnP, PnP-pe, PnP-AF, and PnP-pe-AF.

Phase Error	PnP		PnP-pe		PnP-AF		PnP-pe-AF	
	SNR (dB)	SSIM	SNR (dB)	SSIM	SNR (dB)	SSIM	SNR (dB)	SSIM
0	40.03	0.998	26.83	0.977	26.66	0.978	26.85	0.977
$[-\pi/6, \pi/6]$	14.77	0.801	14.05	0.776	19.96	0.904	23.59	0.959
$[-\pi/4, \pi/4]$	11.39	0.671	10.59	0.642	19.88	0.901	24.09	0.963
$[-\pi/3, \pi/3]$	8.87	0.549	8.23	0.525	19.88	0.902	24.09	0.964
$[-3\pi/8, 3\pi/8]$	7.96	0.499	7.29	0.472	19.86	0.900	24.02	0.963
$[-\pi/2, \pi/2]$	5.66	0.346	5.07	0.325	19.86	0.901	24.22	0.964
$[-2\pi/3, 2\pi/3]$	3.73	0.190	3.26	0.176	19.74	0.840	24.04	0.977

4.3.2 Results

To show the effectiveness of the additional phase error estimation and correction steps as well as training the network with data containing phase errors, we first present results of four different experimental settings, namely, PnP, PnP-pe, PnP-AF, and PnP-pe-AF. In PnP and PnP-pe, the experimental procedure follows the steps in Algorithm 2, i.e., no phase error estimation and correction steps, and in PnP-AF and PnP-pe-AF, the steps given in Algorithm 3 are followed. Also, in PnP and PnP-AF, the network used is the same as the one that is used for the real scene experiments in Chapter 3, and hence trained without phase errors, while in PnP-pe and PnP-pe-AF, the network trained with data containing phase errors is used. Table 4.1 summarizes these four settings. Figures 4.1−4.7 show the reconstruction results of these settings for various scenarios for *Image 26* from the Wonsan test set, and Table 4.2 shows the average SNR and SSIM values obtained with different settings. These results suggest that the additional steps for phase error estimation and correction improve the performance significantly. Another observation is that the network trained with data containing phase errors only help if it is used within the PnP-CNN-SAR-AF framework.

Figures 4.8−4.14 and 4.15−4.21 show the reconstruction results of FFT-based reconstruction, SDA, and PnP-pe-AF, for various scenarios for *Image 26* and *Image 28* from the Wonsan test set, respectively. Table 4.3 show the quantitative comparison between these methods. These results show that PnP-pe-AF outperforms other methods in terms of both visual quality and performance metrics. It is also worth noting that SDA performs quite well in all scenarios for sparse scenes however its

(a) PnP: SNR: 37.94 SSIM: 0.998.

(b) PnP-pe: SNR: 27.35 SSIM: 0.958.

(c) PnP-AF: SNR: 26.46 SSIM: 0.954.

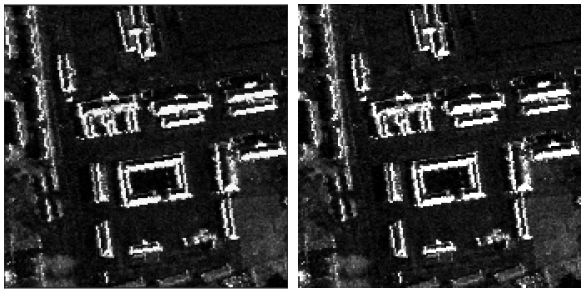

(d) PnP-pe-AF: SNR: 27.30 SSIM: 0.958.

(e) Reference image.

Figure 4.1 Reconstruction results for *Image 26* of the Wonsan test set with no phase error.

(a) PnP: SNR: 15.29 SSIM: 0.722.

(b) PnP-pe: SNR: 13.32 SSIM: 0.651.

(c) PnP-AF: SNR: 20.72 SSIM: 0.862.

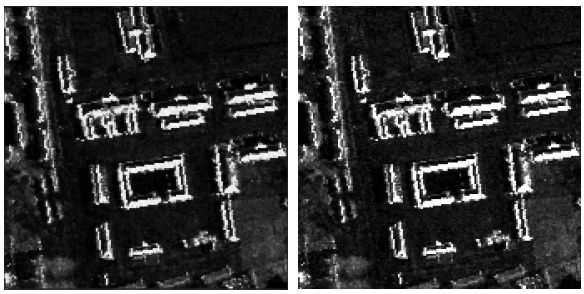

(d) PnP-pe-AF: SNR: 24.78 SSIM: 0.934.

(e) Reference image.

Figure 4.2 Reconstruction results for *Image 26* of the Wonsan test set with phase error in the range $[-\pi/6, \pi/6]$.

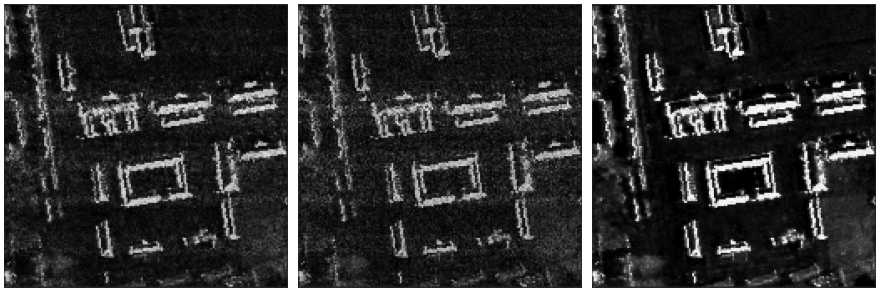

(a) PnP: SNR: 11.84 SSIM: 0.602.

(b) PnP-pe: SNR: 10.25 SSIM: 0.526.

(c) PnP-AF: SNR: 20.73 SSIM: 0.864.

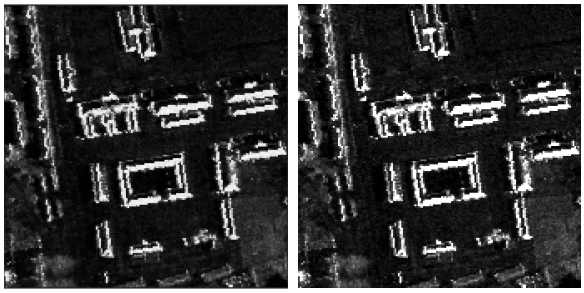

(d) PnP-pe-AF: SNR: 24.62 SSIM: 0.932.

(e) Reference image.

Figure 4.3 Reconstruction results for *Image 26* of the Wonsan test set with phase error in the range $[-\pi/4, \pi/4]$.

(a) PnP: SNR: 7.89 SSIM: 0.442.

(b) PnP-pe: SNR: 7.87 SSIM: 0.435.

(c) PnP-AF: SNR: 20.66 SSIM: 0.863.

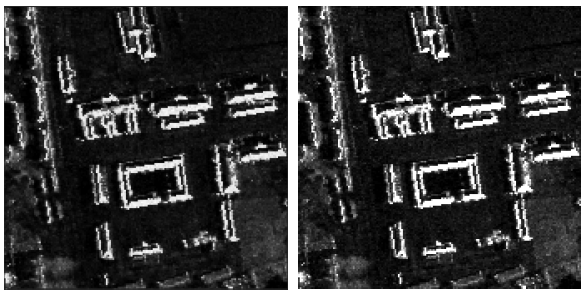

(d) PnP-pe-AF: SNR: 24.71 SSIM: 0.933.

(e) Reference image.

Figure 4.4 Reconstruction results for *Image 26* of the Wonsan test set with phase error in the range $[-\pi/3, \pi/3]$.

(a) PnP: SNR: 7.18 SSIM: 0.414.

(b) PnP-pe: SNR: 6.52 SSIM: 0.377.

(c) PnP-AF: SNR: 20.76 SSIM: 0.865.

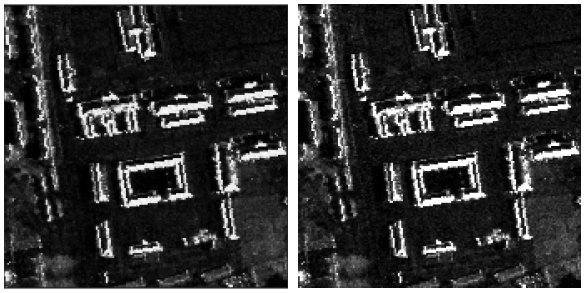

(d) PnP-pe-AF: SNR: 24.70 SSIM: 0.932.

(e) Reference image.

Figure 4.5 Reconstruction results for *Image 26* of the Wonsan test set with phase error in the range $[-3\pi/8, 3\pi/8]$.

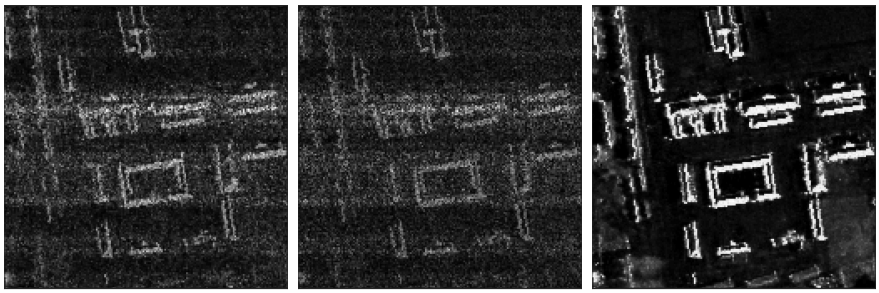

(a) PnP: SNR: 5.18 SSIM: 0.317.

(b) PnP-pe: SNR: 3.79 SSIM: 0.248.

(c) PnP-AF: SNR: 20.63 SSIM: 0.862.

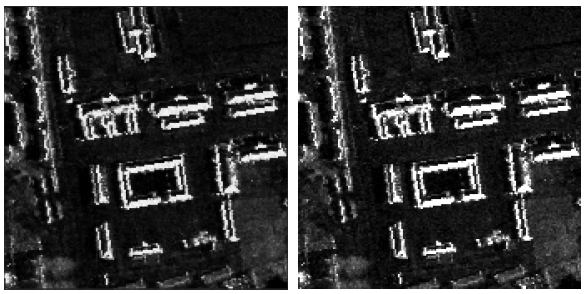

(d) PnP-pe-AF: SNR: 24.66 SSIM: 0.933.

(e) Reference image.

Figure 4.6 Reconstruction results for *Image 26* of the Wonsan test set with phase error in the range $[-\pi/2, \pi/2]$.

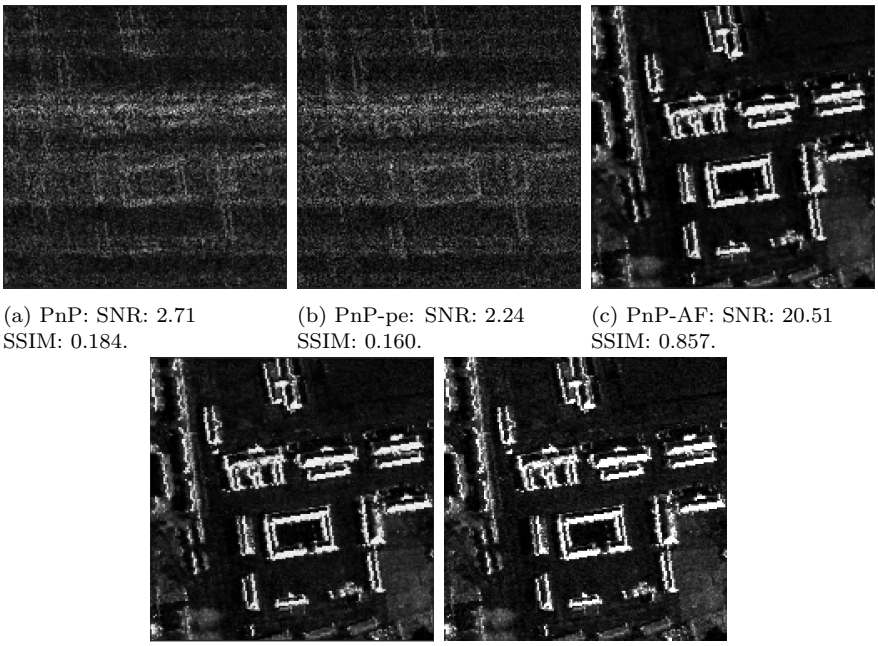

(a) PnP: SNR: 2.71 SSIM: 0.184.
(b) PnP-pe: SNR: 2.24 SSIM: 0.160.
(c) PnP-AF: SNR: 20.51 SSIM: 0.857.
(d) PnP-pe-AF: SNR: 24.69 SSIM: 0.934.
(e) Reference image.

Figure 4.7 Reconstruction results for *Image 26* of the Wonsan test set with phase error in the range $[-2\pi/3, 2\pi/3]$.

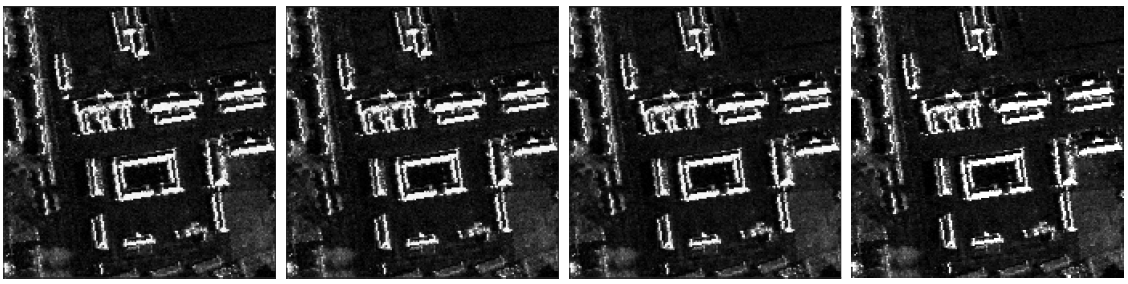

(a) FFT: SNR: 26.70 SSIM: 0.968.
(b) SDA: SNR: 26.88 SSIM: 0.969.
(c) PnP-pe-AF: SNR: 27.30 SSIM: 0.958.
(d) Reference image.

Figure 4.8 Visual comparison of reconstructions for *Image 26* of the Wonsan test set with no phase error.

performance degrades rapidly as the amount of phase error increases for non-sparse scenes. Performing these experiments for lower data availability scenarios would give more insight on the behaviors of the competing methods.

4.3.3 Summary

The preliminary results in this chapter show that joint image reconstruction and 1D phase error correction is indeed achievable with the PnP-CNN-SAR-AF algorithm. Our results suggest that both the phase error estimation and correction steps in the PnP-CNN-SAR-AF algorithm and training the network with phase errors improve the performance significantly. We have also observed that using a network trained

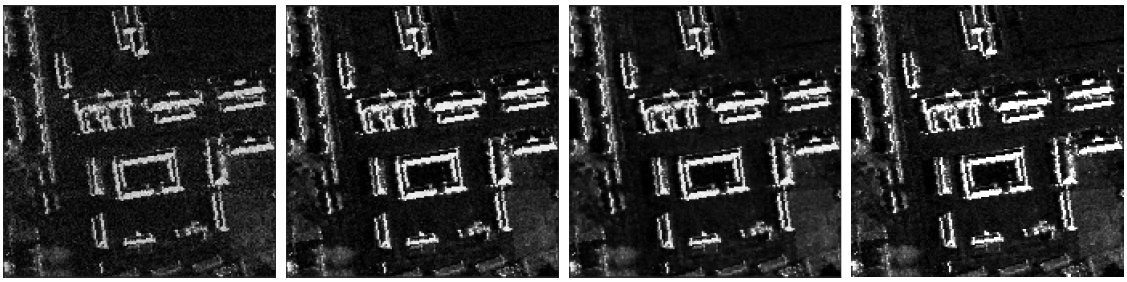

(a) FFT: SNR: 13.60 SSIM: 0.721. (b) SDA: SNR: 25.00 SSIM: 0.960. (c) PnP-pe-AF: SNR: 24.78 SSIM: 0.934. (d) Reference image.

Figure 4.9 Visual comparison of reconstructions for *Image 26* of the Wonsan test set with phase error in the range $[-\pi/6, \pi/6]$.

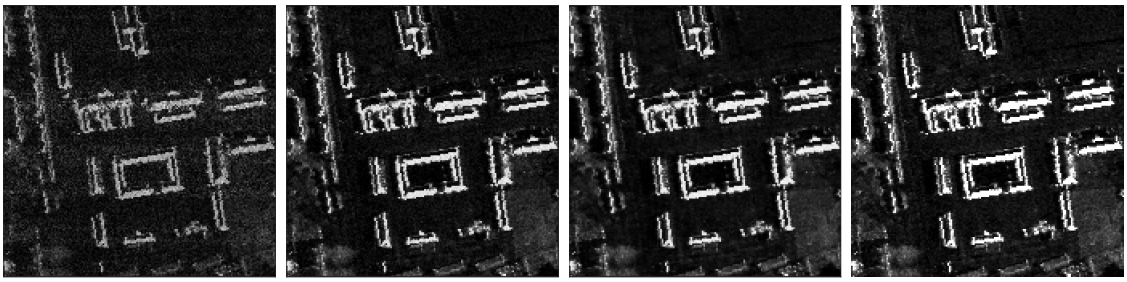

(a) FFT: SNR: 10.23 SSIM: 0.599. (b) SDA: SNR: 23.39 SSIM: 0.957. (c) PnP-pe-AF: SNR: 24.62 SSIM: 0.932. (d) Reference image.

Figure 4.10 Visual comparison of reconstructions for *Image 26* of the Wonsan test set with phase error in the range $[-\pi/4, \pi/4]$.

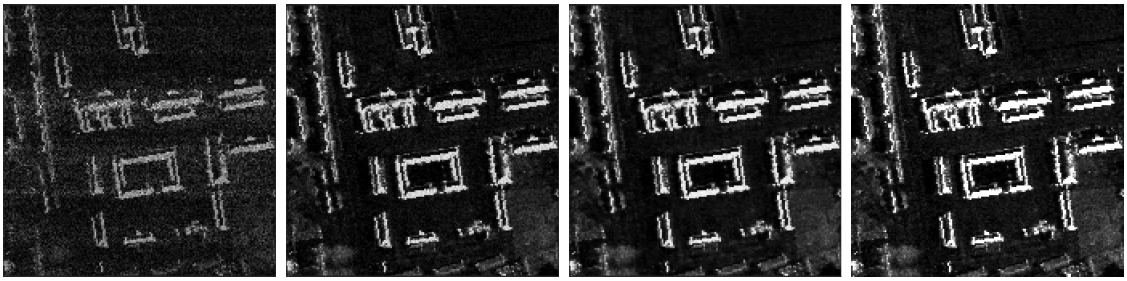

(a) FFT: SNR: 7.90 SSIM: 0.499. (b) SDA: SNR: 20.85 SSIM: 0.952. (c) PnP-pe-AF: SNR: 24.71 SSIM: 0.933. (d) Reference image.

Figure 4.11 Visual comparison of reconstructions for *Image 26* of the Wonsan test set with phase error in the range $[-\pi/3, \pi/3]$.

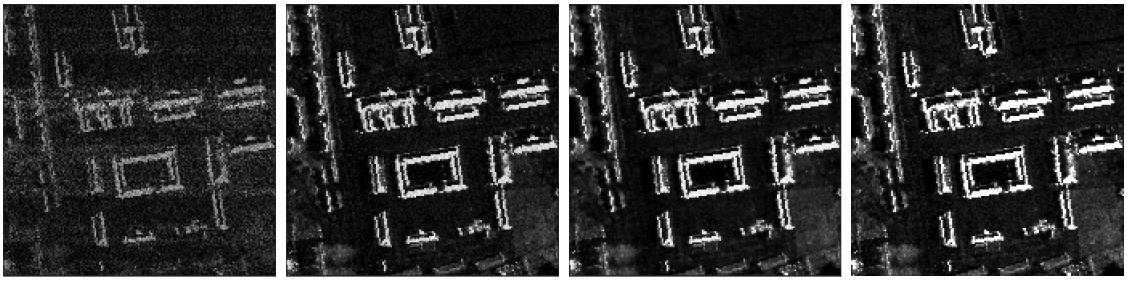

(a) FFT: SNR: 6.63 SSIM: 0.445. (b) SDA: SNR: 20.70 SSIM: 0.944. (c) PnP-pe-AF: SNR: 24.70 SSIM: 0.932. (d) Reference image.

Figure 4.12 Visual comparison of reconstructions for *Image 26* of the Wonsan test set with phase error in the range $[-3\pi/8, 3\pi/8]$.

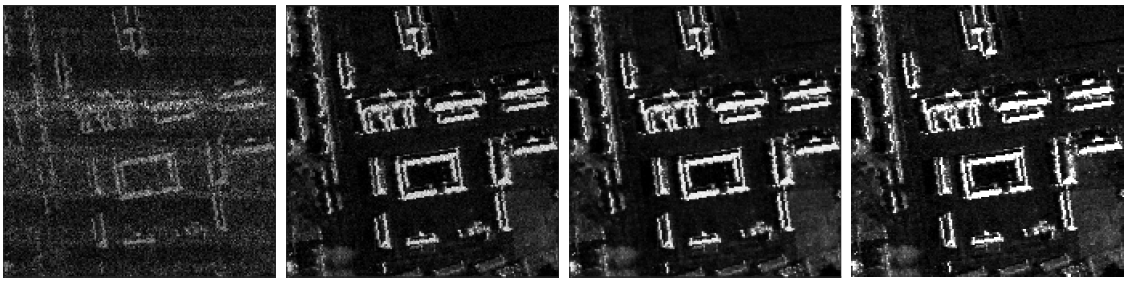

(a) FFT: SNR: 3.95 SSIM: 0.302. (b) SDA: SNR: 18.27 SSIM: 0.937. (c) PnP-pe-AF: SNR: 24.66 SSIM: 0.933. (d) Reference image.

Figure 4.13 Visual comparison of reconstructions for *Image 26* of the Wonsan test set with phase error in the range $[-\pi/2, \pi/2]$.

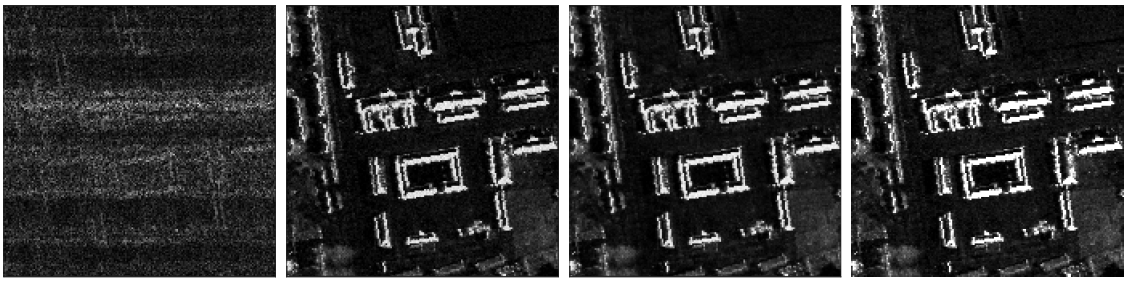

(a) FFT: SNR: 1.99 SSIM: 0.165. (b) SDA: SNR: 22.54 SSIM: 0.958. (c) PnP-pe-AF: SNR: 24.69 SSIM: 0.934. (d) Reference image.

Figure 4.14 Visual comparison of reconstructions for *Image 26* of the Wonsan test set with phase error in the range $[-2\pi/3, 2\pi/3]$.

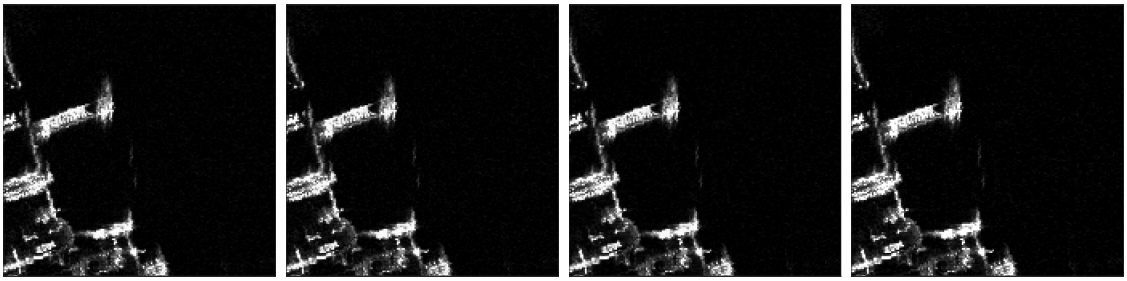

(a) FFT: SNR: 26.10 SSIM: 0.901. (b) SDA: SNR: 26.43 SSIM: 0.911. (c) PnP-pe-AF: SNR: 26.93 SSIM: 0.925. (d) Reference image.

Figure 4.15 Visual comparison of reconstructions for *Image 28* of the Wonsan test set with no phase error.

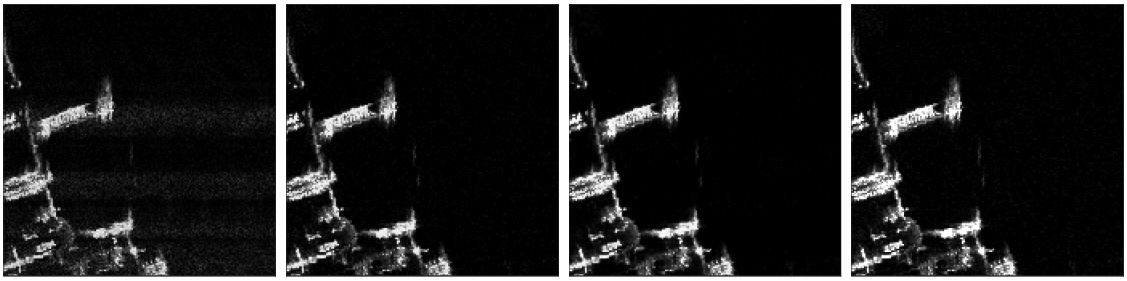

(a) FFT: SNR: 11.85 SSIM: 0.572. (b) SDA: SNR: 24.82 SSIM: 0.947. (c) PnP-pe-AF: SNR: 24.89 SSIM: 0.894. (d) Reference image.

Figure 4.16 Visual comparison of reconstructions for *Image 28* of the Wonsan test set with phase error in the range $[-\pi/6, \pi/6]$.

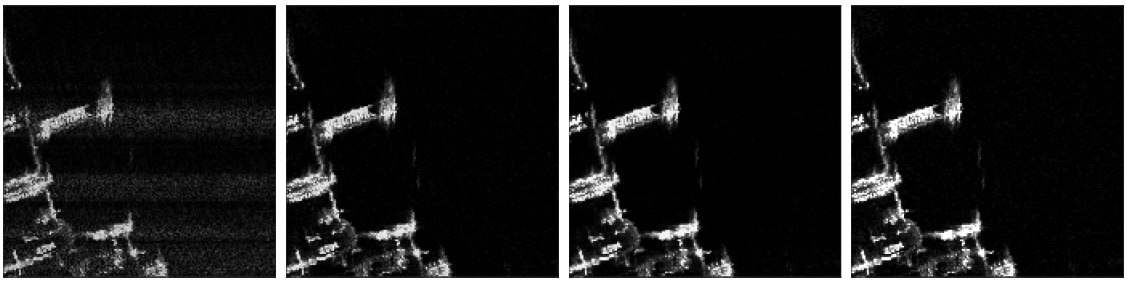

(a) FFT: SNR: 8.05 SSIM: 0.472. (b) SDA: SNR: 22.15 SSIM: 0.945. (c) PnP-pe-AF: SNR: 25.02 SSIM: 0.906. (d) Reference image.

Figure 4.17 Visual comparison of reconstructions for *Image 28* of the Wonsan test set with phase error in the range $[-\pi/4, \pi/4]$.

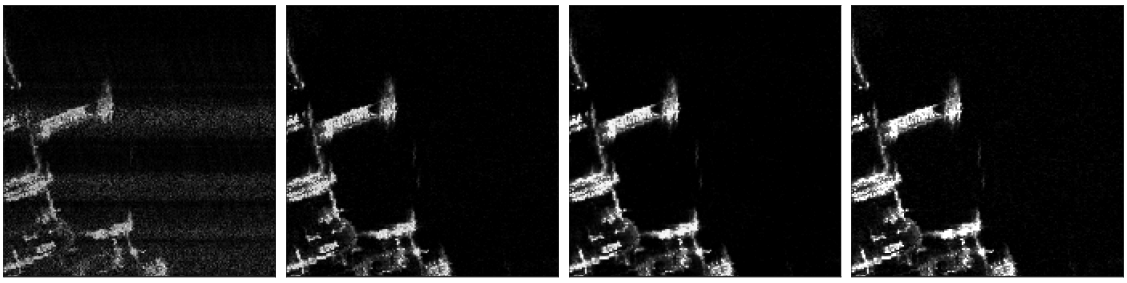

(a) FFT: SNR: 6.62 SSIM: 0.426. (b) SDA: SNR: 20.68 SSIM: 0.944. (c) PnP-pe-AF: SNR: 24.96 SSIM: 0.894. (d) Reference image.

Figure 4.18 Visual comparison of reconstructions for *Image 28* of the Wonsan test set with phase error in the range $[-\pi/3, \pi/3]$.

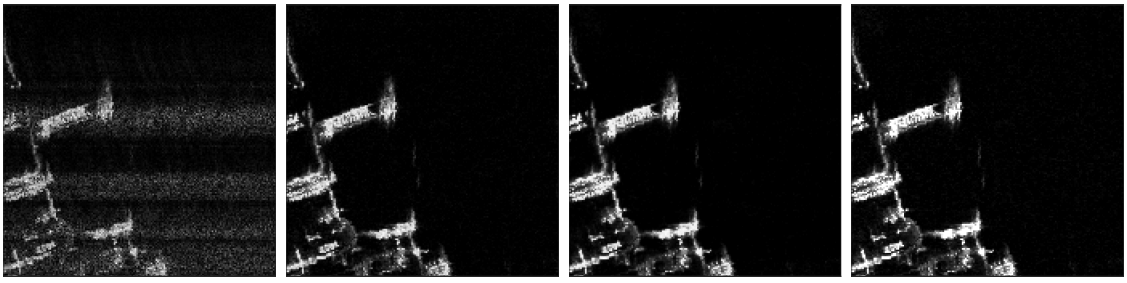

(a) FFT: SNR: 4.51 SSIM: 0.366. (b) SDA: SNR: 21.81 SSIM: 0.931. (c) PnP-pe-AF: SNR: 24.69 SSIM: 0.889. (d) Reference image.

Figure 4.19 Visual comparison of reconstructions for *Image 28* of the Wonsan test set with phase error in the range $[-3\pi/8, 3\pi/8]$.

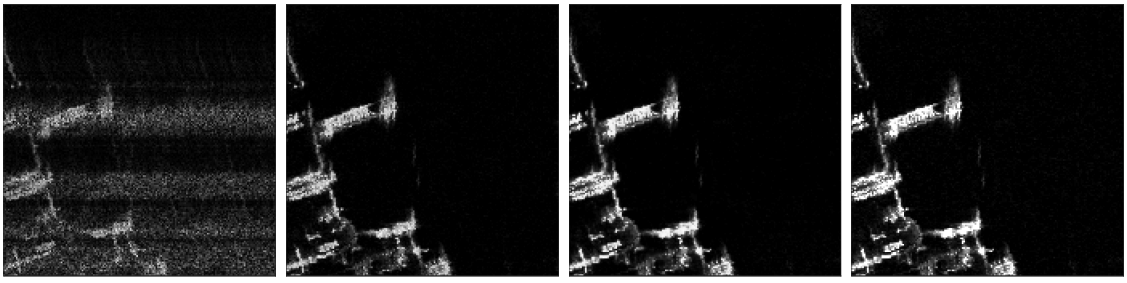

(a) FFT: SNR: 2.27 SSIM: 0.295. (b) SDA: SNR: 18.84 SSIM: 0.933. (c) PnP-pe-AF: SNR: 24.77 SSIM: 0.906. (d) Reference image.

Figure 4.20 Visual comparison of reconstructions for *Image 28* of the Wonsan test set with phase error in the range $[-\pi/2, \pi/2]$.

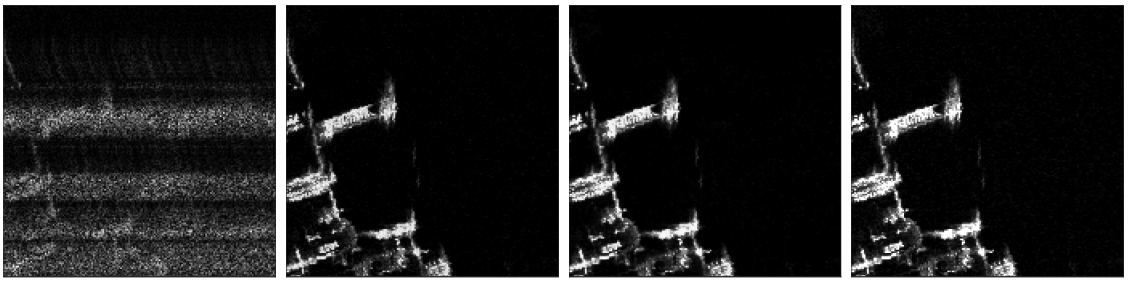

(a) FFT: SNR: 0.54 SSIM: 0.225. (b) SDA: SNR: 23.25 SSIM: 0.951. (c) PnP-pe-AF: SNR: 25.17 SSIM: 0.914. (d) Reference image.

Figure 4.21 Visual comparison of reconstructions for *Image 28* of the Wonsan test set with phase error in the range $[-2\pi/3, 2\pi/3]$.

Table 4.3 Average SNR and SSIM values for different phase error levels and for FFT-based, SDA, and PnP-pe-AF methods.

Phase Error	FFT		SDA		PnP-pe-AF	
	SNR (dB)	SSIM	SNR (dB)	SSIM	SNR (dB)	SSIM
0	26.64	0.973	26.71	0.974	26.85	0.977
$[-\pi/6, \pi/6]$	13.26	0.750	19.89	0.875	23.59	0.959
$[-\pi/4, \pi/4]$	9.99	0.618	18.62	0.851	24.09	0.963
$[-\pi/3, \pi/3]$	7.76	0.502	16.90	0.803	24.09	0.964
$[-3\pi/8, 3\pi/8]$	6.74	0.445	16.10	0.803	24.02	0.963
$[-\pi/2, \pi/2]$	4.75	0.314	14.52	0.764	24.22	0.964
$[-2\pi/3, 2\pi/3]$	3.04	0.171	12.05	0.676	24.04	0.977

with phase error within the PnP-CNN-SAR framework does not generate good results, and the benefit of training the network with phase error can only be observed if it is used within the PnP-CNN-SAR-AF framework.

Chapter 5

SAR ATR in the Phase History Domain

In the previous two chapters, we have focused on the problems of image reconstruction and phase error correction in SAR imaging. In this chapter, we shift our focus towards another important SAR imaging problem, i.e., automatic target recognition (ATR), and we investigate the idea of performing the ATR task in the phase history domain. This is a joint work with Sara Atito, another Ph.D. student in our group.

5.1 Phase History Domain ATR Methodologies

In this section, we present two frameworks for SAR ATR that work in the phase history domain and utilize CNNs for learning and classification.

5.1.1 Phase History Domain Classification (PHDC)

Since the conventional reconstruction for SAR is performed using noisy measurements, and because SAR is a coherent imaging modality, formed images suffer from speckle which also affects the ATR performance. Note that only the magnitudes of the formed images are used in ATR since the phase does not contain much information about the spatial structure of the 2D projection of the scene produced by conventional SAR imaging. Moreover, we know from an information theoretic perspective that, image formation does not provide us any additional information about the scene, it is merely a visualization. Since ATR is performed by computers, in principle it does not really matter if we feed the ATR system with formed images or phase history data. In either case, the system would learn the dependency patterns in the data. Since the information contained in the formed images cannot

be more than the information in the phase histories, we predicted that, in an ideal scenario, using the phase history data instead of formed images may result in equal or better ATR performance. This is something we explore in this study. Hence, our first proposed framework uses phase history data as an input to the ATR system. To evaluate our framework, we used the MSTAR data set and two well-known CNN architectures, AlexNet and VGG16. AlexNet and VGG16 are both originally designed for image classification tasks and they require 3-channel real input data. However, the phase history data we have is complex. Therefore, we needed a way to feed the data to the networks, and using the magnitudes, real parts, and imaginary parts of the phase histories as the three channel inputs gave us the best result. Specifically, we assign the magnitudes, real parts, and imaginary parts of the phase histories of the images in the MSTAR data set as the red, green, and blue channels, respectively, and form an RGB image for each data point in the data set.

5.1.2 Image-Phase Removed Phase History Classification (IPRPHC)

Since the phase of the reconstructed image does not really contain any information about the observed scene, as it is highly dominated by speckle, it is usually discarded in image analysis. Motivated by this, our second framework performs the following steps: image formation, image-phase removal, and phase history data generation. We evaluate our framework in the same way described in Section 5.1.1.

5.2 Experimental Results

5.2.1 Setup

We now evaluate the performance of the ATR methodologies discussed in Section 5.1 using the MSTAR data set. The data set consists of 10 classes, i.e., tanks (T62, T72), armored vehicles (BRDM2, BMP2, BTR60, BTR70), a rocket launcher (2S1), an air defense unit (ZSU234), a military truck (ZIL131), and a bulldozer (D7). The MSTAR data set only provides formed images. Therefore, in order to obtain the phase histories, we undo the final steps of the MSTAR image formation using the method described in Refs. [1, 191]. Also, we resize the generated images to 227×227 for AlexNet and to 224×224 for VGG16 to match their respective input sizes. Figure 5.1 shows sample data of each class for PHDC experiments and Figure 5.2 shows sample data from the same chips for IPRPHC experiments. In our experiments, we use the images at 17° depression angle for training and images at 15° depression angle for testing. Since CNNs require large number of images

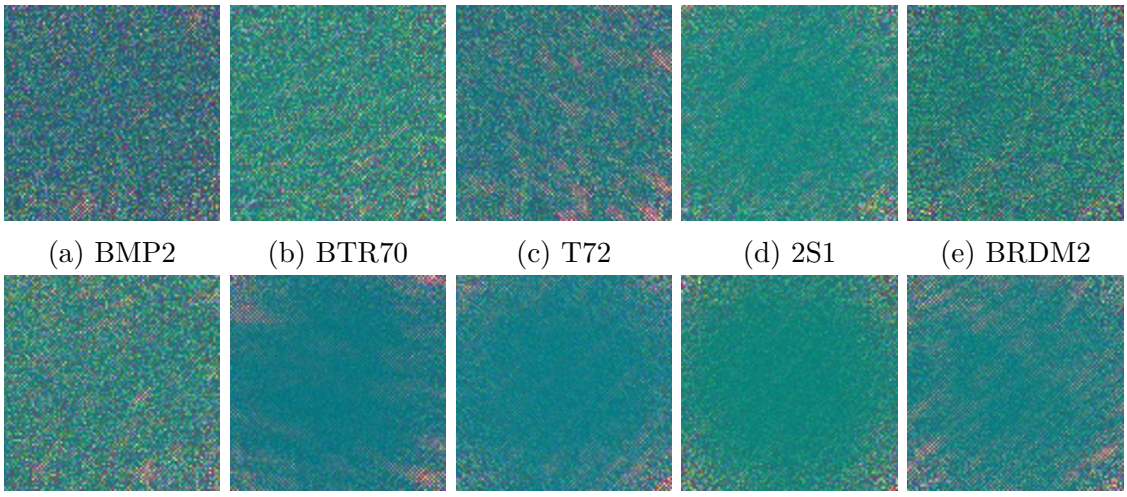

(a) BMP2 (b) BTR70 (c) T72 (d) 2S1 (e) BRDM2

(f) BTR60 (g) D7 (h) T62 (i) ZIL131 (j) ZSU23/4

Figure 5.1 Sample data of each class for PHDC experiments.

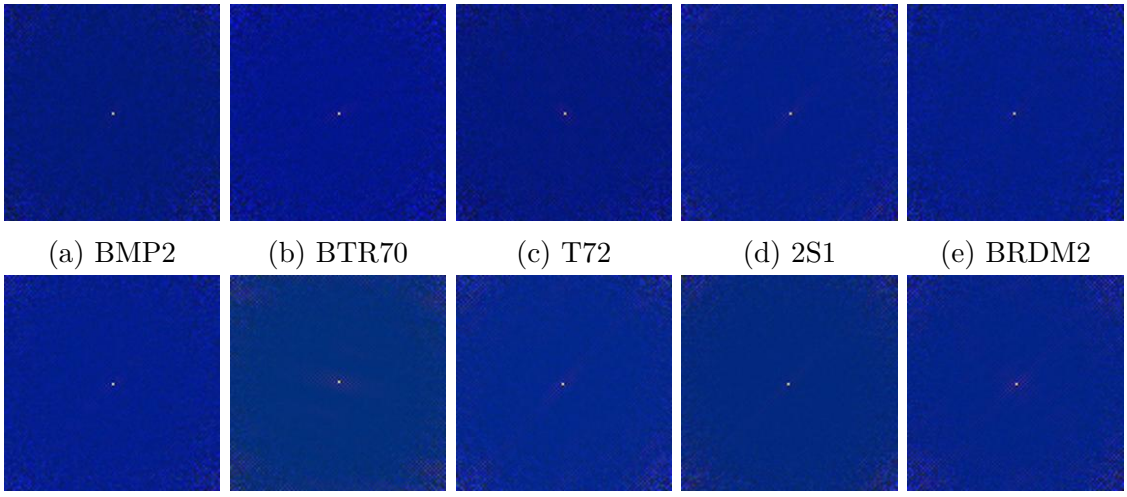

(a) BMP2 (b) BTR70 (c) T72 (d) 2S1 (e) BRDM2

(f) BTR60 (g) D7 (h) T62 (i) ZIL131 (j) ZSU23/4

Figure 5.2 Sample data of each class for IPRPHC experiments.

for training, we augment our training set by rotating each image by [2°, 4°, 6°, 8°, 10°] clockwise and counter-clockwise. Table 5.1 shows the numbers of each type of target images in each of these sets before augmentation. All of the experiments are performed on MATLAB R2018a using NVIDIA TITAN Xp GPU.

In the following subsections, we present the results of phase history domain classification and image-phase removed phase history classification experiments and conclude this section with comparison of the results of other methods and a summary.

5.2.2 PHDC Results

We now present the recognition performance of the phase history domain classification using AlexNet and VGG16 architectures. Tables 5.2 and 5.3 show the results for

Table 5.1 Composition of the MSTAR data set.

	Training set		Test set	
Target	Depression	No. of images	Depression	No. of images
BMP2	17°	233	15°	195
BTR70	17°	233	15°	196
T72	17°	232	15°	196
2S1	17°	299	15°	274
BRDM2	17°	298	15°	274
BTR60	17°	256	15°	195
D7	17°	299	15°	274
T62	17°	299	15°	273
ZIL131	17°	299	15°	274
ZSU23/4	17°	299	15°	274

Table 5.2 Confusion matrix for PHDC results with the AlexNet architecture.

		Predicted Class										Class Accuracy
		BMP2	BTR70	T72	2S1	BRDM2	BTR60	D7	T62	ZIL131	ZSU23/4	
True Class	BMP2	103	8	35	3	0	29	2	3	10	2	52,82%
	BTR70	29	118	1	6	0	29	0	1	12	0	60,20%
	T72	7	0	162	1	0	8	3	14	0	1	82,65%
	2S1	0	0	0	272	0	0	0	1	0	1	99,27%
	BRDM2	3	0	7	0	257	3	0	0	0	4	93,80%
	BTR60	11	19	37	3	0	109	1	6	9	0	55,90%
	D7	0	0	0	0	0	0	257	4	1	12	93,80%
	T62	0	0	0	0	0	0	37	224	3	9	82,05%
	ZIL131	0	0	0	0	0	0	3	0	271	0	98,91%
	ZSU23/4	1	0	0	0	0	0	0	0	0	273	99,64%
							Overall Accuracy					84,37%

AlexNet and VGG16, respectively. The results show that tanks and armored vehicles are harder to distinguish. The overall performance is worse than the competing methods for both architectures.

5.2.3 IPRPHC Results

We now present the recognition performance of the image-phase removed phase history classification using AlexNet and VGG16 architectures. Tables 5.4 and 5.5 show the results for AlexNet and VGG16, respectively. The results show that this methodology works well and the performance is at the same level with the state-of-the-art techniques. Note that, with AlexNet, 7 of the classes, and with VGG16, 5 of the classes reached 100% accuracy.

Table 5.3 Confusion matrix for PHDC results with the VGG16 architecture.

		Predicted Class										Class Accuracy
		BMP2	BTR70	T72	2S1	BRDM2	BTR60	D7	T62	ZIL131	ZSU23/4	
True Class	BMP2	93	18	22	3	4	42	2	6	3	2	47,69%
	BTR70	20	137	0	5	6	17	0	1	10	0	69,90%
	T72	12	1	140	0	3	22	0	15	0	3	71,43%
	2S1	0	0	0	272	0	0	0	0	0	2	99,27%
	BRDM2	7	3	3	0	255	6	0	0	0	0	93,07%
	BTR60	23	29	30	2	3	92	0	8	8	0	47,18%
	D7	0	0	0	0	0	0	247	16	2	9	90,15%
	T62	0	0	0	1	0	0	19	241	1	11	88,28%
	ZIL131	0	0	0	0	0	0	4	2	268	0	97,81%
	ZSU23/4	0	0	0	0	1	0	1	0	0	272	99,27%
		Overall Accuracy										83,18%

Table 5.4 Confusion matrix for IPRPHC results with the AlexNet architecture.

		Predicted Class										Class Accuracy
		BMP2	BTR70	T72	2S1	BRDM2	BTR60	D7	T62	ZIL131	ZSU23/4	
True Class	BMP2	185	1	7	0	0	2	0	0	0	0	94,87%
	BTR70	4	189	0	0	0	3	0	0	0	0	96,43%
	T72	0	0	196	0	0	0	0	0	0	0	100,00%
	2S1	0	0	0	274	0	0	0	0	0	0	100,00%
	BRDM2	0	0	0	0	274	0	0	0	0	0	100,00%
	BTR60	1	1	0	0	0	189	4	0	0	0	96,92%
	D7	0	0	0	0	0	0	274	0	0	0	100,00%
	T62	0	0	0	0	0	0	0	273	0	0	100,00%
	ZIL131	0	0	0	0	0	0	0	0	274	0	100,00%
	ZSU23/4	0	0	0	0	0	0	0	0	0	274	100,00%
		Overall Accuracy										99,05%

Table 5.5 Confusion matrix for IPRPHC results with the VGG16 architecture.

		Predicted Class										Class Accuracy
		BMP2	BTR70	T72	2S1	BRDM2	BTR60	D7	T62	ZIL131	ZSU23/4	
True Class	BMP2	182	2	7	0	0	4	0	0	0	0	93,33%
	BTR70	6	188	0	0	0	2	0	0	0	0	95,92%
	T72	0	0	195	0	0	1	0	0	0	0	99,49%
	2S1	3	0	0	271	0	0	0	0	0	0	98,91%
	BRDM2	0	0	0	0	274	0	0	0	0	0	100,00%
	BTR60	0	1	0	0	0	194	0	0	0	0	99,49%
	D7	0	0	0	0	0	0	274	0	0	0	100,00%
	T62	0	0	0	0	0	0	0	273	0	0	100,00%
	ZIL131	0	0	0	0	0	0	0	0	274	0	100,00%
	ZSU23/4	0	0	0	0	0	0	0	0	0	274	100,00%
		Overall Accuracy										98,93%

Table 5.6 Confusion matrix for conventional reconstruction results with the AlexNet architecture.

		Predicted Class										Class Accuracy
		BMP2	BTR70	T72	2S1	BRDM2	BTR60	D7	T62	ZIL131	ZSU23/4	
True Class	BMP2	191	0	2	0	1	1	0	0	0	0	97,95%
	BTR70	0	195	0	0	1	0	0	0	0	0	99,49%
	T72	0	0	196	0	0	0	0	0	0	0	100,00%
	2S1	0	0	0	273	1	0	0	0	0	0	99,64%
	BRDM2	4	1	0	0	268	1	0	0	0	0	97,81%
	BTR60	1	1	1	0	2	188	0	0	2	0	96,41%
	D7	0	0	0	2	0	0	271	0	0	1	98,91%
	T62	1	0	0	0	0	0	0	265	0	7	97,07%
	ZIL131	0	0	0	0	0	0	2	0	272	0	99,27%
	ZSU23/4	0	0	0	0	0	0	0	0	0	274	100,00%
		Overall Accuracy										98,68%

Table 5.7 Confusion matrix for conventional reconstruction results with the VGG16 architecture.

		Predicted Class										Class Accuracy
		BMP2	BTR70	T72	2S1	BRDM2	BTR60	D7	T62	ZIL131	ZSU23/4	
True Class	BMP2	186	1	5	0	1	2	0	0	0	0	95,38%
	BTR70	0	196	0	0	0	0	0	0	0	0	100,00%
	T72	2	0	194	0	0	0	0	0	0	0	98,98%
	2S1	5	0	1	264	3	0	0	0	0	1	96,35%
	BRDM2	0	0	0	0	274	0	0	0	0	0	100,00%
	BTR60	0	1	1	0	4	189	0	0	0	0	96,92%
	D7	0	0	0	0	0	0	271	1	2	0	98,91%
	T62	0	0	0	0	0	0	0	265	1	7	97,07%
	ZIL131	0	0	0	0	0	0	0	0	274	0	100,00%
	ZSU23/4	1	0	0	0	0	0	0	0	0	273	99,64%
		Overall Accuracy										98,39%

5.2.4 Comparison & Summary

We now compare our results with existing ATR methodologies. First, we train AlexNet and VGG16 with the magnitude of the original MSTAR chips. For this, we feed the magnitude of the chips to all 3 channels of the input layers of both architectures. Tables 5.6 and 5.7 show the results for these networks, respectively.

We also compare our results with the methods in Refs. [117, 119, 120, 123, 125, 126]. Note that, in the MSTAR dataset, there are additional images of different variations of two of the vehicles, namely, T72 and BMP2, in addition to the ones mentioned in Table 5.1, and [119, 120, 123] use these variants in the test set while [126] uses the variants in both training and test sets. Hence, it should be noted that the results of different methods compared here are not based on exactly the same training and test sets. Table 5.8 shows the comparison of the proposed methodologies with the existing methods.

Table 5.8 Comparison of the proposed frameworks with existing methods.

Method	Accuracy
Image Domain (AlexNet)	98,68%
Image Domain (VGG16)	98,39%
PHDC (AlexNet)	84,37%
PHDC (VGG16)	83,18%
IPRPHC (AlexNet)	99,05%
IPRPHC (VGG16)	98,93%
Song et. al. [119]	96,24%
Sun et. al. [120]	91,48%
Chen and Wang [117]	84,7%
Chen et. al. [123]	**99,42%**
El Housseini et. al. [125]	92,63%
Wagner et. al. [126]	98,47%

We observe that our first framework performed poorly compared to existing work while our second framework performed well, only surpassed by the method in Ref. 123. For our second framework, it seems like it was a reasonable judgment to remove the phase of the MSTAR chips before returning back to the phase history domain.

Another observation is that we reached slightly better results with AlexNet architecture compared to VGG16 for all types of experiments. The reason for this might be that VGG16 is a larger network which needs more data to train.

Chapter 6

Conclusions & Future Directions

6.1 Summary & Conclusions

In this dissertation, we have contributed to the SAR imaging literature. We have developed three frameworks that enhance the performance of various SAR imaging tasks. In particular, we have developed a SAR image formation framework that utilizes deep learning-based priors using the plug-and-play (PnP) priors [33] framework. We have also extended our framework to address phase errors along with image formation. Finally, we have proposed a SAR ATR framework that works in the data domain.

In Chapter 3, our image formation framework, namely PnP-CNN-SAR, was established. In this framework, the forward model and the prior model are decoupled using the PnP priors [33] framework. Within our framework, we have used a Fourier transform-based forward model and a CNN-based prior model. We conducted experiments with different settings to evaluate our proposed framework, i.e., we tested our framework in the presence of different levels of noise and data availability. We compared the results with three existing reconstruction methods, namely, FFT-based, NQR-based [1], and DL-based [3] reconstruction, and a PnP framework-based method with BM3D regularizer, using signal-to-noise ratio (SNR) and structural similarity (SSIM) index metrics. We have shown that PnP-CNN-SAR outperforms other methods in terms of visual quality. Overall, this study suggests that deep learning methods may have the potential to learn complicated spatial patterns and enable their incorporation as priors into computational radar imaging.

In Chapter 4, the extension of PnP-CNN-SAR, namely PnP-CNN-SAR-AF, to jointly address image formation and phase error correction, is presented. We have tested our framework in the presence of different levels of phase errors and data

availability. We have first shown the effectiveness of the additional phase error estimation and correction steps as well as training the network with phase errors, by designing four different experimental settings, namely, PnP, PnP-pe, PnP-AF, and PnP-pe-AF. In PnP and PnP-AF, the network trained without phase error is used while in PnP-pe and PnP-pe-AF, the network trained with phase error is used. Also, in PnP and PnP-pe, the PnP-CNN-SAR algorithm is used while in PnP-AF and PnP-pe-AF, the PnP-CNN-SAR-AF algorithm is used which has additional phase error estimation and correction steps. The results obtained in these settings have shown that the additional phase error estimation and correction steps and training the network with phase errors improve the performance significantly. These results have also shown that training the network with phase error is not enough by itself and this network should be used within the PnP-CNN-SAR-AF algorithm. Later, we compared the results of PnP-pe-AF with two existing methods, namely, FFT-based image reconstruction and SDA [52], using SNR and SSIM. We have shown that PnP-CNN-SAR-AF outperforms other methods in all scenarios in terms of both visual quality and the performance metrics.

In Chapter 5, we have introduced a SAR ATR framework that performs the recognition task in the phase history domain. We have designed two ATR modalities, namely, PHDC and IPRPHC. PHDC performs the ATR task using the collected phase history data directly while in IPRPHC, image formation, image phase removal, and phase history generation steps are performed before the ATR task. Within this framework, we have used two well-known CNNs, AlexNet [35] and VGG16 [36], which are designed for classification tasks. While the performance with the PHDC was subpar, we have reached near state-of-the-art performance levels with the IPRPHC modality. Nevertheless, presented results suggest that SAR ATR without image formation or in the phase histories domain can be an important research direction.

Overall, this dissertation brought a new point-of-view to SAR imaging problems, and has shown that deep neural networks can be effectively used in improving the performance of SAR imaging tasks. Although SAR ATR and other classification/detection/segmentation applications have already started benefiting from the deep learning tools, most of these works are essentially either postprocessing conventionally reconstructed images or feature extraction from those. The works presented in this dissertation show that deep neural networks can have a much broader role than just postprocessing within SAR imaging tasks, and can improve the overall performance significantly.

6.2 Topics for Future Research

All three frameworks presented in this dissertation can benefit from further analysis and extensions. In the following subsections, we will focus each of them individually, and present our suggestions.

6.2.1 Further Analysis and Extensions on PnP-CNN-SAR for Image Reconstruction

The PnP-CNN-SAR framework presented in Chapter 3 is open to further extensions and developments in many ways. First of all, in synthetic scene experiments, we have observed that a network trained for a specific scenario might not be the one that performs the best for that particular scenario, rather a network trained with a slightly higher data availability tends to perform better. A deeper analysis to understand the underlying reasons and an extension to the real scene case would be quite helpful. We have also observed that quantitative analyses based on SNR and SSIM do not necessarily harmonize well with qualitative assessments, especially in lower data availability scenarios, i.e., a reconstructed image might have a better perceptual quality compared to another one, while having a worse score in terms of the metrics used. (See, for example, last two rows of Figures 3.5, 3.6, 3.13, 3.14, 3.16, 3.17. In many of these cases, the NQR-based [1] reconstruction achieves the best performance in terms of SNR, while producing least useful reconstructions.) It is clear that new metrics that are more consistent with the visual quality of the reconstructed images are required. Lastly, we observed that the most time consuming process in our algorithm is the phase alignment step in the model update which can take up to 75% of the overall computation time. A more efficient algorithm for the phase alignment step would be useful for time-critical reconstruction tasks.

6.2.2 Further Analysis and Extensions on PnP-CNN-SAR-AF for Joint Image Reconstruction and 1D Phase Error Correction

In Chapter 4, we have used the PnP-CNN-SAR-AF framework to jointly address image reconstruction and 1D phase errors. This framework can easily be extended to address 2D separable and non-separable phase errors as well. Also, in this work, we have only investigated the effects of the amount of phase error in the case of full data availability and relatively low noise. The performance of the proposed framework can be evaluated in more challenging scenarios, i.e., in cases of lower data availability and higher noise levels. Finally, in this work, we have trained the

network with data generated with a particular scenario in mind. A network trained with data generated with various scenarios, i.e., different combinations of different phase error, data availability, and noise levels, would likely have more generalization power, and could give good results in a variety of scenarios.

6.2.3 Further Analysis and Extensions on SAR ATR in the Phase History Domain

The work presented in Chapter 5 can be improved in several ways. We have used an approximation to the phase histories in our experiments for the PHDC. Using the actual phase history data would potentially give better and more realistic results. Also, the CNN architectures we have used in the experiments are relatively old and smaller compared to the recent networks. We can benefit from using a deeper and/or task specific network. Note however that using a deeper network might require a larger training set and longer time to train. Also, the effect of the way the data are used in the CNN can be investigated. Since AlexNet and VGG16 are both designed for image classification, they require 3-channel real input data. However, the phase history data we have is complex. Therefore, we decided to use real and imaginary parts and the magnitude of the phase histories to feed to the 3 channels since this gave us the best result among other methods (using only one part for all channels or another combination like real, imaginary, and phase). But we are still not sure if this is the best way to use the data and that is open for further investigation. One can also use a CNN that is designed to work with complex data like the one proposed by Gao et. al. [196]. In addition, using different augmentation techniques and generating larger training sets might improve the results. Finally, in this work, we only considered the standard operation conditions where the depression angles for the training and test sets are fairly similar (17° vs. 15°). The performance of the proposed modalities can also be investigated for the extended operation conditions, i.e., where depression angles differ by a large margin (Training 17° - Test 30° and Training 17° - Test 45°).

Appendix A

Additional Results from PnP-CNN-SAR for Image Reconstruction

This appendix provides additional results and information in support of Chapter 3. The rest of this supplement is structured as follows. Sections A.1, A.2, and A.3 provide detailed quantitative and qualitative analyses for the synthetic scene experiments, same scene experiments, and different scene experiments, respectively. The results presented in this supplement show that PnP-CNN-SAR outperforms other methods in both quantitative metrics and reconstruction quality, in the majority of the scenarios considered.

A.1 Synthetic Scene Experiments

A.1.1 Experiment 1: 100% Data Availability and $\sigma_{\mathbf{n}} = 0.1\sigma_{\mathbf{y}}$

Table A.1 shows the SNR and SSIM values for this experiment. PnP-CNN-SAR gives the best SNR for all 9 images, and best SSIM for 7 images. Fig. A.1 shows the reconstruction results from all methods for this experiment. NQR-based and PnP-CNN-SAR results in near perfect reconstructions. Other methods also produce good reconstructions.

A.1.2 Experiment 2: 90% Data Availability and $\sigma_{\mathbf{n}} = 0.1\sigma_{\mathbf{y}}$

Table A.2 shows the SNR and SSIM values for this experiment. PnP-CNN-SAR gives the best SNR for 4 images, and best SSIM for 3 images. Fig. A.2 shows the

Table A.1 SNR and SSIM values for synthetic SAR scenes for the case of 100% data availability and $\sigma_{\mathbf{n}} = 0.1\sigma_{\mathbf{y}}$. Best results are shown in bold, second best results are shown in red.

	SNR (dB)					SSIM				
	FFT-based	NQR-based	DL-based	PnP-BM3D	PnP-CNN-SAR	FFT-based	NQR-based	DL-based	PnP-BM3D	PnP-CNN-SAR
Image 1	26.25	25.44	27.12	28.08	**36.88**	0.930	0.978	0.901	0.924	**0.998**
Image 2	23.72	31.15	24.09	24.69	**36.02**	0.691	**0.999**	0.596	0.599	0.989
Image 3	25.76	31.99	26.54	27.37	**37.61**	0.928	0.989	0.894	0.927	**0.998**
Image 4	26.01	24.66	27.06	28.37	**34.29**	0.956	0.976	0.940	0.959	**0.996**
Image 5	26.56	25.51	27.30	28.68	**39.64**	0.954	0.959	0.936	0.952	**0.999**
Image 6	25.04	24.94	25.68	25.88	**38.79**	0.957	0.989	0.945	0.945	**0.997**
Image 7	25.38	24.58	26.22	26.29	**38.30**	0.963	0.989	0.954	0.957	**0.999**
Image 8	25.53	24.91	25.98	26.55	**38.97**	0.966	0.988	0.954	0.962	**0.999**
Image 9	25.72	32.61	26.85	28.74	**40.79**	0.808	**0.996**	0.770	0.827	0.992
Average	25.55	27.31	26.31	27.18	**37.92**	0.906	0.985	0.877	0.895	**0.996**

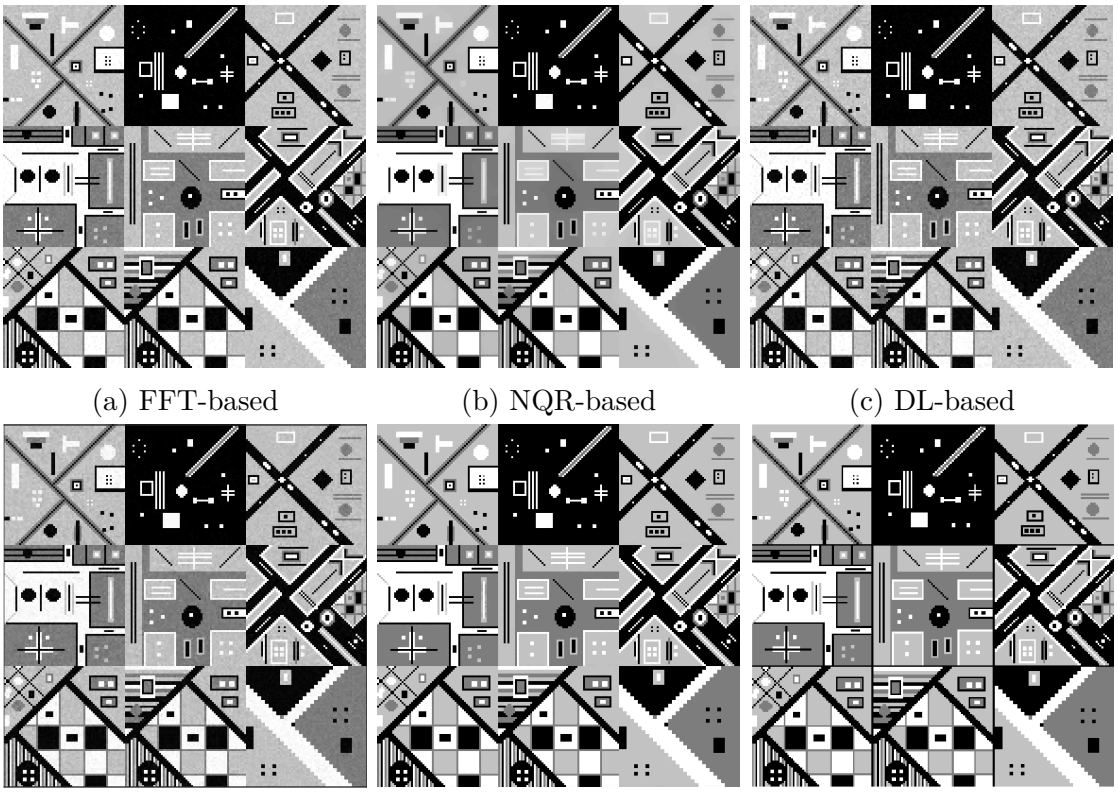

(a) FFT-based (b) NQR-based (c) DL-based

(d) PnP-BM3D (e) PnP-CNN-SAR (f) Ground Truth

Figure A.1 Reconstruction results for the synthetic scenes for the case of 100% data availability and $\sigma_{\mathbf{n}} = 0.1\sigma_{\mathbf{y}}$.

reconstruction results from all methods for this experiment. DL-based and PnP-CNN-SAR generally produces better reconstructions compared to other methods.

Table A.2 SNR and SSIM values for synthetic SAR scenes for the case of 90% data availability and $\sigma_{\mathbf{n}} = 0.1\sigma_{\mathbf{y}}$. Best results are shown in bold, second best results are shown in red.

	SNR (dB)					SSIM				
	FFT-based	NQR-based	DL-based	PnP-BM3D	PnP-CNN-SAR	FFT-based	NQR-based	DL-based	PnP-BM3D	PnP-CNN-SAR
Image 1	11.84	17.85	**27.05**	26.57	23.26	0.457	0.867	0.910	**0.942**	0.922
Image 2	10.12	18.78	**20.98**	19.78	20.83	0.377	**0.991**	0.540	0.520	0.967
Image 3	11.62	**27.05**	25.23	25.17	23.94	0.494	**0.950**	0.894	0.940	0.917
Image 4	11.38	9.27	25.08	**27.07**	23.32	0.627	0.533	0.934	**0.968**	0.960
Image 5	11.70	13.72	26.90	**27.31**	24.63	0.519	0.627	0.941	**0.955**	0.938
Image 6	10.61	18.10	23.20	17.39	**28.38**	0.683	0.944	0.934	0.880	**0.985**
Image 7	11.41	18.58	24.56	20.18	**26.14**	0.668	0.949	0.950	0.934	**0.976**
Image 8	11.18	13.25	24.11	21.05	**28.88**	0.694	0.810	0.950	0.946	**0.987**
Image 9	11.71	23.94	25.73	28.43	**28.56**	0.333	**0.934**	0.766	0.870	0.932
Average	11.29	17.84	24.76	23.66	**25.33**	0.539	0.845	0.869	0.884	**0.954**

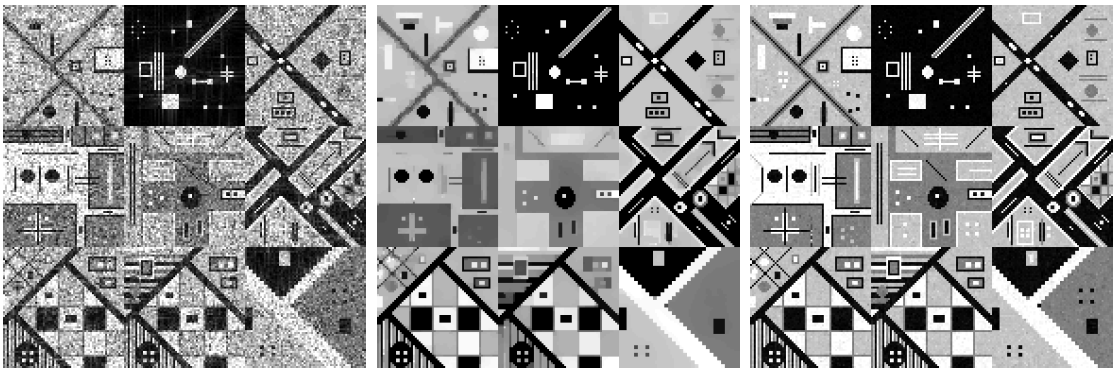

(a) FFT-based (b) NQR-based (c) DL-based

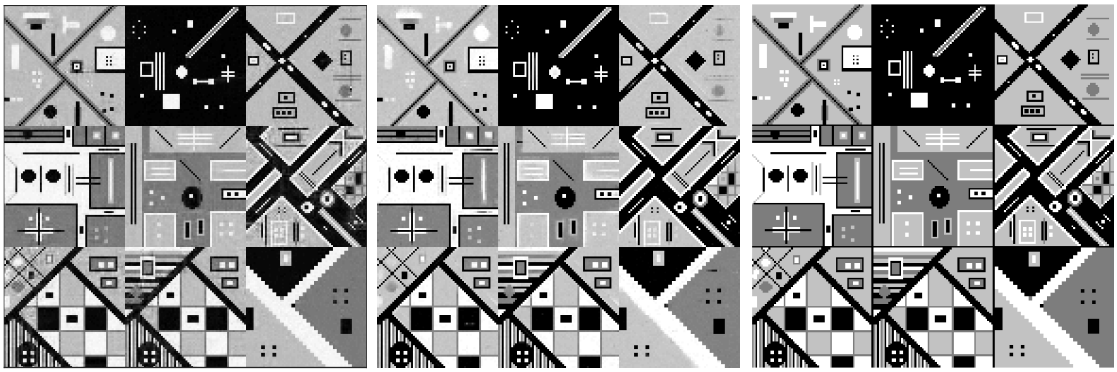

(d) PnP-BM3D (e) PnP-CNN-SAR (f) Ground Truth

Figure A.2 Reconstruction results for the synthetic scenes for the case of 90% data availability and $\sigma_{\mathbf{n}} = 0.1\sigma_{\mathbf{y}}$.

A.1.3 Experiment 3: 80% Data Availability and $\sigma_{\mathbf{n}} = 0.1\sigma_{\mathbf{y}}$

Table A.3 shows the SNR and SSIM values for this experiment. PnP-CNN-SAR gives the best SNR for 4 images, and best SSIM for 5 images. Fig. A.3 shows the reconstruction results from all methods for this experiment. DL-based and PnP-CNN-SAR generally produces better reconstructions compared to other methods.

Table A.3 SNR and SSIM values for synthetic SAR scenes for the case of 80% data availability and $\sigma_{\mathbf{n}} = 0.1\sigma_{\mathbf{y}}$. Best results are shown in bold, second best results are shown in red.

	SNR (dB)					SSIM				
	FFT-based	NQR-based	DL-based	PnP-BM3D	PnP-CNN-SAR	FFT-based	NQR-based	DL-based	PnP-BM3D	PnP-CNN-SAR
Image 1	10.38	15.29	**21.97**	21.86	20.31	0.373	0.748	0.859	0.847	**0.863**
Image 2	7.97	8.85	20.65	8.02	**21.09**	0.360	0.927	0.561	0.406	**0.972**
Image 3	9.67	22.48	**26.13**	16.43	21.32	0.422	**0.913**	0.910	0.771	0.845
Image 4	9.77	10.43	**23.14**	20.75	19.11	0.552	0.525	**0.925**	0.884	0.913
Image 5	10.39	12.87	**22.09**	19.22	20.13	0.430	0.652	**0.895**	0.837	0.853
Image 6	9.17	16.47	20.65	11.30	**24.14**	0.628	0.913	0.918	0.738	**0.970**
Image 7	9.82	13.11	20.62	13.03	**24.28**	0.608	0.769	0.917	0.766	**0.968**
Image 8	9.47	13.84	21.42	13.58	**24.08**	0.613	0.850	0.936	0.817	**0.980**
Image 9	10.25	**26.61**	23.16	21.43	26.29	0.278	**0.978**	0.743	0.664	0.921
Average	9.65	15.55	22.20	16.18	**22.30**	0.474	0.809	0.852	0.748	**0.921**

A.1.4 Experiment 4: 70% Data Availability and $\sigma_{\mathbf{n}} = 0.1\sigma_{\mathbf{y}}$

Table A.4 shows the SNR and SSIM values for this experiment. PnP-CNN-SAR gives the best SNR for 8 images, and best SSIM for 8 images. Fig. A.4 shows

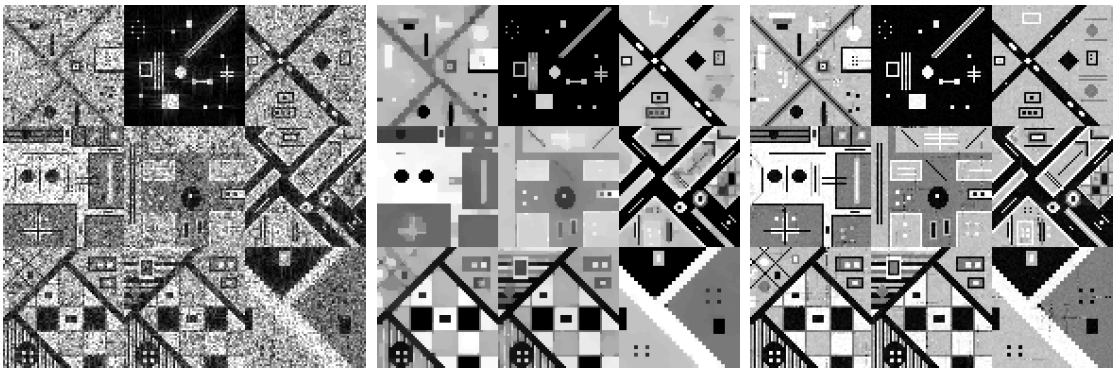

(a) FFT-based (b) NQR-based (c) DL-based

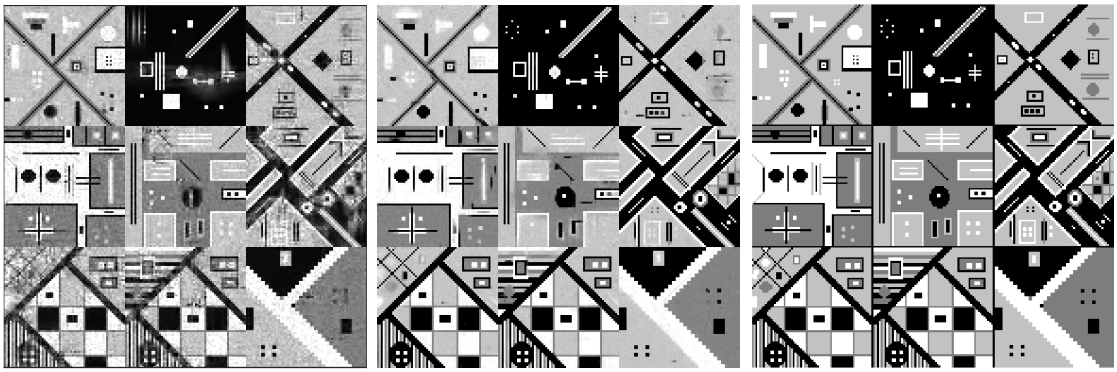

(d) PnP-BM3D (e) PnP-CNN-SAR (f) Ground Truth

Figure A.3 Reconstruction results for the synthetic scenes for the case of 80% data availability and $\sigma_{\mathbf{n}} = 0.1\sigma_{\mathbf{y}}$.

the reconstruction results from all methods for this experiment. PnP-CNN-SAR produces better reconstructions compared to other methods.

Table A.4 SNR and SSIM values for synthetic SAR scenes for the case of 70% data availability and $\sigma_{\mathbf{n}} = 0.1\sigma_{\mathbf{y}}$. Best results are shown in bold, second best results are shown in red.

	SNR (dB)					SSIM				
	FFT-based	NQR-based	DL-based	PnP-BM3D	PnP-CNN-SAR	FFT-based	NQR-based	DL-based	PnP-BM3D	PnP-CNN-SAR
Image 1	8.44	11.92	11.90	13.98	**14.82**	0.284	0.487	0.482	0.560	**0.659**
Image 2	6.52	7.67	**17.84**	2.90	15.27	0.322	0.896	0.536	0.208	**0.963**
Image 3	8.16	12.29	11.12	11.24	**16.47**	0.355	0.602	0.485	0.492	**0.731**
Image 4	8.32	9.21	11.76	13.32	**17.44**	0.434	0.377	0.613	0.688	**0.860**
Image 5	8.49	10.76	11.50	13.70	**17.79**	0.324	0.429	0.526	0.576	**0.743**
Image 6	7.58	8.72	11.22	6.73	**18.21**	0.529	0.570	0.714	0.421	**0.926**
Image 7	7.96	10.74	11.56	8.78	**18.75**	0.500	0.642	0.697	0.506	**0.921**
Image 8	7.84	8.87	10.81	8.95	**18.42**	0.529	0.571	0.675	0.572	**0.935**
Image 9	8.11	17.27	12.24	15.69	**17.38**	0.233	**0.789**	0.360	0.510	0.739
Average	7.94	10.83	12.22	10.59	**17.17**	0.390	0.596	0.566	0.504	**0.831**

A.1.5 Experiment 5: 50% Data Availability and $\sigma_{\mathbf{n}} = 0.1\sigma_{\mathbf{y}}$

Table A.5 shows the SNR and SSIM values for this experiment. PnP-CNN-SAR gives the best SNR for all 9 images, and best SSIM for 8 images. Fig. A.5 shows the reconstruction results from all methods for this experiment. PnP-CNN-SAR produces better reconstructions compared to other methods.

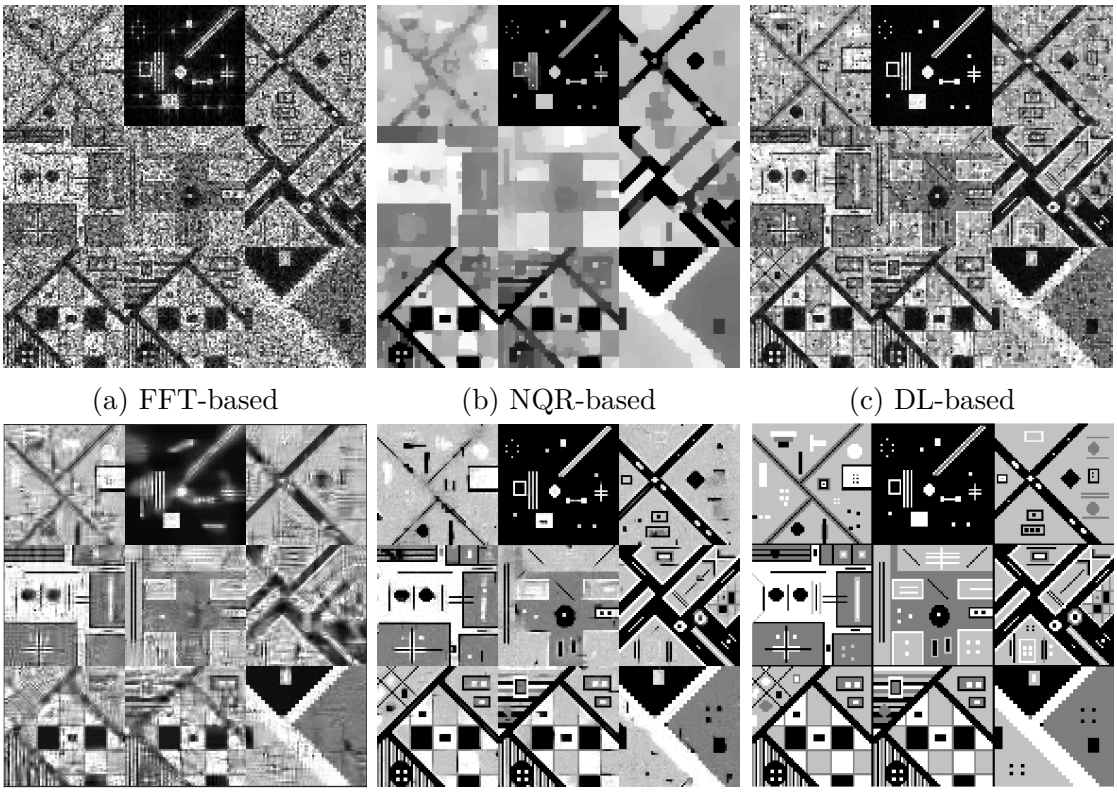

(a) FFT-based (b) NQR-based (c) DL-based

(d) PnP-BM3D (e) PnP-CNN-SAR (f) Ground Truth

Figure A.4 Reconstruction results for the synthetic scenes for the case of 70% data availability and $\sigma_{\mathbf{n}} = 0.1\sigma_{\mathbf{y}}$.

Table A.5 SNR and SSIM values for synthetic SAR scenes for the case of 50% data availability and $\sigma_{\mathbf{n}} = 0.1\sigma_{\mathbf{y}}$. Best results are shown in bold, second best results are shown in red.

	SNR (dB)					SSIM				
	FFT-based	NQR-based	DL-based	PnP-BM3D	PnP-CNN-SAR	FFT-based	NQR-based	DL-based	PnP-BM3D	PnP-CNN-SAR
Image 1	6.44	10.83	8.14	10.60	**11.68**	0.222	0.268	0.277	0.302	**0.400**
Image 2	4.39	6.03	6.08	2.49	**8.49**	0.280	0.839	0.346	0.141	**0.887**
Image 3	6.29	9.64	7.60	8.54	**11.79**	0.244	0.414	0.287	0.230	**0.550**
Image 4	6.26	8.22	7.40	8.76	**9.83**	0.297	0.265	0.344	0.398	**0.472**
Image 5	6.50	10.76	8.09	10.74	**11.82**	0.248	0.348	0.291	0.319	**0.388**
Image 6	5.53	6.97	6.69	5.97	**10.86**	0.364	0.414	0.429	0.267	**0.714**
Image 7	6.01	7.74	7.38	7.52	**11.03**	0.371	0.363	0.433	0.342	**0.659**
Image 8	6.11	7.05	7.19	7.26	**10.64**	0.394	0.318	0.460	0.369	**0.689**
Image 9	6.49	13.49	8.35	11.04	**14.95**	0.177	**0.657**	0.229	0.347	0.607
Average	6.00	8.97	7.44	8.10	**11.23**	0.289	0.432	0.344	0.302	**0.596**

A.1.6 Experiment 6: 30% Data Availability and $\sigma_{\mathbf{n}} = 0.1\sigma_{\mathbf{y}}$

Table A.6 shows the SNR and SSIM values for this experiment. PnP-CNN-SAR gives the best SNR for 5 images, and best SSIM for 6 images. Fig. A.6 shows the reconstruction results from all methods for this experiment. None of the methods are able to produce acceptable reconstructions for most of the images.

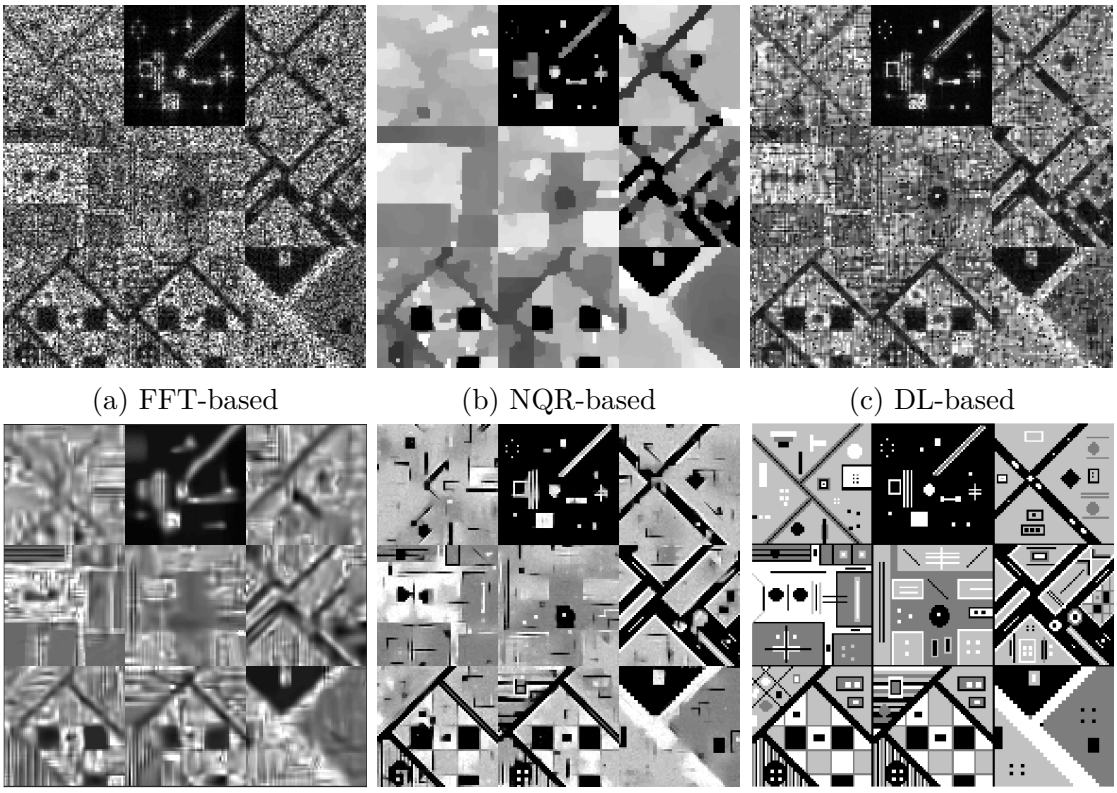

(a) FFT-based (b) NQR-based (c) DL-based

(d) PnP-BM3D (e) PnP-CNN-SAR (f) Ground Truth

Figure A.5 Reconstruction results for the synthetic scenes for the case of 50% data availability and $\sigma_{\mathbf{n}} = 0.1\sigma_{\mathbf{y}}$.

Table A.6 SNR and SSIM values for synthetic SAR scenes for the case of 30% data availability and $\sigma_{\mathbf{n}} = 0.1\sigma_{\mathbf{y}}$. Best results are shown in bold, second best results are shown in red.

	SNR (dB)					SSIM				
	FFT-based	NQR-based	DL-based	PnP-BM3D	PnP-CNN-SAR	FFT-based	NQR-based	DL-based	PnP-BM3D	PnP-CNN-SAR
Image 1	4.84	**10.06**	6.95	6.92	9.54	0.156	0.223	0.167	0.203	**0.237**
Image 2	3.14	4.08	3.17	2.60	**5.21**	0.215	0.704	0.200	0.122	**0.766**
Image 3	4.72	7.87	6.21	6.30	**8.81**	0.171	0.247	0.171	0.201	**0.372**
Image 4	4.61	**7.74**	5.94	6.02	5.97	0.182	0.219	**0.224**	0.215	0.160
Image 5	4.67	**10.68**	6.98	6.96	8.93	0.135	0.213	**0.246**	0.182	0.171
Image 6	4.09	5.38	4.88	5.01	**7.22**	0.237	0.189	0.229	0.187	**0.526**
Image 7	4.40	6.56	5.52	5.41	**7.63**	0.241	0.211	0.237	0.176	**0.410**
Image 8	4.38	5.97	5.38	5.30	**7.12**	0.258	0.172	0.270	0.168	**0.455**
Image 9	4.83	**10.93**	6.36	7.15	9.71	0.130	**0.489**	0.201	0.342	0.416
Average	4.41	7.70	5.71	5.74	**7.79**	0.191	0.296	0.216	0.200	**0.390**

A.1.7 Experiment 7: 100% Data Availability and $\sigma_{\mathbf{n}} = \sigma_{\mathbf{y}}$

Table A.7 shows the SNR and SSIM values for this experiment. PnP-CNN-SAR gives the best SNR for 8 images, and best SSIM for 6 images. Fig. A.7 shows the reconstruction results from all methods for this experiment. PnP-CNN-SAR produces better reconstructions compared to other methods.

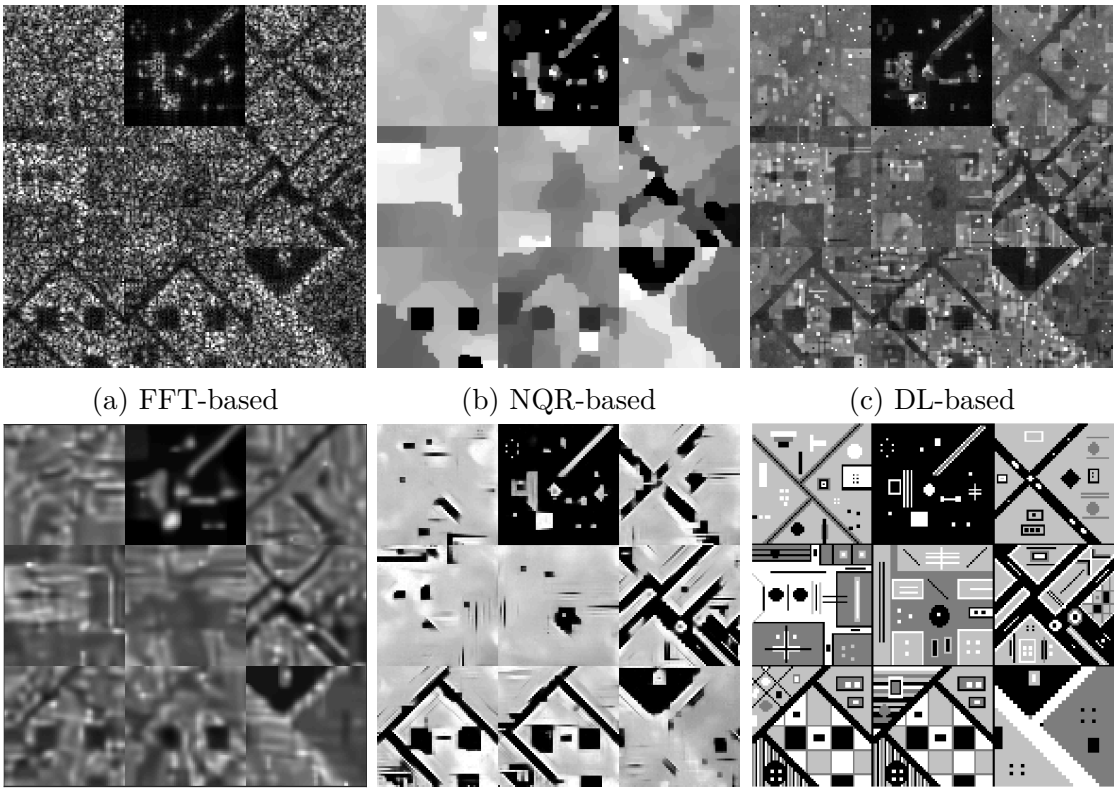

(a) FFT-based (b) NQR-based (c) DL-based

(d) PnP-BM3D (e) PnP-CNN-SAR (f) Ground Truth

Figure A.6 Reconstruction results for the synthetic scenes for the case of 30% data availability and $\sigma_{\mathbf{n}} = 0.1\sigma_{\mathbf{y}}$.

Table A.7 SNR and SSIM values for synthetic SAR scenes for the case of 100% data availability and $\sigma_{\mathbf{n}} = \sigma_{\mathbf{y}}$. Best results are shown in bold, second best results are shown in red.

	SNR (dB)					SSIM				
	FFT-based	NQR-based	DL-based	PnP-BM3D	PnP-CNN-SAR	FFT-based	NQR-based	DL-based	PnP-BM3D	PnP-CNN-SAR
Image 1	6.76	13.26	6.97	10.62	**13.69**	0.364	0.560	0.252	0.336	**0.568**
Image 2	3.93	**14.45**	4.02	3.75	14.34	0.313	**0.907**	0.275	0.244	0.735
Image 3	6.19	13.96	6.36	9.03	**14.23**	0.403	**0.678**	0.291	0.360	0.669
Image 4	6.31	10.04	6.77	9.60	**12.79**	0.507	0.447	0.387	0.501	**0.668**
Image 5	6.69	12.79	7.16	11.06	**13.45**	0.393	0.453	0.288	0.431	**0.529**
Image 6	5.21	9.94	5.60	6.63	**14.23**	0.622	0.651	0.486	0.520	**0.832**
Image 7	5.66	10.50	6.07	7.75	**13.90**	0.593	0.644	0.447	0.526	**0.789**
Image 8	5.54	10.19	5.91	7.66	**13.15**	0.591	0.655	0.462	0.558	**0.802**
Image 9	6.23	16.11	6.31	9.91	**16.18**	0.256	**0.684**	0.195	0.322	0.594
Average	5.84	12.36	6.13	8.45	**13.99**	0.449	0.631	0.343	0.422	**0.687**

A.1.8 Experiment 8: 90% Data Availability and $\sigma_{\mathbf{n}} = \sigma_{\mathbf{y}}$

Table A.8 shows the SNR and SSIM values for this experiment. PnP-CNN-SAR gives the best SNR for 5 images, and best SSIM for 6 images. Fig. A.8 shows the reconstruction results from all methods for this experiment. PnP-CNN-SAR produces better reconstructions compared to other methods.

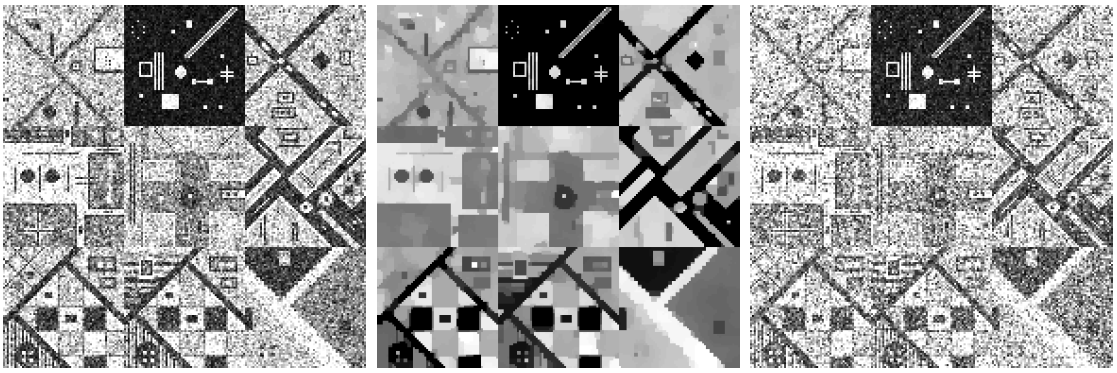

(a) FFT-based (b) NQR-based (c) DL-based

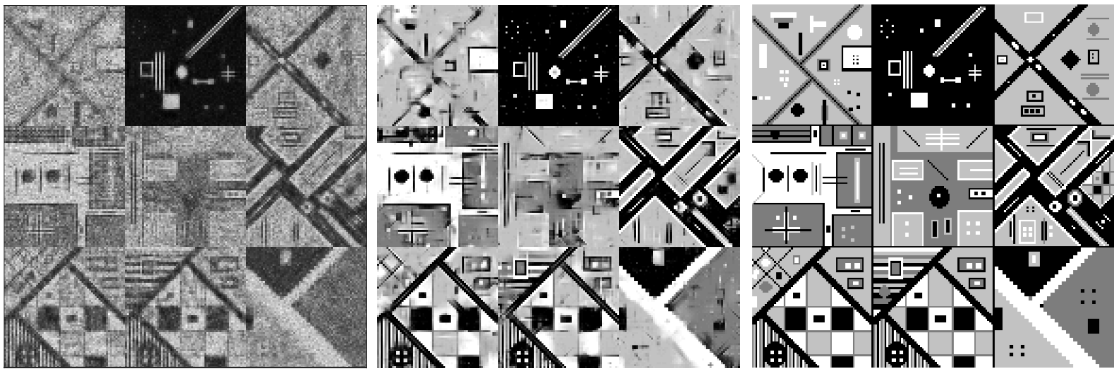

(d) PnP-BM3D (e) PnP-CNN-SAR (f) Ground Truth

Figure A.7 Reconstruction results for the synthetic scenes for the case of 100% data availability and $\sigma_{\mathbf{n}} = \sigma_{\mathbf{y}}$.

Table A.8 SNR and SSIM values for synthetic SAR scenes for the case of 90% data availability and $\sigma_{\mathbf{n}} = \sigma_{\mathbf{y}}$. Best results are shown in bold, second best results are shown in red.

	SNR (dB)					SSIM				
	FFT-based	NQR-based	DL-based	PnP-BM3D	PnP-CNN-SAR	FFT-based	NQR-based	DL-based	PnP-BM3D	PnP-CNN-SAR
Image 1	6.54	**12.25**	6.04	10.74	10.96	0.270	**0.427**	0.191	0.312	0.415
Image 2	3.21	**13.58**	3.10	2.98	12.84	0.285	**0.912**	0.260	0.225	0.566
Image 3	5.80	10.11	4.98	8.35	**10.56**	0.311	0.488	0.202	0.290	**0.507**
Image 4	6.41	9.82	5.39	9.03	**11.03**	0.426	0.432	0.312	0.431	**0.621**
Image 5	6.75	**11.80**	5.88	10.78	11.69	0.314	0.423	0.219	0.357	**0.436**
Image 6	4.99	7.81	3.78	6.08	**12.80**	0.518	0.468	0.393	0.447	**0.793**
Image 7	5.52	8.95	4.56	7.05	**12.01**	0.483	0.507	0.359	0.431	**0.725**
Image 8	5.47	9.06	4.01	6.84	**12.59**	0.483	0.551	0.329	0.444	**0.767**
Image 9	5.93	**15.86**	5.59	9.13	15.14	0.206	**0.737**	0.159	0.258	0.488
Average	5.62	11.03	4.81	7.89	**12.18**	0.366	0.549	0.269	0.355	**0.591**

A.1.9 Experiment 9: 80% Data Availability and $\sigma_{\mathbf{n}} = \sigma_{\mathbf{y}}$

Table A.9 shows the SNR and SSIM values for this experiment. PnP-CNN-SAR gives the best SNR for 6 images, and best SSIM for 5 images. Fig. A.9 shows the reconstruction results from all methods for this experiment. PnP-CNN-SAR produces better reconstructions compared to other methods.

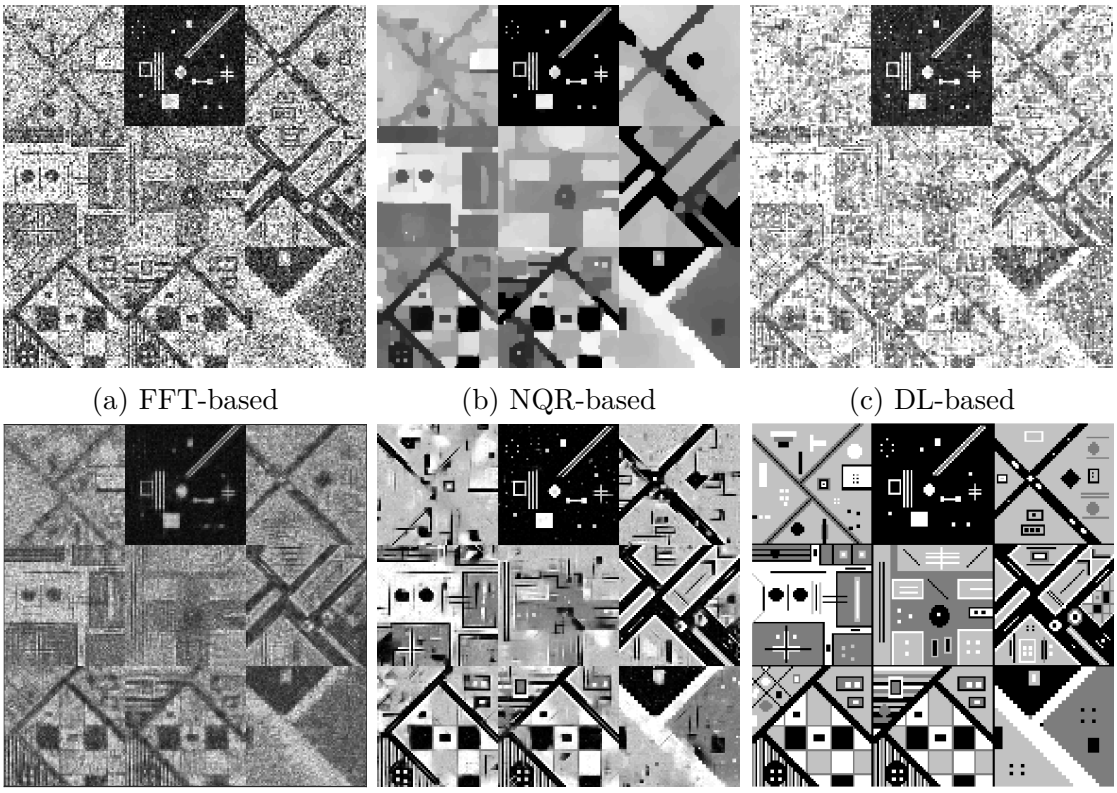

(a) FFT-based (b) NQR-based (c) DL-based

(d) PnP-BM3D (e) PnP-CNN-SAR (f) Ground Truth

Figure A.8 Reconstruction results for the synthetic scenes for the case of 90% data availability and $\sigma_{\mathbf{n}} = \sigma_{\mathbf{y}}$.

Table A.9 SNR and SSIM values for synthetic SAR scenes for the case of 80% data availability and $\sigma_{\mathbf{n}} = \sigma_{\mathbf{y}}$. Best results are shown in bold, second best results are shown in red.

	SNR (dB)					SSIM				
	FFT-based	NQR-based	DL-based	PnP-BM3D	PnP-CNN-SAR	FFT-based	NQR-based	DL-based	PnP-BM3D	PnP-CNN-SAR
Image 1	6.70	**11.19**	6.99	11.00	10.65	0.246	0.328	0.206	0.241	**0.352**
Image 2	3.38	9.11	3.55	2.07	**11.93**	0.271	**0.846**	0.254	0.176	0.420
Image 3	5.95	10.60	5.81	8.60	**11.07**	0.295	**0.511**	0.214	0.248	0.460
Image 4	6.36	9.16	5.71	8.60	**9.94**	0.375	0.357	0.295	0.343	**0.498**
Image 5	6.84	**12.24**	6.66	10.86	11.42	0.292	**0.431**	0.235	0.261	0.387
Image 6	4.89	8.69	4.26	5.24	**11.11**	0.468	0.578	0.362	0.279	**0.707**
Image 7	5.36	7.75	5.12	6.67	**9.83**	0.456	0.350	0.366	0.297	**0.572**
Image 8	5.29	6.50	4.72	6.29	**10.36**	0.437	0.273	0.360	0.322	**0.635**
Image 9	5.95	**14.90**	5.92	9.47	12.99	0.185	**0.702**	0.153	0.283	0.363
Average	5.64	10.02	5.42	7.64	**11.03**	0.336	0.486	0.272	0.272	**0.488**

A.1.10 Experiment 10: 70% Data Availability and $\sigma_{\mathbf{n}} = \sigma_{\mathbf{y}}$

Table A.10 shows the SNR and SSIM values for this experiment. PnP-CNN-SAR gives the best SNR for 8 images, and best SSIM for 6 images. Fig. A.10 shows the reconstruction results from all methods for this experiment. PnP-CNN-SAR produces better reconstructions compared to other methods.

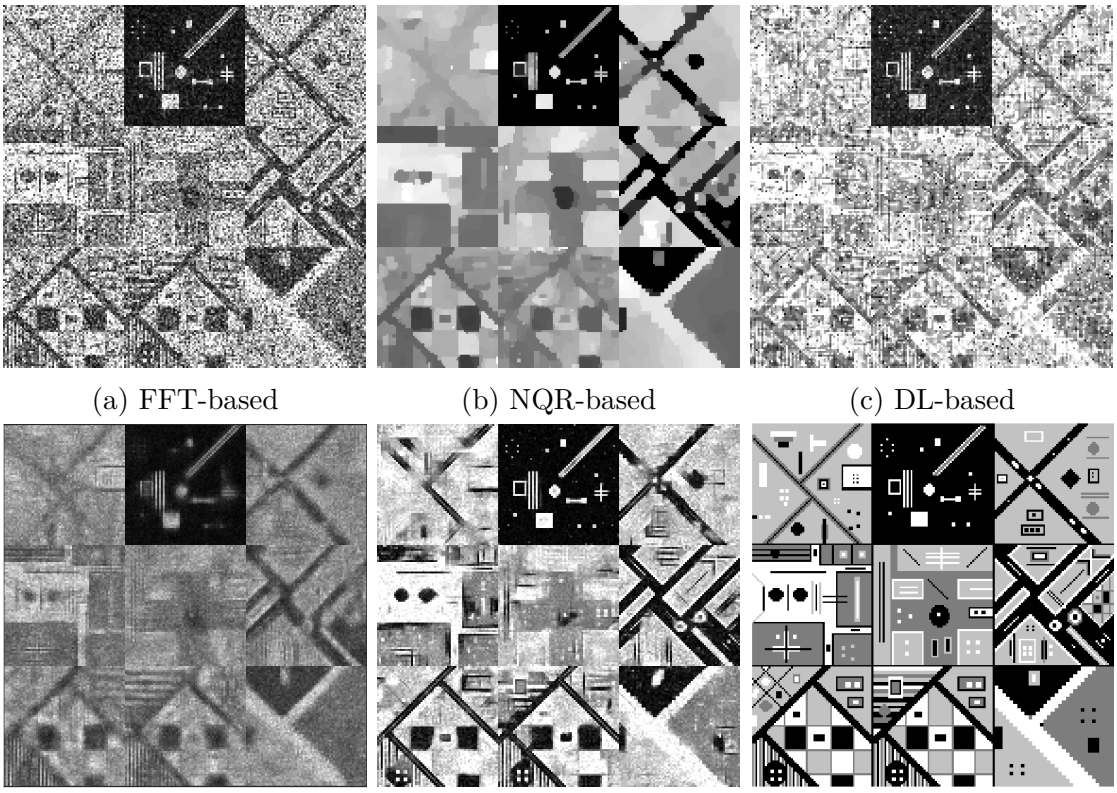

(a) FFT-based (b) NQR-based (c) DL-based

(d) PnP-BM3D (e) PnP-CNN-SAR (f) Ground Truth

Figure A.9 Reconstruction results for the synthetic scenes for the case of 80% data availability and $\sigma_{\mathbf{n}} = 0.1\sigma_{\mathbf{y}}$.

Table A.10 SNR and SSIM values for synthetic SAR scenes for the case of 70% data availability and $\sigma_{\mathbf{n}} = \sigma_{\mathbf{y}}$. Best results are shown in bold, second best results are shown in red.

	SNR (dB)					SSIM				
	FFT-based	NQR-based	DL-based	PnP-BM3D	PnP-CNN-SAR	FFT-based	NQR-based	DL-based	PnP-BM3D	PnP-CNN-SAR
Image 1	6.64	10.51	7.44	10.13	**10.65**	0.223	0.264	0.185	0.211	**0.297**
Image 2	2.98	6.54	3.53	2.54	**11.17**	0.249	**0.807**	0.239	0.175	0.427
Image 3	5.81	9.29	6.31	8.38	**9.38**	0.242	**0.392**	0.192	0.212	0.307
Image 4	6.21	8.93	6.51	8.38	**10.02**	0.314	0.327	0.291	0.290	**0.475**
Image 5	6.56	10.09	7.69	10.29	**10.95**	0.250	0.304	0.231	0.257	**0.339**
Image 6	4.61	7.33	4.73	5.59	**9.36**	0.412	0.480	0.330	0.301	**0.606**
Image 7	5.41	7.57	5.48	6.93	**9.97**	0.383	0.306	0.322	0.320	**0.565**
Image 8	5.15	7.01	5.48	6.64	**9.10**	0.402	0.348	0.340	0.331	**0.548**
Image 9	5.87	**13.45**	7.00	8.94	12.71	0.170	**0.654**	0.159	0.196	0.338
Average	5.47	8.97	6.02	7.54	**10.37**	0.294	0.431	0.254	0.255	**0.433**

A.1.11 Experiment 11: 50% Data Availability and $\sigma_{\mathbf{n}} = \sigma_{\mathbf{y}}$

Table A.11 shows the SNR and SSIM values for this experiment. PnP-CNN-SAR gives the best SNR for 5 images, and best SSIM for 6 images. Fig. A.11 shows the reconstruction results from all methods for this experiment. PnP-CNN-SAR produces better reconstructions compared to other methods.

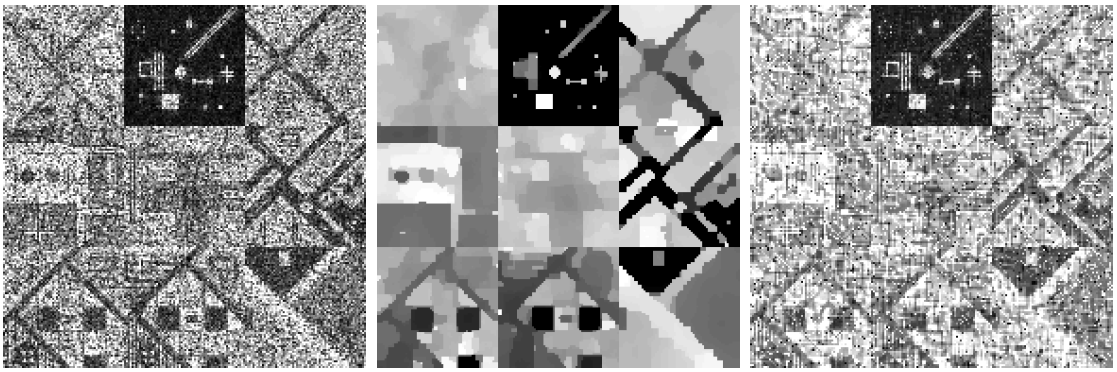

(a) FFT-based (b) NQR-based (c) DL-based

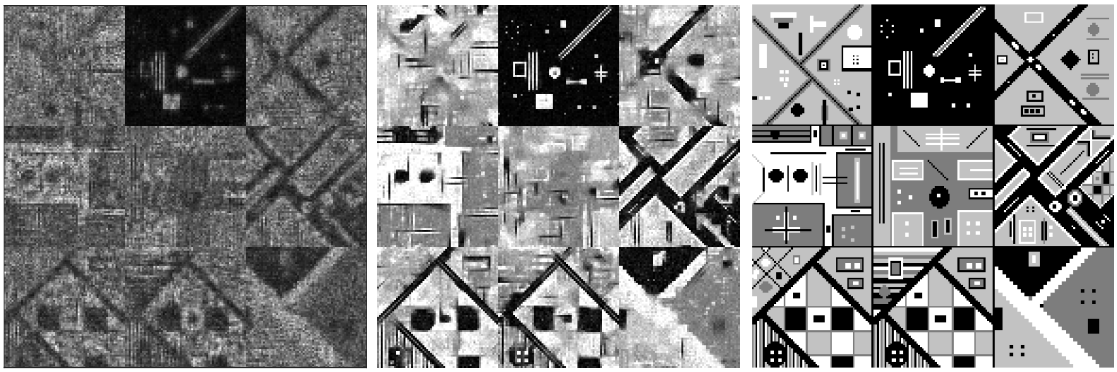

(d) PnP-BM3D (e) PnP-CNN-SAR (f) Ground Truth

Figure A.10 Reconstruction results for the synthetic scenes for the case of 70% data availability and $\sigma_{\mathbf{n}} = \sigma_{\mathbf{y}}$.

Table A.11 SNR and SSIM values for synthetic SAR scenes for the case of 50% data availability and $\sigma_{\mathbf{n}} = \sigma_{\mathbf{y}}$. Best results are shown in bold, second best results are shown in red.

	SNR (dB)					SSIM				
	FFT-based	NQR-based	DL-based	PnP-BM3D	PnP-CNN-SAR	FFT-based	NQR-based	DL-based	PnP-BM3D	PnP-CNN-SAR
Image 1	6.43	9.21	8.77	9.63	**9.72**	0.162	0.213	0.173	0.209	**0.248**
Image 2	2.43	4.41	3.07	1.58	**8.20**	0.209	**0.638**	0.202	0.098	0.412
Image 3	5.71	**8.79**	7.00	7.83	8.70	0.188	0.302	0.154	0.223	**0.316**
Image 4	5.78	**8.35**	7.23	7.67	7.72	0.233	0.258	0.227	0.191	**0.260**
Image 5	6.50	**10.90**	8.57	9.84	10.19	0.185	**0.259**	0.208	0.201	0.220
Image 6	4.49	5.83	4.95	5.02	**7.30**	0.317	0.245	0.248	0.134	**0.466**
Image 7	5.15	6.65	6.14	6.08	**7.49**	0.296	0.218	0.253	0.143	**0.371**
Image 8	5.00	6.47	5.71	5.87	**7.18**	0.314	0.227	0.269	0.170	**0.433**
Image 9	5.84	**11.60**	7.56	8.73	9.22	0.141	**0.480**	0.150	0.374	0.288
Average	5.26	8.02	6.55	6.92	**8.41**	0.227	0.316	0.209	0.194	**0.335**

A.1.12 Experiment 12: 30% Data Availability and $\sigma_{\mathbf{n}} = \sigma_{\mathbf{y}}$

Table A.12 shows the SNR and SSIM values for this experiment. PnP-CNN-SAR gives the best SNR for 3 images, and best SSIM for 3 images. Fig. A.12 shows the reconstruction results from all methods for this experiment. None of the methods are able to produce acceptable reconstructions for most of the images.

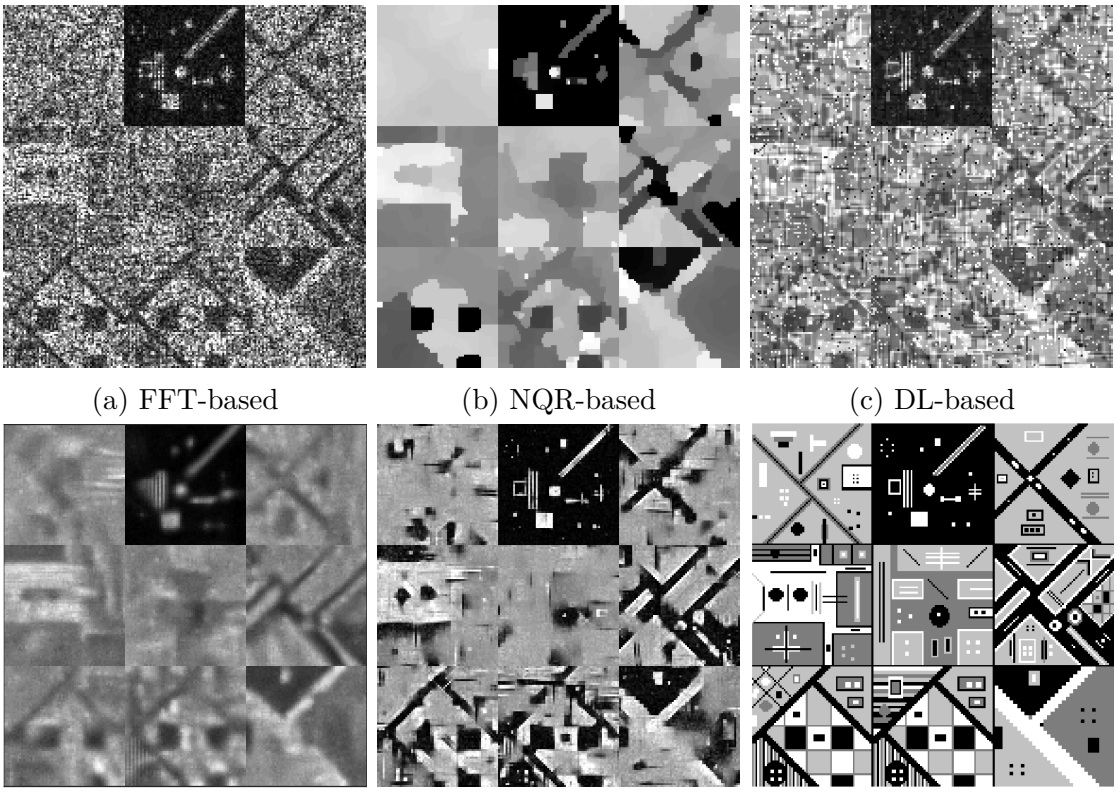

(a) FFT-based (b) NQR-based (c) DL-based

(d) PnP-BM3D (e) PnP-CNN-SAR (f) Ground Truth

Figure A.11 Reconstruction results for the synthetic scenes for the case of 50% data availability and $\sigma_{\mathbf{n}} = \sigma_{\mathbf{y}}$.

Table A.12 SNR and SSIM values for synthetic SAR scenes for the case of 30% data availability and $\sigma_{\mathbf{n}} = \sigma_{\mathbf{y}}$. Best results are shown in bold, second best results are shown in red.

	SNR (dB)					SSIM				
	FFT-based	NQR-based	DL-based	PnP-BM3D	PnP-CNN-SAR	FFT-based	NQR-based	DL-based	PnP-BM3D	PnP-CNN-SAR
Image 1	5.40	**10.16**	9.30	7.77	8.65	0.120	**0.219**	0.192	0.134	0.154
Image 2	2.16	**4.10**	2.08	1.68	3.83	0.149	**0.681**	0.119	0.085	0.285
Image 3	4.89	6.38	6.89	6.76	**7.00**	0.136	0.196	0.149	0.171	**0.201**
Image 4	4.71	**7.62**	7.06	6.53	6.90	0.145	0.186	**0.192**	0.163	0.167
Image 5	5.48	**10.36**	9.04	7.96	9.02	0.154	**0.184**	0.183	0.165	0.158
Image 6	3.99	**5.12**	4.17	4.62	5.07	**0.209**	0.174	0.067	0.116	0.204
Image 7	4.56	6.12	5.70	5.69	**6.35**	0.205	0.138	0.112	0.155	**0.261**
Image 8	4.40	5.68	5.14	5.39	**5.90**	0.201	0.129	0.091	0.152	**0.208**
Image 9	5.09	**10.34**	7.41	7.22	8.31	0.106	**0.460**	0.303	0.243	0.309
Average	4.52	**7.32**	6.31	5.96	6.78	0.158	**0.263**	0.156	0.154	0.216

A.2 Same Scene Experiments

A.2.1 Experiment 1: 100% Data Availability and $\sigma_{\mathbf{n}} = 0.1\sigma_{\mathbf{y}}$

Table A.13 shows the SNR and SSIM values for this experiment. PnP-CNN-SAR gives the best SNR and SSIM for all 31 images. Fig. A.13 shows the reconstruction results for a selection of images from the Wonsan test set from all methods for this experiment. All methods produce good reconstructions.

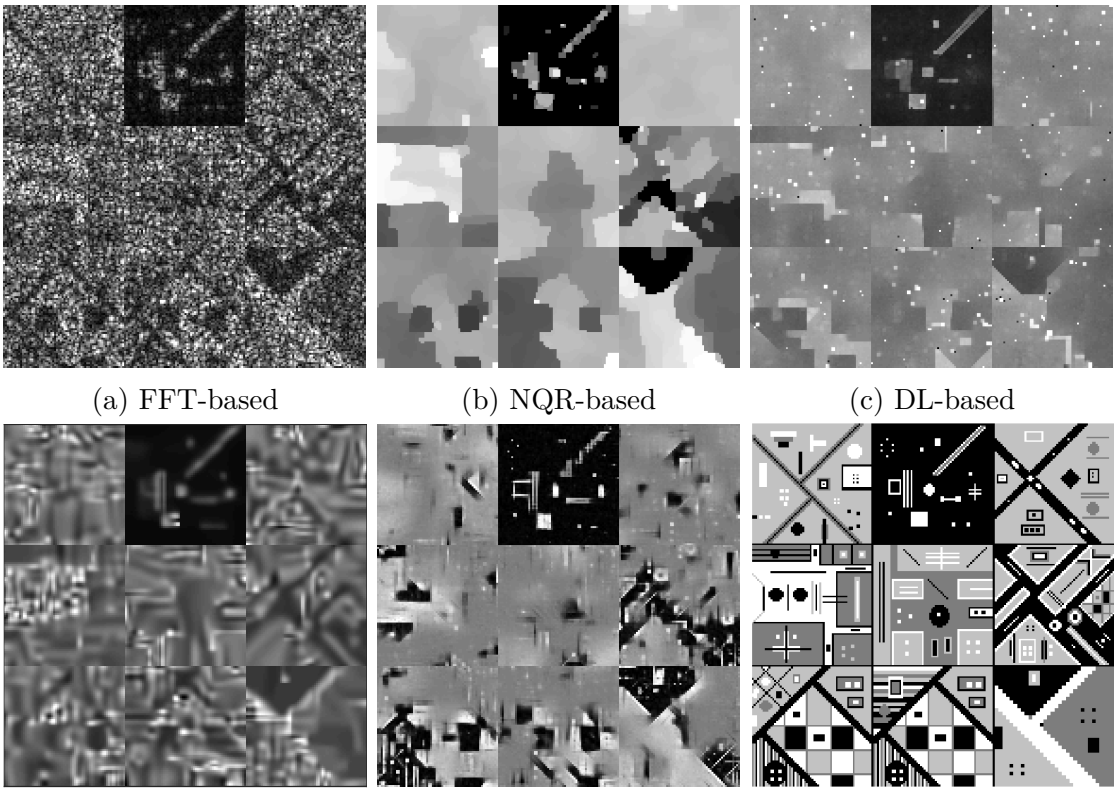

(a) FFT-based (b) NQR-based (c) DL-based

(d) PnP-BM3D (e) PnP-CNN-SAR (f) Ground Truth

Figure A.12 Reconstruction results for the synthetic scenes for the case of 30% data availability and $\sigma_{\mathbf{n}} = \sigma_{\mathbf{y}}$.

Table A.13 SNR and SSIM values for images from the Wonsan Test Set for the case of 100% data availability and $\sigma_{\mathbf{n}} = 0.1\sigma_{\mathbf{y}}$. Best results are shown in bold, second best results are shown in red.

	SNR (dB)					SSIM				
	FFT-based	NQR-based	DL-based	PnP-BM3D	PnP-CNN-SAR	FFT-based	NQR-based	DL-based	PnP-BM3D	PnP-CNN-SAR
Image 1	26.31	24.60	22.58	26.28	**40.91**	0.900	0.906	0.937	0.899	**0.992**
Image 2	26.74	24.59	22.61	26.79	**43.99**	0.986	0.985	0.982	0.986	**1.000**
Image 3	26.67	12.02	26.13	26.62	**35.68**	0.983	0.856	0.981	0.983	**0.998**
Image 4	26.75	25.65	21.41	26.82	**39.38**	0.989	0.989	0.984	0.989	**0.999**
Image 5	26.76	25.14	21.77	26.70	**42.66**	0.990	0.989	0.984	0.990	**1.000**
Image 6	26.36	25.10	21.73	26.35	**40.02**	0.938	0.941	0.957	0.939	**0.994**
Image 7	26.67	25.22	21.36	26.66	**40.81**	0.987	0.987	0.983	0.987	**0.999**
Image 8	26.75	25.45	21.88	26.73	**41.24**	0.984	0.984	0.981	0.984	**0.999**
Image 9	26.64	24.53	21.74	26.73	**42.06**	0.979	0.979	0.978	0.979	**0.999**
Image 10	26.63	25.84	21.99	26.75	**38.59**	0.978	0.979	0.980	0.979	**0.999**
Image 11	26.72	24.93	22.83	26.72	**41.32**	0.986	0.985	0.982	0.986	**1.000**
Image 12	26.29	24.93	22.24	26.36	**41.16**	0.927	0.931	0.953	0.928	**0.994**
Image 13	26.71	17.00	26.46	26.67	**37.39**	0.979	0.935	0.979	0.979	**0.998**
Image 14	26.65	24.58	21.25	26.68	**41.48**	0.980	0.980	0.978	0.980	**0.999**
Image 15	26.65	26.01	23.08	26.70	**41.33**	0.988	0.987	0.984	0.988	**1.000**
Image 16	26.69	24.71	21.94	26.73	**41.57**	0.987	0.986	0.982	0.987	**0.999**
Image 17	26.95	24.98	25.77	26.75	**34.66**	0.957	0.960	0.973	0.955	**0.992**
Image 18	26.73	25.46	22.94	26.69	**43.06**	0.985	0.985	0.982	0.985	**1.000**
Image 19	26.61	24.81	21.33	26.83	**41.72**	0.985	0.985	0.982	0.986	**1.000**
Image 20	26.74	25.58	23.12	26.69	**39.18**	0.987	0.987	0.984	0.987	**0.999**
Image 21	26.64	24.80	24.05	26.75	**41.17**	0.984	0.984	0.982	0.985	**1.000**
Image 22	26.73	24.76	21.51	26.78	**40.01**	0.985	0.984	0.982	0.985	**0.999**
Image 23	26.75	25.02	24.29	26.72	**40.95**	0.986	0.985	0.983	0.986	**1.000**
Image 24	26.78	24.63	23.35	26.73	**41.59**	0.981	0.981	0.981	0.981	**0.999**
Image 25	26.79	12.07	26.64	26.67	**35.27**	0.981	0.851	0.978	0.980	**0.997**
Image 26	26.74	24.26	21.27	26.75	**37.94**	0.968	0.969	0.975	0.968	**0.998**
Image 27	26.65	24.10	22.77	26.70	**41.25**	0.985	0.984	0.983	0.985	**0.999**
Image 28	25.97	25.25	22.20	25.97	**37.01**	0.898	0.904	0.942	0.898	**0.985**
Image 29	26.74	26.48	25.03	26.70	**41.78**	0.985	0.985	0.983	0.985	**0.999**
Image 30	26.52	24.40	21.48	26.52	**40.51**	0.947	0.950	0.959	0.949	**0.996**
Image 31	26.71	13.35	24.67	26.72	**35.22**	0.989	0.956	0.985	0.989	**0.998**
Average	26.65	23.56	22.95	26.65	**40.03**	0.973	0.963	0.976	0.973	**0.998**

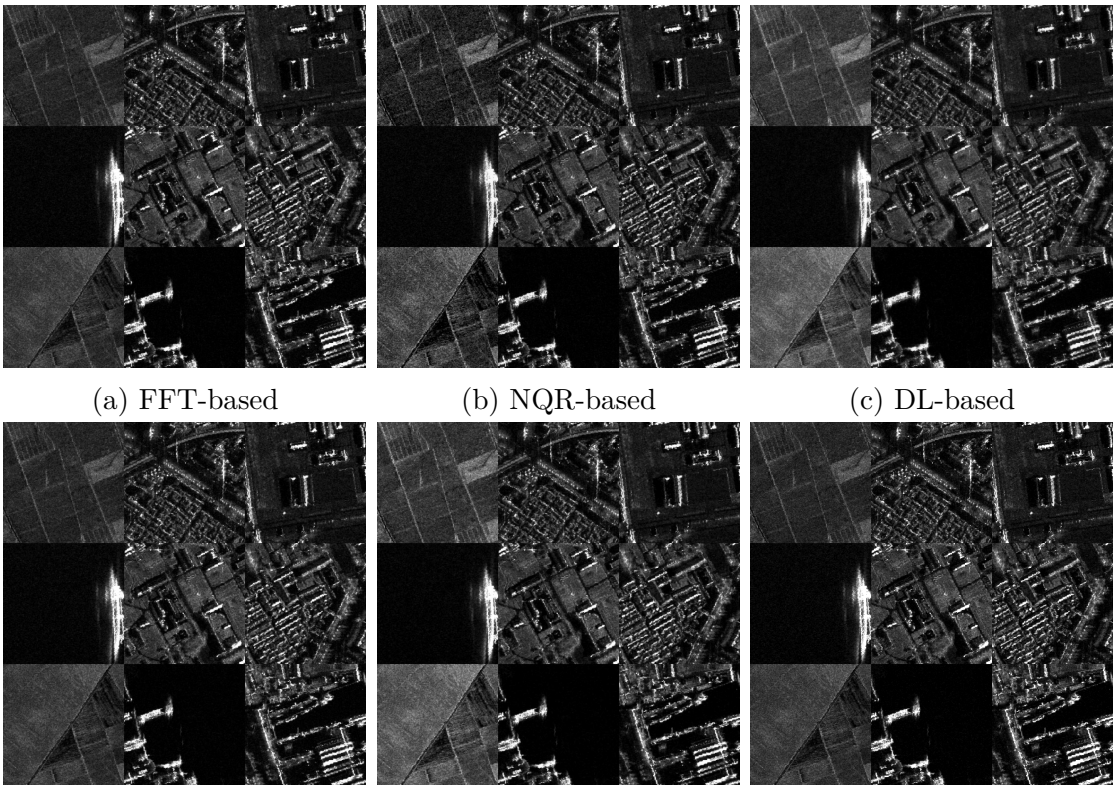

(a) FFT-based (b) NQR-based (c) DL-based

(d) PnP-BM3D (e) PnP-CNN-SAR (f) Ground Truth

Figure A.13 Reconstruction results for Images 3, 4, 10, 17, 18, 19, 25, 28, and 30 from the Wonsan test set for the case of 100% data availability and $\sigma_{\mathbf{n}} = 0.1\sigma_{\mathbf{y}}$.

A.2.2 Experiment 2: 90% Data Availability and $\sigma_{\mathbf{n}} = 0.1\sigma_{\mathbf{y}}$

Table A.14 shows the SNR and SSIM values for this experiment. PnP-CNN-SAR gives the best SNR for 27 images, and best SSIM for 29 images. Fig. A.14 shows the reconstruction results for a selection of images from the Wonsan test set from all methods for this experiment. All methods produce good reconstructions.

A.2.3 Experiment 3: 80% Data Availability and $\sigma_{\mathbf{n}} = 0.1\sigma_{\mathbf{y}}$

Table A.15 shows the SNR and SSIM values for this experiment. PnP-CNN-SAR gives the best SNR for 27 images, and best SSIM for 29 images. Fig. A.15 shows the reconstruction results for a selection of images from the Wonsan test set from all methods for this experiment. PnP-BM3D and PnP-CNN-SAR produce better reconstructions compared to other methods.

A.2.4 Experiment 4: 70% Data Availability and $\sigma_{\mathbf{n}} = 0.1\sigma_{\mathbf{y}}$

Table A.16 shows the SNR and SSIM values for this experiment. PnP-CNN-SAR gives the best SNR for 29 images, and best SSIM for 28 images. Fig. A.16 shows

Table A.14 SNR and SSIM values for images from the Wonsan Test Set for the case of 90% data availability and $\sigma_{\mathbf{n}} = 0.1\sigma_{\mathbf{y}}$. Best results are shown in bold, second best results are shown in red.

	SNR (dB)					SSIM				
	FFT-based	NQR-based	DL-based	PnP-BM3D	PnP-CNN-SAR	FFT-based	NQR-based	DL-based	PnP-BM3D	PnP-CNN-SAR
Image 1	13.19	13.25	12.32	15.55	**18.06**	0.706	0.608	0.698	0.783	**0.925**
Image 2	13.47	11.48	12.14	14.43	**17.16**	0.832	0.667	0.790	0.858	**0.926**
Image 3	13.55	9.82	16.45	**17.73**	17.00	0.762	0.601	0.829	**0.872**	0.843
Image 4	13.37	10.67	11.56	13.01	**15.24**	0.862	0.831	0.802	0.846	**0.901**
Image 5	13.31	11.57	11.73	13.25	**15.71**	0.859	0.839	0.809	0.851	**0.913**
Image 6	12.84	11.43	10.70	13.49	**17.11**	0.751	0.765	0.679	0.770	**0.937**
Image 7	13.21	11.90	11.15	13.01	**16.40**	0.850	0.842	0.781	0.841	**0.934**
Image 8	13.26	10.81	11.68	13.57	**14.79**	0.837	0.647	0.783	0.846	**0.875**
Image 9	13.16	11.92	11.14	13.96	**15.49**	0.822	0.676	0.748	0.846	**0.888**
Image 10	13.21	10.18	11.60	15.12	**16.59**	0.802	0.526	0.787	0.838	**0.901**
Image 11	13.36	11.64	13.08	14.22	**16.07**	0.830	0.816	0.822	0.853	**0.892**
Image 12	12.99	11.28	11.69	14.41	**17.01**	0.733	0.587	0.691	0.788	**0.925**
Image 13	13.28	12.60	16.45	17.48	**17.66**	0.729	0.710	0.814	0.848	**0.849**
Image 14	13.11	11.44	10.43	13.54	**15.74**	0.830	0.681	0.733	0.842	**0.902**
Image 15	13.36	12.47	13.34	14.39	**16.34**	0.835	0.829	0.831	0.850	**0.902**
Image 16	13.23	10.96	11.76	13.44	**15.42**	0.847	0.663	0.791	0.851	**0.899**
Image 17	13.10	12.23	15.62	**18.22**	17.89	0.818	0.689	0.854	0.784	**0.907**
Image 18	13.25	11.61	12.67	15.29	**17.45**	0.801	0.792	0.790	0.859	**0.909**
Image 19	13.32	11.35	10.77	13.31	**16.94**	0.846	0.829	0.780	0.854	**0.925**
Image 20	13.41	11.34	13.64	13.96	**15.59**	0.842	0.824	0.846	0.836	**0.896**
Image 21	13.40	12.66	14.31	15.31	**16.48**	0.813	0.811	0.831	0.855	**0.890**
Image 22	13.29	11.05	11.20	13.52	**16.73**	0.849	0.667	0.770	0.846	**0.921**
Image 23	13.29	11.62	14.52	15.80	**16.59**	0.797	0.505	0.827	0.862	**0.878**
Image 24	13.13	12.14	13.38	15.12	**17.37**	0.806	0.616	0.816	0.853	**0.908**
Image 25	13.40	10.13	16.74	**18.21**	17.95	0.711	0.559	0.806	**0.860**	0.835
Image 26	13.12	12.89	10.03	15.44	**18.13**	0.781	0.581	0.695	0.830	**0.895**
Image 27	13.29	9.57	13.08	14.52	**16.29**	0.827	0.450	0.827	0.856	**0.897**
Image 28	12.65	14.40	10.59	17.01	**19.23**	0.698	0.545	0.668	0.769	**0.934**
Image 29	13.32	12.99	15.14	**16.81**	16.54	0.786	0.787	0.843	0.871	**0.881**
Image 30	12.97	12.92	10.33	14.79	**19.01**	0.754	0.677	0.671	0.830	**0.919**
Image 31	13.40	10.54	14.89	13.75	**16.18**	0.835	0.557	0.858	0.816	**0.884**
Average	13.23	11.64	12.71	14.89	**16.78**	0.802	0.683	0.783	0.838	**0.900**

(a) FFT-based (b) NQR-based (c) DL-based

(d) PnP-BM3D (e) PnP-CNN-SAR (f) Ground Truth

Figure A.14 Reconstruction results for Images 3, 4, 10, 17, 18, 19, 25, 28, and 30 from the Wonsan test set for the case of 100% data availability and $\sigma_{\mathbf{n}} = 0.1\sigma_{\mathbf{y}}$.

Table A.15 SNR and SSIM values for images from the Wonsan Test Set for the case of 80% data availability and $\sigma_{\mathbf{n}} = 0.1\sigma_{\mathbf{y}}$. Best results are shown in bold, second best results are shown in red.

	SNR (dB)					SSIM				
	FFT-based	NQR-based	DL-based	PnP-BM3D	PnP-CNN-SAR	FFT-based	NQR-based	DL-based	PnP-BM3D	PnP-CNN-SAR
Image 1	9.77	8.98	9.69	11.73	**13.41**	0.653	0.485	0.632	0.697	**0.867**
Image 2	9.96	7.23	9.65	11.33	**13.30**	0.722	0.334	0.671	0.757	**0.854**
Image 3	10.15	8.55	13.04	**14.50**	13.69	0.597	0.566	0.681	**0.747**	0.715
Image 4	10.12	5.36	8.76	10.00	**12.84**	0.775	0.338	0.681	0.735	**0.872**
Image 5	10.20	8.90	9.16	10.55	**12.57**	0.763	0.732	0.681	0.747	**0.848**
Image 6	9.83	8.80	8.61	10.21	**11.97**	0.702	0.500	0.613	0.678	**0.873**
Image 7	9.99	9.35	8.56	10.06	**12.84**	0.765	0.754	0.659	0.737	**0.873**
Image 8	9.96	8.19	8.96	10.52	**12.93**	0.750	0.714	0.666	0.746	**0.867**
Image 9	9.99	7.64	8.87	10.90	**13.60**	0.742	0.483	0.650	0.752	**0.868**
Image 10	10.09	7.23	9.10	11.32	**13.18**	0.720	0.443	0.692	0.732	**0.825**
Image 11	10.07	7.48	10.12	11.28	**13.07**	0.712	0.306	0.686	0.734	**0.813**
Image 12	9.78	6.76	9.23	10.86	**12.47**	0.667	0.363	0.631	0.684	**0.867**
Image 13	10.10	11.59	13.12	14.07	**14.40**	0.571	0.511	0.668	0.712	**0.724**
Image 14	9.82	7.99	8.16	10.25	**13.29**	0.748	0.530	0.631	0.749	**0.888**
Image 15	10.10	9.27	10.37	11.45	**12.85**	0.721	0.487	0.697	0.741	**0.817**
Image 16	10.23	8.60	9.25	10.71	**13.10**	0.753	0.715	0.673	0.755	**0.845**
Image 17	9.86	12.48	12.43	**14.19**	13.84	0.780	0.655	0.803	0.719	**0.850**
Image 18	10.10	9.73	9.84	11.94	**13.70**	0.685	0.521	0.658	0.744	**0.828**
Image 19	9.85	8.77	8.32	10.24	**13.38**	0.752	0.574	0.663	0.755	**0.871**
Image 20	10.07	9.79	10.45	11.24	**12.73**	0.728	0.725	0.720	0.717	**0.815**
Image 21	10.19	9.16	11.28	12.14	**13.08**	0.685	0.335	0.698	0.732	**0.785**
Image 22	9.95	8.12	8.66	10.39	**13.32**	0.761	0.522	0.659	0.740	**0.876**
Image 23	10.28	9.75	11.52	12.42	**13.13**	0.663	0.345	0.691	0.736	**0.772**
Image 24	10.07	8.27	10.56	11.74	**13.57**	0.696	0.358	0.695	0.742	**0.820**
Image 25	10.19	10.45	13.21	**15.28**	14.44	0.543	0.502	0.631	**0.731**	0.684
Image 26	10.07	9.32	7.81	11.75	**14.92**	0.714	0.527	0.613	0.742	**0.857**
Image 27	10.17	7.71	10.09	11.47	**13.00**	0.710	0.353	0.695	0.739	**0.814**
Image 28	9.67	10.31	8.45	**13.10**	12.61	0.685	0.529	0.646	0.703	**0.884**
Image 29	10.12	8.71	11.99	13.41	**13.60**	0.645	0.386	0.707	0.754	**0.788**
Image 30	9.65	9.55	8.13	10.98	**13.86**	0.689	0.573	0.585	0.732	**0.883**
Image 31	10.11	9.66	11.67	11.05	**13.43**	0.713	0.522	0.735	0.680	**0.788**
Average	10.02	8.83	9.97	11.65	**13.29**	0.704	0.506	0.671	0.731	**0.830**

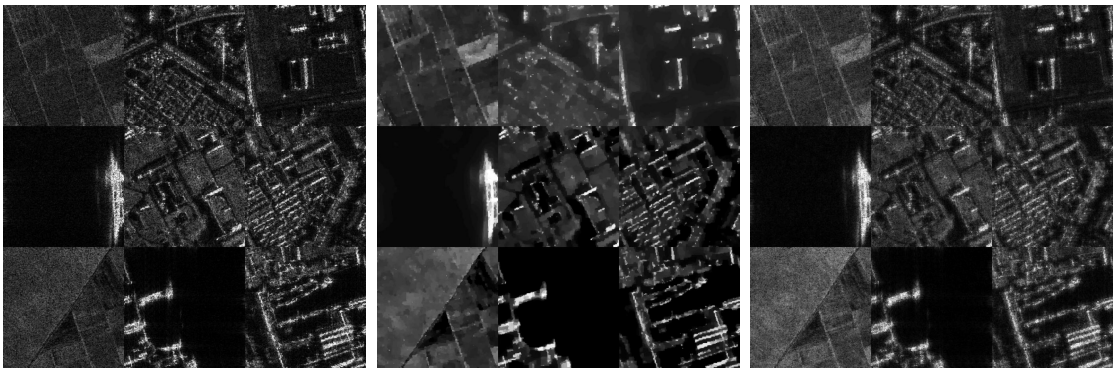

(a) FFT-based (b) NQR-based (c) DL-based

(d) PnP-BM3D (e) PnP-CNN-SAR (f) Ground Truth

Figure A.15 Reconstruction results for Images 3, 4, 10, 17, 18, 19, 25, 28, and 30 from the Wonsan test set for the case of 100% data availability and $\sigma_{\mathbf{n}} = 0.1\sigma_{\mathbf{y}}$.

the reconstruction results for a selection of images from the Wonsan test set from all methods for this experiment. PnP-CNN-SAR produce better reconstructions compared to other methods.

Table A.16 SNR and SSIM values for images from the Wonsan Test Set for the case of 70% data availability and $\sigma_{\mathbf{n}} = 0.1\sigma_{\mathbf{y}}$. Best results are shown in bold, second best results are shown in red.

	SNR (dB)					SSIM				
	FFT-based	NQR-based	DL-based	PnP-BM3D	PnP-CNN-SAR	FFT-based	NQR-based	DL-based	PnP-BM3D	PnP-CNN-SAR
Image 1	8.32	7.53	8.47	9.30	**10.56**	0.605	0.432	0.579	0.626	**0.793**
Image 2	8.49	6.97	8.47	9.20	**10.94**	0.650	0.279	0.587	0.655	**0.768**
Image 3	8.52	8.24	11.01	**12.12**	11.59	0.503	0.427	0.550	**0.597**	0.572
Image 4	8.45	6.64	7.65	8.47	**10.18**	0.705	0.634	0.594	0.648	**0.793**
Image 5	8.43	7.18	7.86	8.71	**10.09**	0.678	0.631	0.583	0.646	**0.752**
Image 6	8.18	6.47	7.52	8.58	**10.25**	0.652	0.430	0.562	0.612	**0.820**
Image 7	8.35	7.30	7.46	8.43	**10.21**	0.696	0.664	0.585	0.652	**0.800**
Image 8	8.29	6.62	7.89	8.66	**10.31**	0.681	0.368	0.592	0.653	**0.792**
Image 9	8.30	6.53	7.62	8.92	**10.85**	0.669	0.372	0.563	0.665	**0.799**
Image 10	8.36	6.24	7.89	9.01	**10.30**	0.648	0.398	0.620	0.646	**0.741**
Image 11	8.42	6.16	8.74	9.62	**10.49**	0.619	0.296	0.584	0.633	**0.697**
Image 12	8.32	7.48	8.14	9.11	**10.35**	0.635	0.441	0.582	0.618	**0.807**
Image 13	8.53	10.62	11.17	11.39	**11.81**	0.481	0.466	0.538	**0.560**	0.554
Image 14	8.13	6.74	7.17	8.48	**10.47**	0.687	0.438	0.558	0.668	**0.819**
Image 15	8.64	6.78	9.09	9.56	**10.62**	0.641	0.270	0.599	0.620	**0.708**
Image 16	8.36	7.00	7.94	8.99	**10.38**	0.669	0.621	0.563	0.656	**0.753**
Image 17	8.57	10.52	10.38	10.26	**10.90**	0.748	0.620	0.757	0.685	**0.796**
Image 18	8.48	7.83	8.68	9.70	**10.83**	0.606	0.340	0.564	0.629	**0.724**
Image 19	8.29	6.86	7.29	8.62	**10.51**	0.687	0.635	0.580	0.664	**0.795**
Image 20	8.44	7.11	9.20	9.57	**10.19**	0.635	0.299	0.634	0.605	**0.710**
Image 21	8.56	8.73	9.70	10.12	**10.87**	0.598	0.330	0.586	0.618	**0.668**
Image 22	8.37	4.66	7.53	8.64	**10.73**	0.690	0.253	0.577	0.659	**0.801**
Image 23	8.63	8.26	9.89	10.21	**10.92**	0.569	0.284	0.572	0.605	**0.645**
Image 24	8.67	7.49	9.13	9.67	**11.12**	0.626	0.316	0.596	0.636	**0.720**
Image 25	8.56	9.20	11.21	**12.22**	11.97	0.445	0.425	0.500	**0.555**	0.500
Image 26	8.11	7.03	6.96	8.79	**11.83**	0.649	0.420	0.568	0.657	**0.779**
Image 27	8.31	6.83	8.82	9.49	**10.54**	0.616	0.252	0.588	0.625	**0.710**
Image 28	8.32	8.96	7.75	9.72	**10.03**	0.684	0.512	0.651	0.651	**0.842**
Image 29	8.55	8.23	10.35	11.10	**11.33**	0.556	0.317	0.606	0.616	**0.681**
Image 30	8.13	8.38	7.11	8.90	**10.80**	0.640	0.528	0.525	0.652	**0.812**
Image 31	8.56	7.71	10.13	9.97	**11.23**	0.633	0.531	0.639	0.570	**0.677**
Average	8.41	7.49	8.65	9.53	**10.75**	0.632	0.427	0.587	0.632	**0.736**

A.2.5 Experiment 5: 50% Data Availability and $\sigma_{\mathbf{n}} = 0.1\sigma_{\mathbf{y}}$

Table A.17 shows the SNR and SSIM values for this experiment. PnP-CNN-SAR gives the best SNR for 23 images, and best SSIM for 29 images. Fig. A.17 shows the reconstruction results for a selection of images from the Wonsan test set from all methods for this experiment. PnP-CNN-SAR produce better reconstructions compared to other methods.

A.2.6 Experiment 6: 30% Data Availability and $\sigma_{\mathbf{n}} = 0.1\sigma_{\mathbf{y}}$

Table A.18 shows the SNR and SSIM values for this experiment. PnP-CNN-SAR gives the best SNR for 5 images, and best SSIM for 23 images. Fig. A.18 shows the reconstruction results for a selection of images from the Wonsan test set from all methods for this experiment. PnP-CNN-SAR produce better reconstructions compared to other methods.

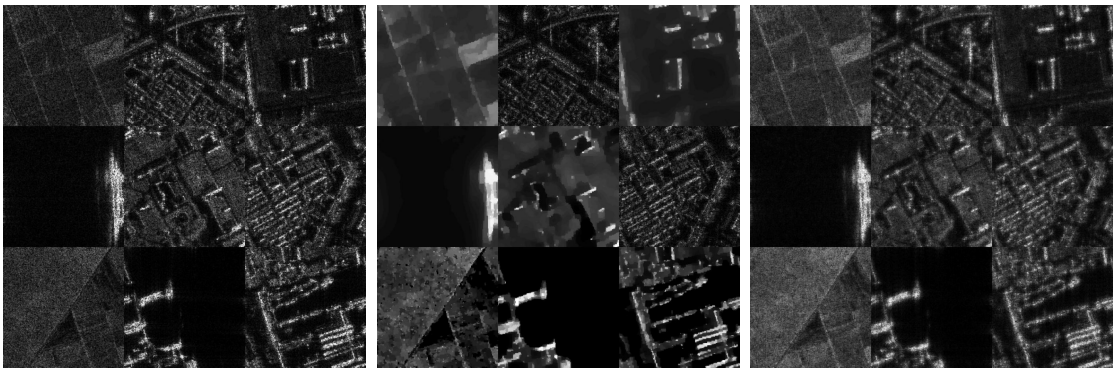

(a) FFT-based (b) NQR-based (c) DL-based

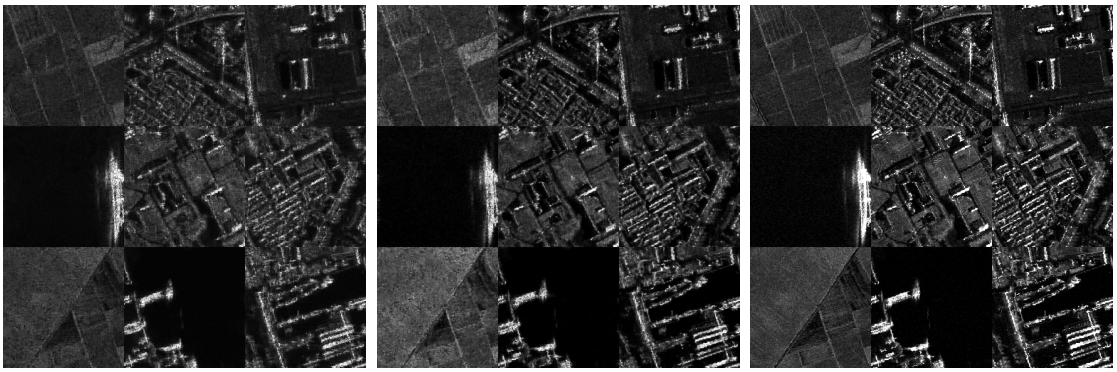

(d) PnP-BM3D (e) PnP-CNN-SAR (f) Ground Truth

Figure A.16 Reconstruction results for Images 3, 4, 10, 17, 18, 19, 25, 28, and 30 from the Wonsan test set for the case of 100% data availability and $\sigma_{\mathbf{n}} = 0.1\sigma_{\mathbf{y}}$.

Table A.17 SNR and SSIM values for images from the Wonsan Test Set for the case of 50% data availability and $\sigma_{\mathbf{n}} = 0.1\sigma_{\mathbf{y}}$. Best results are shown in bold, second best results are shown in red.

	SNR (dB)					SSIM				
	FFT-based	NQR-based	DL-based	PnP-BM3D	PnP-CNN-SAR	FFT-based	NQR-based	DL-based	PnP-BM3D	PnP-CNN-SAR
Image 1	6.10	7.06	6.68	7.26	**8.20**	0.541	0.410	0.505	0.487	**0.656**
Image 2	6.26	4.80	6.78	7.44	**7.97**	0.513	0.190	0.437	0.461	**0.595**
Image 3	6.61	7.93	8.68	**10.63**	8.81	0.384	**0.418**	0.374	0.404	0.393
Image 4	6.10	5.76	5.99	6.41	**7.40**	0.555	0.343	0.441	0.444	**0.620**
Image 5	6.17	6.03	6.33	6.77	**7.52**	0.527	0.266	0.419	0.421	**0.580**
Image 6	6.09	3.54	6.19	6.54	**7.56**	0.579	0.200	0.488	0.468	**0.651**
Image 7	6.13	6.09	6.02	6.25	**7.46**	0.563	0.561	0.444	0.435	**0.631**
Image 8	6.03	3.42	6.28	6.84	**7.64**	0.546	0.175	0.451	0.469	**0.625**
Image 9	6.10	4.06	6.11	6.82	**7.70**	0.548	0.187	0.438	0.484	**0.657**
Image 10	6.21	5.12	6.31	7.22	**7.74**	0.533	0.357	0.505	0.492	**0.618**
Image 11	6.29	5.51	7.03	7.80	**7.93**	0.478	0.207	0.419	0.424	**0.539**
Image 12	6.15	6.76	6.49	7.00	**7.95**	0.558	0.407	0.502	0.474	**0.642**
Image 13	6.49	**11.04**	8.67	9.97	9.22	0.348	0.354	0.364	0.362	**0.386**
Image 14	6.04	3.13	5.75	6.38	**7.62**	0.563	0.150	0.429	0.478	**0.674**
Image 15	6.32	7.33	7.05	7.90	**8.08**	0.486	0.282	0.429	0.416	**0.539**
Image 16	6.19	4.40	6.36	6.94	**7.70**	0.519	0.151	0.408	0.426	**0.589**
Image 17	6.35	**8.81**	7.98	8.33	8.26	0.680	0.588	0.694	0.648	**0.719**
Image 18	6.31	5.13	6.84	7.78	**8.31**	0.472	0.184	0.413	0.414	**0.557**
Image 19	6.06	2.99	5.87	6.57	**7.73**	0.550	0.177	0.437	0.476	**0.642**
Image 20	6.31	5.50	7.24	7.83	**8.00**	0.500	0.263	0.464	0.401	**0.543**
Image 21	6.40	6.44	7.73	**8.57**	8.34	0.447	0.200	0.420	0.414	**0.492**
Image 22	6.16	3.40	6.08	6.61	**7.71**	0.553	0.175	0.439	0.465	**0.639**
Image 23	6.30	6.29	7.80	**8.70**	8.45	0.410	0.196	0.393	0.392	**0.469**
Image 24	6.28	5.72	7.25	7.93	**8.24**	0.475	0.230	0.446	0.455	**0.562**
Image 25	6.51	9.99	8.75	**10.75**	9.25	0.326	0.336	0.330	**0.346**	0.328
Image 26	5.91	5.51	5.51	6.60	**8.46**	0.530	0.371	0.456	0.505	**0.670**
Image 27	6.25	5.63	6.94	7.69	**7.86**	0.480	0.198	0.428	0.419	**0.531**
Image 28	5.88	6.72	6.02	7.11	**8.23**	0.668	0.482	0.629	0.591	**0.710**
Image 29	6.45	5.49	8.11	**9.66**	8.79	0.430	0.251	0.455	0.401	**0.505**
Image 30	6.05	5.70	5.65	6.55	**8.25**	0.540	0.373	0.411	0.473	**0.687**
Image 31	6.41	6.26	8.05	**9.22**	8.95	0.511	0.472	0.495	0.475	**0.537**
Average	6.22	5.86	6.85	7.68	**8.11**	0.510	0.295	0.450	0.452	**0.580**

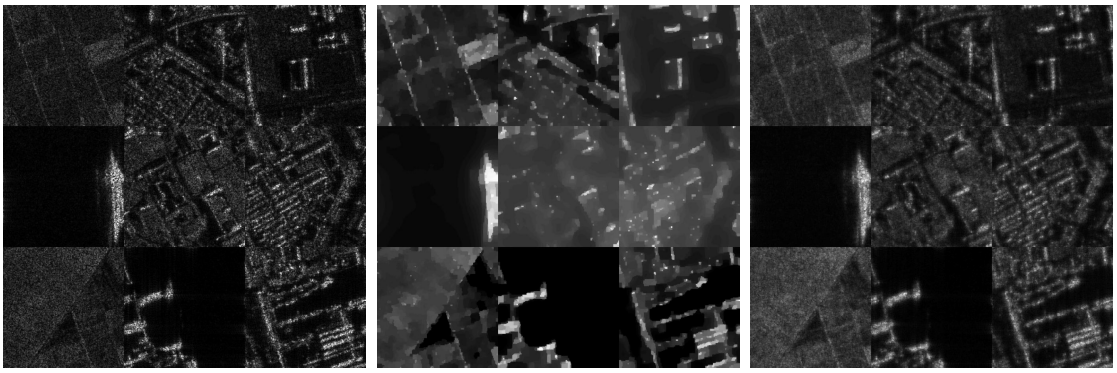

(a) FFT-based (b) NQR-based (c) DL-based

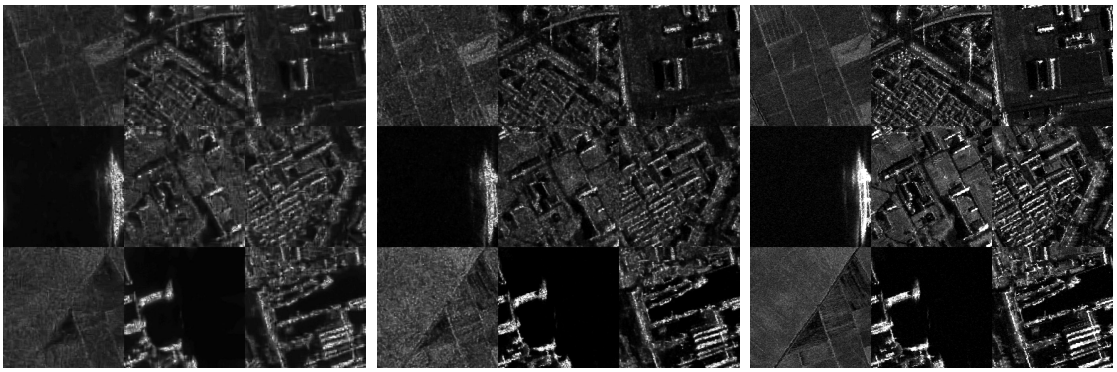

(d) PnP-BM3D (e) PnP-CNN-SAR (f) Ground Truth

Figure A.17 Reconstruction results for Images 3, 4, 10, 17, 18, 19, 25, 28, and 30 from the Wonsan test set for the case of 100% data availability and $\sigma_{\mathbf{n}} = 0.1\sigma_{\mathbf{y}}$.

Table A.18 SNR and SSIM values for images from the Wonsan Test Set for the case of 30% data availability and $\sigma_{\mathbf{n}} = 0.1\sigma_{\mathbf{y}}$. Best results are shown in bold, second best results are shown in red.

	SNR (dB)					SSIM				
	FFT-based	NQR-based	DL-based	PnP-BM3D	PnP-CNN-SAR	FFT-based	NQR-based	DL-based	PnP-BM3D	PnP-CNN-SAR
Image 1	4.58	5.75	5.05	**5.78**	5.75	0.489	0.372	0.440	0.431	**0.490**
Image 2	4.60	5.39	5.09	**5.76**	5.40	0.371	0.174	0.296	0.302	**0.405**
Image 3	4.86	6.55	6.37	**7.94**	5.95	0.291	0.327	0.253	**0.335**	0.268
Image 4	4.46	3.37	4.57	**5.10**	5.08	**0.416**	0.180	0.313	0.289	0.410
Image 5	4.41	4.13	4.81	**5.33**	5.14	0.366	0.166	0.272	0.247	**0.381**
Image 6	4.36	5.60	4.60	5.16	**5.71**	0.501	0.379	0.414	0.384	**0.502**
Image 7	4.39	**5.50**	4.52	4.92	5.25	0.416	0.349	0.313	0.279	**0.428**
Image 8	4.39	**5.61**	4.75	5.33	5.24	**0.410**	0.288	0.320	0.311	0.401
Image 9	4.27	4.16	4.76	**5.19**	5.15	0.400	0.173	0.314	0.328	**0.437**
Image 10	4.43	4.98	4.73	**5.81**	5.34	0.415	0.354	0.401	0.416	**0.467**
Image 11	4.61	**6.07**	5.25	6.03	5.49	0.338	0.199	0.278	0.270	**0.356**
Image 12	4.38	4.73	4.90	5.59	**6.18**	0.481	0.238	0.419	0.413	**0.512**
Image 13	4.87	**10.37**	6.43	7.64	6.15	0.257	**0.312**	0.242	0.264	0.257
Image 14	4.30	3.52	4.41	4.92	**4.97**	0.419	0.149	0.306	0.325	**0.443**
Image 15	4.56	**6.82**	5.34	6.18	5.66	0.345	0.273	0.285	0.265	**0.369**
Image 16	4.50	4.90	4.78	**5.43**	5.37	**0.372**	0.137	0.263	0.254	**0.372**
Image 17	4.91	**8.67**	5.75	6.89	5.88	0.607	0.605	0.637	**0.649**	0.585
Image 18	4.55	5.37	5.18	**5.92**	5.48	0.339	0.183	0.285	0.279	**0.371**
Image 19	4.44	3.51	4.44	**5.14**	5.11	0.404	0.183	0.304	0.310	**0.419**
Image 20	4.67	6.17	5.45	**6.29**	5.62	0.373	0.265	0.341	0.305	**0.388**
Image 21	4.68	**6.90**	5.77	6.52	5.67	0.324	0.166	0.281	0.241	**0.327**
Image 22	4.45	4.02	4.59	**5.22**	5.13	0.406	0.172	0.304	0.313	**0.420**
Image 23	4.67	**7.72**	5.87	6.64	5.80	0.284	0.181	0.252	0.234	**0.321**
Image 24	4.59	5.95	5.34	**6.26**	5.53	0.359	0.232	0.304	0.309	**0.387**
Image 25	4.90	**8.26**	6.44	8.02	6.13	0.246	**0.294**	0.211	0.285	0.222
Image 26	4.24	4.11	4.22	**5.19**	4.92	0.416	0.287	0.362	0.412	**0.474**
Image 27	4.61	5.82	5.19	**6.05**	5.37	0.349	0.208	0.290	0.274	**0.356**
Image 28	4.09	5.08	4.57	5.50	**6.50**	**0.666**	0.466	0.631	0.605	0.576
Image 29	4.76	**7.77**	5.99	7.10	6.17	0.322	0.265	0.321	0.297	**0.359**
Image 30	4.30	4.68	4.31	5.16	**5.34**	0.427	0.314	0.318	0.362	**0.495**
Image 31	4.69	5.60	5.94	**7.44**	5.91	0.408	**0.462**	0.385	0.443	0.403
Average	4.53	5.71	5.14	**5.98**	5.56	0.394	0.270	0.334	0.336	**0.406**

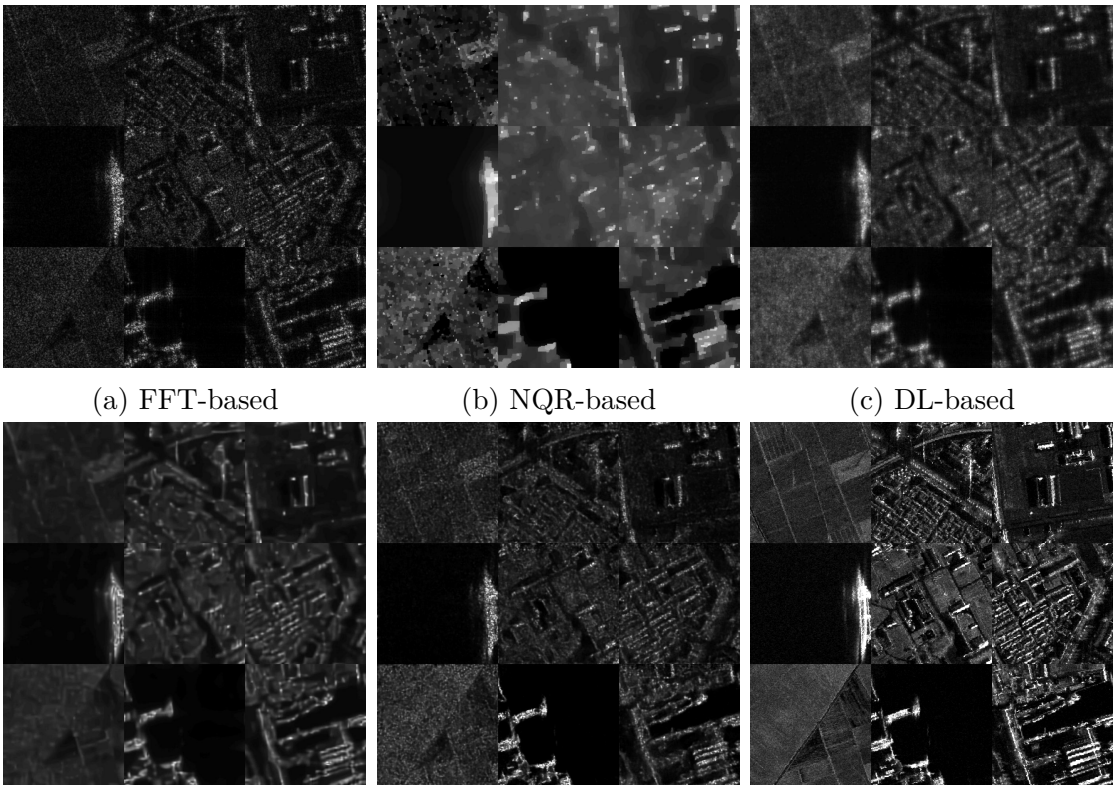

(a) FFT-based (b) NQR-based (c) DL-based

(d) PnP-BM3D (e) PnP-CNN-SAR (f) Ground Truth

Figure A.18 Reconstruction results for Images 3, 4, 10, 17, 18, 19, 25, 28, and 30 from the Wonsan test set for the case of 100% data availability and $\sigma_{\mathbf{n}} = 0.1\sigma_{\mathbf{y}}$.

A.2.7 Experiment 7: 100% Data Availability and $\sigma_{\mathbf{n}} = \sigma_{\mathbf{y}}$

Table A.19 shows the SNR and SSIM values for this experiment. PnP-CNN-SAR gives the best SNR and best SSIM for all 31 images. Fig. A.19 shows the reconstruction results for a selection of images from the Wonsan test set from all methods for this experiment. DL-based and PnP-CNN-SAR produce better reconstructions compared to other methods.

A.2.8 Experiment 8: 90% Data Availability and $\sigma_{\mathbf{n}} = \sigma_{\mathbf{y}}$

Table A.20 shows the SNR and SSIM values for this experiment. PnP-CNN-SAR gives the best SNR and best SSIM for all 31 images. Fig. A.20 shows the reconstruction results for a selection of images from the Wonsan test set from all methods for this experiment. PnP-CNN-SAR produce better reconstructions compared to other methods.

Table A.19 SNR and SSIM values for images from the Wonsan Test Set for the case of 100% data availability and $\sigma_{\mathbf{n}} = \sigma_{\mathbf{y}}$. Best results are shown in bold, second best results are shown in red.

	SNR (dB)					SSIM				
	FFT-based	NQR-based	DL-based	PnP-BM3D	PnP-CNN-SAR	FFT-based	NQR-based	DL-based	PnP-BM3D	PnP-CNN-SAR
Image 1	5.41	10.06	15.71	5.46	**39.11**	0.345	0.479	0.924	0.343	**0.997**
Image 2	6.48	9.31	15.65	6.59	**40.53**	0.500	0.535	0.925	0.504	**1.000**
Image 3	6.97	10.14	20.18	7.21	**33.66**	0.408	0.481	0.921	0.420	**0.997**
Image 4	6.49	8.61	14.28	6.61	**36.84**	0.578	0.582	0.924	0.582	**0.999**
Image 5	6.52	9.06	14.69	6.63	**37.93**	0.557	0.544	0.922	0.563	**0.999**
Image 6	5.37	9.12	14.76	5.49	**39.21**	0.395	0.552	0.917	0.401	**0.995**
Image 7	6.21	9.00	14.24	6.28	**38.49**	0.548	0.582	0.923	0.555	**0.999**
Image 8	6.26	7.45	14.82	6.33	**37.92**	0.522	0.459	0.925	0.526	**0.999**
Image 9	6.17	8.73	14.67	6.18	**35.93**	0.511	0.561	0.922	0.508	**0.997**
Image 10	6.54	10.86	14.85	6.68	**37.82**	0.415	0.556	0.931	0.420	**0.998**
Image 11	6.71	9.20	15.93	6.80	**36.95**	0.504	0.470	0.923	0.511	**0.999**
Image 12	5.42	9.68	15.33	5.60	**39.86**	0.373	0.540	0.922	0.379	**0.995**
Image 13	6.93	12.16	20.66	6.97	**32.68**	0.372	0.486	0.921	0.370	**0.995**
Image 14	5.98	8.57	14.14	6.03	**35.48**	0.526	0.577	0.921	0.530	**0.997**
Image 15	6.64	10.21	16.19	6.78	**38.05**	0.505	0.535	0.925	0.511	**0.999**
Image 16	6.46	9.00	14.89	6.54	**34.12**	0.558	0.563	0.920	0.565	**0.998**
Image 17	5.51	13.30	19.52	5.57	**35.60**	0.193	0.601	0.949	0.199	**0.994**
Image 18	6.61	9.11	16.00	6.63	**39.79**	0.486	0.456	0.924	0.485	**0.999**
Image 19	6.28	8.77	14.17	6.45	**37.46**	0.548	0.580	0.924	0.555	**0.999**
Image 20	6.70	10.09	16.26	6.89	**37.06**	0.495	0.524	0.928	0.508	**0.999**
Image 21	6.76	10.11	17.34	6.81	**36.62**	0.466	0.497	0.924	0.475	**0.999**
Image 22	6.42	8.68	14.40	6.43	**36.85**	0.537	0.556	0.923	0.540	**0.999**
Image 23	6.88	10.35	17.66	7.03	**33.88**	0.472	0.454	0.922	0.476	**0.998**
Image 24	6.54	10.14	16.53	6.63	**37.66**	0.458	0.539	0.928	0.464	**0.999**
Image 25	7.01	8.08	21.07	7.10	**31.47**	0.367	0.402	0.917	0.367	**0.993**
Image 26	6.04	9.95	14.06	6.15	**37.39**	0.418	0.569	0.926	0.417	**0.998**
Image 27	6.67	9.66	15.82	6.70	**37.46**	0.491	0.511	0.924	0.494	**0.999**
Image 28	4.74	11.68	15.28	4.67	**37.08**	0.206	0.721	0.922	0.208	**0.987**
Image 29	6.90	11.57	18.58	7.00	**38.68**	0.444	0.535	0.929	0.454	**0.999**
Image 30	5.68	8.23	14.40	5.74	**36.19**	0.464	0.526	0.916	0.464	**0.992**
Image 31	6.86	9.81	18.07	7.16	**33.57**	0.513	0.599	0.930	0.522	**0.997**
Average	6.33	9.70	16.13	6.42	**36.82**	0.457	0.535	0.924	0.462	**0.997**

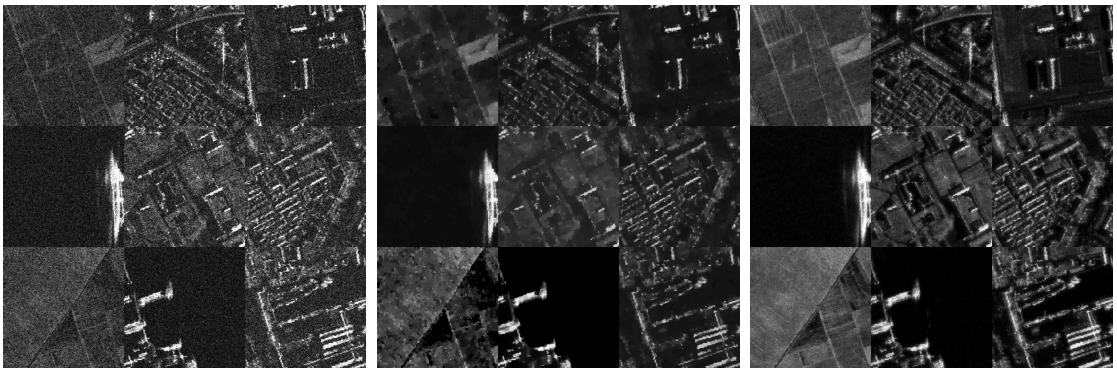

(a) FFT-based (b) NQR-based (c) DL-based

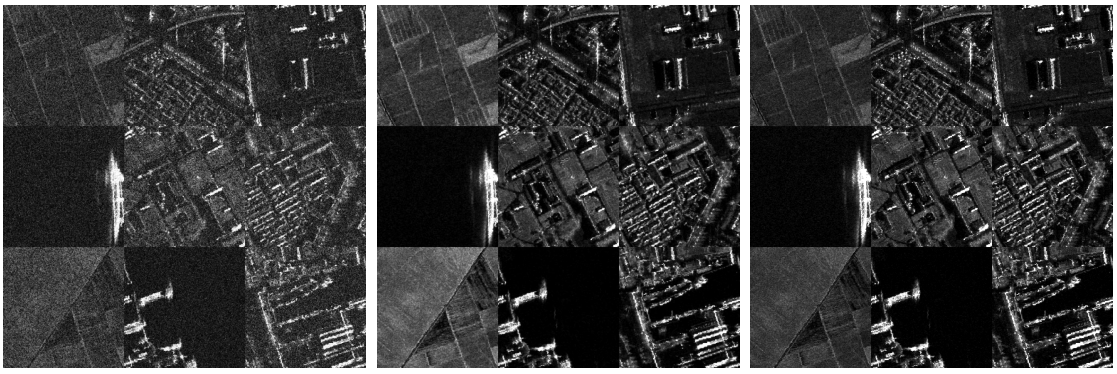

(d) PnP-BM3D (e) PnP-CNN-SAR (f) Ground Truth

Figure A.19 Reconstruction results for Images 3, 4, 10, 17, 18, 19, 25, 28, and 30 from the Wonsan test set for the case of 100% data availability and $\sigma_{\mathbf{n}} = \sigma_{\mathbf{y}}$.

Table A.20 SNR and SSIM values for images from the Wonsan Test Set for the case of 90% data availability and $\sigma_{\mathbf{n}} = \sigma_{\mathbf{y}}$. Best results are shown in bold, second best results are shown in red.

	SNR (dB)					SSIM				
	FFT-based	NQR-based	DL-based	PnP-BM3D	PnP-CNN-SAR	FFT-based	NQR-based	DL-based	PnP-BM3D	PnP-CNN-SAR
Image 1	5.23	9.27	7.59	4.97	**17.27**	0.317	0.486	0.387	0.309	**0.854**
Image 2	6.19	6.88	8.78	6.12	**15.93**	0.457	0.319	0.572	0.447	**0.891**
Image 3	7.03	7.55	12.23	7.65	**15.43**	0.377	0.452	0.556	0.391	**0.798**
Image 4	6.21	8.20	7.97	6.25	**14.06**	0.535	0.530	0.600	0.537	**0.872**
Image 5	6.40	8.00	8.42	6.31	**15.24**	0.524	0.454	0.600	0.512	**0.901**
Image 6	5.18	8.47	7.25	5.02	**17.84**	0.372	0.543	0.445	0.363	**0.882**
Image 7	6.15	7.77	7.71	5.99	**13.95**	0.519	0.496	0.578	0.511	**0.869**
Image 8	6.01	8.26	8.03	5.96	**14.08**	0.483	0.512	0.563	0.478	**0.859**
Image 9	5.85	7.93	7.76	5.49	**14.29**	0.472	0.499	0.542	0.449	**0.861**
Image 10	6.30	9.66	8.28	6.27	**16.88**	0.385	0.518	0.546	0.391	**0.874**
Image 11	6.48	8.93	9.34	6.55	**15.39**	0.459	0.458	0.587	0.461	**0.870**
Image 12	5.28	8.87	7.55	5.13	**17.12**	0.350	0.538	0.432	0.347	**0.873**
Image 13	6.82	11.91	11.90	7.16	**16.32**	0.327	0.383	0.524	0.337	**0.806**
Image 14	5.78	7.74	7.34	5.40	**15.13**	0.500	0.515	0.545	0.472	**0.887**
Image 15	6.61	8.75	9.51	6.67	**15.66**	0.468	0.432	0.595	0.469	**0.879**
Image 16	6.30	7.90	8.46	6.18	**14.74**	0.520	0.467	0.591	0.509	**0.881**
Image 17	5.40	12.87	9.17	5.07	**14.39**	0.187	0.610	0.405	0.193	**0.705**
Image 18	6.41	7.50	8.91	6.25	**16.31**	0.443	0.333	0.563	0.429	**0.873**
Image 19	6.07	7.94	7.57	5.97	**15.34**	0.515	0.515	0.574	0.501	**0.892**
Image 20	6.58	9.62	9.73	6.73	**15.13**	0.460	0.484	0.615	0.463	**0.875**
Image 21	6.60	10.11	10.22	6.77	**15.60**	0.424	0.461	0.577	0.423	**0.860**
Image 22	6.05	7.42	7.80	5.83	**15.01**	0.497	0.469	0.565	0.483	**0.883**
Image 23	6.81	10.21	10.71	6.94	**15.60**	0.425	0.443	0.587	0.427	**0.854**
Image 24	6.42	9.56	9.46	6.28	**16.15**	0.424	0.485	0.557	0.412	**0.872**
Image 25	6.98	11.86	12.35	7.51	**16.31**	0.329	0.368	0.505	0.336	**0.787**
Image 26	5.82	9.50	7.13	4.75	**17.03**	0.393	0.552	0.481	0.360	**0.850**
Image 27	6.48	8.87	9.30	6.49	**15.67**	0.450	0.442	0.579	0.444	**0.873**
Image 28	4.38	11.17	6.34	4.13	**21.56**	0.191	0.721	0.275	0.196	**0.836**
Image 29	6.80	10.91	11.16	7.16	**16.27**	0.405	0.481	0.607	0.414	**0.860**
Image 30	5.42	8.69	7.01	4.93	**16.03**	0.434	0.605	0.482	0.412	**0.851**
Image 31	6.83	9.40	10.87	7.04	**15.50**	0.476	0.507	0.636	0.483	**0.848**
Average	6.16	9.09	8.90	6.10	**15.85**	0.423	0.486	0.538	0.418	**0.857**

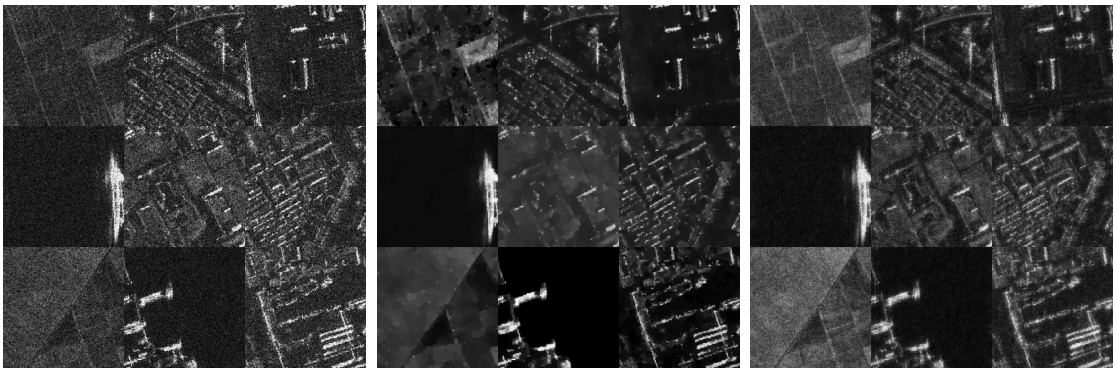

(a) FFT-based (b) NQR-based (c) DL-based

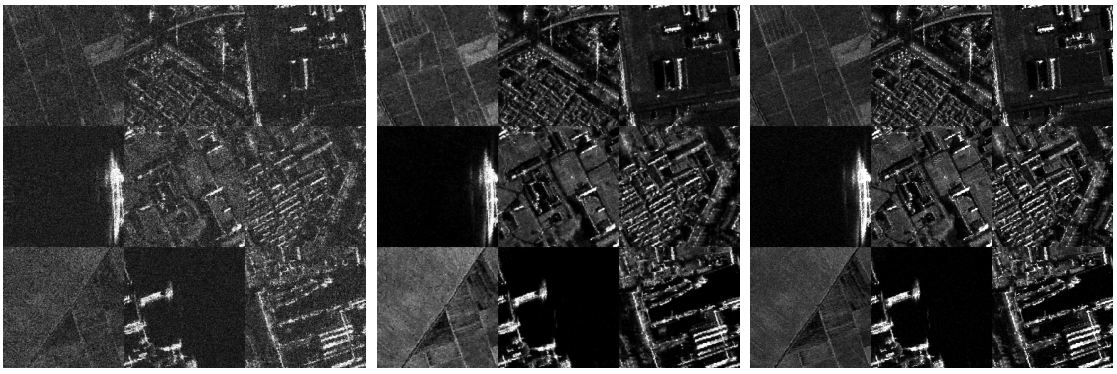

(d) PnP-BM3D (e) PnP-CNN-SAR (f) Ground Truth

Figure A.20 Reconstruction results for Images 3, 4, 10, 17, 18, 19, 25, 28, and 30 from the Wonsan test set for the case of 90% data availability and $\sigma_{\mathbf{n}} = \sigma_{\mathbf{y}}$.

A.2.9 Experiment 9: 80% Data Availability and $\sigma_{\mathbf{n}} = \sigma_{\mathbf{y}}$

Table A.21 shows the SNR and SSIM values for this experiment. PnP-CNN-SAR gives the best SNR and best SSIM for all 31 images. Fig. A.21 shows the reconstruction results for a selection of images from the Wonsan test set from all methods for this experiment. PnP-CNN-SAR produce better reconstructions compared to other methods.

Table A.21 SNR and SSIM values for images from the Wonsan Test Set for the case of 80% data availability and $\sigma_{\mathbf{n}} = \sigma_{\mathbf{y}}$. Best results are shown in bold, second best results are shown in red.

	SNR (dB)					SSIM				
	FFT-based	NQR-based	DL-based	PnP-BM3D	PnP-CNN-SAR	FFT-based	NQR-based	DL-based	PnP-BM3D	PnP-CNN-SAR
Image 1	5.07	7.78	6.94	4.99	**12.73**	0.290	0.522	0.351	0.293	**0.789**
Image 2	6.08	8.01	7.86	6.31	**12.85**	0.425	0.406	0.493	0.433	**0.826**
Image 3	7.04	9.29	11.76	7.83	**12.45**	0.343	0.430	0.486	0.375	**0.653**
Image 4	5.95	6.84	6.92	6.07	**12.10**	0.491	0.426	0.510	0.501	**0.842**
Image 5	6.13	6.79	7.42	6.29	**12.41**	0.476	0.356	0.510	0.491	**0.834**
Image 6	5.04	6.23	6.32	5.04	**12.49**	0.343	0.460	0.389	0.348	**0.825**
Image 7	5.80	7.17	6.80	5.89	**12.44**	0.472	0.441	0.496	0.481	**0.855**
Image 8	5.93	7.22	7.14	5.92	**12.19**	0.450	0.434	0.491	0.455	**0.830**
Image 9	5.71	6.57	6.82	5.68	**12.77**	0.436	0.404	0.465	0.437	**0.828**
Image 10	6.10	7.76	7.35	6.37	**12.29**	0.369	0.430	0.510	0.389	**0.782**
Image 11	6.48	7.98	8.44	6.58	**12.41**	0.425	0.380	0.505	0.433	**0.784**
Image 12	5.19	7.50	6.75	5.22	**12.68**	0.325	0.407	0.385	0.330	**0.822**
Image 13	6.93	11.67	11.48	7.14	**13.01**	0.300	0.358	0.461	0.304	**0.655**
Image 14	5.48	6.75	6.21	5.54	**12.40**	0.456	0.435	0.454	0.457	**0.829**
Image 15	6.37	8.37	8.60	6.58	**12.22**	0.427	0.381	0.514	0.437	**0.787**
Image 16	6.18	7.44	7.45	6.18	**12.35**	0.481	0.406	0.494	0.478	**0.822**
Image 17	5.19	10.91	8.61	5.28	**12.78**	0.192	0.337	0.414	0.206	**0.716**
Image 18	6.20	7.25	8.21	6.47	**12.50**	0.402	0.285	0.493	0.415	**0.781**
Image 19	5.81	7.21	6.59	5.90	**12.76**	0.468	0.451	0.491	0.476	**0.836**
Image 20	6.42	8.56	8.78	6.70	**11.93**	0.424	0.418	0.535	0.437	**0.782**
Image 21	6.47	8.16	9.51	6.72	**12.61**	0.381	0.245	0.498	0.392	**0.760**
Image 22	5.91	6.26	6.74	5.90	**12.79**	0.466	0.390	0.480	0.464	**0.844**
Image 23	6.75	8.16	9.90	6.97	**12.44**	0.382	0.252	0.500	0.397	**0.735**
Image 24	6.26	8.43	8.67	6.47	**12.75**	0.387	0.406	0.491	0.396	**0.776**
Image 25	6.98	10.92	11.97	7.53	**12.48**	0.296	0.382	0.433	0.310	**0.593**
Image 26	5.56	7.12	6.03	5.29	**11.99**	0.371	0.451	0.429	0.362	**0.766**
Image 27	6.36	7.92	8.43	6.57	**12.48**	0.415	0.372	0.500	0.423	**0.779**
Image 28	4.21	9.47	5.78	4.24	**13.29**	0.185	0.667	0.270	0.197	**0.790**
Image 29	6.79	9.80	10.41	7.18	**12.60**	0.376	0.393	0.529	0.392	**0.733**
Image 30	5.16	7.57	6.13	5.21	**13.27**	0.397	0.435	0.419	0.403	**0.813**
Image 31	6.71	8.89	10.21	7.39	**12.56**	0.443	0.511	0.574	0.476	**0.750**
Average	6.01	8.07	8.07	6.18	**12.55**	0.390	0.409	0.470	0.400	**0.781**

A.2.10 Experiment 10: 70% Data Availability and $\sigma_{\mathbf{n}} = \sigma_{\mathbf{y}}$

Table A.22 shows the SNR and SSIM values for this experiment. PnP-CNN-SAR gives the best SNR for 28 images, and best SSIM for all 31 images. Fig. A.22 shows the reconstruction results for a selection of images from the Wonsan test set from all methods for this experiment. PnP-CNN-SAR produce better reconstructions compared to other methods.

A.2.11 Experiment 11: 50% Data Availability and $\sigma_{\mathbf{n}} = \sigma_{\mathbf{y}}$

Table A.23 shows the SNR and SSIM values for this experiment. PnP-CNN-SAR gives the best SNR for 24 images, and best SSIM for 27 images. Fig. A.23 shows the reconstruction results for a selection of images from the Wonsan test set from all methods for this experiment. PnP-CNN-SAR produce better reconstructions compared to other methods.

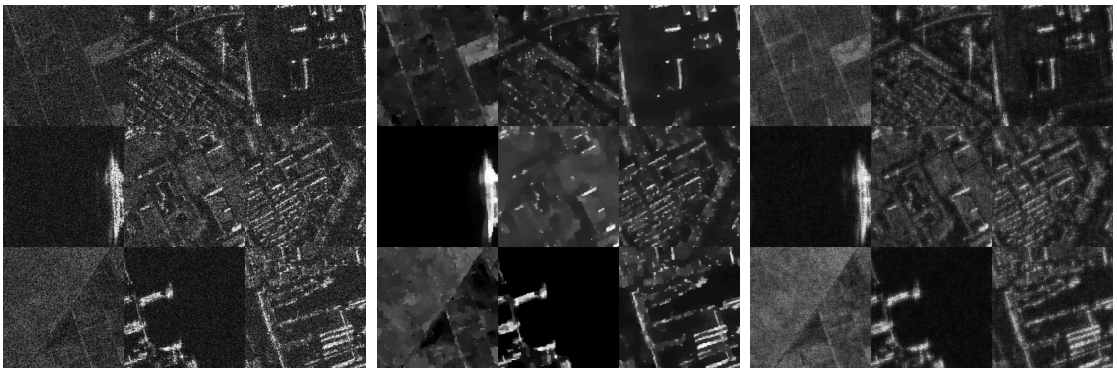

(a) FFT-based (b) NQR-based (c) DL-based

(d) PnP-BM3D (e) PnP-CNN-SAR (f) Ground Truth

Figure A.21 Reconstruction results for Images 3, 4, 10, 17, 18, 19, 25, 28, and 30 from the Wonsan test set for the case of 80% data availability and $\sigma_{\mathbf{n}} = \sigma_{\mathbf{y}}$.

Table A.22 SNR and SSIM values for images from the Wonsan Test Set for the case of 70% data availability and $\sigma_{\mathbf{n}} = \sigma_{\mathbf{y}}$. Best results are shown in bold, second best results are shown in red.

	SNR (dB)					SSIM				
	FFT-based	NQR-based	DL-based	PnP-BM3D	PnP-CNN-SAR	FFT-based	NQR-based	DL-based	PnP-BM3D	PnP-CNN-SAR
Image 1	4.93	7.48	6.44	4.97	**9.93**	0.272	0.521	0.320	0.280	**0.707**
Image 2	5.96	6.73	7.30	6.23	**10.47**	0.397	0.251	0.435	0.411	**0.740**
Image 3	6.94	8.58	**11.12**	8.35	10.72	0.317	0.414	0.419	0.358	**0.530**
Image 4	5.77	6.29	6.41	5.93	**9.96**	0.463	0.380	0.449	0.465	**0.764**
Image 5	5.96	6.44	6.83	6.19	**10.21**	0.439	0.317	0.433	0.454	**0.745**
Image 6	4.79	6.24	5.91	4.84	**9.83**	0.317	0.389	0.357	0.328	**0.756**
Image 7	5.63	6.10	6.35	5.75	**9.79**	0.445	0.370	0.444	0.453	**0.764**
Image 8	5.66	6.02	6.66	5.81	**9.96**	0.416	0.358	0.433	0.424	**0.746**
Image 9	5.50	6.22	6.31	5.67	**10.20**	0.405	0.322	0.413	0.412	**0.744**
Image 10	5.86	6.74	6.66	5.99	**10.38**	0.345	0.407	0.473	0.388	**0.716**
Image 11	6.31	5.08	7.85	6.72	**10.39**	0.399	0.233	0.437	0.408	**0.684**
Image 12	5.01	6.52	6.29	5.08	**10.37**	0.302	0.464	0.354	0.316	**0.745**
Image 13	6.68	**11.45**	11.00	7.49	11.16	0.262	0.281	0.395	0.285	**0.522**
Image 14	5.31	5.68	5.80	5.45	**10.16**	0.425	0.353	0.403	0.426	**0.762**
Image 15	6.20	7.65	7.95	6.74	**10.13**	0.393	0.330	0.442	0.416	**0.690**
Image 16	5.89	6.38	6.94	6.19	**10.11**	0.433	0.290	0.424	0.451	**0.727**
Image 17	4.90	10.18	8.29	5.06	**10.58**	0.188	0.345	0.447	0.232	**0.647**
Image 18	6.12	4.89	7.61	6.48	**10.46**	0.378	0.224	0.437	0.392	**0.687**
Image 19	5.64	6.29	6.11	5.73	**10.25**	0.437	0.387	0.429	0.441	**0.761**
Image 20	6.27	7.19	8.20	6.80	**10.20**	0.392	0.298	0.478	0.418	**0.693**
Image 21	6.37	8.08	8.90	6.84	**10.61**	0.348	0.229	0.426	0.366	**0.651**
Image 22	5.62	5.51	6.25	5.77	**10.03**	0.429	0.332	0.424	0.432	**0.767**
Image 23	6.65	7.04	9.31	7.15	**10.45**	0.350	0.209	0.426	0.366	**0.617**
Image 24	6.16	7.32	8.04	6.45	**10.80**	0.357	0.260	0.432	0.368	**0.684**
Image 25	6.89	10.50	**11.50**	8.19	10.99	0.267	0.370	0.376	0.300	**0.469**
Image 26	5.29	6.12	5.59	5.40	**9.84**	0.346	0.414	0.398	0.359	**0.703**
Image 27	6.23	7.80	7.74	6.59	**10.36**	0.385	0.341	0.434	0.395	**0.675**
Image 28	4.15	7.92	5.30	3.95	**10.36**	0.180	0.651	0.276	0.201	**0.731**
Image 29	6.70	9.97	9.85	7.57	**10.81**	0.343	0.374	0.478	0.374	**0.640**
Image 30	5.04	6.19	5.69	5.13	**10.14**	0.371	0.395	0.375	0.380	**0.754**
Image 31	6.59	8.21	9.70	7.53	**10.76**	0.423	0.508	0.526	0.457	**0.653**
Average	5.84	7.19	7.54	6.19	**10.34**	0.362	0.355	0.419	0.379	**0.693**

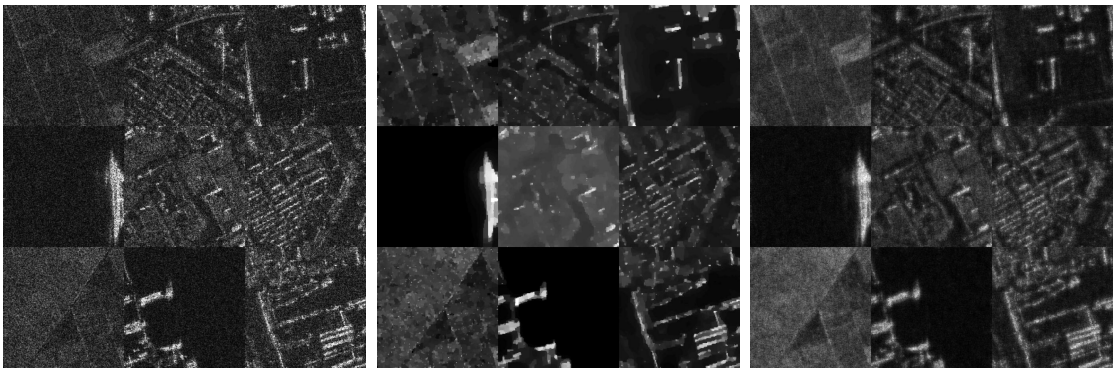

(a) FFT-based (b) NQR-based (c) DL-based

(d) PnP-BM3D (e) PnP-CNN-SAR (f) Ground Truth

Figure A.22 Reconstruction results for Images 3, 4, 10, 17, 18, 19, 25, 28, and 30 from the Wonsan test set for the case of 70% data availability and $\sigma_{\mathbf{n}} = \sigma_{\mathbf{y}}$.

Table A.23 SNR and SSIM values for images from the Wonsan Test Set for the case of 50% data availability and $\sigma_{\mathbf{n}} = \sigma_{\mathbf{y}}$. Best results are shown in bold, second best results are shown in red.

	SNR (dB)					SSIM				
	FFT-based	NQR-based	DL-based	PnP-BM3D	PnP-CNN-SAR	FFT-based	NQR-based	DL-based	PnP-BM3D	PnP-CNN-SAR
Image 1	4.59	6.24	5.57	4.71	**8.08**	0.232	0.287	0.276	0.255	**0.606**
Image 2	5.53	5.14	6.32	6.00	**8.26**	0.339	0.201	0.333	0.346	**0.606**
Image 3	6.50	8.83	9.39	**9.51**	9.28	0.274	**0.380**	0.309	0.338	0.375
Image 4	5.29	5.68	5.57	5.49	**7.74**	0.395	0.333	0.344	0.383	**0.642**
Image 5	5.48	4.09	5.86	5.89	**7.85**	0.379	0.188	0.315	0.359	**0.598**
Image 6	4.59	5.29	5.10	4.37	**7.67**	0.288	0.268	0.300	0.283	**0.648**
Image 7	5.14	5.82	5.41	5.17	**7.75**	0.378	0.346	0.333	0.356	**0.647**
Image 8	5.19	5.98	5.74	5.39	**7.88**	0.358	0.333	0.335	0.345	**0.637**
Image 9	5.06	5.20	5.42	5.35	**8.02**	0.349	0.245	0.317	0.354	**0.659**
Image 10	5.36	5.83	5.76	5.73	**8.13**	0.334	0.386	0.425	0.380	**0.611**
Image 11	5.69	6.13	6.78	6.67	**8.26**	0.329	0.236	0.321	0.348	**0.543**
Image 12	4.69	5.99	5.59	4.66	**8.11**	0.262	0.379	0.310	0.282	**0.629**
Image 13	6.37	**11.19**	9.27	8.44	9.70	0.224	0.275	0.293	0.264	**0.378**
Image 14	4.89	5.34	5.00	4.99	**7.85**	0.356	0.318	0.302	0.354	**0.680**
Image 15	5.85	6.66	6.88	6.73	**8.41**	0.343	0.243	0.332	0.340	**0.553**
Image 16	5.45	5.65	5.97	5.92	**7.92**	0.366	0.192	0.299	0.360	**0.599**
Image 17	4.72	**9.07**	7.27	4.59	8.66	0.228	0.335	0.490	0.297	**0.704**
Image 18	5.66	6.50	6.62	6.52	**8.47**	0.318	0.226	0.328	0.329	**0.551**
Image 19	5.17	4.82	5.25	5.42	**7.91**	0.368	0.239	0.323	0.369	**0.650**
Image 20	5.77	7.42	7.07	6.83	**8.10**	0.344	0.351	0.390	0.364	**0.556**
Image 21	5.97	7.00	7.74	7.19	**8.71**	0.301	0.249	0.319	0.321	**0.504**
Image 22	5.19	5.87	5.38	5.40	**7.90**	0.374	0.328	0.317	0.363	**0.656**
Image 23	6.17	8.53	7.97	7.72	**8.60**	0.288	0.243	0.305	0.328	**0.463**
Image 24	5.67	6.20	7.01	6.53	**8.42**	0.302	0.214	0.339	0.340	**0.561**
Image 25	6.54	**9.95**	9.72	9.56	9.54	0.233	**0.320**	0.266	0.280	0.317
Image 26	4.81	**5.16**	4.90	4.93	2.99	0.309	0.350	**0.355**	0.343	0.254
Image 27	5.73	6.53	6.75	6.62	**8.28**	0.318	0.224	0.332	0.339	**0.529**
Image 28	3.98	**6.94**	4.77	3.48	6.68	0.178	**0.647**	0.294	0.215	0.604
Image 29	6.12	7.93	8.38	8.27	**8.87**	0.288	0.261	0.381	0.346	**0.504**
Image 30	4.66	4.71	4.92	4.77	**7.85**	0.318	0.235	0.288	0.324	**0.650**
Image 31	6.21	**9.07**	8.30	7.85	9.03	0.390	0.493	0.440	0.448	**0.518**
Average	5.42	6.60	6.51	6.15	**8.09**	0.315	0.301	0.333	0.334	**0.562**

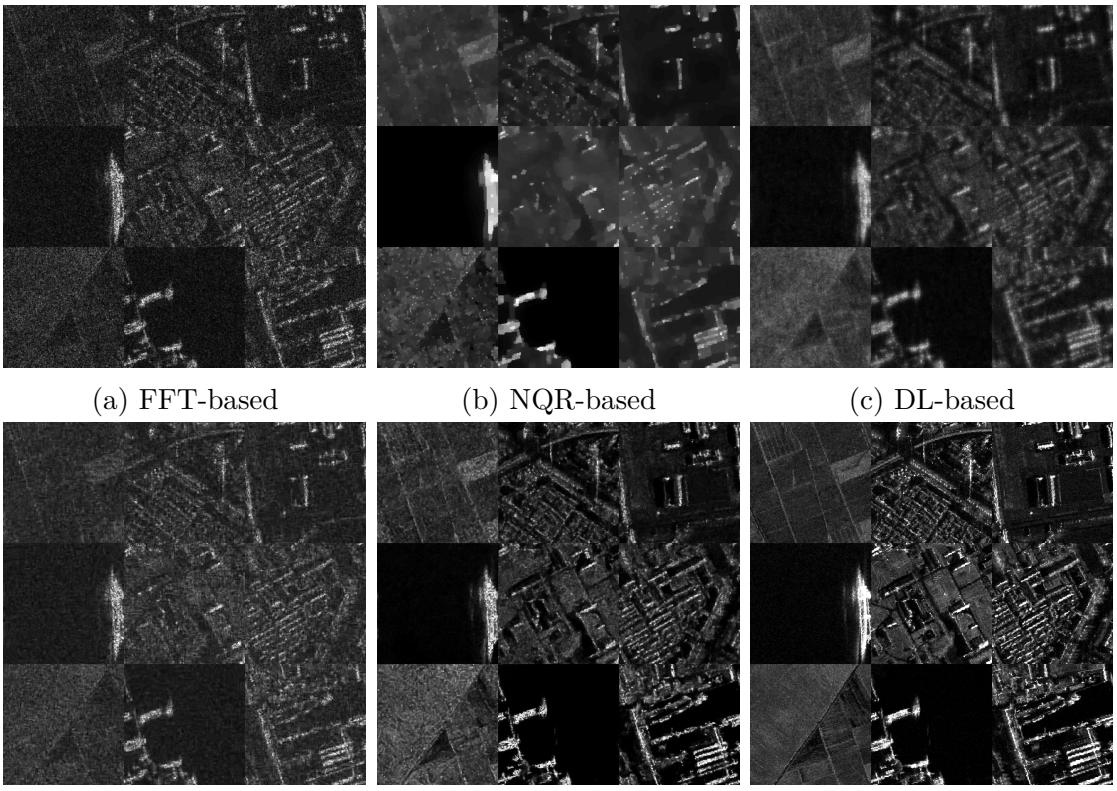

(a) FFT-based (b) NQR-based (c) DL-based

(d) PnP-BM3D (e) PnP-CNN-SAR (f) Ground Truth

Figure A.23 Reconstruction results for Images 3, 4, 10, 17, 18, 19, 25, 28, and 30 from the Wonsan test set for the case of 50% data availability and $\sigma_{\mathbf{n}} = \sigma_{\mathbf{y}}$.

A.2.12 Experiment 12: 30% Data Availability and $\sigma_{\mathbf{n}} = \sigma_{\mathbf{y}}$

Table A.24 shows the SNR and SSIM values for this experiment. PnP-CNN-SAR gives the best SNR for 14 images, and best SSIM for 25 images. Fig. A.24 shows the reconstruction results for a selection of images from the Wonsan test set from all methods for this experiment. PnP-CNN-SAR produce better reconstructions compared to other methods.

A.3 Different Scene Experiments

A.3.1 Experiment 1: 100% Data Availability and $\sigma_{\mathbf{n}} = 0.1\sigma_{\mathbf{y}}$

Table A.25 shows the SNR and SSIM values for this experiment. PnP-CNN-SAR gives the best SNR and best SSIM for all 110 images. Fig. A.25 shows the reconstruction results for a selection of images from the Kapıkule test set from all methods for this experiment. All methods produce good reconstructions.

Table A.24 SNR and SSIM values for images from the Wonsan Test Set for the case of 30% data availability and $\sigma_{\mathbf{n}} = \sigma_{\mathbf{y}}$. Best results are shown in bold, second best results are shown in red.

	SNR (dB)					SSIM				
	FFT-based	NQR-based	DL-based	PnP-BM3D	PnP-CNN-SAR	FFT-based	NQR-based	DL-based	PnP-BM3D	PnP-CNN-SAR
Image 1	4.04	5.32	4.55	4.70	**5.61**	0.203	0.307	0.245	0.232	**0.410**
Image 2	4.60	5.73	4.94	5.66	**5.94**	0.269	0.199	0.231	0.264	**0.368**
Image 3	5.51	7.28	6.99	**9.30**	7.12	0.249	0.313	0.230	**0.338**	0.261
Image 4	4.32	5.32	4.36	4.98	**5.34**	0.311	0.295	0.249	0.261	**0.373**
Image 5	4.49	4.31	4.67	5.35	**5.60**	0.291	0.144	0.208	0.239	**0.359**
Image 6	3.86	**5.27**	4.21	4.28	4.32	0.248	0.334	0.261	0.241	**0.374**
Image 7	4.30	5.08	4.31	4.81	**5.10**	0.307	0.291	0.246	0.252	**0.352**
Image 8	4.32	5.33	4.57	5.09	**5.34**	0.287	0.291	0.249	0.267	**0.359**
Image 9	4.30	4.61	4.38	4.87	**5.43**	0.281	0.273	0.233	0.255	**0.382**
Image 10	4.47	**5.69**	4.54	5.56	5.57	0.310	0.379	0.368	0.379	**0.451**
Image 11	4.85	**6.82**	5.29	6.23	6.19	0.269	0.275	0.226	0.259	**0.334**
Image 12	4.13	**5.17**	4.40	4.66	4.83	0.238	**0.389**	0.265	0.248	0.374
Image 13	5.33	**9.98**	7.02	8.30	7.22	0.187	0.237	0.210	**0.252**	0.246
Image 14	4.08	4.93	4.04	4.56	**5.17**	0.284	0.281	0.216	0.259	**0.391**
Image 15	4.83	**6.47**	5.29	6.33	6.10	0.274	0.207	0.233	0.257	**0.328**
Image 16	4.48	5.31	4.75	5.40	**5.67**	0.277	0.175	0.200	0.232	**0.336**
Image 17	4.24	**8.94**	5.62	5.21	6.86	0.297	0.360	0.538	0.419	**0.580**
Image 18	4.74	5.42	5.13	**6.02**	5.93	0.259	0.162	0.230	0.256	**0.322**
Image 19	4.33	5.00	4.23	5.00	**5.29**	0.295	0.280	0.228	0.265	**0.374**
Image 20	4.83	**6.70**	5.48	6.53	6.38	0.292	0.292	0.298	0.296	**0.368**
Image 21	4.99	**7.33**	5.85	6.71	6.32	0.232	0.187	0.216	0.235	**0.304**
Image 22	4.31	5.09	4.26	4.98	**5.22**	0.295	0.278	0.227	0.269	**0.377**
Image 23	5.21	6.84	6.07	**7.15**	6.72	0.236	0.162	0.203	0.229	**0.292**
Image 24	4.87	**6.58**	5.31	6.15	6.01	0.252	0.225	0.249	0.267	**0.355**
Image 25	5.56	7.85	7.17	**9.15**	7.25	0.201	0.263	0.188	**0.281**	0.194
Image 26	4.09	4.61	3.91	4.63	**5.17**	0.276	0.323	0.304	0.327	**0.431**
Image 27	4.84	**6.32**	5.31	6.25	6.03	0.267	0.211	0.236	0.256	**0.341**
Image 28	3.47	5.64	3.76	3.72	**5.76**	0.211	**0.608**	0.326	0.246	0.519
Image 29	5.27	**8.93**	6.38	7.84	7.29	0.248	0.321	0.292	0.298	**0.335**
Image 30	4.00	4.53	3.97	4.54	**5.07**	0.264	0.286	0.225	0.264	**0.370**
Image 31	5.09	7.87	6.28	**8.12**	6.65	0.352	**0.462**	0.369	0.440	0.389
Average	4.57	**6.14**	5.06	5.87	5.89	0.267	0.284	0.258	0.277	**0.363**

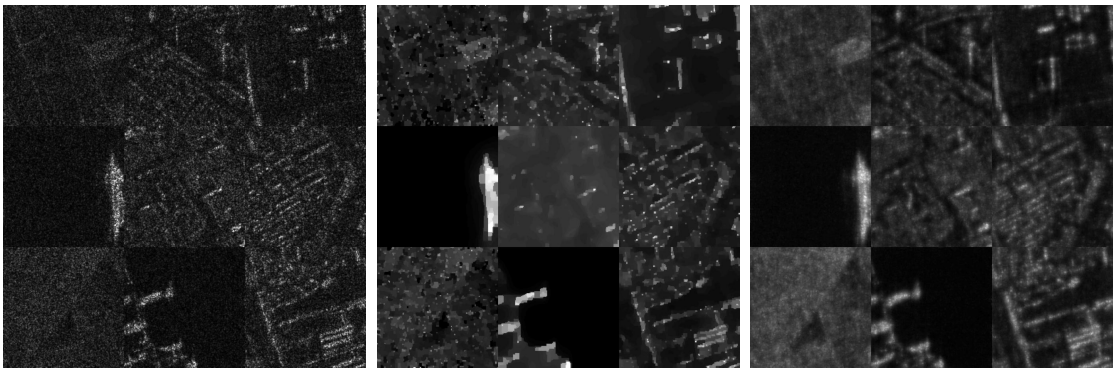

(a) FFT-based (b) NQR-based (c) DL-based

(d) PnP-BM3D (e) PnP-CNN-SAR (f) Ground Truth

Figure A.24 Reconstruction results for Images 3, 4, 10, 17, 18, 19, 25, 28, and 30 from the Wonsan test set for the case of 30% data availability and $\sigma_{\mathbf{n}} = \sigma_{\mathbf{y}}$.

Table A.25 SNR and SSIM values for images from the Kapıkule Test Set for the case of 100% data availability and $\sigma_{\mathbf{n}} = 0.1\sigma_{\mathbf{y}}$. Best results are shown in bold, second best results are shown in red.

	SNR (dB)					SSIM				
	FFT-based	NQR-based	DL-based	PnP-BM3D	PnP-CNN-SAR	FFT-based	NQR-based	DL-based	PnP-BM3D	PnP-CNN-SAR

Table A.25 continued from previous page

	SNR (dB)					SSIM				
Image 1	26.72	10.46	25.45	26.56	**38.87**	0.991	0.823	0.982	0.984	**0.999**
Image 2	26.46	26.22	24.76	26.61	**36.84**	0.987	0.973	0.978	0.974	**0.996**
Image 3	26.69	14.24	25.84	26.69	**34.78**	0.993	0.917	0.985	0.987	**0.998**
Image 4	26.69	26.34	24.16	26.72	**37.22**	0.992	0.985	0.984	0.985	**0.999**
Image 5	26.62	23.93	22.61	26.58	**39.61**	0.987	0.974	0.977	0.973	**0.998**
Image 6	26.68	18.46	26.26	26.67	**39.05**	0.991	0.941	0.983	0.983	**0.999**
Image 7	26.81	25.18	24.43	26.71	**37.30**	0.989	0.979	0.982	0.979	**0.999**
Image 8	26.63	25.45	23.84	26.73	**39.35**	0.991	0.982	0.984	0.983	**0.999**
Image 9	26.68	25.23	22.91	26.65	**39.87**	0.987	0.976	0.977	0.975	**0.997**
Image 10	26.69	26.61	25.08	26.65	**41.54**	0.986	0.974	0.979	0.973	**0.997**
Image 11	26.67	26.44	25.91	26.66	**39.57**	0.990	0.981	0.982	0.981	**0.999**
Image 12	26.68	24.97	21.11	26.75	**38.48**	0.989	0.979	0.978	0.979	**0.998**
Image 13	26.47	26.49	24.30	26.45	**39.95**	0.983	0.967	0.975	0.967	**0.996**
Image 14	26.77	25.98	24.93	26.65	**37.79**	0.991	0.982	0.983	0.982	**0.999**
Image 15	26.68	25.99	25.27	26.69	**36.78**	0.993	0.987	0.986	0.987	**0.999**
Image 16	26.16	25.31	21.18	26.22	**39.01**	0.963	0.937	0.955	0.934	**0.993**
Image 17	26.78	12.41	26.30	26.64	**36.99**	0.991	0.902	0.983	0.985	**0.998**
Image 18	26.71	26.53	25.33	26.70	**36.79**	0.993	0.986	0.985	0.986	**0.999**
Image 19	26.66	25.79	23.87	26.72	**39.39**	0.994	0.988	0.986	0.989	**0.999**
Image 20	26.61	25.67	22.84	26.68	**37.68**	0.991	0.982	0.983	0.982	**0.998**
Image 21	26.47	18.22	24.73	26.47	**38.78**	0.983	0.956	0.974	0.971	**0.997**
Image 22	26.43	26.16	24.45	26.46	**39.77**	0.978	0.960	0.970	0.959	**0.996**
Image 23	26.58	23.45	25.47	26.65	**41.90**	0.989	0.977	0.981	0.981	**0.999**
Image 24	26.69	26.70	24.78	26.75	**36.22**	0.993	0.987	0.986	0.987	**0.999**
Image 25	26.75	12.56	27.02	26.66	**34.80**	0.990	0.900	0.981	0.982	**0.997**
Image 26	26.70	26.68	24.69	26.71	**40.17**	0.992	0.986	0.985	0.985	**0.999**
Image 27	26.64	20.15	25.80	26.68	**35.81**	0.993	0.980	0.985	0.987	**0.998**
Image 28	26.63	23.47	26.15	26.70	**36.99**	0.991	0.981	0.983	0.983	**0.998**
Image 29	26.69	26.58	24.69	26.59	**44.13**	0.992	0.985	0.983	0.984	**1.000**
Image 30	26.72	17.05	25.39	26.71	**39.42**	0.992	0.969	0.983	0.985	**0.999**
Image 31	26.65	26.64	25.12	26.73	**40.05**	0.995	0.989	0.986	0.989	**0.999**
Image 32	26.70	12.57	25.34	26.68	**36.69**	0.993	0.901	0.984	0.988	**0.999**
Image 33	26.51	16.85	25.40	26.55	**36.82**	0.985	0.954	0.976	0.974	**0.996**
Image 34	26.31	26.28	24.28	26.34	**40.94**	0.972	0.949	0.964	0.948	**0.996**
Image 35	26.69	20.67	25.32	26.62	**43.21**	0.993	0.980	0.985	0.987	**1.000**
Image 36	26.53	26.52	25.02	26.53	**39.51**	0.985	0.971	0.976	0.972	**0.998**
Image 37	26.77	13.17	25.57	26.70	**37.05**	0.993	0.912	0.984	0.987	**0.999**
Image 38	26.62	13.18	26.04	26.66	**36.24**	0.991	0.911	0.982	0.984	**0.998**
Image 39	26.70	10.07	25.61	26.76	**36.33**	0.992	0.877	0.983	0.987	**0.998**
Image 40	26.64	25.20	23.78	26.67	**37.94**	0.989	0.978	0.981	0.979	**0.999**
Image 41	26.61	26.39	25.53	26.68	**36.59**	0.992	0.984	0.985	0.984	**0.998**
Image 42	26.82	16.63	25.59	26.73	**38.63**	0.992	0.938	0.984	0.986	**0.999**
Image 43	26.40	23.49	24.88	26.39	**40.50**	0.976	0.951	0.969	0.956	**0.996**
Image 44	26.73	26.45	24.96	26.68	**36.94**	0.994	0.988	0.986	0.988	**0.999**
Image 45	26.61	25.75	22.87	26.72	**39.01**	0.992	0.983	0.983	0.984	**0.999**
Image 46	26.54	24.37	20.98	26.53	**39.67**	0.983	0.970	0.973	0.967	**0.996**
Image 47	26.75	26.47	24.68	26.68	**37.42**	0.994	0.988	0.986	0.988	**0.999**
Image 48	26.60	26.60	24.44	26.64	**40.76**	0.989	0.978	0.980	0.978	**0.998**
Image 49	26.72	19.72	26.93	26.65	**35.35**	0.991	0.974	0.983	0.982	**0.998**
Image 50	26.49	26.08	24.26	26.46	**39.68**	0.982	0.965	0.973	0.964	**0.996**
Image 51	26.69	26.11	23.78	26.65	**38.92**	0.993	0.986	0.985	0.986	**0.999**
Image 52	26.53	26.42	25.85	26.68	**35.85**	0.988	0.975	0.979	0.976	**0.995**
Image 53	26.67	25.86	22.79	26.73	**38.64**	0.991	0.982	0.983	0.982	**0.999**
Image 54	26.63	26.65	25.45	26.55	**37.02**	0.988	0.977	0.980	0.977	**0.997**
Image 55	26.61	26.63	26.06	26.64	**40.94**	0.989	0.980	0.982	0.979	**0.999**
Image 56	26.63	26.37	24.77	26.70	**39.96**	0.992	0.985	0.984	0.985	**0.999**
Image 57	26.70	26.26	23.52	26.68	**38.81**	0.993	0.986	0.985	0.986	**0.999**
Image 58	26.51	25.16	25.15	26.55	**40.82**	0.985	0.969	0.977	0.971	**0.998**
Image 59	26.35	26.32	24.56	26.32	**37.70**	0.976	0.955	0.968	0.955	**0.996**
Image 60	26.70	26.16	24.74	26.74	**38.12**	0.993	0.985	0.985	0.985	**0.999**
Image 61	26.57	25.61	23.44	26.58	**38.34**	0.990	0.980	0.982	0.980	**0.998**
Image 62	26.59	18.74	25.54	26.68	**39.29**	0.993	0.948	0.984	0.986	**0.999**
Image 63	26.69	14.67	25.83	26.67	**35.83**	0.992	0.907	0.985	0.986	**0.998**
Image 64	26.65	26.10	24.36	26.71	**37.95**	0.991	0.983	0.983	0.983	**0.999**
Image 65	26.74	25.08	24.06	26.75	**37.34**	0.990	0.980	0.982	0.981	**0.998**
Image 66	26.68	25.22	23.09	26.73	**39.78**	0.991	0.982	0.983	0.982	**0.999**
Image 67	26.33	25.40	24.34	26.32	**42.47**	0.972	0.953	0.965	0.951	**0.997**
Image 68	26.64	26.47	24.96	26.72	**37.17**	0.993	0.986	0.985	0.987	**0.999**
Image 69	26.68	20.18	25.97	26.70	**39.28**	0.992	0.977	0.984	0.984	**0.999**
Image 70	26.65	16.99	25.81	26.71	**37.20**	0.993	0.938	0.984	0.986	**0.999**
Image 71	26.45	25.50	24.83	26.54	**38.15**	0.986	0.972	0.977	0.972	**0.997**
Image 72	26.70	24.93	23.19	26.74	**37.06**	0.988	0.977	0.981	0.977	**0.999**
Image 73	26.65	26.12	22.46	26.65	**37.47**	0.994	0.989	0.986	0.989	**0.999**
Image 74	26.68	26.69	25.88	26.66	**37.41**	0.991	0.982	0.982	0.982	**0.998**
Image 75	26.67	14.79	26.05	26.70	**36.54**	0.992	0.913	0.983	0.985	**0.998**
Image 76	26.71	26.46	24.83	26.65	**37.76**	0.993	0.987	0.985	0.986	**0.999**
Image 77	26.71	17.65	26.04	26.63	**37.92**	0.991	0.940	0.983	0.984	**0.999**
Image 78	26.68	26.44	23.97	26.64	**38.64**	0.994	0.988	0.985	0.988	**0.999**
Image 79	26.52	26.50	25.00	26.50	**37.56**	0.984	0.969	0.975	0.969	**0.996**
Image 80	26.64	26.33	24.63	26.63	**40.29**	0.993	0.985	0.984	0.985	**0.999**
Image 81	26.66	25.53	25.46	26.74	**36.28**	0.989	0.978	0.981	0.978	**0.998**
Image 82	26.64	25.31	21.54	26.61	**38.75**	0.986	0.974	0.975	0.973	**0.997**
Image 83	26.75	14.14	25.12	26.67	**37.40**	0.993	0.911	0.984	0.987	**0.999**
Image 84	26.62	26.62	24.67	26.62	**38.59**	0.988	0.977	0.981	0.977	**0.997**
Image 85	26.68	25.72	22.47	26.70	**38.35**	0.992	0.984	0.983	0.984	**0.998**
Image 86	26.58	25.23	22.01	26.69	**41.08**	0.991	0.982	0.981	0.982	**0.998**
Image 87	26.50	24.99	22.62	26.48	**41.37**	0.987	0.975	0.977	0.974	**0.998**
Image 88	26.72	22.94	25.82	26.74	**36.90**	0.992	0.982	0.984	0.985	**0.998**
Image 89	26.66	26.60	25.02	26.46	**43.24**	0.992	0.985	0.984	0.984	**0.999**
Image 90	26.64	14.80	25.46	26.77	**36.87**	0.993	0.961	0.985	0.986	**0.999**
Image 91	26.72	25.26	23.65	26.66	**38.79**	0.990	0.981	0.983	0.981	**0.999**
Image 92	26.63	26.21	25.20	26.62	**37.44**	0.993	0.985	0.985	0.985	**0.999**
Image 93	26.67	25.33	22.82	26.75	**38.17**	0.992	0.984	0.983	0.984	**0.999**
Image 94	26.72	26.46	24.95	26.69	**39.76**	0.993	0.986	0.985	0.986	**0.999**
Image 95	26.64	26.57	25.50	26.72	**37.54**	0.993	0.986	0.985	0.986	**0.999**
Image 96	26.57	25.38	24.01	26.56	**43.27**	0.989	0.980	0.981	0.980	**0.999**

Table A.25 continued from previous page

	SNR (dB)					SSIM				
Image 97	26.46	24.06	24.62	26.39	**39.21**	0.980	0.960	0.972	0.964	**0.996**
Image 98	26.69	26.64	26.12	26.70	**37.58**	0.992	0.985	0.985	0.985	**0.999**
Image 99	26.73	19.28	25.60	26.70	**39.34**	0.993	0.977	0.984	0.986	**0.999**
Image 100	26.27	24.80	20.57	26.27	**38.81**	0.966	0.941	0.955	0.938	**0.994**
Image 101	26.65	17.38	25.37	26.67	**38.56**	0.992	0.970	0.984	0.985	**0.999**
Image 102	26.73	16.12	25.52	26.72	**39.18**	0.992	0.904	0.984	0.985	**0.999**
Image 103	26.70	17.41	27.39	26.71	**35.63**	0.988	0.937	0.979	0.978	**0.997**
Image 104	26.76	10.18	25.18	26.70	**37.55**	0.994	0.796	0.985	0.989	**0.999**
Image 105	26.39	26.41	24.22	26.31	**40.49**	0.971	0.950	0.963	0.948	**0.995**
Image 106	26.74	26.38	24.07	26.75	**39.32**	0.991	0.983	0.984	0.983	**0.999**
Image 107	26.68	26.67	24.56	26.61	**42.85**	0.993	0.987	0.984	0.986	**1.000**
Image 108	26.67	26.63	25.01	26.66	**37.19**	0.993	0.986	0.985	0.986	**0.999**
Image 109	26.78	26.31	23.43	26.67	**37.54**	0.992	0.984	0.984	0.984	**0.999**
Image 110	26.68	17.05	27.11	26.73	**36.13**	0.989	0.931	0.980	0.981	**0.998**
Average	26.63	23.11	24.66	26.63	**38.52**	0.989	0.964	0.981	0.979	**0.998**

(a) FFT-based (b) NQR-based (c) DL-based

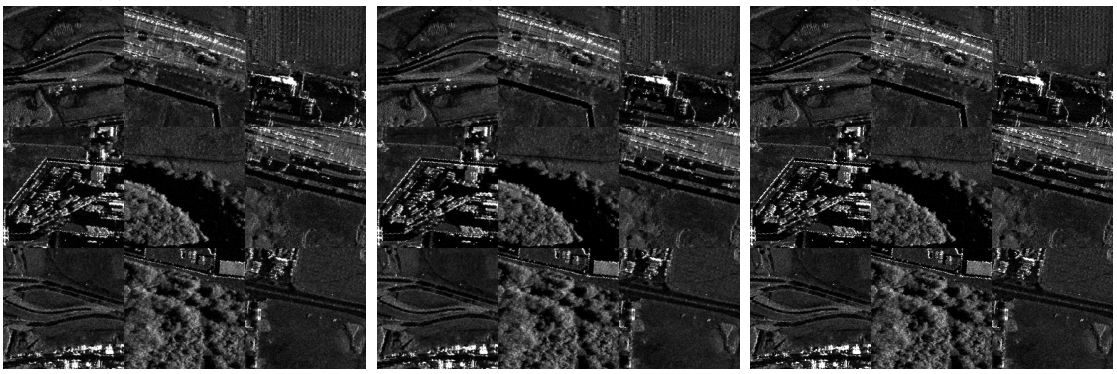

(d) PnP-BM3D (e) PnP-CNN-SAR (f) Ground Truth

Figure A.25 Reconstruction results for Images 19, 40, 45, 46, 59, 61, 66, 96, and 109 from the Kapıkule test set for the case of 100% data availability and $\sigma_{\mathbf{n}} = 0.1\sigma_{\mathbf{y}}$.

A.3.2 Experiment 2: 90% Data Availability and $\sigma_{\mathbf{n}} = 0.1\sigma_{\mathbf{y}}$

Table A.26 shows the SNR and SSIM values for this experiment. PnP-CNN-SAR gives the best SNR for 106 images, and best SSIM for 105 images. Fig. A.26 shows the reconstruction results for a selection of images from the Kapıkule test set from all methods for this experiment. All methods except the NQR-based produce good reconstructions for all images.

Table A.26 SNR and SSIM values for images from the KapıkuleTest Set for the case of 90% data availability and $\sigma_{\mathbf{n}} = 0.1\sigma_{\mathbf{y}}$. Best results are shown in bold, second best results are shown in red.

	SNR (dB)					SSIM				
	FFT-based	NQR-based	DL-based	PnP-BM3D	PnP-CNN-SAR	FFT-based	NQR-based	DL-based	PnP-BM3D	PnP-CNN-SAR
Image 1	13.29	8.16	15.29	15.57	**16.67**	0.756	0.627	0.837	0.853	**0.871**
Image 2	13.22	11.45	14.22	14.48	**16.90**	0.762	0.528	0.815	0.814	**0.901**
Image 3	13.10	10.33	15.79	15.48	**16.60**	0.767	0.755	0.860	0.839	**0.862**
Image 4	13.10	12.48	14.01	14.62	**16.56**	0.766	0.790	0.843	0.845	**0.894**
Image 5	13.11	11.20	11.78	14.62	**15.48**	0.780	0.585	0.755	0.840	**0.853**
Image 6	13.17	11.77	15.93	17.16	**17.52**	0.711	0.575	0.834	0.867	**0.877**
Image 7	13.39	12.08	14.42	15.74	**17.36**	0.744	0.779	0.835	0.855	**0.889**
Image 8	13.37	9.71	13.46	15.39	**16.64**	0.767	0.435	0.830	0.857	**0.886**
Image 9	12.85	8.43	11.68	15.08	**17.59**	0.760	0.444	0.776	0.851	**0.910**
Image 10	13.18	12.56	14.51	15.68	**16.73**	0.780	0.628	0.818	0.843	**0.913**
Image 11	13.29	12.23	15.72	16.45	**17.24**	0.751	0.758	0.840	0.854	**0.897**
Image 12	12.99	10.86	9.75	12.74	**17.42**	0.813	0.808	0.740	0.838	**0.928**
Image 13	13.11	13.03	13.51	14.22	**17.00**	0.756	0.768	0.778	0.810	**0.915**
Image 14	13.43	11.75	15.07	16.48	**16.79**	0.739	0.768	0.839	0.867	**0.879**
Image 15	13.24	13.04	15.08	15.71	**16.76**	0.767	0.801	0.863	0.859	**0.889**
Image 16	12.74	11.59	9.81	12.57	**17.48**	0.746	0.618	0.635	0.753	**0.944**
Image 17	13.35	8.53	16.07	16.75	**17.33**	0.727	0.583	0.838	**0.861**	0.855
Image 18	13.33	12.49	15.34	16.30	**16.65**	0.758	0.790	0.862	0.862	**0.881**
Image 19	13.40	13.29	13.54	14.74	**16.22**	0.811	0.834	0.845	0.857	**0.902**
Image 20	13.27	9.96	12.07	14.64	**17.28**	0.775	0.525	0.811	0.855	**0.908**
Image 21	13.10	11.41	14.19	14.46	**17.27**	0.749	0.750	0.801	0.814	**0.906**
Image 22	13.10	13.12	13.87	14.29	**16.96**	0.753	0.772	0.790	0.808	**0.918**
Image 23	13.23	12.13	15.05	15.98	**16.79**	0.761	0.687	0.831	0.859	**0.886**
Image 24	13.38	12.21	14.32	14.71	**16.59**	0.772	0.807	0.858	0.839	**0.889**
Image 25	13.38	10.15	16.89	**17.79**	17.42	0.679	0.527	0.829	**0.860**	0.838
Image 26	13.38	13.39	14.02	14.77	**16.52**	0.788	0.821	0.847	0.849	**0.901**
Image 27	13.27	11.72	15.91	15.37	**16.83**	0.764	0.766	0.862	0.837	**0.882**
Image 28	13.25	11.87	15.96	16.84	**17.02**	0.720	0.528	0.841	0.861	**0.871**
Image 29	13.26	13.28	14.30	14.97	**16.04**	0.791	0.816	0.836	0.858	**0.908**
Image 30	13.35	12.03	14.86	15.70	**16.88**	0.759	0.772	0.836	0.854	**0.887**
Image 31	13.27	13.30	15.03	14.92	**15.79**	0.789	0.819	0.862	0.853	**0.888**
Image 32	13.27	9.92	15.13	14.62	**16.33**	0.778	0.598	0.849	0.835	**0.874**
Image 33	13.33	12.99	14.89	15.05	**17.29**	0.727	0.760	0.812	0.823	**0.893**
Image 34	13.26	12.88	13.62	13.81	**16.76**	0.747	0.755	0.780	0.790	**0.922**
Image 35	13.41	12.45	14.96	15.63	**16.56**	0.779	0.795	0.847	0.864	**0.901**
Image 36	13.14	12.19	14.05	15.12	**17.49**	0.739	0.765	0.801	0.826	**0.906**
Image 37	13.24	9.68	15.40	15.33	**16.49**	0.741	0.611	0.837	0.848	**0.860**
Image 38	13.41	9.07	15.98	16.49	**16.99**	0.732	0.542	0.841	0.850	**0.853**
Image 39	13.27	8.19	15.66	15.38	**16.69**	0.743	0.594	0.843	0.847	**0.856**
Image 40	13.19	10.75	13.91	15.19	**16.58**	0.772	0.509	0.826	0.852	**0.894**
Image 41	13.20	10.21	15.11	16.13	**16.88**	0.748	0.457	0.849	0.858	**0.880**
Image 42	13.51	11.32	15.46	16.00	**16.67**	0.746	0.626	0.845	0.861	**0.870**
Image 43	13.19	12.83	14.46	14.74	**16.86**	0.744	0.755	0.797	0.806	**0.913**
Image 44	13.29	13.11	14.81	14.28	**15.96**	0.808	0.821	0.868	0.827	**0.890**
Image 45	13.39	10.41	12.06	14.48	**16.46**	0.786	0.796	0.800	0.845	**0.901**
Image 46	12.76	9.80	9.30	13.56	**18.52**	0.776	0.605	0.694	0.829	**0.928**
Image 47	13.27	12.12	14.65	15.20	**16.48**	0.779	0.807	0.859	0.858	**0.892**
Image 48	13.14	13.18	13.88	14.27	**16.17**	0.794	0.809	0.837	0.831	**0.905**
Image 49	13.15	11.61	16.77	**17.83**	17.80	0.700	0.503	0.842	0.862	**0.872**
Image 50	12.92	12.10	13.45	14.17	**17.06**	0.762	0.776	0.780	0.794	**0.919**
Image 51	13.28	12.98	13.42	13.69	**16.55**	0.775	0.809	0.841	0.846	**0.906**
Image 52	13.15	12.92	15.56	16.45	**17.85**	0.713	0.723	0.823	0.848	**0.889**
Image 53	13.26	12.00	11.91	14.40	**16.61**	0.774	0.798	0.812	0.850	**0.896**
Image 54	13.06	13.10	14.90	15.83	**17.50**	0.721	0.743	0.817	0.839	**0.893**
Image 55	13.28	13.30	15.73	16.49	**17.35**	0.750	0.776	0.837	0.853	**0.899**
Image 56	13.10	12.91	14.54	15.46	**16.45**	0.774	0.794	0.849	0.863	**0.895**
Image 57	13.30	11.80	13.12	14.86	**16.60**	0.780	0.803	0.833	0.853	**0.899**
Image 58	13.06	12.47	14.75	15.45	**17.18**	0.747	0.621	0.817	0.835	**0.905**
Image 59	12.92	12.44	13.85	14.63	**17.23**	0.738	0.734	0.777	0.805	**0.915**
Image 60	13.31	11.98	14.26	15.46	**16.24**	0.758	0.786	0.847	0.862	**0.885**
Image 61	13.34	11.26	13.38	14.87	**16.20**	0.783	0.795	0.816	0.850	**0.892**
Image 62	13.22	11.40	15.25	15.72	**16.63**	0.760	0.665	0.841	0.856	**0.873**
Image 63	13.30	9.25	15.57	15.64	**16.81**	0.748	0.727	0.850	0.848	**0.875**
Image 64	13.25	13.08	13.92	15.04	**17.02**	0.761	0.792	0.828	0.837	**0.896**
Image 65	13.44	10.17	13.71	15.02	**17.27**	0.734	0.461	0.820	0.849	**0.889**
Image 66	13.06	8.90	12.51	15.12	**16.84**	0.790	0.446	0.821	0.862	**0.901**
Image 67	12.90	12.92	13.54	14.43	**16.99**	0.759	0.761	0.775	0.811	**0.929**
Image 68	13.32	13.30	14.71	15.02	**15.85**	0.788	0.814	0.863	0.854	**0.883**
Image 69	13.38	11.23	15.60	16.60	**17.03**	0.741	0.575	0.843	0.866	**0.885**
Image 70	13.36	9.79	15.65	15.89	**17.13**	0.731	0.611	0.842	0.856	**0.875**
Image 71	13.00	12.62	13.99	15.47	**17.54**	0.731	0.739	0.793	0.833	**0.909**
Image 72	13.31	11.56	12.98	14.88	**16.06**	0.756	0.772	0.818	0.858	**0.885**
Image 73	13.30	12.14	12.05	13.05	**16.52**	0.832	0.845	0.823	0.823	**0.921**
Image 74	13.33	13.31	15.57	16.99	**17.69**	0.720	0.743	0.835	0.863	**0.885**
Image 75	13.28	9.83	15.84	16.13	**16.72**	0.747	0.737	0.850	0.854	**0.861**
Image 76	13.37	12.92	14.42	15.21	**16.59**	0.768	0.802	0.851	0.846	**0.890**
Image 77	13.28	11.45	15.84	16.90	**17.30**	0.714	0.590	0.836	**0.869**	0.867
Image 78	13.22	13.22	13.74	14.61	**16.08**	0.794	0.820	0.839	0.852	**0.897**
Image 79	13.00	12.56	14.28	15.46	**17.25**	0.733	0.743	0.800	0.835	**0.897**
Image 80	13.16	12.52	14.25	15.12	**16.39**	0.777	0.801	0.837	0.848	**0.890**
Image 81	13.17	12.02	14.65	16.99	**18.53**	0.685	0.438	0.831	0.860	**0.875**
Image 82	12.95	10.76	9.96	13.34	**17.25**	0.793	0.543	0.735	0.823	**0.922**
Image 83	13.34	10.77	14.83	14.89	**16.30**	0.777	0.781	0.849	0.839	**0.868**
Image 84	13.35	13.39	14.00	15.05	**16.84**	0.773	0.794	0.820	0.823	**0.903**
Image 85	13.07	11.23	11.27	14.35	**16.85**	0.785	0.793	0.788	0.846	**0.899**
Image 86	12.97	10.80	10.80	13.50	**16.81**	0.798	0.618	0.760	0.835	**0.922**
Image 87	13.00	10.54	11.75	14.32	**16.74**	0.779	0.599	0.763	0.833	**0.920**
Image 88	13.31	11.49	15.77	16.24	**17.20**	0.732	0.538	0.846	0.859	**0.880**

Table A.26 continued from previous page

	SNR (dB)					SSIM				
Image 89	13.22	12.74	14.43	15.36	**16.58**	0.781	0.798	0.830	0.858	**0.908**
Image 90	13.23	10.00	15.28	15.35	**16.60**	0.754	0.582	0.849	0.847	**0.879**
Image 91	13.31	11.34	13.22	15.59	**16.80**	0.765	0.779	0.822	0.857	**0.888**
Image 92	13.18	12.36	15.33	15.73	**17.13**	0.764	0.784	0.862	0.852	**0.889**
Image 93	13.08	10.28	12.31	14.03	**16.40**	0.801	0.796	0.811	0.845	**0.898**
Image 94	13.36	12.14	14.71	15.64	**16.58**	0.763	0.797	0.847	0.863	**0.892**
Image 95	13.18	13.22	15.42	15.54	**16.70**	0.766	0.791	0.865	0.856	**0.890**
Image 96	13.02	11.83	13.49	14.93	**17.13**	0.778	0.793	0.814	0.858	**0.919**
Image 97	12.97	12.56	14.02	14.58	**16.95**	0.745	0.756	0.796	0.807	**0.908**
Image 98	13.21	12.84	15.93	16.73	**17.00**	0.729	0.749	0.850	0.862	**0.877**
Image 99	13.28	12.60	15.28	15.85	**16.79**	0.766	0.783	0.846	0.857	**0.889**
Image 100	12.90	11.15	8.69	12.00	**17.50**	0.746	0.664	0.627	0.769	**0.941**
Image 101	13.26	12.11	15.04	15.24	**16.47**	0.771	0.779	0.842	0.839	**0.877**
Image 102	13.29	10.68	15.20	15.57	**16.86**	0.762	0.752	0.843	0.847	**0.882**
Image 103	13.32	13.54	17.09	**18.47**	18.44	0.624	0.546	0.808	**0.852**	0.839
Image 104	13.10	8.49	14.85	14.85	**16.12**	0.783	0.655	0.846	0.852	**0.873**
Image 105	12.82	12.60	13.51	14.72	**17.13**	0.734	0.747	0.758	0.802	**0.921**
Image 106	13.29	12.38	14.04	15.40	**16.47**	0.766	0.791	0.846	0.858	**0.890**
Image 107	13.20	13.11	14.17	14.97	**16.31**	0.802	0.818	0.841	0.865	**0.905**
Image 108	13.30	13.15	15.32	15.36	**16.40**	0.782	0.811	0.864	0.847	**0.888**
Image 109	13.17	12.10	13.02	15.01	**16.77**	0.786	0.803	0.837	0.858	**0.896**
Image 110	13.33	11.39	17.05	**18.41**	18.32	0.657	0.524	0.828	**0.867**	0.852
Average	13.21	11.70	14.22	15.27	**16.87**	0.758	0.705	0.822	0.844	**0.892**

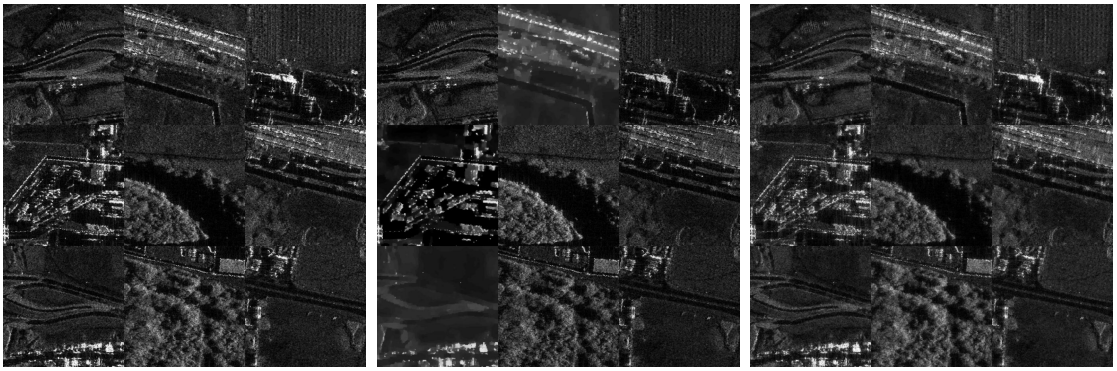

(a) FFT-based (b) NQR-based (c) DL-based

(d) PnP-BM3D (e) PnP-CNN-SAR (f) Ground Truth

Figure A.26 Reconstruction results for Images 19, 40, 45, 46, 59, 61, 66, 96, and 109 from the Kapıkule test set for the case of 90% data availability and $\sigma_{\mathbf{n}} = 0.1\sigma_{\mathbf{y}}$.

A.3.3 Experiment 3: 80% Data Availability and $\sigma_{\mathbf{n}} = 0.1\sigma_{\mathbf{y}}$

Table A.27 shows the SNR and SSIM values for this experiment. PnP-CNN-SAR gives the best SNR for 105 images, and best SSIM for 105 images. Fig. A.27 shows the reconstruction results for a selection of images from the Kapıkule test set from all methods for this experiment. PnP-BM3D and PnP-CNN-SAR produce better reconstructions compared to other methods.

Table A.27 SNR and SSIM values for images from the KapıkuleTest Set for the case of 80% data availability and $\sigma_{\mathbf{n}} = 0.1\sigma_{\mathbf{y}}$. Best results are shown in bold, second best results are shown in red.

	SNR (dB)					SSIM				
	FFT-based	NQR-based	DL-based	PnP-BM3D	PnP-CNN-SAR	FFT-based	NQR-based	DL-based	PnP-BM3D	PnP-CNN-SAR
Image 1	10.24	8.48	12.11	13.02	**13.96**	0.649	0.610	0.705	0.746	**0.775**
Image 2	10.01	10.67	11.35	11.85	**13.84**	0.659	0.499	0.703	0.687	**0.815**
Image 3	10.16	10.55	12.42	12.99	**13.66**	0.655	0.489	0.720	0.716	**0.744**
Image 4	10.13	9.35	11.02	11.87	**13.33**	0.672	0.660	0.721	0.736	**0.800**
Image 5	10.08	8.48	9.05	**11.04**	9.39	0.707	0.457	0.642	**0.732**	0.704
Image 6	10.12	9.91	12.67	14.21	**14.39**	0.596	0.537	0.698	0.756	**0.764**
Image 7	10.10	8.91	11.30	12.27	**13.67**	0.646	0.385	0.704	0.736	**0.780**
Image 8	10.13	7.91	10.53	12.27	**13.37**	0.672	0.379	0.703	0.747	**0.790**
Image 9	9.90	7.17	9.22	11.39	**14.26**	0.674	0.384	0.663	0.737	**0.834**
Image 10	10.10	11.44	11.57	12.73	**13.47**	0.691	0.583	0.719	0.746	**0.838**
Image 11	10.23	11.78	12.38	13.43	**14.18**	0.653	0.502	0.709	0.738	**0.794**
Image 12	9.85	8.13	7.60	9.81	**13.46**	0.733	0.527	0.632	0.736	**0.859**
Image 13	9.85	9.79	10.77	11.77	**13.42**	0.688	0.548	0.682	0.720	**0.849**
Image 14	10.24	9.70	11.74	13.35	**13.57**	0.626	0.368	0.700	0.751	**0.769**
Image 15	10.25	8.60	12.02	12.84	**13.42**	0.664	0.435	0.741	0.737	**0.784**
Image 16	9.71	8.33	7.49	9.49	**13.25**	0.704	0.523	0.566	0.663	**0.899**
Image 17	10.08	9.77	12.70	13.97	**14.16**	0.600	0.540	0.699	**0.746**	0.732
Image 18	10.17	8.91	11.94	13.20	**13.68**	0.650	0.419	0.731	0.742	**0.775**
Image 19	9.97	9.39	10.58	11.76	**13.30**	0.717	0.701	0.721	0.739	**0.824**
Image 20	9.97	6.71	9.45	11.36	**14.00**	0.681	0.402	0.694	0.744	**0.823**
Image 21	10.01	10.77	11.13	11.88	**13.72**	0.663	0.602	0.687	0.692	**0.820**
Image 22	10.13	10.63	11.12	11.76	**13.57**	0.689	0.563	0.694	0.695	**0.847**
Image 23	10.03	11.02	11.97	13.01	**13.78**	0.649	0.619	0.704	0.744	**0.780**
Image 24	10.17	10.31	11.43	12.10	**13.56**	0.677	0.668	0.744	0.720	**0.793**
Image 25	10.15	10.52	13.34	**15.16**	14.32	0.554	0.467	0.670	**0.744**	0.690
Image 26	10.04	10.41	11.11	12.14	**13.23**	0.703	0.580	0.731	0.739	**0.816**
Image 27	10.27	10.67	12.45	12.81	**13.82**	0.659	0.486	0.724	0.715	**0.776**
Image 28	10.10	10.76	12.48	13.87	**14.17**	0.606	0.498	0.697	0.737	**0.757**
Image 29	10.11	9.94	11.22	12.20	**13.04**	0.701	0.534	0.710	0.752	**0.828**
Image 30	9.99	10.41	11.89	12.86	**13.82**	0.659	0.571	0.706	0.739	**0.785**
Image 31	10.11	9.68	11.88	12.33	**12.81**	0.692	0.521	0.733	0.730	**0.783**
Image 32	10.09	10.24	11.90	12.27	**13.53**	0.671	0.544	0.711	0.717	**0.776**
Image 33	10.07	11.40	11.98	12.39	**13.98**	0.632	0.543	0.694	0.693	**0.796**
Image 34	10.09	10.66	10.85	11.43	**13.42**	0.691	0.615	0.685	0.690	**0.857**
Image 35	10.17	11.28	11.83	12.89	**13.64**	0.681	0.562	0.721	0.760	**0.805**
Image 36	9.93	11.34	11.33	12.56	**13.74**	0.645	0.561	0.691	0.720	**0.815**
Image 37	10.11	9.14	12.14	12.77	**13.48**	0.627	0.574	0.693	0.724	**0.739**
Image 38	9.98	7.78	12.40	13.65	**14.03**	0.619	0.531	0.689	0.726	**0.735**
Image 39	10.12	7.86	12.34	12.74	**13.72**	0.631	0.554	0.704	0.725	**0.744**
Image 40	10.21	8.36	10.95	11.88	**13.23**	0.681	0.350	0.703	0.735	**0.799**
Image 41	10.15	8.50	11.99	13.28	**13.78**	0.633	0.422	0.722	0.733	**0.773**
Image 42	10.15	10.36	12.07	13.16	**13.66**	0.633	0.584	0.697	0.744	**0.754**
Image 43	10.20	10.75	11.62	12.23	**13.47**	0.670	0.608	0.703	0.703	**0.837**
Image 44	10.16	9.60	11.66	11.71	**12.94**	0.713	0.708	0.755	0.699	**0.800**
Image 45	10.13	6.56	9.37	11.24	**12.82**	0.704	0.320	0.683	0.738	**0.818**
Image 46	9.66	7.56	7.19	9.98	**14.40**	0.718	0.513	0.593	0.732	**0.877**
Image 47	10.19	10.11	11.52	12.22	**13.43**	0.681	0.679	0.733	0.733	**0.792**
Image 48	9.91	9.72	11.05	11.67	**13.16**	0.704	0.681	0.724	0.720	**0.822**
Image 49	10.32	10.17	13.28	**15.08**	14.85	0.583	0.452	0.701	0.747	**0.751**
Image 50	10.11	9.62	10.61	11.52	**13.39**	0.696	0.541	0.689	0.692	**0.851**
Image 51	9.93	9.16	10.43	10.96	**13.25**	0.677	0.668	0.714	0.726	**0.818**
Image 52	10.05	11.89	12.38	13.64	**14.70**	0.605	0.513	0.697	0.727	**0.787**
Image 53	10.09	6.37	9.21	11.14	**12.98**	0.683	0.352	0.694	0.739	**0.812**
Image 54	10.10	7.82	11.80	13.19	**14.10**	0.618	0.383	0.687	0.728	**0.790**
Image 55	9.93	11.84	12.50	13.56	**14.36**	0.656	0.543	0.717	0.739	**0.800**
Image 56	10.15	10.71	11.39	12.33	**13.34**	0.674	0.540	0.726	0.739	**0.796**
Image 57	10.11	9.03	9.99	11.93	**12.95**	0.689	0.683	0.704	0.742	**0.808**
Image 58	9.95	11.49	11.71	12.58	**13.77**	0.652	0.574	0.703	0.721	**0.814**
Image 59	9.91	10.11	10.98	11.77	**13.52**	0.662	0.571	0.675	0.675	**0.834**
Image 60	10.14	7.25	11.43	12.35	**13.60**	0.651	0.405	0.720	0.742	**0.798**
Image 61	10.07	7.31	10.37	11.42	**13.10**	0.697	0.324	0.692	0.733	**0.806**
Image 62	10.11	10.85	12.04	12.96	**13.45**	0.649	0.598	0.699	0.734	**0.752**
Image 63	10.14	10.70	12.48	13.19	**13.92**	0.639	0.531	0.722	0.735	**0.775**
Image 64	10.08	10.03	11.00	12.30	**13.52**	0.669	0.660	0.703	0.730	**0.794**
Image 65	10.23	8.13	10.65	12.08	**13.74**	0.627	0.369	0.682	0.744	**0.772**
Image 66	10.14	6.83	9.68	11.70	**13.96**	0.705	0.352	0.703	0.760	**0.830**
Image 67	10.13	10.95	10.82	11.87	**13.37**	0.688	0.645	0.675	0.713	**0.863**
Image 68	10.11	10.14	11.81	12.19	**13.10**	0.684	0.671	0.745	0.734	**0.787**
Image 69	10.12	10.75	12.35	13.63	**14.12**	0.625	0.541	0.707	0.751	**0.776**
Image 70	10.20	9.37	12.39	13.30	**13.84**	0.608	0.576	0.696	0.737	**0.750**
Image 71	9.98	11.34	11.35	12.42	**13.79**	0.655	0.561	0.694	0.717	**0.820**
Image 72	10.15	7.57	10.05	11.50	**12.68**	0.662	0.355	0.686	0.745	**0.784**
Image 73	10.00	8.42	9.25	10.29	**13.04**	0.753	0.722	0.712	0.712	**0.852**
Image 74	10.10	12.13	12.23	13.85	**14.40**	0.599	0.493	0.691	0.742	**0.775**
Image 75	10.18	8.17	12.60	13.41	**13.94**	0.634	0.536	0.715	0.735	**0.750**
Image 76	10.05	9.81	11.61	12.25	**13.65**	0.668	0.669	0.737	0.723	**0.799**
Image 77	10.15	11.30	12.44	14.00	**14.20**	0.599	0.500	0.683	0.748	**0.749**
Image 78	10.04	9.94	11.01	11.70	**13.20**	0.703	0.697	0.727	0.731	**0.814**
Image 79	10.08	11.01	11.52	12.59	**13.57**	0.646	0.517	0.684	0.716	**0.795**
Image 80	10.13	7.87	11.17	12.31	**13.45**	0.677	0.315	0.704	0.727	**0.796**
Image 81	10.15	10.60	11.65	13.50	**14.48**	0.576	0.404	0.693	0.736	**0.757**
Image 82	9.89	7.69	7.70	10.03	**13.42**	0.730	0.692	0.635	0.720	**0.855**
Image 83	10.08	9.10	11.66	12.38	**13.24**	0.675	0.550	0.713	0.729	**0.763**
Image 84	9.97	9.91	11.30	12.43	**13.67**	0.699	0.542	0.728	0.727	**0.830**
Image 85	9.71	5.84	8.93	10.90	**13.28**	0.698	0.281	0.675	0.722	**0.807**
Image 86	9.88	7.81	8.47	10.28	**13.27**	0.721	0.483	0.649	0.725	**0.856**
Image 87	10.01	6.15	9.20	11.24	**13.26**	0.699	0.284	0.648	0.732	**0.851**
Image 88	10.17	11.58	12.38	13.41	**13.91**	0.622	0.456	0.700	0.735	**0.759**

Table A.27 continued from previous page

	SNR (dB)					SSIM				
Image 89	9.92	10.11	11.40	12.40	**13.49**	0.695	0.648	0.708	0.748	**0.829**
Image 90	10.13	9.40	12.25	12.64	**13.30**	0.641	0.554	0.724	0.724	**0.765**
Image 91	10.06	7.94	10.47	12.07	**13.62**	0.672	0.355	0.701	0.741	**0.794**
Image 92	10.03	8.78	11.92	13.03	**13.66**	0.655	0.419	0.733	0.745	**0.787**
Image 93	10.07	6.67	9.55	10.79	**12.89**	0.722	0.318	0.697	0.730	**0.790**
Image 94	10.06	8.02	11.62	12.74	**13.44**	0.660	0.371	0.718	0.746	**0.799**
Image 95	10.11	10.30	12.33	12.94	**13.58**	0.661	0.500	0.746	0.741	**0.792**
Image 96	10.02	9.71	10.47	11.90	**13.72**	0.688	0.557	0.689	0.749	**0.839**
Image 97	9.84	10.22	11.15	11.89	**13.45**	0.677	0.614	0.697	0.686	**0.827**
Image 98	10.19	10.97	12.65	13.79	**13.91**	0.621	0.466	0.718	0.739	**0.766**
Image 99	10.10	10.51	12.08	12.84	**13.89**	0.668	0.542	0.713	0.734	**0.786**
Image 100	9.49	6.96	6.64	8.94	**13.44**	0.700	0.508	0.550	0.667	**0.896**
Image 101	10.13	9.36	11.92	12.57	**13.52**	0.661	0.558	0.720	0.724	**0.777**
Image 102	10.09	10.11	12.06	12.82	**13.81**	0.654	0.653	0.715	0.734	**0.780**
Image 103	10.12	12.03	13.41	**15.08**	14.97	0.500	0.497	0.632	**0.703**	0.688
Image 104	10.14	8.72	11.98	12.24	**13.19**	0.678	0.566	0.722	0.733	**0.766**
Image 105	9.85	11.31	10.72	12.00	**13.85**	0.672	0.651	0.667	0.704	**0.862**
Image 106	10.03	7.97	10.74	12.08	**13.48**	0.662	0.401	0.717	0.748	**0.800**
Image 107	10.05	9.62	11.31	11.84	**13.22**	0.696	0.513	0.722	0.746	**0.813**
Image 108	10.22	8.88	11.77	12.56	**13.09**	0.690	0.433	0.743	0.716	**0.789**
Image 109	10.04	7.50	10.27	11.64	**13.77**	0.688	0.404	0.721	0.744	**0.807**
Image 110	10.17	9.76	13.27	**15.35**	14.82	0.532	0.515	0.663	**0.737**	0.707
Average	10.07	9.47	11.22	12.36	**13.60**	0.662	0.518	0.699	0.729	**0.796**

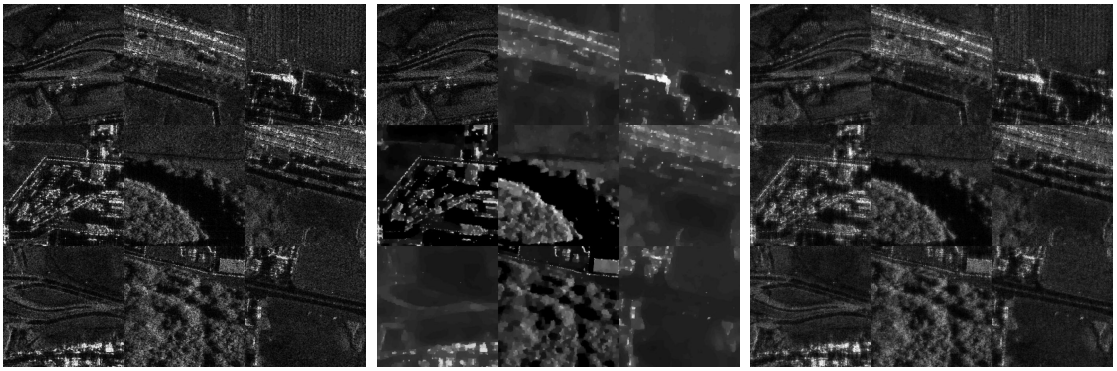

(a) FFT-based (b) NQR-based (c) DL-based

(d) PnP-BM3D (e) PnP-CNN-SAR (f) Ground Truth

Figure A.27 Reconstruction results for Images 19, 40, 45, 46, 59, 61, 66, 96, and 109 from the Kapıkule test set for the case of 80% data availability and $\sigma_{\mathbf{n}} = 0.1\sigma_{\mathbf{y}}$.

A.3.4 Experiment 4: 70% Data Availability and $\sigma_{\mathbf{n}} = 0.1\sigma_{\mathbf{y}}$

Table A.28 shows the SNR and SSIM values for this experiment. PnP-CNN-SAR gives the best SNR for 104 images, and best SSIM for 106 images. Fig. A.28 shows the reconstruction results for a selection of images from the Kapıkule test set from all methods for this experiment. PnP-CNN-SAR produce better reconstructions compared to other methods.

Table A.28 SNR and SSIM values for images from the KapıkuleTest Set for the case of 70% data availability and $\sigma_{\mathbf{n}} = 0.1\sigma_{\mathbf{y}}$. Best results are shown in bold, second best results are shown in red.

	SNR (dB)					SSIM				
	FFT-based	NQR-based	DL-based	PnP-BM3D	PnP-CNN-SAR	FFT-based	NQR-based	DL-based	PnP-BM3D	PnP-CNN-SAR
Image 1	8.44	10.29	10.42	11.16	**11.34**	0.554	0.507	0.589	0.621	**0.641**
Image 2	8.33	9.90	9.67	10.50	**11.24**	0.587	0.462	0.604	0.574	**0.701**
Image 3	8.50	10.23	10.63	11.23	**11.39**	0.550	0.468	0.616	0.574	**0.625**
Image 4	8.52	5.90	9.48	10.11	**10.91**	0.582	0.370	0.621	0.601	**0.682**
Image 5	8.20	6.89	7.93	8.84	**11.08**	0.646	0.348	0.557	0.633	**0.739**
Image 6	8.52	11.59	10.78	11.84	**12.03**	0.506	0.482	0.579	0.606	**0.624**
Image 7	8.56	8.13	9.67	10.40	**11.17**	0.560	0.355	0.603	0.611	**0.655**
Image 8	8.63	7.32	8.98	10.20	**10.75**	0.581	0.324	0.606	0.628	**0.691**
Image 9	8.28	7.50	8.14	9.38	**11.06**	0.592	0.391	0.572	0.638	**0.735**
Image 10	8.54	6.92	9.96	10.45	**11.17**	0.614	0.321	0.635	0.648	**0.752**
Image 11	8.51	10.06	10.68	11.35	**11.58**	0.567	0.480	0.611	0.614	**0.679**
Image 12	7.98	6.32	6.50	8.01	**10.07**	0.666	0.606	0.547	0.638	**0.773**
Image 13	8.18	9.41	9.38	9.98	**10.87**	0.620	0.588	0.614	0.620	**0.759**
Image 14	8.53	8.45	10.13	10.94	**11.24**	0.536	0.337	0.593	0.606	**0.633**
Image 15	8.54	9.65	10.44	11.10	**11.27**	0.568	0.439	0.646	0.607	**0.675**
Image 16	8.12	6.51	6.70	7.87	**10.15**	0.661	0.650	0.526	0.594	**0.833**
Image 17	8.54	7.51	10.84	**11.97**	11.95	0.498	0.529	0.578	**0.602**	0.597
Image 18	8.42	9.51	10.33	11.24	**11.48**	0.561	0.414	0.633	0.605	**0.664**
Image 19	8.38	5.92	9.10	10.02	**10.93**	0.628	0.292	0.624	0.630	**0.723**
Image 20	8.38	5.21	8.17	9.48	**11.07**	0.600	0.316	0.603	0.630	**0.719**
Image 21	8.44	9.97	9.54	10.39	**11.18**	0.589	0.545	0.595	0.596	**0.726**
Image 22	8.35	8.39	9.57	10.16	**11.22**	0.621	0.471	0.615	0.606	**0.767**
Image 23	8.53	10.87	10.38	10.91	**11.37**	0.562	0.488	0.603	0.617	**0.660**
Image 24	8.46	8.41	9.73	10.48	**11.42**	0.587	0.463	0.647	0.591	**0.686**
Image 25	8.57	7.05	11.42	**12.37**	11.94	0.450	0.360	0.551	**0.570**	0.547
Image 26	8.40	8.64	9.68	10.24	**10.95**	0.613	0.612	0.638	0.616	**0.713**
Image 27	8.39	10.39	10.64	11.37	**11.54**	0.566	0.436	0.621	0.585	**0.651**
Image 28	8.56	11.34	10.73	11.85	**11.95**	0.510	0.438	0.582	0.587	**0.622**
Image 29	8.40	9.99	9.68	10.16	**10.77**	0.611	0.527	0.612	0.631	**0.729**
Image 30	8.52	10.37	10.21	11.00	**11.52**	0.566	0.514	0.602	0.620	**0.670**
Image 31	8.50	8.63	10.17	10.66	**10.97**	0.593	0.312	0.621	0.594	**0.682**
Image 32	8.60	7.26	10.35	10.69	**11.32**	0.575	0.551	0.608	0.586	**0.647**
Image 33	8.35	10.80	10.44	10.86	**11.42**	0.552	0.516	0.608	0.564	**0.677**
Image 34	8.34	7.44	9.48	10.02	**10.94**	0.621	0.495	0.617	0.616	**0.774**
Image 35	8.31	10.48	10.18	10.79	**11.64**	0.590	0.534	0.616	0.632	**0.701**
Image 36	8.41	9.31	9.74	10.71	**11.35**	0.561	0.458	0.599	0.600	**0.707**
Image 37	8.51	7.50	10.43	10.94	**11.44**	0.530	0.539	0.575	0.577	**0.606**
Image 38	8.56	7.78	10.87	**11.54**	11.45	0.527	0.472	0.582	0.592	**0.594**
Image 39	8.48	7.98	10.60	11.10	**11.43**	0.539	0.491	0.587	0.598	**0.606**
Image 40	8.40	7.52	9.35	10.05	**10.68**	0.600	0.304	0.605	0.626	**0.686**
Image 41	8.59	8.89	10.23	11.46	**11.62**	0.540	0.390	0.613	0.583	**0.660**
Image 42	8.49	7.20	10.42	11.01	**11.29**	0.544	0.443	0.585	0.596	**0.626**
Image 43	8.34	9.27	9.86	10.52	**11.13**	0.606	0.565	0.615	0.608	**0.750**
Image 44	8.58	8.86	9.92	10.28	**10.87**	0.630	0.626	0.660	0.593	**0.702**
Image 45	8.32	6.82	8.14	9.22	**10.24**	0.628	0.295	0.596	0.627	**0.709**
Image 46	7.98	5.93	6.25	8.04	**10.36**	0.652	0.439	0.522	0.639	**0.801**
Image 47	8.57	9.05	9.83	10.41	**11.16**	0.588	0.403	0.633	0.600	**0.683**
Image 48	8.44	8.69	9.62	10.12	**10.69**	0.618	0.617	0.636	0.618	**0.726**
Image 49	8.51	9.52	11.14	**12.70**	12.11	0.490	0.461	0.583	0.598	**0.610**
Image 50	8.22	5.81	9.43	9.88	**10.86**	0.633	0.311	0.628	0.618	**0.770**
Image 51	8.22	8.45	8.93	9.72	**10.73**	0.584	0.586	0.616	0.607	**0.706**
Image 52	8.56	10.67	10.63	11.73	**12.11**	0.508	0.414	0.595	0.582	**0.659**
Image 53	8.32	5.41	8.09	9.36	**10.62**	0.601	0.312	0.604	0.625	**0.715**
Image 54	8.38	9.96	10.12	11.18	**11.58**	0.526	0.419	0.586	0.593	**0.669**
Image 55	8.44	11.05	10.72	11.04	**11.89**	0.563	0.505	0.619	0.608	**0.682**
Image 56	8.46	8.72	9.80	10.57	**11.06**	0.580	0.415	0.623	0.623	**0.694**
Image 57	8.39	6.41	8.66	9.59	**10.89**	0.602	0.298	0.607	0.616	**0.703**
Image 58	8.51	10.63	9.98	10.99	**11.33**	0.572	0.526	0.605	0.612	**0.715**
Image 59	8.31	9.57	9.55	10.20	**11.19**	0.591	0.478	0.597	0.575	**0.745**
Image 60	8.46	5.64	9.88	10.61	**11.12**	0.570	0.368	0.622	0.614	**0.682**
Image 61	8.49	6.45	8.91	9.63	**10.57**	0.617	0.264	0.592	0.622	**0.704**
Image 62	8.45	10.00	10.37	10.88	**11.34**	0.549	0.523	0.583	0.600	**0.632**
Image 63	8.35	8.93	10.59	11.43	**11.72**	0.543	0.512	0.610	0.596	**0.649**
Image 64	8.48	5.23	9.38	10.55	**11.23**	0.580	0.352	0.612	0.603	**0.687**
Image 65	8.44	6.44	9.29	10.17	**11.19**	0.542	0.335	0.580	0.606	**0.649**
Image 66	8.25	5.99	8.42	9.35	**10.71**	0.617	0.330	0.611	0.657	**0.734**
Image 67	8.39	9.63	9.32	10.11	**10.95**	0.609	0.551	0.599	0.621	**0.784**
Image 68	8.48	5.29	9.99	10.55	**11.01**	0.589	0.375	0.635	0.607	**0.681**
Image 69	8.57	10.80	10.59	11.41	**11.81**	0.533	0.501	0.608	0.616	**0.646**
Image 70	8.41	10.69	10.55	11.43	**11.77**	0.517	0.453	0.577	0.590	**0.618**
Image 71	8.38	9.24	9.67	10.74	**11.45**	0.577	0.430	0.599	0.614	**0.719**
Image 72	8.41	6.13	8.66	9.52	**10.57**	0.568	0.287	0.584	0.623	**0.675**
Image 73	8.27	4.53	8.07	8.71	**10.31**	0.675	0.275	0.630	0.615	**0.765**
Image 74	8.58	11.62	10.45	11.62	**11.76**	0.510	0.469	0.580	0.586	**0.641**
Image 75	8.52	7.40	10.69	11.58	**11.83**	0.537	0.402	0.600	0.611	**0.614**
Image 76	8.56	6.33	9.90	10.60	**11.32**	0.581	0.396	0.635	0.598	**0.690**
Image 77	8.54	10.52	10.66	11.71	**11.80**	0.502	0.512	0.570	0.592	**0.609**
Image 78	8.38	8.33	9.32	10.10	**10.95**	0.622	0.390	0.624	0.615	**0.715**
Image 79	8.41	8.88	9.97	10.64	**11.23**	0.562	0.493	0.589	0.572	**0.687**
Image 80	8.37	6.45	9.68	10.32	**10.96**	0.581	0.235	0.604	0.598	**0.680**
Image 81	8.46	8.62	10.08	11.20	**12.52**	0.483	0.376	0.585	0.597	**0.623**
Image 82	7.98	6.07	6.73	8.38	**10.37**	0.654	0.368	0.561	0.631	**0.789**
Image 83	8.44	7.54	9.96	10.55	**11.05**	0.580	0.519	0.604	0.597	**0.648**
Image 84	8.51	9.41	9.65	10.67	**10.80**	0.626	0.524	0.646	0.628	**0.732**
Image 85	8.26	5.31	7.81	9.14	**10.50**	0.610	0.267	0.585	0.608	**0.717**
Image 86	8.20	5.79	7.36	8.69	**10.46**	0.646	0.281	0.567	0.634	**0.771**
Image 87	8.25	7.16	7.89	9.19	**10.60**	0.621	0.359	0.564	0.627	**0.761**
Image 88	8.46	8.49	10.62	11.51	**11.72**	0.517	0.457	0.588	0.596	**0.621**

Table A.28 continued from previous page

	SNR (dB)					SSIM				
Image 89	8.50	9.31	9.94	10.47	**11.07**	0.611	0.586	0.613	0.638	**0.730**
Image 90	8.44	6.95	10.51	11.08	**11.52**	0.556	0.524	0.625	0.603	**0.659**
Image 91	8.52	6.62	8.98	10.06	**10.99**	0.573	0.321	0.599	0.622	**0.685**
Image 92	8.46	7.64	10.23	11.16	**11.40**	0.564	0.397	0.633	0.607	**0.669**
Image 93	8.17	6.68	8.18	9.02	**10.78**	0.640	0.306	0.602	0.621	**0.724**
Image 94	8.47	6.97	9.88	10.84	**11.16**	0.572	0.320	0.616	0.620	**0.690**
Image 95	8.58	6.72	10.34	11.12	**11.41**	0.577	0.402	0.639	0.609	**0.683**
Image 96	8.36	5.95	9.12	9.79	**11.18**	0.601	0.260	0.592	0.639	**0.735**
Image 97	8.27	9.30	9.68	10.29	**11.07**	0.599	0.577	0.619	0.596	**0.740**
Image 98	8.51	10.71	10.82	**11.78**	11.60	0.528	0.476	0.616	0.593	**0.644**
Image 99	8.42	10.63	10.52	11.16	**11.59**	0.566	0.485	0.611	0.621	**0.667**
Image 100	7.82	6.28	5.80	7.54	**10.11**	0.651	0.621	0.491	0.588	**0.822**
Image 101	8.54	9.69	10.28	10.77	**11.38**	0.577	0.504	0.620	0.606	**0.666**
Image 102	8.50	8.82	10.21	10.84	**11.35**	0.560	0.472	0.603	0.606	**0.656**
Image 103	8.49	9.87	11.48	12.17	**12.38**	0.392	0.445	0.510	**0.532**	0.509
Image 104	8.48	7.83	10.16	10.60	**11.17**	0.584	0.523	0.602	0.606	**0.650**
Image 105	8.21	10.32	9.31	10.09	**10.91**	0.602	0.604	0.592	0.611	**0.775**
Image 106	8.31	6.48	9.38	10.24	**10.97**	0.578	0.371	0.622	0.623	**0.686**
Image 107	8.44	9.70	9.74	10.13	**10.92**	0.607	0.495	0.615	0.639	**0.705**
Image 108	8.54	3.78	10.23	10.84	**11.18**	0.603	0.388	0.647	0.599	**0.690**
Image 109	8.42	6.11	8.76	9.92	**10.94**	0.605	0.374	0.624	0.633	**0.711**
Image 110	8.55	10.65	11.47	**12.85**	12.56	0.430	0.471	0.542	**0.576**	0.562
Average	8.41	8.22	9.65	10.49	**11.20**	0.576	0.439	0.601	0.608	**0.688**

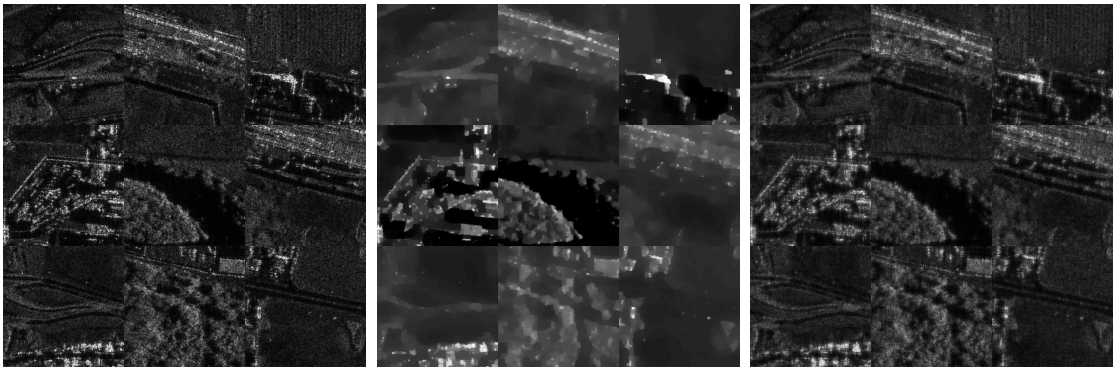

(a) FFT-based (b) NQR-based (c) DL-based

(d) PnP-BM3D (e) PnP-CNN-SAR (f) Ground Truth

Figure A.28 Reconstruction results for Images 19, 40, 45, 46, 59, 61, 66, 96, and 109 from the Kapıkule test set for the case of 70% data availability and $\sigma_{\mathbf{n}} = 0.1\sigma_{\mathbf{y}}$.

A.3.5 Experiment 5: 50% Data Availability and $\sigma_{\mathbf{n}} = 0.1\sigma_{\mathbf{y}}$

Table A.29 shows the SNR and SSIM values for this experiment. PnP-CNN-SAR gives the best SNR for 37 images, and best SSIM for 101 images. Fig. A.29 shows the reconstruction results for a selection of images from the Kapıkule test set from all methods for this experiment. PnP-CNN-SAR produce better reconstructions compared to other methods.

Table A.29 SNR and SSIM values for images from the KapıkuleTest Set for the case of 50% data availability and $\sigma_{\mathbf{n}} = 0.1\sigma_{\mathbf{y}}$. Best results are shown in bold, second best results are shown in red.

	SNR (dB)					SSIM				
	FFT-based	NQR-based	DL-based	PnP-BM3D	PnP-CNN-SAR	FFT-based	NQR-based	DL-based	PnP-BM3D	PnP-CNN-SAR
Image 1	6.45	8.67	8.25	**9.51**	8.72	0.379	0.463	0.422	0.411	**0.480**
Image 2	6.29	**9.11**	7.65	8.93	8.90	0.346	0.440	0.468	0.402	**0.529**
Image 3	6.46	7.29	8.24	**10.13**	8.81	0.311	0.452	0.442	0.420	**0.461**
Image 4	6.42	5.98	7.52	**8.47**	8.41	0.339	0.355	0.475	0.421	**0.523**
Image 5	6.05	6.29	6.42	6.92	**7.88**	0.459	0.333	0.432	0.452	**0.621**
Image 6	6.45	**10.90**	8.51	10.40	8.96	0.300	0.420	0.422	0.405	**0.445**
Image 7	6.36	7.99	7.67	**8.66**	8.39	0.341	0.329	0.457	0.417	**0.503**
Image 8	6.28	6.79	7.20	**8.08**	7.92	0.361	0.296	0.464	0.439	**0.533**
Image 9	6.06	6.18	6.52	7.46	**8.28**	0.416	0.278	0.427	0.444	**0.550**
Image 10	6.40	8.07	7.89	8.70	**8.83**	0.399	0.382	0.502	0.464	**0.594**
Image 11	6.47	8.64	8.29	**9.82**	9.22	0.355	0.434	0.458	0.402	**0.508**
Image 12	5.88	5.08	5.27	5.91	**7.52**	0.466	0.497	0.412	0.442	**0.635**
Image 13	6.25	**8.79**	7.32	8.15	8.58	0.399	0.517	0.483	0.437	**0.615**
Image 14	6.42	8.58	7.96	**9.18**	8.62	0.318	0.319	0.436	0.404	**0.471**
Image 15	6.34	9.23	8.13	**9.68**	8.77	0.307	0.427	0.504	0.446	**0.524**
Image 16	5.82	4.95	5.34	5.63	**8.04**	0.400	0.363	0.450	0.434	**0.723**
Image 17	6.51	6.91	8.37	**10.59**	8.98	0.293	**0.447**	0.405	0.424	0.418
Image 18	6.49	5.70	8.04	**9.76**	8.63	0.302	0.372	0.484	0.426	**0.498**
Image 19	6.32	6.15	7.28	8.15	**8.24**	0.412	0.280	0.473	0.435	**0.540**
Image 20	6.16	5.72	6.60	7.36	**8.03**	0.369	0.333	0.476	0.449	**0.576**
Image 21	6.33	7.98	7.63	8.60	**8.92**	0.370	0.449	0.466	0.419	**0.567**
Image 22	6.31	8.13	7.56	8.37	**8.81**	0.380	0.435	0.486	0.411	**0.601**
Image 23	6.43	8.36	8.13	**9.25**	8.84	0.376	0.314	0.434	0.388	**0.502**
Image 24	6.36	7.35	7.76	**9.17**	8.95	0.312	0.448	0.504	0.457	**0.536**
Image 25	6.52	8.94	8.77	**11.55**	9.16	0.250	0.387	0.371	**0.399**	0.365
Image 26	6.33	**8.61**	7.53	8.60	8.49	0.387	0.459	0.485	0.441	**0.560**
Image 27	6.51	6.08	8.40	**10.21**	9.05	0.327	0.401	0.472	0.410	**0.486**
Image 28	6.54	9.91	8.37	**10.26**	9.18	0.291	0.416	0.431	0.394	**0.452**
Image 29	6.37	7.85	7.66	**8.52**	8.45	0.427	0.328	0.461	0.417	**0.545**
Image 30	6.44	9.14	8.07	**9.32**	8.73	0.354	0.462	0.445	0.410	**0.498**
Image 31	6.45	8.99	8.00	**9.04**	8.58	0.370	0.374	0.455	0.363	**0.501**
Image 32	6.38	5.45	8.11	**9.24**	8.72	0.375	0.457	0.430	0.392	**0.471**
Image 33	6.40	9.43	8.06	**9.64**	9.22	0.322	0.496	0.456	0.414	**0.512**
Image 34	6.44	**8.73**	7.42	8.13	8.69	0.368	0.530	0.488	0.429	**0.611**
Image 35	6.51	**9.60**	8.01	9.14	8.73	0.389	0.461	0.454	0.422	**0.521**
Image 36	6.32	7.58	7.73	9.06	**9.12**	0.356	0.429	0.465	0.416	**0.556**
Image 37	6.43	6.72	8.21	**9.65**	8.67	0.319	**0.437**	0.407	0.392	0.425
Image 38	6.55	8.99	8.41	**10.19**	9.04	0.330	**0.433**	0.404	0.402	0.430
Image 39	6.48	4.61	8.27	**9.89**	8.80	0.329	**0.447**	0.411	0.440	0.437
Image 40	6.25	7.11	7.42	8.10	**8.17**	0.387	0.284	0.446	0.426	**0.534**
Image 41	6.47	9.68	8.08	**10.01**	9.08	0.290	0.414	0.474	0.422	**0.503**
Image 42	6.48	5.65	8.09	**9.48**	8.75	0.334	0.433	0.408	0.392	**0.450**
Image 43	6.35	8.47	7.85	8.86	**8.93**	0.367	0.504	0.496	0.440	**0.589**
Image 44	6.50	8.10	7.86	**9.07**	8.56	0.366	0.457	0.528	0.462	**0.559**
Image 45	5.99	5.59	6.60	7.09	**8.01**	0.411	0.262	0.456	0.417	**0.573**
Image 46	5.81	4.37	5.08	5.76	**7.67**	0.459	0.466	0.409	0.448	**0.670**
Image 47	6.35	8.66	7.85	**8.91**	8.63	0.355	0.388	0.488	0.410	**0.525**
Image 48	6.34	8.23	7.44	8.31	**8.43**	0.392	0.488	0.481	0.427	**0.564**
Image 49	6.53	**11.43**	8.82	11.25	9.25	0.258	0.441	**0.443**	0.420	0.440
Image 50	6.17	5.68	7.32	8.09	**8.72**	0.392	0.311	0.507	0.450	**0.636**
Image 51	6.30	7.28	7.23	7.83	**8.00**	0.369	0.371	0.473	0.420	**0.527**
Image 52	6.41	**10.60**	8.31	10.31	9.43	0.286	0.453	0.452	0.402	**0.494**
Image 53	6.03	4.67	6.57	7.17	**8.16**	0.390	0.319	0.467	0.434	**0.576**
Image 54	6.38	9.28	8.15	**9.54**	9.15	0.311	0.362	0.458	0.394	**0.506**
Image 55	6.34	**9.95**	8.37	9.70	9.13	0.374	0.440	0.464	0.416	**0.519**
Image 56	6.47	7.99	7.66	**8.79**	8.61	0.366	0.397	0.473	0.419	**0.527**
Image 57	6.31	5.46	7.04	7.93	**8.54**	0.393	0.306	0.476	0.429	**0.547**
Image 58	6.35	9.16	7.90	**9.29**	9.11	0.356	0.492	0.471	0.428	**0.560**
Image 59	6.30	8.63	7.58	8.73	**8.85**	0.343	0.486	0.479	0.410	**0.584**
Image 60	6.38	8.79	7.70	**8.85**	8.55	0.337	0.398	0.475	0.420	**0.522**
Image 61	6.21	6.25	7.18	7.83	**8.08**	0.402	0.252	0.449	0.423	**0.553**
Image 62	6.42	**9.93**	8.20	9.25	8.73	0.365	0.387	0.415	0.362	**0.466**
Image 63	6.50	7.92	8.32	**10.09**	9.01	0.313	**0.482**	0.455	0.429	**0.482**
Image 64	6.37	6.12	7.59	**8.73**	8.61	0.355	0.327	0.467	0.418	**0.522**
Image 65	6.25	7.05	7.30	**8.44**	8.43	0.326	0.306	0.436	0.418	**0.499**
Image 66	6.07	5.51	6.59	7.31	**8.05**	0.399	0.285	0.469	0.466	**0.576**
Image 67	6.25	7.87	7.36	8.22	**8.66**	0.397	0.413	0.472	0.430	**0.628**
Image 68	6.43	**8.97**	7.84	8.95	8.51	0.337	0.453	0.489	0.404	**0.527**
Image 69	6.47	**10.25**	8.34	9.83	9.02	0.330	0.444	0.449	0.408	**0.479**
Image 70	6.43	9.25	8.21	**9.91**	8.72	0.320	0.387	0.402	0.382	**0.432**
Image 71	6.38	9.01	7.65	8.98	**9.04**	0.348	0.455	0.469	0.428	**0.567**
Image 72	6.26	6.39	6.98	7.46	**7.82**	0.354	0.301	0.429	0.413	**0.511**
Image 73	6.08	4.84	6.48	6.79	**7.76**	0.454	0.269	0.495	0.434	**0.611**
Image 74	6.49	9.83	8.27	**10.13**	9.07	0.305	0.438	0.431	0.400	**0.470**
Image 75	6.55	6.72	8.40	**10.27**	8.78	0.300	0.383	0.444	0.444	**0.451**
Image 76	6.37	8.66	7.68	**9.05**	8.62	0.322	0.412	0.489	0.429	**0.528**
Image 77	6.49	**10.69**	8.41	10.29	8.82	0.305	0.418	0.404	0.392	**0.420**
Image 78	6.31	7.78	7.34	8.17	**8.28**	0.386	0.356	0.469	0.403	**0.541**
Image 79	6.33	**9.29**	7.79	9.07	9.01	0.341	0.436	0.444	0.373	**0.512**
Image 80	6.36	7.37	7.65	**8.71**	8.55	0.375	0.247	0.444	0.372	**0.493**
Image 81	6.43	8.81	7.95	**9.44**	8.58	0.259	0.371	0.449	0.408	**0.465**
Image 82	5.87	4.01	5.59	6.24	**7.87**	0.454	0.247	0.444	0.458	**0.657**
Image 83	6.42	8.01	7.96	**8.95**	8.46	0.361	0.408	0.449	0.411	**0.491**
Image 84	6.27	8.08	7.62	8.65	**8.75**	0.376	0.456	0.526	0.475	**0.598**
Image 85	6.07	5.27	6.32	7.01	**7.82**	0.416	0.261	0.441	0.402	**0.556**
Image 86	5.97	4.37	6.01	6.43	**7.80**	0.465	0.207	0.426	0.424	**0.618**
Image 87	6.11	6.58	6.50	6.85	**8.18**	0.438	0.327	0.435	0.408	**0.600**
Image 88	6.51	9.88	8.38	**9.90**	9.01	0.317	0.395	0.428	0.376	**0.456**

Table A.29 continued from previous page

	SNR (dB)					SSIM				
Image 89	6.36	**9.08**	7.83	8.71	8.63	0.420	0.481	0.463	0.424	**0.550**
Image 90	6.39	9.36	8.25	**9.71**	8.69	0.319	0.473	0.470	0.446	**0.494**
Image 91	6.30	6.87	7.12	7.91	**8.05**	0.365	0.311	0.460	0.424	**0.531**
Image 92	6.37	8.55	8.07	**9.69**	8.78	0.306	0.388	0.492	0.433	**0.514**
Image 93	6.12	5.46	6.66	7.33	**7.67**	0.418	0.268	0.454	0.436	**0.565**
Image 94	6.41	8.33	7.87	**8.93**	8.67	0.361	0.376	0.469	0.410	**0.516**
Image 95	6.42	7.67	8.25	**9.80**	8.86	0.318	0.401	0.504	0.437	**0.528**
Image 96	6.27	7.48	7.27	8.01	**8.50**	0.427	0.366	0.446	0.429	**0.565**
Image 97	6.26	8.53	7.74	8.54	**8.88**	0.356	0.495	0.504	0.433	**0.593**
Image 98	6.49	7.22	8.50	**10.56**	9.11	0.292	0.407	0.466	0.403	**0.482**
Image 99	6.37	**9.89**	8.19	9.51	8.81	0.360	0.438	0.446	0.398	**0.497**
Image 100	5.71	4.72	4.79	5.13	**7.91**	0.413	0.375	0.407	0.402	**0.702**
Image 101	6.34	8.86	8.10	**9.27**	8.67	0.364	0.406	0.462	0.417	**0.503**
Image 102	6.34	9.19	8.08	**9.44**	8.68	0.349	0.419	0.449	0.424	**0.491**
Image 103	6.51	**10.74**	8.90	10.71	9.51	0.230	**0.336**	0.326	0.319	0.323
Image 104	6.37	6.33	8.03	**9.03**	8.44	0.392	0.379	0.430	0.407	**0.479**
Image 105	6.29	**8.87**	7.30	8.16	8.72	0.377	0.555	0.479	0.435	**0.638**
Image 106	6.22	6.04	7.31	**8.42**	8.41	0.340	0.356	0.475	0.437	**0.536**
Image 107	6.30	**8.79**	7.58	8.49	8.29	0.438	0.422	0.438	0.423	**0.526**
Image 108	6.38	8.49	8.06	**9.37**	8.89	0.345	0.377	0.505	0.432	**0.541**
Image 109	6.26	6.03	7.05	7.92	**8.33**	0.361	0.354	0.489	0.459	**0.567**
Image 110	6.54	10.21	8.87	**11.64**	9.53	0.247	**0.394**	0.371	0.368	0.368
Average	6.33	7.78	7.63	**8.81**	8.62	0.358	0.393	0.455	0.419	**0.527**

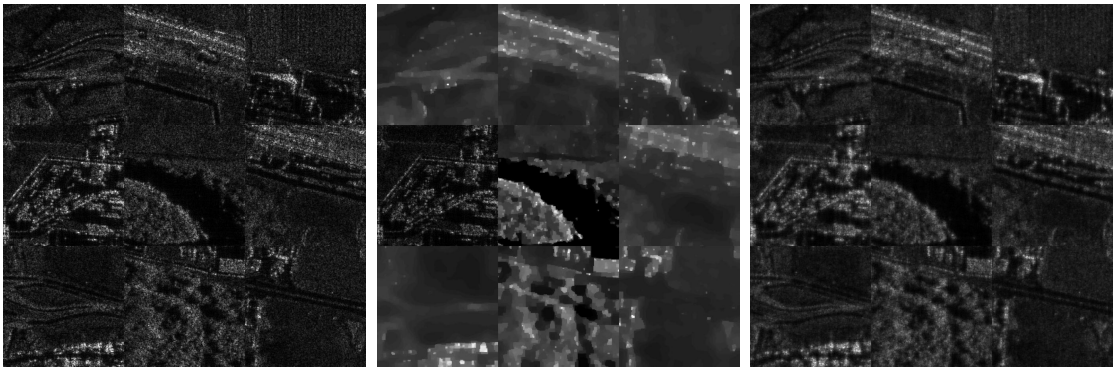

(a) FFT-based (b) NQR-based (c) DL-based

(d) PnP-BM3D (e) PnP-CNN-SAR (f) Ground Truth

Figure A.29 Reconstruction results for Images 19, 40, 45, 46, 59, 61, 66, 96, and 109 from the Kapıkule test set for the case of 50% data availability and $\sigma_{\mathbf{n}} = 0.1\sigma_{\mathbf{y}}$.

A.3.6 Experiment 6: 30% Data Availability and $\sigma_{\mathbf{n}} = 0.1\sigma_{\mathbf{y}}$

Table A.30 shows the SNR and SSIM values for this experiment. PnP-CNN-SAR gives the best SNR for 7 images, and best SSIM for 63 images. Fig. A.30 shows the reconstruction results for a selection of images from the Kapıkule test set from all methods for this experiment. PnP-CNN-SAR produce better reconstructions compared to other methods.

Table A.30 SNR and SSIM values for images from the KapıkuleTest Set for the case of 30% data availability and $\sigma_{\mathbf{n}} = 0.1\sigma_{\mathbf{y}}$. Best results are shown in bold, second best results are shown in red.

	SNR (dB)					SSIM				
	FFT-based	NQR-based	DL-based	PnP-BM3D	PnP-CNN-SAR	FFT-based	NQR-based	DL-based	PnP-BM3D	PnP-CNN-SAR
Image 1	4.77	**9.07**	6.04	7.15	5.83	0.232	**0.392**	0.281	0.303	0.313
Image 2	4.65	**8.15**	5.79	6.79	6.51	0.211	0.364	0.367	0.323	**0.410**
Image 3	4.76	6.62	6.15	**7.74**	6.05	0.176	0.370	0.332	**0.377**	0.338
Image 4	4.77	5.67	5.63	**6.67**	5.78	0.204	0.330	0.370	0.347	**0.394**
Image 5	4.33	4.66	4.84	**5.37**	5.19	0.295	0.197	0.315	0.319	**0.422**
Image 6	4.75	**9.71**	6.07	7.59	6.13	0.196	**0.374**	0.291	0.308	0.317
Image 7	4.66	**7.51**	5.70	6.75	5.62	0.193	0.316	0.335	0.333	**0.359**
Image 8	4.68	5.94	5.42	**6.39**	5.53	0.208	0.285	0.345	0.342	**0.389**
Image 9	4.41	4.34	4.91	**5.62**	5.61	0.268	0.198	0.300	0.294	**0.408**
Image 10	4.71	**7.57**	5.75	6.84	6.64	0.253	0.348	0.381	0.354	**0.439**
Image 11	4.78	**9.28**	6.25	7.44	6.30	0.230	**0.367**	0.350	0.310	0.364
Image 12	4.23	4.70	4.06	4.68	**4.83**	0.292	0.425	0.298	0.314	**0.431**
Image 13	4.63	**7.55**	5.47	6.26	6.73	0.265	0.397	0.378	0.342	**0.456**
Image 14	4.82	6.28	5.95	**7.11**	5.97	0.186	0.298	0.324	0.301	**0.341**
Image 15	4.75	**7.88**	6.01	7.45	6.04	0.177	0.390	0.400	0.390	**0.407**
Image 16	4.08	2.77	4.07	4.47	**5.42**	0.281	0.179	0.377	0.360	**0.562**
Image 17	4.82	**8.29**	6.24	7.84	6.10	0.165	**0.423**	0.292	0.375	0.295
Image 18	4.74	**8.74**	6.08	7.45	5.87	0.176	**0.419**	0.377	0.365	0.387
Image 19	4.58	**6.82**	5.39	6.42	5.82	0.254	0.338	0.344	0.323	**0.394**
Image 20	4.44	5.05	5.05	**5.71**	5.54	0.234	0.298	0.367	0.355	**0.426**
Image 21	4.65	**8.11**	5.58	6.60	6.42	0.233	**0.465**	0.343	0.339	0.434
Image 22	4.68	4.53	5.51	6.48	**6.61**	0.255	0.217	0.381	0.334	**0.461**
Image 23	4.77	**8.95**	5.90	7.10	6.07	0.238	**0.345**	0.287	0.251	0.337
Image 24	4.77	**7.62**	5.93	7.16	5.95	0.188	**0.420**	0.412	0.404	**0.420**
Image 25	4.86	7.10	6.49	**8.38**	6.12	0.136	0.295	0.263	**0.357**	0.259
Image 26	4.63	**7.30**	5.66	6.61	5.95	0.247	0.351	0.366	0.335	**0.403**
Image 27	4.79	5.18	6.18	**7.66**	6.16	0.180	0.258	0.357	0.357	**0.368**
Image 28	4.79	**9.95**	6.32	7.75	6.22	0.173	**0.374**	0.327	0.318	0.328
Image 29	4.79	**8.05**	5.76	6.51	6.01	0.278	**0.393**	0.324	0.269	0.360
Image 30	4.74	**8.25**	5.98	7.07	6.05	0.215	0.341	0.320	0.308	**0.345**
Image 31	4.71	**7.20**	5.94	7.11	5.95	0.228	0.334	0.325	0.269	**0.355**
Image 32	4.74	6.81	5.94	**7.32**	6.03	0.226	**0.373**	0.293	0.327	0.328
Image 33	4.65	**7.39**	5.98	7.38	6.83	0.193	**0.428**	0.356	0.362	0.381
Image 34	4.76	**7.54**	5.47	6.31	6.59	0.243	0.478	0.386	0.339	**0.483**
Image 35	4.69	**8.23**	5.93	6.95	6.03	0.258	**0.391**	0.314	0.285	0.349
Image 36	4.63	**7.85**	5.73	6.98	6.44	0.223	**0.418**	0.351	0.335	0.395
Image 37	4.86	6.56	6.08	**7.45**	6.01	0.185	**0.382**	0.273	0.327	0.298
Image 38	4.82	7.27	6.20	**7.76**	6.01	0.178	0.319	0.281	**0.330**	0.300
Image 39	4.76	**8.86**	6.13	7.52	6.00	0.192	**0.436**	0.289	0.375	0.304
Image 40	4.71	5.98	5.48	**6.29**	5.57	0.246	0.256	0.319	0.302	**0.379**
Image 41	4.76	**8.48**	6.06	7.44	6.10	0.169	0.363	0.380	0.367	**0.381**
Image 42	4.78	**7.33**	5.99	7.28	6.01	0.216	**0.354**	0.286	0.292	0.322
Image 43	4.78	**6.91**	5.85	6.84	6.75	0.237	**0.454**	0.393	0.359	0.453
Image 44	4.75	**7.35**	5.85	6.99	5.85	0.205	**0.460**	0.411	0.392	0.433
Image 45	4.38	5.12	5.00	**5.56**	5.24	0.263	0.223	0.338	0.303	**0.410**
Image 46	4.11	2.86	3.94	4.42	**4.78**	0.302	0.180	0.297	0.314	**0.440**
Image 47	4.63	**7.16**	5.69	7.05	5.93	0.207	0.381	0.362	0.348	**0.385**
Image 48	4.67	**6.98**	5.55	6.43	6.07	0.235	0.332	0.360	0.318	**0.424**
Image 49	4.79	3.76	6.51	**8.30**	6.18	0.142	0.183	0.345	**0.371**	0.331
Image 50	4.72	**7.26**	5.41	6.37	6.51	0.254	0.408	0.411	0.381	**0.493**
Image 51	4.55	**6.53**	5.37	6.28	5.65	0.232	**0.440**	0.360	0.331	0.389
Image 52	4.72	**9.89**	6.13	7.61	6.47	0.172	0.393	0.357	0.345	**0.395**
Image 53	4.43	4.57	4.97	**5.60**	5.45	0.235	0.290	0.356	0.343	**0.411**
Image 54	4.72	**8.95**	5.92	7.24	6.44	0.184	0.370	0.349	0.334	**0.382**
Image 55	4.80	**9.44**	6.10	7.39	6.27	0.234	**0.378**	0.341	0.306	0.375
Image 56	4.74	**7.67**	5.79	6.82	5.90	0.223	0.358	0.357	0.334	**0.390**
Image 57	4.66	5.75	5.21	**6.23**	5.60	0.233	0.274	0.350	0.325	**0.397**
Image 58	4.76	**8.50**	5.78	6.94	6.51	0.221	**0.423**	0.359	0.323	0.410
Image 59	4.60	**7.72**	5.69	6.70	6.89	0.225	0.367	0.380	0.328	**0.469**
Image 60	4.74	**7.83**	5.73	6.96	5.80	0.205	0.344	0.367	0.346	**0.386**
Image 61	4.56	4.91	5.36	**6.20**	5.44	0.246	0.226	0.319	0.306	**0.394**
Image 62	4.81	**7.13**	6.07	**7.13**	6.01	0.215	**0.326**	0.277	0.252	0.302
Image 63	4.75	7.46	6.04	**7.51**	6.11	0.174	**0.439**	0.343	0.379	0.351
Image 64	4.62	**7.40**	5.68	6.62	6.08	0.216	0.376	0.353	0.325	**0.389**
Image 65	4.64	5.90	5.50	**6.44**	5.74	0.196	0.293	0.332	0.325	**0.368**
Image 66	4.50	5.19	4.94	**5.86**	5.28	0.250	0.268	0.348	0.352	**0.412**
Image 67	4.68	**7.44**	5.50	6.30	6.40	0.267	0.423	0.359	0.308	**0.458**
Image 68	4.69	**8.36**	5.89	7.11	5.77	0.187	**0.420**	0.377	0.351	0.398
Image 69	4.84	**8.25**	6.11	7.44	6.10	0.208	**0.370**	0.327	0.315	0.342
Image 70	4.79	6.46	6.12	**7.56**	6.07	0.181	**0.354**	0.286	0.309	0.303
Image 71	4.67	**7.39**	5.70	6.79	6.51	0.227	0.396	0.368	0.340	**0.437**
Image 72	4.59	**5.98**	5.28	5.97	5.39	0.214	0.258	0.313	0.309	**0.358**
Image 73	4.42	3.11	4.85	**5.43**	5.37	0.281	0.243	0.371	0.336	**0.454**
Image 74	4.77	**9.30**	6.10	7.44	6.23	0.186	**0.374**	0.323	0.313	0.342
Image 75	4.82	**7.82**	6.28	7.75	6.05	0.175	**0.418**	0.327	0.390	0.336
Image 76	4.68	**8.39**	5.84	7.06	5.93	0.195	**0.439**	0.385	0.366	0.406
Image 77	4.80	**9.23**	6.15	7.63	6.15	0.189	**0.368**	0.281	0.312	0.292
Image 78	4.59	**7.51**	5.62	6.58	5.81	0.236	0.342	0.352	0.317	**0.397**
Image 79	4.74	**7.79**	5.86	6.96	6.51	0.208	0.320	0.335	0.297	**0.386**
Image 80	4.73	**7.95**	5.77	6.80	6.00	0.227	0.290	0.310	0.265	**0.343**
Image 81	4.86	**7.58**	5.98	7.07	5.86	0.146	**0.365**	0.350	0.356	0.354
Image 82	4.27	3.08	4.21	4.88	**5.10**	0.288	0.218	0.330	0.328	**0.473**
Image 83	4.77	**7.72**	5.91	6.96	5.92	0.209	**0.433**	0.315	0.344	0.345
Image 84	4.73	**7.39**	5.61	6.68	6.77	0.229	0.412	0.417	0.404	**0.468**
Image 85	4.35	4.57	4.69	**5.59**	5.39	0.256	0.228	0.316	0.306	**0.407**
Image 86	4.33	3.85	4.58	5.10	**5.17**	0.303	0.165	0.298	0.292	**0.428**
Image 87	4.43	4.77	4.85	**5.56**	5.46	0.281	0.174	0.308	0.293	**0.419**
Image 88	4.88	**9.21**	6.15	7.52	6.10	0.185	**0.362**	0.309	0.286	0.315

Table A.30 continued from previous page

	SNR (dB)					SSIM				
Image 89	4.77	**8.49**	5.85	6.73	6.12	0.274	**0.416**	0.329	0.286	0.375
Image 90	4.75	**7.85**	6.01	7.45	6.10	0.182	**0.460**	0.357	0.395	0.370
Image 91	4.72	**6.38**	5.40	6.13	5.56	0.220	0.280	0.342	0.323	**0.398**
Image 92	4.79	5.81	5.99	**7.30**	6.09	0.178	0.368	0.391	0.380	**0.397**
Image 93	4.48	5.26	4.91	**5.72**	5.38	0.265	0.226	0.328	0.307	**0.398**
Image 94	4.76	**8.58**	5.80	6.98	5.92	0.221	**0.414**	0.351	0.313	0.368
Image 95	4.77	5.60	5.99	**7.44**	6.01	0.190	**0.417**	0.390	0.375	0.403
Image 96	4.64	**7.31**	5.48	6.27	5.97	0.282	0.308	0.310	0.278	**0.376**
Image 97	4.62	**7.63**	5.59	6.54	6.47	0.225	0.428	0.391	0.360	**0.476**
Image 98	4.85	6.06	6.18	**7.80**	6.20	0.175	0.336	0.355	0.338	**0.359**
Image 99	4.72	**9.11**	5.98	7.24	6.09	0.231	**0.379**	0.310	0.293	0.341
Image 100	4.04	4.09	3.79	4.19	**5.20**	0.276	0.444	0.332	0.321	**0.533**
Image 101	4.82	**7.55**	5.88	7.17	6.03	0.218	**0.382**	0.335	0.342	0.357
Image 102	4.71	**8.49**	5.98	7.21	6.12	0.216	**0.365**	0.329	0.336	0.348
Image 103	4.90	**8.14**	6.57	7.88	6.29	0.128	**0.274**	0.227	0.241	0.224
Image 104	4.85	**7.89**	5.84	7.12	5.97	0.242	**0.385**	0.286	0.317	0.326
Image 105	4.59	**7.33**	5.56	6.28	6.79	0.261	0.409	0.385	0.346	**0.473**
Image 106	4.62	5.14	5.53	**6.50**	5.69	0.209	0.329	0.370	0.348	**0.401**
Image 107	4.73	**7.40**	5.58	6.49	5.84	0.281	0.249	0.291	0.250	**0.357**
Image 108	4.68	7.07	5.93	**7.32**	5.98	0.197	0.353	0.391	0.373	**0.401**
Image 109	4.55	5.88	5.26	**6.30**	5.52	0.219	0.328	0.378	0.378	**0.420**
Image 110	4.85	7.77	6.51	**8.27**	6.25	0.138	0.298	0.263	**0.322**	0.263
Average	4.67	**7.01**	5.67	6.77	5.98	0.220	0.346	0.339	0.330	**0.384**

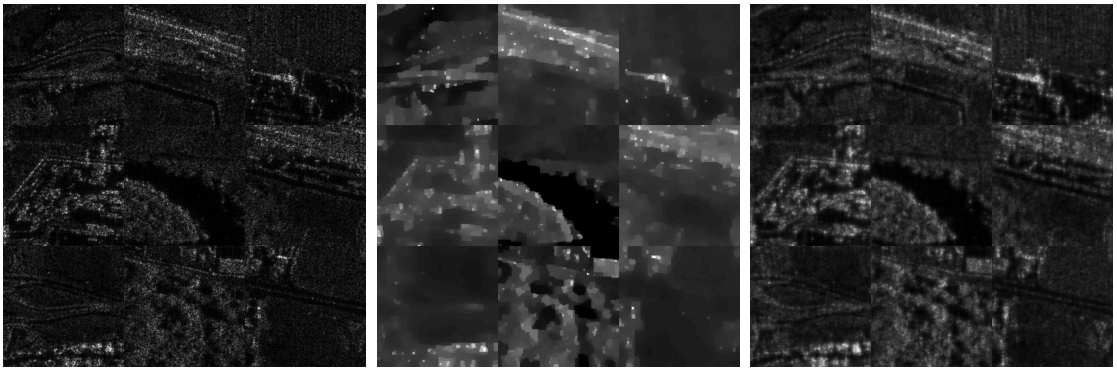

(a) FFT-based (b) NQR-based (c) DL-based

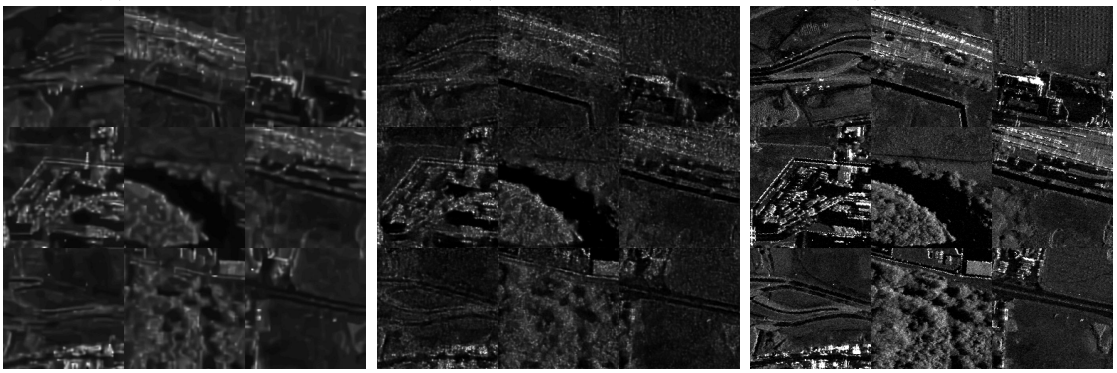

(d) PnP-BM3D (e) PnP-CNN-SAR (f) Ground Truth

Figure A.30 Reconstruction results for Images 19, 40, 45, 46, 59, 61, 66, 96, and 109 from the Kapıkule test set for the case of 30% data availability and $\sigma_{\mathbf{n}} = 0.1\sigma_{\mathbf{y}}$.

A.3.7 Experiment 7: 100% Data Availability and $\sigma_{\mathbf{n}} = \sigma_{\mathbf{y}}$

Table A.31 shows the SNR and SSIM values for this experiment. PnP-CNN-SAR gives the best SNR and best SSIM for all 110 images. Fig. A.31 shows the reconstruction results for a selection of images from the Kapıkule test set from all methods for this experiment. PnP-CNN-SAR produce better reconstructions compared to other methods.

Table A.31 SNR and SSIM values for images from the KapıkuleTest Set for the case of 100% data availability and $\sigma_{\mathbf{n}} = \sigma_{\mathbf{y}}$. Best results are shown in bold, second best results are shown in red.

	SNR (dB)					SSIM				
	FFT-based	NQR-based	DL-based	PnP-BM3D	PnP-CNN-SAR	FFT-based	NQR-based	DL-based	PnP-BM3D	PnP-CNN-SAR
Image 1	6.68	8.88	11.36	6.76	**35.90**	0.603	0.593	0.651	0.472	**0.998**
Image 2	6.45	11.09	10.68	6.57	**35.52**	0.591	0.606	0.638	0.461	**0.996**
Image 3	6.93	10.64	12.18	7.20	**33.40**	0.607	0.534	0.678	0.473	**0.997**
Image 4	6.84	10.35	11.29	6.97	**35.02**	0.611	0.507	0.673	0.467	**0.998**
Image 5	6.07	8.51	9.66	6.14	**34.62**	0.583	0.500	0.606	0.454	**0.994**
Image 6	6.90	11.60	12.05	6.99	**36.60**	0.571	0.552	0.642	0.423	**0.998**
Image 7	6.82	11.02	11.44	6.97	**35.33**	0.554	0.513	0.617	0.415	**0.998**
Image 8	6.78	10.38	11.07	6.97	**36.49**	0.579	0.489	0.634	0.433	**0.999**
Image 9	6.34	9.40	9.99	6.48	**37.86**	0.606	0.520	0.632	0.475	**0.996**
Image 10	6.24	10.61	10.46	6.32	**39.05**	0.584	0.625	0.620	0.453	**0.997**
Image 11	6.57	11.45	11.28	6.65	**37.21**	0.585	0.580	0.639	0.435	**0.998**
Image 12	6.09	8.73	9.01	6.28	**36.49**	0.628	0.560	0.632	0.510	**0.997**
Image 13	5.82	11.00	9.80	5.96	**37.81**	0.586	0.644	0.609	0.460	**0.994**
Image 14	7.03	10.88	11.89	7.11	**35.42**	0.575	0.447	0.641	0.422	**0.998**
Image 15	7.02	10.30	11.96	7.20	**34.91**	0.627	0.442	0.697	0.475	**0.998**
Image 16	5.20	8.97	7.98	5.29	**37.46**	0.505	0.592	0.495	0.412	**0.993**
Image 17	6.91	8.14	12.17	7.05	**34.63**	0.563	0.523	0.636	0.436	**0.997**
Image 18	7.04	11.26	12.02	7.23	**34.95**	0.611	0.492	0.683	0.458	**0.998**
Image 19	6.52	9.76	10.80	6.80	**36.63**	0.657	0.520	0.695	0.517	**0.999**
Image 20	6.62	9.41	10.46	6.82	**36.07**	0.589	0.516	0.638	0.448	**0.998**
Image 21	6.36	11.04	10.65	6.39	**36.49**	0.587	0.640	0.633	0.462	**0.996**
Image 22	5.86	10.37	10.01	6.11	**37.56**	0.576	0.637	0.609	0.455	**0.996**
Image 23	6.59	10.27	11.44	6.80	**37.62**	0.638	0.586	0.678	0.481	**0.998**
Image 24	6.86	10.72	11.72	7.11	**34.39**	0.619	0.514	0.704	0.477	**0.998**
Image 25	7.05	7.40	12.52	7.16	**33.36**	0.511	0.450	0.588	0.392	**0.996**
Image 26	6.61	10.46	11.15	6.81	**37.78**	0.628	0.569	0.682	0.487	**0.999**
Image 27	6.92	11.09	12.00	6.99	**34.22**	0.621	0.555	0.687	0.472	**0.998**
Image 28	6.94	10.86	12.15	7.12	**35.45**	0.575	0.473	0.647	0.423	**0.998**
Image 29	6.48	10.70	10.87	6.49	**40.56**	0.654	0.630	0.692	0.503	**0.999**
Image 30	6.89	11.22	11.52	6.97	**36.75**	0.607	0.591	0.654	0.462	**0.998**
Image 31	6.88	9.68	11.74	7.08	**37.49**	0.667	0.447	0.718	0.519	**0.999**
Image 32	6.74	8.41	11.43	6.95	**34.52**	0.637	0.573	0.676	0.504	**0.998**
Image 33	6.43	11.20	11.15	6.71	**35.15**	0.582	0.618	0.640	0.457	**0.995**
Image 34	5.93	9.75	9.80	5.96	**38.83**	0.568	0.522	0.596	0.454	**0.995**
Image 35	6.65	10.37	11.24	6.69	**39.07**	0.641	0.616	0.684	0.484	**0.999**
Image 36	6.35	10.39	10.80	6.59	**37.27**	0.582	0.516	0.639	0.447	**0.996**
Image 37	6.84	8.94	11.98	7.10	**34.54**	0.608	0.544	0.662	0.483	**0.998**
Image 38	6.85	9.11	12.06	7.03	**34.71**	0.560	0.512	0.629	0.433	**0.998**
Image 39	7.01	7.94	11.90	7.19	**34.41**	0.598	0.529	0.649	0.486	**0.997**
Image 40	6.73	9.91	10.92	6.79	**35.18**	0.577	0.508	0.623	0.444	**0.998**
Image 41	6.92	11.37	11.82	7.08	**34.80**	0.588	0.492	0.659	0.435	**0.997**
Image 42	6.92	10.99	11.82	7.12	**35.80**	0.606	0.582	0.659	0.469	**0.998**
Image 43	5.96	11.08	10.11	6.13	**37.74**	0.562	0.629	0.589	0.434	**0.996**
Image 44	6.95	10.62	11.54	7.05	**35.12**	0.658	0.537	0.708	0.503	**0.998**
Image 45	6.50	10.12	10.22	6.66	**37.77**	0.614	0.490	0.651	0.476	**0.999**
Image 46	5.86	7.57	8.70	5.94	**35.22**	0.597	0.532	0.600	0.486	**0.991**
Image 47	6.92	11.11	11.65	7.06	**35.09**	0.642	0.527	0.702	0.494	**0.998**
Image 48	6.55	10.48	10.80	6.71	**38.28**	0.624	0.563	0.669	0.491	**0.997**
Image 49	6.94	11.83	12.41	7.04	**34.06**	0.539	0.442	0.625	0.386	**0.997**
Image 50	5.90	10.04	9.89	6.02	**38.03**	0.564	0.533	0.595	0.442	**0.995**
Image 51	6.67	10.13	10.94	6.80	**36.65**	0.629	0.527	0.684	0.490	**0.998**
Image 52	6.60	11.71	11.59	6.89	**34.36**	0.560	0.560	0.634	0.421	**0.994**
Image 53	6.61	10.59	10.51	6.82	**36.89**	0.599	0.532	0.653	0.457	**0.998**
Image 54	6.63	11.01	11.32	6.69	**35.48**	0.567	0.556	0.628	0.417	**0.996**
Image 55	6.49	11.38	11.23	6.60	**37.56**	0.581	0.570	0.635	0.429	**0.998**
Image 56	6.90	10.80	11.46	7.04	**37.47**	0.618	0.532	0.673	0.474	**0.999**
Image 57	6.71	9.12	10.73	6.87	**36.95**	0.624	0.441	0.670	0.486	**0.998**
Image 58	6.38	10.50	10.79	6.53	**38.13**	0.591	0.522	0.636	0.457	**0.998**
Image 59	6.02	10.93	9.95	6.03	**36.17**	0.550	0.642	0.581	0.430	**0.995**
Image 60	6.92	10.53	11.45	7.03	**36.02**	0.611	0.509	0.669	0.465	**0.998**
Image 61	6.48	9.13	10.50	6.54	**35.48**	0.599	0.490	0.634	0.457	**0.998**
Image 62	6.77	10.71	11.68	6.88	**35.98**	0.625	0.572	0.673	0.471	**0.998**
Image 63	6.89	10.66	11.90	7.12	**34.41**	0.595	0.571	0.666	0.465	**0.997**
Image 64	6.77	11.20	11.12	6.93	**35.94**	0.607	0.533	0.661	0.464	**0.998**
Image 65	6.86	10.13	11.14	6.98	**35.57**	0.561	0.464	0.626	0.423	**0.998**
Image 66	6.59	10.66	10.47	6.78	**37.58**	0.584	0.539	0.631	0.444	**0.999**
Image 67	5.86	9.95	9.81	5.92	**39.72**	0.593	0.643	0.613	0.473	**0.997**
Image 68	7.02	10.88	11.82	7.18	**35.15**	0.636	0.522	0.697	0.489	**0.998**
Image 69	6.88	9.65	11.79	7.02	**36.79**	0.585	0.551	0.648	0.449	**0.998**
Image 70	6.96	9.04	11.92	7.08	**35.09**	0.590	0.540	0.655	0.460	**0.998**
Image 71	6.24	10.55	10.62	6.43	**36.60**	0.579	0.511	0.621	0.438	**0.996**
Image 72	6.81	8.93	10.89	6.94	**34.45**	0.552	0.445	0.605	0.425	**0.998**
Image 73	6.40	9.01	10.12	6.55	**35.99**	0.673	0.514	0.705	0.531	**0.999**
Image 74	6.95	11.72	11.88	6.98	**35.78**	0.571	0.541	0.641	0.418	**0.997**
Image 75	6.98	7.91	12.04	7.18	**34.43**	0.574	0.501	0.640	0.448	**0.997**
Image 76	6.89	10.47	11.61	7.01	**35.91**	0.625	0.505	0.689	0.467	**0.998**
Image 77	6.91	11.36	12.06	7.06	**35.28**	0.571	0.511	0.640	0.433	**0.998**
Image 78	6.76	9.95	11.06	6.82	**36.20**	0.660	0.517	0.706	0.511	**0.999**
Image 79	6.35	10.50	10.79	6.51	**35.97**	0.584	0.485	0.629	0.450	**0.995**
Image 80	6.68	10.56	11.32	6.83	**37.44**	0.642	0.494	0.685	0.484	**0.998**
Image 81	7.07	12.19	11.96	7.24	**35.30**	0.507	0.417	0.598	0.358	**0.997**
Image 82	6.02	9.57	9.09	6.10	**37.10**	0.576	0.542	0.599	0.452	**0.996**
Image 83	6.81	10.66	11.46	6.96	**35.13**	0.620	0.588	0.665	0.490	**0.998**
Image 84	6.35	10.85	10.59	6.52	**36.69**	0.579	0.565	0.631	0.450	**0.996**
Image 85	6.52	10.09	10.12	6.62	**36.55**	0.618	0.503	0.646	0.471	**0.998**
Image 86	6.14	8.13	9.42	6.31	**38.38**	0.635	0.497	0.644	0.505	**0.998**
Image 87	6.17	8.90	9.71	6.22	**38.73**	0.624	0.496	0.641	0.487	**0.998**
Image 88	6.93	11.56	12.05	7.16	**35.55**	0.596	0.480	0.660	0.448	**0.998**

Table A.31 continued from previous page

	SNR (dB)					SSIM				
Image 89	6.40	10.43	10.85	6.31	**39.57**	0.637	0.601	0.675	0.480	**0.999**
Image 90	6.93	10.84	11.85	7.19	**34.87**	0.610	0.577	0.670	0.474	**0.998**
Image 91	6.76	10.63	10.89	6.88	**36.79**	0.578	0.488	0.629	0.433	**0.998**
Image 92	6.92	10.68	11.77	6.99	**35.59**	0.599	0.494	0.674	0.438	**0.998**
Image 93	6.49	9.83	10.25	6.69	**36.24**	0.625	0.518	0.649	0.481	**0.999**
Image 94	6.83	11.17	11.56	6.98	**37.23**	0.620	0.540	0.685	0.476	**0.999**
Image 95	6.99	11.57	11.97	7.14	**35.51**	0.613	0.539	0.688	0.468	**0.998**
Image 96	6.39	9.69	10.45	6.38	**39.15**	0.644	0.531	0.672	0.494	**0.998**
Image 97	6.19	10.98	10.29	6.23	**37.06**	0.564	0.654	0.611	0.441	**0.995**
Image 98	7.01	11.30	12.13	7.12	**35.58**	0.594	0.541	0.668	0.446	**0.998**
Image 99	6.71	11.07	11.56	6.94	**36.77**	0.622	0.571	0.668	0.474	**0.999**
Image 100	5.37	8.29	7.97	5.45	**37.08**	0.557	0.537	0.542	0.460	**0.994**
Image 101	6.69	10.95	11.47	6.87	**35.76**	0.597	0.579	0.651	0.463	**0.998**
Image 102	6.77	10.67	11.54	6.96	**36.06**	0.592	0.542	0.648	0.463	**0.998**
Image 103	6.98	12.59	12.67	7.08	**34.44**	0.483	0.384	0.569	0.335	**0.996**
Image 104	6.86	7.93	11.50	6.91	**35.06**	0.649	0.582	0.687	0.519	**0.998**
Image 105	5.79	10.85	9.70	5.91	**38.33**	0.557	0.673	0.586	0.446	**0.994**
Image 106	6.92	10.65	11.34	7.06	**36.97**	0.587	0.534	0.663	0.448	**0.998**
Image 107	6.65	10.53	11.04	6.64	**38.98**	0.678	0.621	0.707	0.521	**0.999**
Image 108	6.85	11.01	11.64	6.97	**35.39**	0.616	0.522	0.685	0.467	**0.998**
Image 109	6.89	10.29	10.98	6.89	**35.42**	0.596	0.514	0.657	0.448	**0.998**
Image 110	7.03	9.26	12.54	7.26	**34.55**	0.514	0.453	0.590	0.376	**0.997**
Average	6.62	10.28	11.08	6.75	**36.27**	0.597	0.537	0.647	0.459	**0.997**

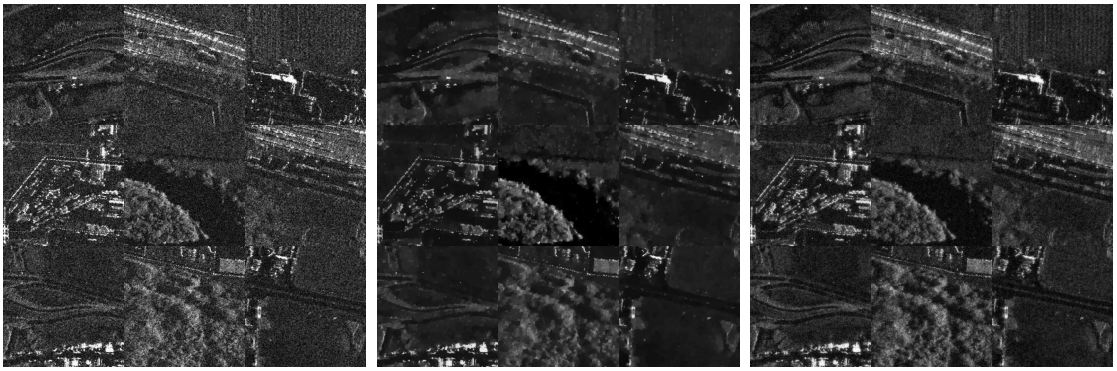

(a) FFT-based (b) NQR-based (c) DL-based

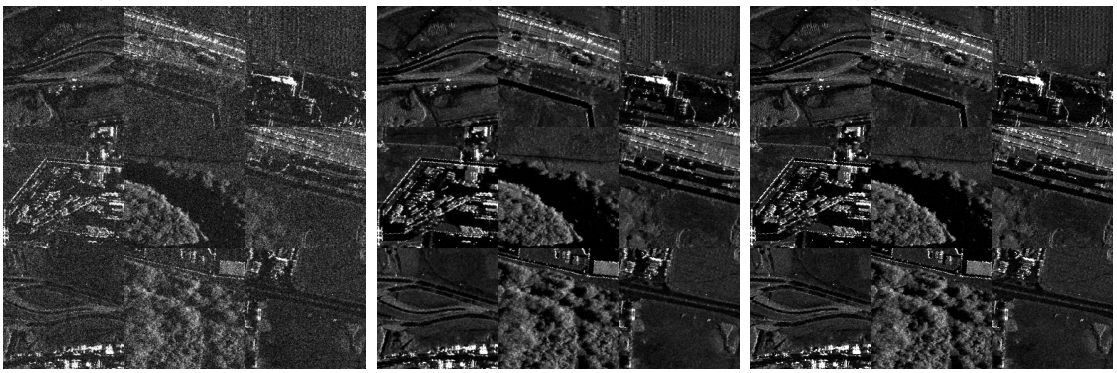

(d) PnP-BM3D (e) PnP-CNN-SAR (f) Ground Truth

Figure A.31 Reconstruction results for Images 19, 40, 45, 46, 59, 61, 66, 96, and 109 from the Kapıkule test set for the case of 100% data availability and $\sigma_{\mathbf{n}} = \sigma_{\mathbf{y}}$.

A.3.8 Experiment 8: 90% Data Availability and $\sigma_{\mathbf{n}} = \sigma_{\mathbf{y}}$

Table A.32 shows the SNR and SSIM values for this experiment. PnP-CNN-SAR gives the best SNR and best SSIM for all 110 images. Fig. A.32 shows the reconstruction results for a selection of images from the Kapıkule test set from all methods for this experiment. PnP-CNN-SAR produce better reconstructions compared to other methods.

Table A.32 SNR and SSIM values for images from the KapıkuleTest Set for the case of 90% data availability and $\sigma_{\mathbf{n}} = \sigma_{\mathbf{y}}$. Best results are shown in bold, second best results are shown in red.

	SNR (dB)					SSIM				
	FFT-based	NQR-based	DL-based	PnP-BM3D	PnP-CNN-SAR	FFT-based	NQR-based	DL-based	PnP-BM3D	PnP-CNN-SAR
Image 1	6.61	9.37	10.88	6.77	**15.49**	0.514	0.555	0.589	0.427	**0.846**
Image 2	6.28	9.82	9.94	6.51	**15.49**	0.508	0.447	0.584	0.421	**0.854**
Image 3	6.89	10.07	11.61	7.43	**15.09**	0.523	0.509	0.613	0.440	**0.823**
Image 4	6.71	9.55	10.32	7.06	**15.48**	0.531	0.470	0.614	0.441	**0.851**
Image 5	5.89	7.93	8.20	5.17	**16.19**	0.519	0.453	0.531	0.392	**0.870**
Image 6	6.89	11.16	11.62	7.19	**16.07**	0.474	0.446	0.583	0.385	**0.839**
Image 7	6.78	10.59	10.48	6.90	**15.26**	0.484	0.476	0.567	0.381	**0.829**
Image 8	6.69	9.74	9.70	6.87	**15.22**	0.510	0.449	0.576	0.397	**0.838**
Image 9	6.14	8.20	8.54	6.06	**15.54**	0.532	0.446	0.558	0.428	**0.870**
Image 10	6.01	9.56	9.79	6.12	**15.51**	0.506	0.474	0.563	0.406	**0.865**
Image 11	6.40	10.84	10.82	6.74	**15.79**	0.493	0.531	0.583	0.399	**0.854**
Image 12	5.83	7.85	7.18	5.66	**15.66**	0.570	0.498	0.548	0.464	**0.897**
Image 13	5.70	9.33	8.95	5.76	**15.96**	0.510	0.615	0.552	0.420	**0.882**
Image 14	6.98	11.12	11.13	7.33	**14.65**	0.492	0.456	0.580	0.394	**0.800**
Image 15	6.93	10.87	11.26	7.35	**14.91**	0.543	0.489	0.642	0.439	**0.835**
Image 16	5.00	8.15	6.51	4.68	**16.47**	0.457	0.477	0.433	0.377	**0.900**
Image 17	6.90	8.10	11.78	7.43	**15.24**	0.472	0.482	0.575	0.413	**0.800**
Image 18	6.93	10.77	11.44	7.44	**15.01**	0.526	0.460	0.632	0.433	**0.834**
Image 19	6.42	9.37	9.75	6.63	**15.23**	0.582	0.478	0.629	0.473	**0.875**
Image 20	6.45	9.00	8.90	6.52	**15.78**	0.518	0.484	0.573	0.415	**0.858**
Image 21	6.19	9.55	9.71	6.32	**15.56**	0.511	0.469	0.571	0.426	**0.862**
Image 22	5.81	9.20	9.18	5.88	**15.82**	0.506	0.447	0.547	0.410	**0.888**
Image 23	6.51	10.42	10.80	6.73	**15.29**	0.535	0.522	0.606	0.428	**0.856**
Image 24	6.77	10.89	10.60	7.14	**15.41**	0.542	0.501	0.637	0.446	**0.853**
Image 25	6.93	6.32	12.51	7.63	**15.02**	0.415	0.386	0.542	0.369	**0.775**
Image 26	6.47	9.93	10.08	6.69	**15.24**	0.550	0.517	0.617	0.449	**0.864**
Image 27	6.84	10.60	11.56	7.22	**15.50**	0.528	0.515	0.632	0.436	**0.847**
Image 28	6.91	10.85	11.72	7.25	**15.28**	0.481	0.504	0.588	0.388	**0.813**
Image 29	6.30	9.29	9.97	6.48	**15.26**	0.569	0.561	0.610	0.457	**0.885**
Image 30	6.70	10.37	10.86	6.95	**15.07**	0.512	0.538	0.594	0.420	**0.840**
Image 31	6.90	10.26	11.07	7.14	**14.48**	0.578	0.548	0.648	0.471	**0.846**
Image 32	6.66	6.50	10.90	7.01	**15.03**	0.543	0.530	0.607	0.466	**0.848**
Image 33	6.40	9.98	10.50	6.67	**16.01**	0.495	0.465	0.584	0.421	**0.861**
Image 34	5.75	9.96	8.95	5.74	**15.91**	0.500	0.650	0.535	0.409	**0.888**
Image 35	6.60	10.24	10.63	6.79	**15.19**	0.548	0.576	0.616	0.442	**0.864**
Image 36	6.23	10.07	9.93	6.50	**16.31**	0.497	0.464	0.581	0.408	**0.873**
Image 37	6.91	10.22	11.33	7.16	**14.89**	0.517	0.540	0.591	0.432	**0.821**
Image 38	6.74	9.40	11.47	7.20	**15.33**	0.466	0.454	0.559	0.397	**0.814**
Image 39	6.82	7.07	11.40	7.38	**15.04**	0.513	0.490	0.585	0.458	**0.816**
Image 40	6.60	8.68	9.93	6.60	**14.93**	0.509	0.364	0.560	0.403	**0.849**
Image 41	6.86	11.29	11.17	7.46	**15.45**	0.505	0.471	0.610	0.417	**0.833**
Image 42	6.94	10.46	11.18	7.27	**15.04**	0.514	0.542	0.586	0.431	**0.825**
Image 43	5.86	9.46	9.52	6.00	**15.60**	0.483	0.450	0.536	0.400	**0.872**
Image 44	6.74	10.11	10.83	6.98	**14.91**	0.571	0.509	0.658	0.465	**0.859**
Image 45	6.26	9.34	8.81	6.24	**15.61**	0.540	0.442	0.578	0.427	**0.865**
Image 46	5.58	6.81	6.74	5.07	**16.40**	0.544	0.480	0.505	0.435	**0.898**
Image 47	6.86	10.45	10.81	7.17	**14.98**	0.560	0.483	0.640	0.458	**0.848**
Image 48	6.37	9.30	9.79	6.47	**15.14**	0.548	0.530	0.601	0.446	**0.872**
Image 49	6.99	11.51	12.31	7.52	**16.00**	0.450	0.486	0.576	0.370	**0.817**
Image 50	5.67	9.42	8.87	5.74	**16.16**	0.494	0.503	0.537	0.405	**0.878**
Image 51	6.55	9.63	9.65	6.75	**15.29**	0.553	0.496	0.617	0.451	**0.861**
Image 52	6.60	11.01	11.00	7.05	**16.05**	0.476	0.534	0.577	0.392	**0.838**
Image 53	6.47	9.54	8.83	6.56	**15.47**	0.529	0.487	0.580	0.427	**0.857**
Image 54	6.42	10.64	10.58	6.78	**15.77**	0.474	0.456	0.569	0.382	**0.840**
Image 55	6.42	10.49	10.79	6.64	**15.55**	0.495	0.455	0.581	0.389	**0.848**
Image 56	6.73	9.06	10.61	7.06	**15.17**	0.537	0.458	0.616	0.438	**0.852**
Image 57	6.53	9.30	9.47	6.84	**15.27**	0.544	0.458	0.604	0.448	**0.853**
Image 58	6.19	10.08	10.03	6.49	**15.86**	0.505	0.580	0.572	0.415	**0.867**
Image 59	5.81	9.99	9.15	5.94	**15.94**	0.477	0.609	0.527	0.393	**0.877**
Image 60	6.79	10.35	10.65	7.09	**14.90**	0.525	0.482	0.614	0.428	**0.829**
Image 61	6.31	7.38	9.52	6.45	**14.93**	0.527	0.336	0.573	0.423	**0.857**
Image 62	6.65	10.16	11.10	7.06	**14.96**	0.524	0.459	0.599	0.425	**0.838**
Image 63	6.79	10.46	11.34	7.31	**15.61**	0.501	0.526	0.605	0.433	**0.840**
Image 64	6.69	9.64	10.15	6.93	**15.35**	0.528	0.460	0.598	0.430	**0.849**
Image 65	6.72	9.85	10.11	6.87	**15.23**	0.493	0.459	0.567	0.383	**0.821**
Image 66	6.39	9.60	8.97	6.46	**15.63**	0.521	0.484	0.565	0.411	**0.864**
Image 67	5.68	9.81	8.98	5.81	**16.04**	0.518	0.609	0.548	0.430	**0.900**
Image 68	6.91	10.17	11.09	7.21	**14.53**	0.559	0.478	0.643	0.455	**0.838**
Image 69	6.75	10.40	11.34	7.08	**15.61**	0.502	0.534	0.593	0.403	**0.842**
Image 70	6.86	8.88	11.44	7.25	**15.27**	0.494	0.458	0.586	0.415	**0.824**
Image 71	6.13	9.69	9.75	6.33	**16.04**	0.498	0.476	0.559	0.400	**0.866**
Image 72	6.66	8.79	9.55	6.72	**14.93**	0.482	0.450	0.540	0.390	**0.828**
Image 73	6.28	8.62	8.59	6.27	**15.09**	0.604	0.482	0.623	0.492	**0.892**
Image 74	6.78	11.06	11.40	7.27	**15.47**	0.485	0.503	0.586	0.390	**0.825**
Image 75	6.93	7.72	11.68	7.36	**15.01**	0.486	0.529	0.592	0.425	**0.813**
Image 76	6.80	10.57	10.68	7.18	**15.24**	0.537	0.491	0.625	0.439	**0.849**
Image 77	6.88	10.87	11.71	7.34	**15.41**	0.477	0.508	0.583	0.404	**0.816**
Image 78	6.60	9.86	10.04	6.84	**15.21**	0.577	0.501	0.634	0.476	**0.872**
Image 79	6.26	10.59	10.07	6.61	**15.74**	0.501	0.530	0.573	0.415	**0.855**
Image 80	6.62	9.77	10.32	6.83	**15.04**	0.554	0.420	0.607	0.436	**0.851**
Image 81	6.94	11.55	11.12	7.29	**15.65**	0.431	0.404	0.551	0.339	**0.786**
Image 82	5.72	8.10	7.24	5.43	**15.91**	0.521	0.477	0.520	0.413	**0.890**
Image 83	6.64	9.69	10.77	6.95	**14.79**	0.533	0.565	0.605	0.449	**0.839**
Image 84	6.15	9.67	9.69	6.28	**15.56**	0.509	0.527	0.583	0.416	**0.865**
Image 85	6.38	8.93	8.41	6.33	**15.28**	0.548	0.444	0.572	0.431	**0.864**
Image 86	5.97	7.78	7.85	5.72	**15.64**	0.564	0.450	0.561	0.447	**0.894**
Image 87	6.01	8.81	8.27	5.90	**15.57**	0.552	0.462	0.558	0.445	**0.886**
Image 88	6.92	10.89	11.56	7.28	**15.35**	0.495	0.514	0.597	0.405	**0.830**

Table A.32 continued from previous page

	SNR (dB)					SSIM				
Image 89	6.19	9.60	10.04	6.33	**15.56**	0.548	0.552	0.605	0.438	**0.881**
Image 90	6.77	10.32	11.28	7.33	**15.04**	0.518	0.552	0.613	0.439	**0.827**
Image 91	6.65	10.06	9.66	6.69	**15.17**	0.507	0.447	0.565	0.394	**0.835**
Image 92	6.85	10.92	11.01	7.21	**15.38**	0.517	0.483	0.623	0.420	**0.837**
Image 93	6.34	8.58	8.88	6.47	**15.33**	0.556	0.450	0.580	0.447	**0.874**
Image 94	6.69	9.42	10.67	7.01	**15.40**	0.541	0.443	0.617	0.439	**0.855**
Image 95	6.81	10.83	11.36	7.30	**15.37**	0.529	0.511	0.636	0.439	**0.851**
Image 96	6.16	8.13	9.36	6.24	**15.73**	0.558	0.426	0.592	0.448	**0.892**
Image 97	6.01	10.24	9.50	6.00	**15.92**	0.498	0.632	0.559	0.404	**0.873**
Image 98	6.89	11.01	11.72	7.43	**15.42**	0.501	0.523	0.615	0.407	**0.829**
Image 99	6.61	9.97	10.99	6.94	**15.28**	0.528	0.469	0.607	0.426	**0.847**
Image 100	5.05	7.22	6.10	4.91	**16.42**	0.504	0.461	0.454	0.422	**0.903**
Image 101	6.66	10.20	10.88	6.88	**14.93**	0.517	0.539	0.598	0.426	**0.834**
Image 102	6.58	10.68	10.89	6.95	**15.42**	0.509	0.561	0.589	0.419	**0.849**
Image 103	7.06	9.61	12.62	7.37	**16.16**	0.388	0.380	0.510	0.305	**0.776**
Image 104	6.69	7.37	10.90	6.90	**14.84**	0.564	0.526	0.622	0.475	**0.850**
Image 105	5.65	9.27	8.73	5.68	**16.13**	0.490	0.487	0.524	0.401	**0.888**
Image 106	6.72	9.85	10.18	7.00	**15.14**	0.513	0.494	0.596	0.421	**0.837**
Image 107	6.52	9.88	9.99	6.69	**14.86**	0.583	0.570	0.618	0.476	**0.875**
Image 108	6.77	10.41	10.96	7.10	**15.13**	0.539	0.491	0.628	0.439	**0.849**
Image 109	6.65	9.41	9.72	7.01	**15.24**	0.526	0.478	0.603	0.433	**0.849**
Image 110	7.06	10.08	12.41	7.53	**15.86**	0.410	0.413	0.531	0.340	**0.789**
Average	6.49	9.65	10.21	6.71	**15.43**	0.516	0.492	0.584	0.422	**0.851**

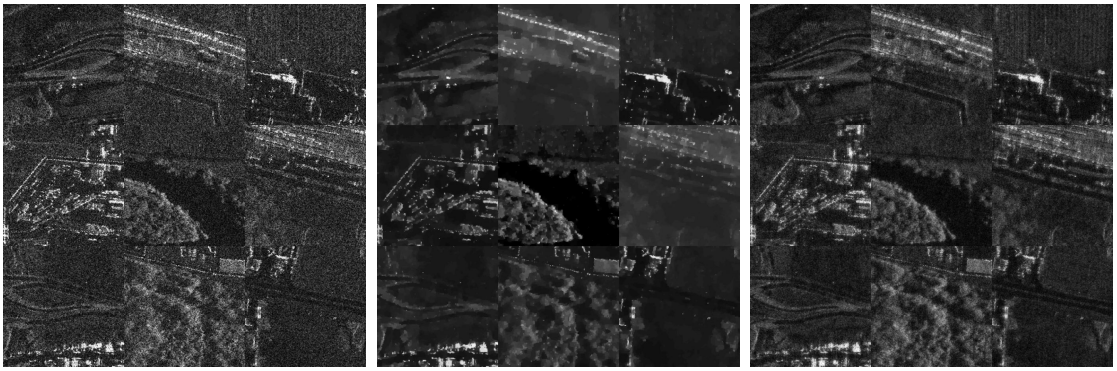

(a) FFT-based (b) NQR-based (c) DL-based

(d) PnP-BM3D (e) PnP-CNN-SAR (f) Ground Truth

Figure A.32 Reconstruction results for Images 19, 40, 45, 46, 59, 61, 66, 96, and 109 from the Kapıkule test set for the case of 90% data availability and $\sigma_{\mathbf{n}} = \sigma_{\mathbf{y}}$.

A.3.9 Experiment 9: 80% Data Availability and $\sigma_{\mathbf{n}} = \sigma_{\mathbf{y}}$

Table A.33 shows the SNR and SSIM values for this experiment. PnP-CNN-SAR gives the best SNR and best SSIM for all 110 images. Fig. A.33 shows the reconstruction results for a selection of images from the Kapıkule test set from all methods for this experiment. PnP-CNN-SAR produce better reconstructions compared to other methods.

Table A.33 SNR and SSIM values for images from the KapıkuleTest Set for the case of 80% data availability and $\sigma_{\mathbf{n}} = \sigma_{\mathbf{y}}$. Best results are shown in bold, second best results are shown in red.

	SNR (dB)					SSIM				
	FFT-based	NQR-based	DL-based	PnP-BM3D	PnP-CNN-SAR	FFT-based	NQR-based	DL-based	PnP-BM3D	PnP-CNN-SAR
Image 1	6.50	9.56	10.22	6.93	**12.93**	0.459	0.515	0.512	0.409	**0.727**
Image 2	6.19	8.46	9.36	6.59	**13.31**	0.466	0.400	0.525	0.394	**0.764**
Image 3	6.85	8.11	11.03	7.69	**12.74**	0.475	0.432	0.552	0.433	**0.703**
Image 4	6.71	9.41	9.42	7.10	**12.64**	0.487	0.444	0.546	0.418	**0.749**
Image 5	5.66	6.32	7.17	5.47	**9.11**	0.489	0.295	0.459	0.387	**0.681**
Image 6	6.77	9.85	11.18	7.30	**13.32**	0.421	0.455	0.520	0.367	**0.706**
Image 7	6.63	9.25	9.65	6.99	**12.84**	0.441	0.419	0.506	0.366	**0.735**
Image 8	6.58	7.05	8.94	6.95	**12.71**	0.467	0.323	0.523	0.388	**0.750**
Image 9	5.92	7.14	7.66	6.08	**12.99**	0.493	0.379	0.490	0.401	**0.782**
Image 10	5.98	9.04	9.18	6.17	**13.17**	0.454	0.420	0.503	0.378	**0.782**
Image 11	6.42	10.02	10.33	6.72	**12.97**	0.446	0.481	0.519	0.362	**0.710**
Image 12	5.52	5.66	6.08	5.66	**12.84**	0.531	0.436	0.466	0.445	**0.815**
Image 13	5.64	8.64	8.26	5.82	**13.37**	0.469	0.443	0.491	0.398	**0.797**
Image 14	6.85	9.05	10.47	7.34	**12.72**	0.443	0.338	0.521	0.370	**0.706**
Image 15	6.85	9.65	10.52	7.64	**13.03**	0.489	0.422	0.589	0.430	**0.748**
Image 16	4.82	5.71	5.52	4.75	**13.80**	0.430	0.435	0.369	0.362	**0.832**
Image 17	6.80	9.50	11.33	7.66	**13.26**	0.419	0.493	0.511	0.400	**0.690**
Image 18	6.87	9.91	10.73	7.64	**13.06**	0.472	0.455	0.574	0.413	**0.740**
Image 19	6.36	8.75	8.85	6.71	**12.88**	0.530	0.433	0.556	0.449	**0.792**
Image 20	6.22	8.87	7.97	6.60	**13.27**	0.484	0.467	0.525	0.400	**0.750**
Image 21	6.02	9.65	9.13	6.41	**13.17**	0.476	0.575	0.513	0.403	**0.779**
Image 22	5.70	8.83	8.50	6.02	**13.08**	0.457	0.430	0.482	0.391	**0.796**
Image 23	6.51	9.85	10.16	6.85	**13.09**	0.481	0.476	0.527	0.406	**0.750**
Image 24	6.69	9.99	9.85	7.45	**13.36**	0.496	0.472	0.584	0.433	**0.765**
Image 25	6.92	11.47	12.09	7.76	**12.75**	0.369	0.403	0.476	0.348	**0.625**
Image 26	6.24	9.08	9.33	6.72	**13.04**	0.510	0.462	0.554	0.423	**0.780**
Image 27	6.76	10.30	10.94	7.52	**13.28**	0.479	0.409	0.563	0.424	**0.741**
Image 28	6.86	11.01	11.19	7.49	**13.47**	0.426	0.408	0.529	0.363	**0.713**
Image 29	6.22	9.34	9.31	6.48	**12.71**	0.507	0.520	0.536	0.428	**0.793**
Image 30	6.58	9.89	10.24	7.10	**13.17**	0.460	0.500	0.528	0.401	**0.750**
Image 31	6.76	9.13	10.37	7.34	**12.52**	0.523	0.364	0.570	0.443	**0.756**
Image 32	6.53	6.46	10.27	7.19	**12.78**	0.484	0.428	0.531	0.445	**0.729**
Image 33	6.29	9.09	9.87	6.77	**13.26**	0.448	0.431	0.518	0.397	**0.749**
Image 34	5.62	9.35	8.26	5.75	**13.19**	0.457	0.615	0.476	0.383	**0.816**
Image 35	6.44	9.71	9.99	6.80	**12.99**	0.491	0.519	0.541	0.413	**0.761**
Image 36	6.10	9.36	9.23	6.53	**13.49**	0.457	0.422	0.516	0.385	**0.777**
Image 37	6.77	7.12	10.76	7.51	**12.86**	0.463	0.444	0.516	0.421	**0.702**
Image 38	6.78	9.06	10.94	7.36	**13.22**	0.423	0.472	0.491	0.381	**0.692**
Image 39	6.85	9.01	10.82	7.57	**12.87**	0.453	0.488	0.516	0.438	**0.699**
Image 40	6.41	7.58	9.02	6.63	**12.54**	0.467	0.327	0.494	0.378	**0.755**
Image 41	6.81	10.82	10.58	7.51	**13.56**	0.464	0.450	0.552	0.392	**0.735**
Image 42	6.81	10.10	10.57	7.28	**12.88**	0.461	0.490	0.516	0.403	**0.716**
Image 43	5.74	9.19	8.90	5.93	**13.22**	0.441	0.574	0.477	0.372	**0.791**
Image 44	6.67	9.93	9.97	7.19	**12.72**	0.531	0.493	0.596	0.457	**0.771**
Image 45	6.03	5.82	7.79	6.40	**13.15**	0.501	0.256	0.506	0.422	**0.770**
Image 46	5.27	6.05	5.74	5.26	**13.76**	0.511	0.421	0.442	0.426	**0.835**
Image 47	6.84	8.63	10.04	7.41	**12.88**	0.510	0.368	0.576	0.436	**0.758**
Image 48	6.22	8.80	9.13	6.63	**12.74**	0.506	0.443	0.544	0.431	**0.786**
Image 49	6.88	7.72	11.80	7.73	**13.61**	0.398	0.439	0.517	0.353	**0.693**
Image 50	5.63	7.84	8.20	5.80	**13.31**	0.457	0.417	0.491	0.384	**0.807**
Image 51	6.39	8.93	8.87	6.90	**12.96**	0.510	0.455	0.548	0.432	**0.778**
Image 52	6.68	10.23	10.56	7.25	**13.87**	0.421	0.452	0.521	0.368	**0.736**
Image 53	6.24	8.00	7.85	6.67	**12.97**	0.488	0.425	0.527	0.416	**0.769**
Image 54	6.46	9.92	10.05	6.90	**13.62**	0.445	0.407	0.519	0.366	**0.747**
Image 55	6.24	10.13	10.22	6.66	**13.27**	0.442	0.427	0.512	0.359	**0.739**
Image 56	6.63	9.04	9.79	7.09	**13.04**	0.481	0.428	0.552	0.415	**0.768**
Image 57	6.40	8.43	8.47	6.80	**12.77**	0.502	0.414	0.536	0.420	**0.765**
Image 58	6.16	9.92	9.40	6.50	**13.37**	0.454	0.531	0.506	0.386	**0.777**
Image 59	5.67	8.45	8.62	5.92	**13.33**	0.436	0.542	0.473	0.367	**0.788**
Image 60	6.65	8.37	9.84	7.21	**13.10**	0.482	0.380	0.557	0.413	**0.753**
Image 61	6.24	8.05	8.58	6.45	**11.92**	0.488	0.387	0.507	0.396	**0.731**
Image 62	6.69	10.07	10.44	7.03	**12.81**	0.467	0.481	0.516	0.393	**0.724**
Image 63	6.77	9.80	10.77	7.56	**13.47**	0.460	0.490	0.547	0.418	**0.733**
Image 64	6.52	9.40	9.46	7.00	**13.35**	0.484	0.428	0.540	0.408	**0.766**
Image 65	6.56	6.45	9.21	6.88	**9.90**	0.450	0.338	0.507	0.370	**0.543**
Image 66	6.32	7.46	8.05	6.48	**13.13**	0.484	0.348	0.520	0.398	**0.782**
Image 67	5.59	8.24	8.30	5.83	**13.22**	0.477	0.378	0.479	0.400	**0.822**
Image 68	6.80	9.83	10.27	7.53	**12.54**	0.510	0.459	0.579	0.446	**0.748**
Image 69	6.66	10.14	10.77	7.24	**13.46**	0.451	0.439	0.531	0.381	**0.734**
Image 70	6.79	8.15	10.95	7.51	**13.06**	0.449	0.465	0.523	0.394	**0.706**
Image 71	6.02	9.14	9.18	6.39	**13.56**	0.445	0.420	0.505	0.383	**0.780**
Image 72	6.56	7.71	8.61	6.74	**12.31**	0.456	0.388	0.481	0.370	**0.735**
Image 73	6.09	7.32	7.55	6.32	**13.02**	0.562	0.423	0.552	0.473	**0.825**
Image 74	6.73	10.65	10.81	7.32	**13.64**	0.432	0.422	0.526	0.364	**0.728**
Image 75	6.84	8.27	11.11	7.61	**13.15**	0.447	0.507	0.531	0.409	**0.703**
Image 76	6.70	10.04	10.01	7.31	**13.32**	0.494	0.466	0.574	0.420	**0.762**
Image 77	6.88	10.01	11.15	7.51	**13.31**	0.429	0.426	0.513	0.377	**0.703**
Image 78	6.53	9.04	9.22	6.95	**12.84**	0.533	0.436	0.563	0.451	**0.783**
Image 79	6.20	9.88	9.49	6.57	**13.11**	0.458	0.500	0.503	0.386	**0.749**
Image 80	6.51	9.16	9.62	6.85	**12.94**	0.500	0.366	0.533	0.408	**0.761**
Image 81	6.84	10.84	10.40	7.40	**13.85**	0.390	0.392	0.507	0.318	**0.693**
Image 82	5.50	6.68	6.24	5.47	**12.66**	0.484	0.415	0.458	0.400	**0.792**
Image 83	6.61	9.05	9.96	7.11	**12.81**	0.490	0.529	0.531	0.432	**0.739**
Image 84	6.06	9.15	9.04	6.44	**13.10**	0.479	0.486	0.540	0.411	**0.778**
Image 85	6.17	7.36	7.44	6.31	**12.73**	0.507	0.373	0.503	0.407	**0.751**
Image 86	5.76	6.59	6.78	5.75	**13.09**	0.526	0.371	0.481	0.428	**0.818**
Image 87	5.92	7.83	7.31	5.97	**13.24**	0.504	0.396	0.485	0.419	**0.819**
Image 88	6.81	9.51	10.94	7.46	**13.11**	0.448	0.405	0.526	0.384	**0.719**

Table A.33 continued from previous page

	SNR (dB)					SSIM				
Image 89	6.12	8.76	9.43	6.42	**12.85**	0.499	0.387	0.530	0.408	**0.779**
Image 90	6.83	9.61	10.60	7.56	**12.98**	0.472	0.514	0.557	0.428	**0.726**
Image 91	6.37	6.86	8.68	6.85	**12.74**	0.461	0.309	0.509	0.382	**0.743**
Image 92	6.73	10.04	10.22	7.49	**13.41**	0.469	0.449	0.565	0.407	**0.751**
Image 93	6.21	7.80	7.99	6.35	**8.33**	0.512	0.404	0.515	0.418	**0.598**
Image 94	6.65	8.49	9.95	7.20	**13.27**	0.490	0.328	0.555	0.416	**0.768**
Image 95	6.87	9.72	10.73	7.46	**12.98**	0.486	0.483	0.581	0.421	**0.744**
Image 96	6.08	8.17	8.69	6.27	**13.24**	0.504	0.389	0.523	0.418	**0.804**
Image 97	5.93	9.24	8.91	6.15	**13.16**	0.459	0.451	0.504	0.391	**0.782**
Image 98	6.96	9.36	11.36	7.70	**13.18**	0.454	0.476	0.561	0.390	**0.718**
Image 99	6.58	8.61	10.37	6.99	**13.17**	0.474	0.439	0.533	0.400	**0.752**
Image 100	4.89	6.51	5.11	4.78	**13.97**	0.473	0.414	0.386	0.398	**0.845**
Image 101	6.51	9.08	10.05	7.05	**12.89**	0.471	0.524	0.528	0.408	**0.740**
Image 102	6.56	9.55	10.26	7.06	**12.97**	0.458	0.419	0.526	0.398	**0.739**
Image 103	7.00	9.27	12.27	7.35	**13.16**	0.333	0.347	0.443	0.266	**0.598**
Image 104	6.62	6.62	10.13	7.13	**12.66**	0.499	0.471	0.535	0.455	**0.740**
Image 105	5.51	8.68	8.13	5.67	**13.67**	0.450	0.464	0.469	0.382	**0.824**
Image 106	6.66	9.55	9.32	7.14	**13.26**	0.484	0.463	0.541	0.409	**0.753**
Image 107	6.34	8.50	9.31	6.65	**12.46**	0.532	0.423	0.532	0.439	**0.777**
Image 108	6.68	9.98	10.22	7.24	**13.01**	0.497	0.457	0.572	0.420	**0.760**
Image 109	6.54	6.15	8.68	6.98	**12.79**	0.488	0.366	0.544	0.420	**0.764**
Image 110	7.04	8.50	12.16	7.69	**13.37**	0.366	0.402	0.475	0.320	**0.631**
Average	6.39	8.79	9.50	6.82	**12.98**	0.471	0.434	0.520	0.401	**0.749**

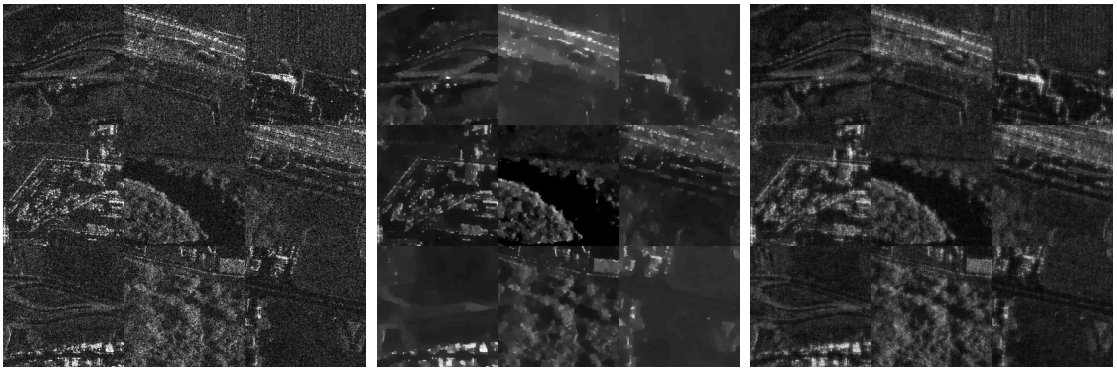

(a) FFT-based (b) NQR-based (c) DL-based

(d) PnP-BM3D (e) PnP-CNN-SAR (f) Ground Truth

Figure A.33 Reconstruction results for Images 19, 40, 45, 46, 59, 61, 66, 96, and 109 from the Kapıkule test set for the case of 80% data availability and $\sigma_{\mathbf{n}} = \sigma_{\mathbf{y}}$.

A.3.10 Experiment 10: 70% Data Availability and $\sigma_{\mathbf{n}} = \sigma_{\mathbf{y}}$

Table A.34 shows the SNR and SSIM values for this experiment. PnP-CNN-SAR gives the best SNR for 107 images, and best SSIM for all 110 images. Fig. A.34 shows the reconstruction results for a selection of images from the Kapıkule test set from all methods for this experiment. PnP-CNN-SAR produce better reconstructions compared to other methods.

Table A.34 SNR and SSIM values for images from the KapıkuleTest Set for the case of 70% data availability and $\sigma_{\mathbf{n}} = \sigma_{\mathbf{y}}$. Best results are shown in bold, second best results are shown in red.

	SNR (dB)					SSIM				
	FFT-based	NQR-based	DL-based	PnP-BM3D	PnP-CNN-SAR	FFT-based	NQR-based	DL-based	PnP-BM3D	PnP-CNN-SAR
Image 1	6.41	9.38	9.73	7.33	**11.01**	0.406	0.475	0.447	0.397	**0.600**
Image 2	6.12	8.81	8.76	6.76	**11.09**	0.422	0.389	0.466	0.373	**0.656**
Image 3	6.81	10.64	10.53	7.96	**11.20**	0.412	0.437	0.501	0.404	**0.585**
Image 4	6.54	7.83	8.80	7.38	**10.90**	0.451	0.365	0.504	0.405	**0.656**
Image 5	5.48	6.04	**6.66**	5.63	5.24	0.446	0.270	0.406	0.370	**0.512**
Image 6	6.77	10.11	10.59	7.85	**11.48**	0.376	0.357	0.460	0.355	**0.586**
Image 7	6.56	8.18	9.07	7.16	**10.81**	0.402	0.355	0.470	0.349	**0.628**
Image 8	6.44	7.77	8.37	7.01	**10.91**	0.437	0.332	0.478	0.373	**0.652**
Image 9	5.80	6.39	7.13	6.06	**10.80**	0.447	0.271	0.434	0.381	**0.694**
Image 10	5.80	8.64	8.71	6.14	**10.95**	0.422	0.376	0.452	0.355	**0.695**
Image 11	6.30	9.00	9.82	6.98	**11.24**	0.395	0.361	0.458	0.341	**0.615**
Image 12	5.36	5.50	5.52	5.46	**10.31**	0.494	0.362	0.412	0.421	**0.747**
Image 13	5.43	7.52	7.82	5.78	**11.02**	0.435	0.527	0.446	0.368	**0.711**
Image 14	6.76	8.23	9.73	7.77	**10.80**	0.402	0.324	0.470	0.370	**0.593**
Image 15	6.80	9.50	9.99	8.05	**11.26**	0.447	0.443	0.547	0.426	**0.646**
Image 16	4.53	5.53	5.08	4.46	**10.60**	0.405	0.363	0.336	0.340	**0.773**
Image 17	6.79	9.78	10.76	8.18	**11.50**	0.370	0.470	0.456	0.393	**0.553**
Image 18	6.81	10.17	10.13	8.11	**11.19**	0.435	0.424	0.526	0.405	**0.627**
Image 19	6.22	7.82	8.30	6.78	**11.02**	0.483	0.380	0.494	0.422	**0.701**
Image 20	6.20	7.25	7.29	6.65	**10.99**	0.442	0.417	0.473	0.395	**0.672**
Image 21	5.95	6.16	8.53	6.48	**11.13**	0.423	0.409	0.458	0.389	**0.683**
Image 22	5.66	8.18	7.99	5.92	**10.87**	0.420	0.369	0.435	0.360	**0.708**
Image 23	6.41	9.28	9.63	7.07	**11.03**	0.431	0.331	0.456	0.371	**0.636**
Image 24	6.52	9.81	9.26	7.63	**11.34**	0.447	0.466	0.540	0.421	**0.659**
Image 25	6.91	9.28	**11.51**	8.49	11.13	0.316	0.412	0.417	0.333	**0.501**
Image 26	6.29	8.98	8.74	6.96	**11.04**	0.457	0.512	0.500	0.411	**0.693**
Image 27	6.68	8.70	10.37	7.87	**11.64**	0.433	0.374	0.508	0.399	**0.629**
Image 28	6.79	9.48	10.61	8.05	**11.53**	0.385	0.372	0.470	0.356	**0.582**
Image 29	6.16	7.32	8.71	6.68	**10.80**	0.464	0.247	0.473	0.401	**0.704**
Image 30	6.46	7.31	9.59	7.36	**11.21**	0.416	0.368	0.465	0.383	**0.637**
Image 31	6.64	8.62	9.76	7.67	**10.78**	0.470	0.318	0.504	0.409	**0.651**
Image 32	6.53	7.25	9.64	7.43	**10.95**	0.437	0.440	0.459	0.414	**0.616**
Image 33	6.21	9.80	9.41	7.16	**11.42**	0.404	0.447	0.474	0.384	**0.645**
Image 34	5.52	8.27	7.79	5.87	**10.88**	0.415	0.431	0.425	0.371	**0.733**
Image 35	6.29	9.12	9.39	7.02	**11.12**	0.444	0.467	0.477	0.386	**0.668**
Image 36	6.02	8.68	8.71	6.79	**11.15**	0.417	0.400	0.471	0.376	**0.673**
Image 37	6.71	9.61	10.26	7.89	**11.03**	0.404	0.462	0.457	0.399	**0.580**
Image 38	6.63	9.53	10.47	7.59	**11.23**	0.379	0.437	0.441	0.363	**0.563**
Image 39	6.76	7.79	10.14	7.90	**11.20**	0.406	0.489	0.452	0.414	**0.583**
Image 40	6.33	7.53	8.40	6.73	**10.36**	0.426	0.296	0.452	0.359	**0.651**
Image 41	6.71	10.45	10.09	8.01	**11.64**	0.421	0.438	0.510	0.385	**0.623**
Image 42	6.68	9.25	9.95	7.75	**10.87**	0.408	0.459	0.450	0.383	**0.586**
Image 43	5.75	8.86	8.41	6.07	**10.85**	0.396	0.411	0.431	0.355	**0.690**
Image 44	6.58	9.56	9.46	7.29	**10.81**	0.485	0.478	0.558	0.438	**0.677**
Image 45	5.92	4.91	7.11	6.26	**10.88**	0.459	0.243	0.456	0.388	**0.672**
Image 46	5.01	5.67	5.18	5.04	**10.88**	0.476	0.384	0.390	0.400	**0.761**
Image 47	6.58	9.31	9.48	7.69	**11.04**	0.462	0.415	0.524	0.425	**0.658**
Image 48	6.06	8.19	8.60	6.54	**10.88**	0.461	0.403	0.498	0.401	**0.701**
Image 49	6.89	10.21	11.35	8.30	**11.83**	0.353	0.390	0.480	0.347	**0.568**
Image 50	5.53	8.08	7.76	5.68	**10.83**	0.426	0.500	0.449	0.365	**0.725**
Image 51	6.28	8.09	8.34	7.18	**10.88**	0.462	0.413	0.500	0.418	**0.684**
Image 52	6.55	10.38	9.99	7.68	**11.77**	0.378	0.453	0.472	0.353	**0.614**
Image 53	6.02	7.47	7.32	6.60	**10.78**	0.449	0.409	0.483	0.398	**0.677**
Image 54	6.32	9.49	9.57	7.34	**11.72**	0.392	0.381	0.473	0.364	**0.636**
Image 55	6.26	9.34	9.79	6.88	**11.32**	0.398	0.380	0.465	0.343	**0.635**
Image 56	6.50	8.23	9.33	7.36	**10.85**	0.438	0.394	0.506	0.398	**0.652**
Image 57	6.26	6.96	7.93	6.73	**10.82**	0.459	0.323	0.484	0.405	**0.652**
Image 58	6.18	8.56	8.98	6.75	**11.26**	0.413	0.407	0.466	0.371	**0.672**
Image 59	5.67	8.61	8.14	5.97	**11.12**	0.396	0.536	0.423	0.344	**0.693**
Image 60	6.62	8.61	9.29	7.62	**11.24**	0.430	0.369	0.502	0.400	**0.652**
Image 61	6.11	7.21	8.05	6.45	**10.54**	0.440	0.281	0.453	0.370	**0.673**
Image 62	6.55	9.35	9.78	7.38	**10.93**	0.410	0.352	0.443	0.370	**0.598**
Image 63	6.67	8.94	10.28	8.04	**11.56**	0.416	0.458	0.499	0.411	**0.612**
Image 64	6.42	8.80	8.80	7.32	**11.35**	0.435	0.398	0.486	0.397	**0.658**
Image 65	6.47	7.94	8.72	7.02	**10.76**	0.407	0.326	0.461	0.352	**0.597**
Image 66	6.00	7.62	7.34	6.39	**10.81**	0.450	0.398	0.464	0.391	**0.701**
Image 67	5.47	7.76	7.88	5.79	**10.87**	0.427	0.357	0.430	0.378	**0.736**
Image 68	6.70	8.89	9.73	7.79	**10.69**	0.457	0.412	0.530	0.421	**0.642**
Image 69	6.64	9.36	10.14	7.60	**11.46**	0.399	0.405	0.472	0.369	**0.611**
Image 70	6.73	9.84	10.33	8.07	**11.29**	0.389	0.444	0.456	0.387	**0.580**
Image 71	5.96	8.59	8.63	6.63	**11.26**	0.413	0.402	0.459	0.372	**0.678**
Image 72	6.38	6.76	7.95	6.72	**10.38**	0.416	0.304	0.429	0.356	**0.638**
Image 73	5.93	6.03	7.07	6.11	**10.68**	0.521	0.447	0.501	0.446	**0.748**
Image 74	6.72	4.46	10.17	7.90	**11.64**	0.386	0.298	0.468	0.351	**0.595**
Image 75	6.77	8.39	10.59	7.96	**11.39**	0.387	0.477	0.477	0.402	**0.581**
Image 76	6.67	8.22	9.35	7.56	**11.11**	0.451	0.394	0.524	0.409	**0.647**
Image 77	6.73	9.99	10.45	8.04	**11.33**	0.375	0.423	0.441	0.363	**0.572**
Image 78	6.34	4.41	8.63	7.01	**10.74**	0.482	0.274	0.501	0.421	**0.681**
Image 79	6.09	9.06	8.93	6.84	**11.19**	0.407	0.350	0.442	0.367	**0.639**
Image 80	6.49	8.85	9.04	7.26	**10.95**	0.439	0.335	0.473	0.397	**0.652**
Image 81	6.77	10.36	9.72	7.83	**11.61**	0.356	0.384	0.468	0.323	**0.572**
Image 82	5.30	5.69	5.69	5.31	**10.34**	0.458	0.332	0.416	0.382	**0.722**
Image 83	6.44	8.70	9.37	7.35	**10.87**	0.436	0.476	0.464	0.411	**0.619**
Image 84	6.01	9.01	8.51	6.48	**10.80**	0.438	0.471	0.500	0.403	**0.691**
Image 85	5.84	6.37	6.97	6.35	**10.59**	0.463	0.281	0.448	0.393	**0.680**
Image 86	5.48	5.72	6.30	5.79	**10.57**	0.483	0.255	0.426	0.410	**0.740**
Image 87	5.67	7.01	6.87	5.88	**10.70**	0.464	0.347	0.430	0.395	**0.729**
Image 88	6.73	9.13	10.34	7.93	**11.30**	0.391	0.367	0.467	0.361	**0.586**

Table A.34 continued from previous page

	SNR (dB)					SSIM				
Image 89	6.07	8.07	8.84	6.54	**10.89**	0.448	0.333	0.463	0.379	**0.685**
Image 90	6.72	8.65	10.03	7.87	**11.30**	0.422	0.444	0.501	0.415	**0.625**
Image 91	6.32	7.47	8.12	6.96	**10.57**	0.427	0.322	0.462	0.377	**0.641**
Image 92	6.66	9.25	9.79	7.85	**11.27**	0.426	0.400	0.524	0.404	**0.641**
Image 93	6.00	6.83	7.36	6.24	**10.35**	0.471	0.355	0.461	0.397	**0.679**
Image 94	6.50	8.02	9.45	7.44	**11.13**	0.444	0.315	0.501	0.400	**0.658**
Image 95	6.71	8.80	10.11	7.93	**11.37**	0.441	0.415	0.537	0.417	**0.648**
Image 96	6.00	8.03	8.11	6.34	**10.95**	0.456	0.368	0.452	0.393	**0.712**
Image 97	5.76	6.76	8.29	6.24	**10.90**	0.418	0.426	0.457	0.380	**0.698**
Image 98	6.84	10.41	10.67	8.28	**11.62**	0.406	0.391	0.498	0.378	**0.614**
Image 99	6.53	8.16	9.86	7.37	**11.16**	0.432	0.389	0.479	0.387	**0.628**
Image 100	4.67	5.53	4.66	4.55	**10.54**	0.436	0.363	0.341	0.372	**0.783**
Image 101	6.42	8.43	9.51	7.20	**10.92**	0.426	0.442	0.479	0.389	**0.629**
Image 102	6.47	8.75	9.64	7.36	**11.20**	0.423	0.479	0.465	0.388	**0.632**
Image 103	6.94	**11.92**	11.75	7.94	11.76	0.288	0.305	0.378	0.262	**0.466**
Image 104	6.52	8.99	9.59	7.40	**10.74**	0.446	0.486	0.469	0.433	**0.627**
Image 105	5.38	8.75	7.71	5.65	**11.21**	0.406	0.586	0.426	0.357	**0.740**
Image 106	6.49	9.11	8.66	7.23	**10.98**	0.434	0.446	0.497	0.390	**0.643**
Image 107	6.21	7.97	8.74	6.74	**10.52**	0.471	0.324	0.463	0.405	**0.678**
Image 108	6.64	8.96	9.59	7.50	**11.26**	0.453	0.388	0.525	0.409	**0.664**
Image 109	6.36	7.44	8.02	6.96	**10.84**	0.452	0.380	0.503	0.402	**0.670**
Image 110	6.98	7.60	11.70	8.38	**11.77**	0.313	0.315	0.420	0.313	**0.503**
Average	6.28	8.29	8.94	7.03	**10.99**	0.426	0.391	0.467	0.384	**0.649**

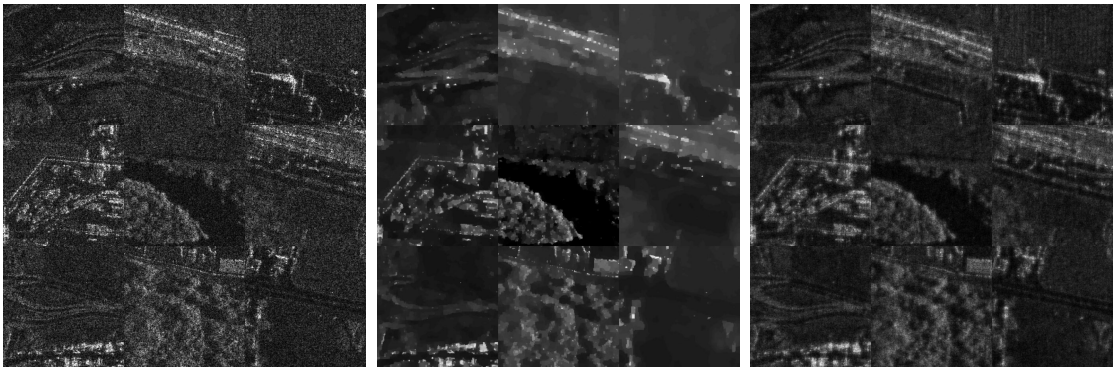

(a) FFT-based (b) NQR-based (c) DL-based

(d) PnP-BM3D (e) PnP-CNN-SAR (f) Ground Truth

Figure A.34 Reconstruction results for Images 19, 40, 45, 46, 59, 61, 66, 96, and 109 from the Kapıkule test set for the case of 70% data availability and $\sigma_{\mathbf{n}} = \sigma_{\mathbf{y}}$.

A.3.11 Experiment 11: 50% Data Availability and $\sigma_{\mathbf{n}} = \sigma_{\mathbf{y}}$

Table A.35 shows the SNR and SSIM values for this experiment. PnP-CNN-SAR gives the best SNR for 95 images, and best SSIM for 108 images. Fig. A.35 shows the reconstruction results for a selection of images from the Kapıkule test set from all methods for this experiment. PnP-CNN-SAR produce better reconstructions compared to other methods.

Table A.35 SNR and SSIM values for images from the KapıkuleTest Set for the case of 50% data availability and $\sigma_{\mathbf{n}} = \sigma_{\mathbf{y}}$. Best results are shown in bold, second best results are shown in red.

	SNR (dB)					SSIM				
	FFT-based	NQR-based	DL-based	PnP-BM3D	PnP-CNN-SAR	FFT-based	NQR-based	DL-based	PnP-BM3D	PnP-CNN-SAR
Image 1	6.07	7.88	8.30	7.87	**9.00**	0.285	0.344	0.326	0.344	**0.471**
Image 2	5.73	8.23	7.65	7.08	**8.96**	0.256	0.387	0.380	0.335	**0.516**
Image 3	6.30	4.38	8.80	8.69	**9.11**	0.241	0.391	0.404	0.391	**0.452**
Image 4	6.12	8.17	7.58	7.44	**8.62**	0.274	0.398	0.417	0.366	**0.511**
Image 5	5.00	5.83	5.80	5.32	**8.15**	0.335	0.256	0.326	0.320	**0.610**
Image 6	6.29	**9.60**	9.04	8.77	9.38	0.246	0.344	0.358	0.323	**0.436**
Image 7	6.01	8.14	7.81	7.39	**8.73**	0.250	0.325	0.392	0.326	**0.499**
Image 8	5.85	7.23	7.18	6.92	**8.14**	0.274	0.310	0.395	0.350	**0.528**
Image 9	5.33	4.68	6.14	6.02	**8.11**	0.324	0.216	0.339	0.334	**0.543**
Image 10	5.53	7.77	7.47	6.49	**8.51**	0.288	0.293	0.365	0.333	**0.544**
Image 11	6.00	8.92	8.46	7.82	**9.45**	0.253	0.326	0.365	0.320	**0.492**
Image 12	4.85	4.20	4.78	4.75	**7.68**	0.366	0.250	0.321	0.336	**0.628**
Image 13	5.21	6.19	6.80	5.97	**8.41**	0.300	0.363	0.359	0.326	**0.589**
Image 14	6.29	**9.07**	8.40	8.28	8.95	0.252	0.345	0.385	0.328	**0.465**
Image 15	6.23	**9.29**	8.65	8.63	9.07	0.241	0.439	0.471	0.406	**0.515**
Image 16	4.25	4.57	4.43	3.87	**7.73**	0.289	0.415	0.281	0.283	**0.672**
Image 17	6.42	8.71	8.98	9.14	**9.39**	0.234	**0.414**	0.348	0.375	0.408
Image 18	6.41	**9.76**	8.66	8.81	8.91	0.246	0.411	0.442	0.390	**0.489**
Image 19	5.79	6.83	7.13	6.85	**8.43**	0.324	0.284	0.398	0.365	**0.544**
Image 20	5.59	6.30	6.38	6.33	**8.17**	0.288	0.342	0.410	0.366	**0.561**
Image 21	5.61	8.37	7.47	6.71	**8.99**	0.278	0.435	0.378	0.352	**0.549**
Image 22	5.34	8.01	6.98	6.16	**8.77**	0.287	0.404	0.353	0.317	**0.587**
Image 23	6.03	8.25	8.31	7.72	**9.10**	0.304	0.277	0.343	0.317	**0.485**
Image 24	6.09	8.05	8.00	8.12	**9.11**	0.244	0.408	0.469	0.411	**0.526**
Image 25	6.54	9.55	**9.89**	**9.89**	9.62	0.178	**0.376**	0.326	0.335	0.351
Image 26	5.84	7.60	7.55	7.17	**8.71**	0.303	0.381	0.419	0.367	**0.555**
Image 27	6.27	5.08	8.88	8.63	**9.34**	0.253	0.381	0.420	0.375	**0.483**
Image 28	6.45	**10.25**	9.01	8.95	9.46	0.229	0.367	0.386	0.331	**0.445**
Image 29	5.77	6.98	7.50	7.01	**8.60**	0.319	0.214	0.356	0.342	**0.541**
Image 30	6.09	5.97	8.33	7.93	**9.00**	0.271	0.356	0.378	0.352	**0.493**
Image 31	6.27	7.73	8.33	8.23	**8.79**	0.297	0.306	0.391	0.353	**0.497**
Image 32	6.11	8.05	8.38	7.90	**9.00**	0.302	0.418	0.355	0.359	**0.470**
Image 33	5.88	8.39	8.01	7.58	**8.95**	0.240	0.413	0.375	0.349	**0.484**
Image 34	5.27	7.45	6.84	6.00	**8.68**	0.288	0.374	0.350	0.321	**0.592**
Image 35	6.01	8.36	8.15	7.59	**9.03**	0.310	0.342	0.369	0.336	**0.517**
Image 36	5.70	8.28	7.55	7.18	**9.06**	0.270	0.375	0.390	0.344	**0.542**
Image 37	6.27	8.21	8.64	8.59	**8.96**	0.264	0.397	0.340	0.358	**0.418**
Image 38	6.29	9.03	8.93	8.63	**9.39**	0.239	0.365	0.342	0.350	**0.419**
Image 39	6.31	5.67	8.81	8.68	**9.09**	0.260	0.418	0.354	0.400	**0.431**
Image 40	5.76	7.16	7.32	6.77	**8.42**	0.280	0.268	0.366	0.328	**0.531**
Image 41	6.29	9.27	8.61	8.74	**9.35**	0.231	0.421	0.439	0.379	**0.496**
Image 42	6.33	8.54	8.66	8.42	**8.98**	0.273	0.391	0.348	0.341	**0.436**
Image 43	5.45	8.39	7.33	6.41	**8.97**	0.272	0.392	0.356	0.319	**0.563**
Image 44	6.13	8.17	8.07	7.68	**8.76**	0.276	0.461	0.477	0.423	**0.560**
Image 45	5.37	6.25	6.32	6.02	**8.30**	0.319	0.270	0.369	0.343	**0.571**
Image 46	4.58	3.99	4.48	4.48	**7.72**	0.351	0.320	0.303	0.336	**0.661**
Image 47	6.12	**8.88**	8.11	7.97	8.87	0.288	0.400	0.434	0.378	**0.528**
Image 48	5.71	7.53	7.37	6.87	**8.53**	0.306	0.385	0.408	0.365	**0.550**
Image 49	6.49	**10.47**	9.77	9.65	9.63	0.200	0.405	0.406	0.348	**0.431**
Image 50	5.13	7.14	6.71	5.72	**8.50**	0.288	0.392	0.385	0.332	**0.607**
Image 51	5.87	7.28	7.12	7.06	**8.28**	0.303	0.376	0.411	0.377	**0.526**
Image 52	6.13	6.58	8.67	8.49	**9.47**	0.218	0.385	0.401	0.338	**0.475**
Image 53	5.49	6.87	6.35	6.26	**8.44**	0.287	0.378	0.406	0.364	**0.568**
Image 54	5.98	8.48	8.21	7.92	**9.26**	0.244	0.323	0.387	0.334	**0.487**
Image 55	5.88	8.61	8.48	7.53	**9.34**	0.270	0.385	0.368	0.308	**0.500**
Image 56	6.11	7.54	7.93	7.66	**8.80**	0.282	0.334	0.415	0.361	**0.525**
Image 57	5.78	6.84	6.94	6.85	**8.78**	0.298	0.305	0.403	0.373	**0.539**
Image 58	5.70	7.84	7.77	7.28	**9.26**	0.272	0.453	0.381	0.339	**0.541**
Image 59	5.27	8.27	7.10	6.19	**8.72**	0.254	0.392	0.342	0.304	**0.558**
Image 60	6.14	7.91	7.92	7.89	**8.85**	0.270	0.385	0.426	0.375	**0.519**
Image 61	5.56	6.60	7.03	6.41	**8.24**	0.293	0.248	0.364	0.315	**0.540**
Image 62	6.16	**9.09**	8.54	8.03	9.08	0.284	0.293	0.334	0.316	**0.454**
Image 63	6.30	8.29	8.79	8.79	**9.32**	0.244	0.432	0.410	0.398	**0.475**
Image 64	5.99	7.87	7.66	7.50	**8.81**	0.284	0.335	0.407	0.361	**0.519**
Image 65	5.92	7.40	7.43	7.38	**8.86**	0.250	0.308	0.381	0.332	**0.492**
Image 66	5.43	6.30	6.28	6.13	**8.33**	0.302	0.304	0.393	0.358	**0.578**
Image 67	5.18	7.50	6.78	5.97	**8.62**	0.308	0.344	0.332	0.326	**0.606**
Image 68	6.28	7.93	8.22	8.27	**8.74**	0.269	0.404	0.444	0.397	**0.519**
Image 69	6.25	**9.76**	8.74	8.33	9.35	0.265	0.368	0.385	0.332	**0.472**
Image 70	6.38	7.75	8.77	8.75	**9.10**	0.242	0.345	0.348	0.343	**0.421**
Image 71	5.64	8.25	7.60	6.87	**9.12**	0.253	0.386	0.387	0.332	**0.552**
Image 72	5.82	4.89	6.95	6.57	**8.09**	0.269	0.269	0.361	0.317	**0.502**
Image 73	5.39	5.44	6.07	5.70	**7.89**	0.339	0.284	0.409	0.382	**0.607**
Image 74	6.37	8.52	8.77	8.76	**9.34**	0.239	0.354	0.384	0.325	**0.462**
Image 75	6.39	8.33	8.95	8.88	**9.17**	0.231	0.425	0.387	0.398	**0.442**
Image 76	6.18	8.34	8.12	8.10	**8.85**	0.259	0.382	0.453	0.392	**0.521**
Image 77	6.49	7.42	9.03	8.90	**9.13**	0.250	0.356	0.347	0.330	**0.410**
Image 78	5.94	7.14	7.52	7.14	**8.46**	0.311	0.290	0.412	0.363	**0.536**
Image 79	5.73	7.82	7.70	7.20	**8.98**	0.262	0.319	0.349	0.306	**0.494**
Image 80	5.95	8.27	7.84	7.64	**8.77**	0.298	0.303	0.366	0.343	**0.486**
Image 81	6.29	**9.54**	8.28	8.32	9.09	0.193	0.372	0.408	0.328	**0.449**
Image 82	4.76	5.58	5.01	4.91	**7.85**	0.329	0.348	0.349	0.340	**0.636**
Image 83	6.06	**8.81**	8.19	7.72	8.70	0.277	0.403	0.381	0.381	**0.485**
Image 84	5.55	7.96	7.24	6.67	**8.60**	0.274	0.434	0.433	0.386	**0.582**
Image 85	5.39	6.02	6.03	5.92	**7.96**	0.306	0.314	0.362	0.339	**0.545**
Image 86	5.03	5.04	5.44	5.25	**7.91**	0.357	0.220	0.332	0.332	**0.606**
Image 87	5.20	5.59	5.99	5.57	**8.26**	0.331	0.282	0.338	0.332	**0.583**
Image 88	6.39	8.39	8.86	8.88	**9.31**	0.243	0.358	0.365	0.323	**0.445**

Table A.35 continued from previous page

	SNR (dB)					SSIM				
Image 89	5.75	7.29	7.69	6.97	**8.89**	0.322	0.331	0.362	0.323	**0.550**
Image 90	6.21	8.05	8.52	8.57	**8.91**	0.249	0.438	0.420	0.412	**0.484**
Image 91	5.89	7.11	6.97	6.74	**8.30**	0.272	0.311	0.383	0.343	**0.522**
Image 92	6.25	8.65	8.37	8.30	**9.09**	0.238	0.379	0.450	0.390	**0.512**
Image 93	5.42	5.91	6.39	6.03	**7.90**	0.323	0.251	0.370	0.339	**0.550**
Image 94	6.08	7.92	7.98	7.76	**8.96**	0.279	0.299	0.405	0.356	**0.512**
Image 95	6.30	**9.45**	8.70	8.63	9.10	0.240	0.426	0.462	0.399	**0.522**
Image 96	5.59	7.31	7.03	6.51	**8.73**	0.333	0.306	0.348	0.340	**0.561**
Image 97	5.44	7.97	7.27	6.37	**8.95**	0.265	0.473	0.387	0.351	**0.578**
Image 98	6.42	7.38	9.11	9.23	**9.30**	0.235	0.380	0.419	0.353	**0.472**
Image 99	6.15	5.05	8.42	8.02	**9.12**	0.289	0.341	0.366	0.334	**0.490**
Image 100	4.16	4.20	4.05	3.78	**7.81**	0.312	0.294	0.265	0.283	**0.679**
Image 101	5.99	7.94	8.20	7.74	**8.93**	0.266	0.391	0.385	0.355	**0.499**
Image 102	6.04	**8.96**	8.38	7.89	8.94	0.268	0.377	0.384	0.362	**0.480**
Image 103	6.58	9.45	10.02	9.52	**10.04**	0.175	0.268	0.288	0.242	**0.303**
Image 104	6.09	6.91	8.14	7.82	**8.75**	0.309	0.393	0.344	0.374	**0.479**
Image 105	5.16	7.69	6.69	5.85	**8.55**	0.289	0.440	0.347	0.318	**0.609**
Image 106	5.95	7.40	7.52	7.46	**8.70**	0.262	0.355	0.427	0.370	**0.532**
Image 107	5.92	7.77	7.53	7.20	**8.55**	0.339	0.296	0.345	0.348	**0.524**
Image 108	6.19	8.97	8.23	7.99	**9.13**	0.262	0.417	0.449	0.389	**0.535**
Image 109	5.78	6.37	7.00	6.93	**8.57**	0.281	0.344	0.435	0.382	**0.561**
Image 110	6.58	**10.05**	9.92	9.83	9.93	0.184	0.335	0.332	0.290	**0.351**
Average	5.86	7.59	7.70	7.39	**8.81**	0.275	0.355	0.380	0.348	**0.516**

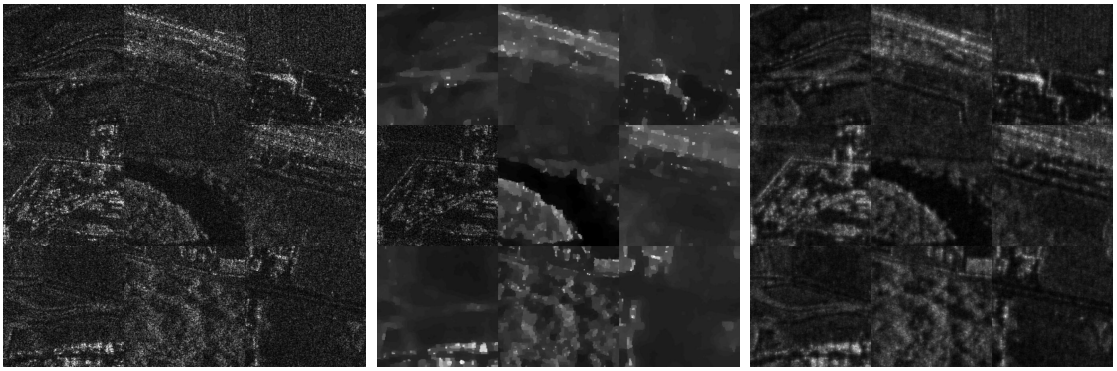

(a) FFT-based (b) NQR-based (c) DL-based

(d) PnP-BM3D (e) PnP-CNN-SAR (f) Ground Truth

Figure A.35 Reconstruction results for Images 19, 40, 45, 46, 59, 61, 66, 96, and 109 from the Kapıkule test set for the case of 50% data availability and $\sigma_{\mathbf{n}} = \sigma_{\mathbf{y}}$.

A.3.12 Experiment 12: 30% Data Availability and $\sigma_{\mathbf{n}} = \sigma_{\mathbf{y}}$

Table A.36 shows the SNR and SSIM values for this experiment. PnP-CNN-SAR gives the best SNR for 13 images, and best SSIM for 59 images. Fig. A.36 shows the reconstruction results for a selection of images from the Kapıkule test set from all methods for this experiment. None of the methods are able to produce acceptable reconstructions for most of the images.

Table A.36 SNR and SSIM values for images from the KapıkuleTest Set for the case of 30% data availability and $\sigma_{\mathbf{n}} = \sigma_{\mathbf{y}}$. Best results are shown in bold, second best results are shown in red.

	SNR (dB)					SSIM				
	FFT-based	NQR-based	DL-based	PnP-BM3D	PnP-CNN-SAR	FFT-based	NQR-based	DL-based	PnP-BM3D	PnP-CNN-SAR
Image 1	5.07	4.89	6.33	**7.61**	6.56	0.197	**0.304**	0.231	0.293	0.279
Image 2	4.90	**7.34**	5.87	6.94	5.87	0.170	**0.363**	0.306	0.292	0.302
Image 3	5.30	**8.80**	6.70	8.77	7.08	0.147	**0.397**	0.317	0.385	0.336
Image 4	5.03	6.91	5.91	**7.19**	6.52	0.167	0.338	0.350	0.348	**0.375**
Image 5	4.25	5.00	4.61	4.92	**5.41**	0.234	0.207	0.243	0.254	**0.369**
Image 6	5.39	**9.44**	6.73	8.46	7.12	0.161	**0.323**	0.270	0.303	0.273
Image 7	5.10	**7.82**	5.97	7.11	6.50	0.160	0.312	0.319	0.324	**0.349**
Image 8	4.89	6.67	5.52	**6.72**	6.26	0.188	0.288	0.324	0.333	**0.366**
Image 9	4.55	5.50	4.93	5.57	**6.00**	0.224	0.217	0.253	0.264	**0.356**
Image 10	4.73	**7.46**	5.70	6.51	6.25	0.201	0.306	0.289	0.276	**0.313**
Image 11	5.11	5.61	6.32	**7.76**	7.19	0.174	0.278	0.281	0.268	**0.309**
Image 12	4.12	4.37	3.95	4.41	**4.94**	0.250	0.276	0.244	0.270	**0.375**
Image 13	4.52	**7.12**	5.28	5.81	5.70	0.209	**0.390**	0.289	0.264	0.319
Image 14	5.21	**8.26**	6.42	7.80	6.99	0.159	0.279	0.305	0.301	**0.315**
Image 15	5.33	**9.17**	6.44	8.43	6.82	0.142	**0.423**	0.388	0.399	0.409
Image 16	3.63	4.00	3.64	3.67	**4.37**	0.199	0.261	0.236	0.222	**0.437**
Image 17	5.32	6.83	6.80	**8.79**	7.24	0.144	0.338	0.273	**0.377**	0.268
Image 18	5.26	**8.86**	6.62	8.46	6.87	0.150	0.365	0.369	0.376	**0.379**
Image 19	4.85	**7.07**	5.57	6.58	6.33	0.218	0.329	0.305	0.307	**0.350**
Image 20	4.58	**6.18**	5.00	5.80	5.85	0.191	0.369	0.334	0.339	**0.390**
Image 21	4.86	**7.83**	5.69	6.60	6.77	0.195	**0.368**	0.295	0.310	0.356
Image 22	4.58	**6.91**	5.43	6.07	6.31	0.202	0.306	0.276	0.260	**0.369**
Image 23	5.04	**8.39**	6.39	7.47	6.88	0.200	0.248	0.236	0.240	**0.296**
Image 24	5.25	**8.45**	6.09	7.77	6.70	0.153	**0.427**	0.391	0.404	0.412
Image 25	5.50	7.41	7.21	**9.76**	7.30	0.108	0.359	0.254	**0.364**	0.232
Image 26	5.01	**7.54**	5.86	6.93	6.45	0.202	0.372	0.332	0.335	**0.375**
Image 27	5.22	2.35	6.71	**8.48**	7.13	0.160	0.179	0.339	**0.355**	0.337
Image 28	5.32	7.11	6.69	**8.73**	7.34	0.146	**0.331**	0.302	0.325	0.306
Image 29	4.92	**7.15**	5.80	6.71	6.41	0.234	0.277	0.258	0.248	**0.326**
Image 30	5.09	6.69	6.31	**7.68**	6.97	0.189	**0.324**	0.287	0.308	0.316
Image 31	5.23	**8.20**	6.35	7.82	6.99	0.196	0.294	0.294	0.282	**0.341**
Image 32	5.08	2.09	6.30	**7.84**	6.87	0.188	0.303	0.253	**0.320**	0.302
Image 33	4.93	4.91	6.15	**7.56**	6.53	0.163	**0.339**	0.306	0.329	0.298
Image 34	4.42	**6.80**	5.37	5.86	4.51	0.198	0.307	0.283	0.263	**0.314**
Image 35	5.14	**7.81**	6.10	7.43	6.93	0.219	0.295	0.259	0.275	**0.319**
Image 36	4.84	6.98	5.79	**7.03**	6.34	0.186	**0.348**	0.308	0.312	0.335
Image 37	5.29	4.81	6.51	**8.40**	7.08	0.165	**0.339**	0.244	0.333	0.282
Image 38	5.28	3.92	6.55	**8.41**	7.29	0.165	0.176	0.254	**0.330**	0.279
Image 39	5.28	7.75	6.55	**8.45**	7.23	0.173	**0.404**	0.263	0.380	0.280
Image 40	4.83	5.55	5.63	**6.46**	6.14	0.196	0.223	0.276	0.281	**0.337**
Image 41	5.35	8.18	6.38	**8.44**	7.13	0.131	0.356	0.362	0.374	**0.380**
Image 42	5.26	6.92	6.44	**8.02**	7.00	0.173	**0.316**	0.249	0.297	0.282
Image 43	4.72	5.59	5.74	**6.36**	5.61	0.182	**0.320**	0.288	0.270	0.307
Image 44	5.04	7.48	6.05	**7.57**	6.47	0.173	**0.430**	0.394	0.400	**0.430**
Image 45	4.59	**5.97**	4.92	5.55	5.61	0.216	0.260	0.283	0.275	**0.361**
Image 46	3.76	3.83	3.58	4.01	**4.64**	0.248	0.220	0.233	0.265	**0.373**
Image 47	5.19	**8.15**	6.06	7.71	6.87	0.174	**0.380**	0.344	0.349	0.376
Image 48	4.88	**7.17**	5.63	6.53	6.49	0.207	0.352	0.316	0.305	**0.388**
Image 49	5.45	**11.04**	7.13	9.45	7.51	0.119	**0.390**	0.337	0.372	0.329
Image 50	4.56	**6.86**	5.20	5.77	5.60	0.199	**0.368**	0.318	0.299	0.341
Image 51	4.88	6.68	5.64	**6.74**	6.14	0.195	**0.368**	0.330	0.335	0.361
Image 52	5.21	**9.27**	6.58	8.26	7.65	0.140	**0.377**	0.331	0.326	0.369
Image 53	4.57	5.70	5.00	**5.78**	5.61	0.197	0.337	0.325	0.336	**0.372**
Image 54	5.06	**8.32**	6.20	7.68	7.15	0.166	0.309	0.315	0.310	**0.345**
Image 55	5.07	**8.46**	6.51	7.49	6.91	0.183	0.259	0.284	0.268	**0.307**
Image 56	5.18	**7.49**	6.04	7.42	6.65	0.184	0.314	0.328	0.336	**0.365**
Image 57	4.95	6.31	5.37	6.49	**6.55**	0.202	0.286	0.315	0.315	**0.378**
Image 58	4.88	**8.14**	6.00	7.01	6.74	0.181	**0.374**	0.299	0.290	0.341
Image 59	4.62	**7.00**	5.60	6.23	3.98	0.170	**0.335**	0.278	0.252	0.267
Image 60	5.21	**7.95**	6.14	7.57	6.76	0.170	0.348	0.350	0.345	**0.376**
Image 61	4.56	**6.67**	5.45	6.18	5.89	0.211	0.283	0.278	0.280	**0.351**
Image 62	5.14	6.52	6.40	**7.83**	6.98	0.185	0.257	0.229	0.253	**0.291**
Image 63	5.25	7.36	6.70	**8.40**	7.19	0.156	**0.401**	0.335	0.386	0.330
Image 64	5.04	**7.63**	5.85	7.08	6.97	0.178	0.358	0.324	0.324	**0.375**
Image 65	4.91	**7.50**	5.69	6.85	6.56	0.170	0.339	0.308	0.314	**0.346**
Image 66	4.69	5.05	4.93	**5.91**	5.85	0.199	0.257	0.311	0.334	**0.386**
Image 67	4.48	**7.18**	5.32	5.90	5.14	0.218	**0.323**	0.250	0.246	0.279
Image 68	5.11	7.94	6.38	**7.96**	6.50	0.164	0.374	0.363	0.367	**0.398**
Image 69	5.19	6.06	6.50	**8.10**	7.07	0.174	0.299	0.294	**0.315**	0.308
Image 70	5.30	**9.18**	6.60	8.57	7.10	0.153	**0.339**	0.261	0.320	0.272
Image 71	4.74	**7.61**	5.73	6.75	6.73	0.177	0.336	0.311	0.298	**0.364**
Image 72	4.90	**6.57**	5.31	6.25	6.09	0.177	0.276	0.284	0.300	**0.344**
Image 73	4.64	5.38	4.77	5.30	**5.55**	0.243	0.281	0.321	0.307	**0.407**
Image 74	5.21	**9.38**	6.61	8.30	7.70	0.151	**0.331**	0.308	0.310	**0.331**
Image 75	5.31	0.97	6.73	**8.67**	7.25	0.142	0.336	0.313	**0.403**	0.325
Image 76	5.21	**8.50**	6.16	7.85	6.80	0.159	**0.408**	0.373	0.377	0.391
Image 77	5.37	**9.13**	6.81	8.73	7.13	0.143	**0.333**	0.263	0.320	0.267
Image 78	4.93	**7.18**	5.74	6.95	6.54	0.207	0.336	0.309	0.310	**0.357**
Image 79	4.81	**7.95**	5.98	7.10	6.29	0.171	**0.332**	0.275	0.262	0.280
Image 80	4.98	**7.81**	6.03	7.26	6.82	0.195	0.283	0.273	0.264	**0.312**
Image 81	5.38	7.46	6.31	**7.89**	6.76	0.119	**0.356**	0.355	**0.356**	0.334
Image 82	4.01	5.12	3.97	4.49	**5.30**	0.218	0.323	0.270	0.276	**0.423**
Image 83	5.07	7.42	6.26	**7.51**	6.69	0.179	**0.378**	0.287	0.347	0.324
Image 84	4.75	**7.39**	5.68	6.55	6.38	0.178	**0.410**	0.366	0.361	0.401
Image 85	4.49	4.16	4.70	5.45	**5.75**	0.212	0.215	0.276	0.279	**0.349**
Image 86	4.21	5.23	4.26	4.85	**5.33**	0.247	0.269	0.233	0.251	**0.363**
Image 87	4.32	5.16	4.72	5.33	**5.64**	0.228	0.193	0.252	0.258	**0.346**
Image 88	5.41	6.23	6.64	**8.48**	7.20	0.161	0.286	0.280	**0.289**	0.288

Table A.36 continued from previous page

	SNR (dB)					SSIM				
Image 89	4.92	6.55	5.90	**6.85**	6.42	0.224	0.287	0.262	0.262	**0.310**
Image 90	5.31	8.27	6.41	**8.30**	6.97	0.160	**0.429**	0.344	0.403	0.347
Image 91	4.89	**6.44**	5.44	6.38	6.18	0.189	0.279	0.309	0.307	**0.360**
Image 92	5.21	**8.28**	6.32	8.08	7.06	0.157	0.375	0.385	**0.386**	0.382
Image 93	4.52	**6.19**	5.01	5.66	5.76	0.226	0.307	0.283	0.288	**0.363**
Image 94	5.13	**8.03**	6.15	7.49	6.86	0.195	0.336	0.317	0.308	**0.353**
Image 95	5.28	6.83	6.52	**8.35**	6.89	0.149	**0.409**	0.380	0.384	0.404
Image 96	4.75	5.31	5.52	6.28	**6.34**	0.229	0.298	0.249	0.254	**0.332**
Image 97	4.70	**7.15**	5.59	6.32	6.09	0.175	**0.420**	0.316	0.309	0.364
Image 98	5.45	5.31	6.86	**8.93**	7.38	0.144	0.342	0.341	0.341	**0.345**
Image 99	5.12	4.93	6.39	**7.96**	7.01	0.188	0.286	0.275	0.296	**0.309**
Image 100	3.54	3.51	3.36	3.54	**3.82**	0.210	0.317	0.205	0.215	**0.345**
Image 101	5.06	7.45	6.26	**7.61**	6.92	0.182	**0.353**	0.305	0.335	0.333
Image 102	5.13	**8.04**	6.30	7.76	7.12	0.172	**0.366**	0.295	0.332	0.321
Image 103	5.52	8.87	7.27	**9.13**	7.45	0.102	0.223	0.201	**0.231**	0.193
Image 104	5.11	6.08	6.19	**7.63**	6.78	0.202	**0.349**	0.245	0.320	0.292
Image 105	4.48	**6.84**	5.27	5.75	5.31	0.200	**0.327**	0.276	0.261	0.301
Image 106	4.98	6.72	5.82	**7.08**	6.76	0.171	0.367	0.348	0.359	**0.388**
Image 107	4.96	**7.23**	5.80	6.84	6.54	0.230	0.250	0.235	0.250	**0.314**
Image 108	5.20	**8.72**	6.40	7.87	6.78	0.166	**0.402**	0.378	0.373	0.396
Image 109	4.77	5.00	5.32	**6.59**	6.24	0.185	0.314	0.353	0.361	**0.404**
Image 110	5.49	7.94	7.16	**9.59**	7.54	0.108	**0.324**	0.254	0.322	0.240
Average	4.94	6.84	5.89	**7.14**	6.48	0.182	0.323	0.298	0.312	**0.339**

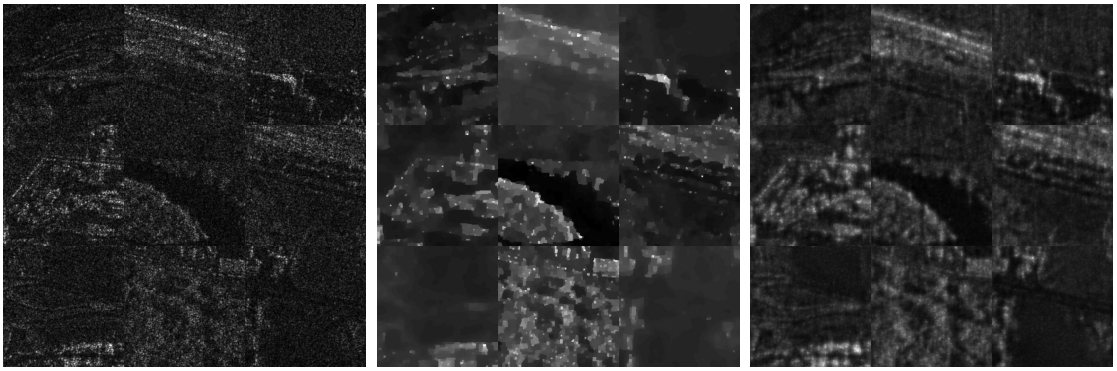

(a) FFT-based (b) NQR-based (c) DL-based

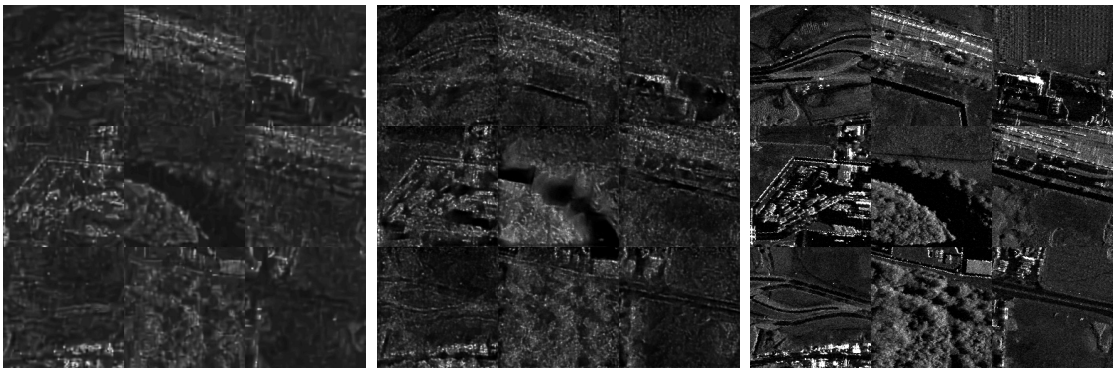

(d) PnP-BM3D (e) PnP-CNN-SAR (f) Ground Truth

Figure A.36 Reconstruction results for Images 19, 40, 45, 46, 59, 61, 66, 96, and 109 from the Kapıkule test set for the case of 30% data availability and $\sigma_{\mathbf{n}} = \sigma_{\mathbf{y}}$.

Bibliography

[1] M. Çetin and W. C. Karl, "Feature-enhanced synthetic aperture radar image formation based on nonquadratic regularization," *IEEE Transactions on Image Processing*, vol. 10, no. 4, pp. 623–631, 2001.

[2] "Air force research laboratory, model based vision laboratory, sensor data management system," MSTAR web page: https://www.sdms.afrl.af.mil/index.php?collection=mstar,"

[3] A. Soğanlı and M. Çetin, "Dictionary learning for sparsity-driven SAR image reconstruction," in *2014 IEEE International Conference on Image Processing (ICIP)*, pp. 1693–1697, IEEE, 2014.

[4] H. Maître, *Processing of Synthetic Aperture Radar (SAR) Images*. John Wiley & Sons, 2013.

[5] C. V. Jakowatz Jr., D. E. Wahl, P. H. Eichel, D. C. Ghiglia, and P. A. Thompson, *Spotlight-mode Synthetic Aperture Radar: A Signal Processing Approach*. Springer, 1996.

[6] G. Franceschetti and R. Lanari, *Synthetic Aperture Radar Processing*. CRC Press, 1999.

[7] C. W. Sherwin, J. Ruina, and R. Rawcliffe, "Some early developments in synthetic aperture radar systems," *IRE Transactions on Military Electronics*, no. 2, pp. 111–115, 1962.

[8] D. A. Ausherman, A. Kozma, J. L. Walker, H. M. Jones, and E. C. Poggio, "Developments in radar imaging," *IEEE Transactions on Aerospace and Electronic Systems*, no. 4, pp. 363–400, 1984.

[9] J. L. Walker, "Range-doppler imaging of rotating objects," *IEEE Transactions on Aerospace and Electronic systems*, no. 1, pp. 23–52, 1980.

[10] D. C. Munson, J. D. O'brien, and W. K. Jenkins, "A tomographic formulation of spotlight-mode synthetic aperture radar," *Proceedings of the IEEE*, vol. 71, no. 8, pp. 917–925, 1983.

[11] D. C. Munson and J. L. Sanz, "Image reconstruction from frequency-offset Fourier data," *Proceedings of the IEEE*, vol. 72, no. 6, pp. 661–669, 1984.

[12] M. Çetin, *Feature-Enhanced Synthetic Aperture Radar Imaging*. Ph.D. dissertation, Boston University, 2001.

[13] A. D. Nichols, J. W. Wilhelm, T. W. Gaffield, D. R. Inkster, and S. K. Leung, "A SAR for real-time ice reconnaissance," *IEEE Transactions on Geoscience and Remote Sensing*, no. 3, pp. 383–389, 1986.

[14] M. Soumekh, "Reconnaissance with slant plane circular SAR imaging," *IEEE Transactions on Image Processing*, vol. 5, no. 8, pp. 1252–1265, 1996.

[15] A. R. Brenner and J. H. Ender, "Demonstration of advanced reconnaissance techniques with the airborne SAR/GMTI sensor PAMIR," *IEE Proceedings-Radar, Sonar and Navigation*, vol. 153, no. 2, pp. 152–162, 2006.

[16] E. J. M. Rignot and J. J. Van Zyl, "Change detection techniques for ERS-1 SAR data," *IEEE Transactions on Geoscience and Remote sensing*, vol. 31, no. 4, pp. 896–906, 1993.

[17] K. Conradsen, A. A. Nielsen, J. Schou, and H. Skriver, "A test statistic in the complex Wishart distribution and its application to change detection in polarimetric SAR data," *IEEE Transactions on Geoscience and Remote Sensing*, vol. 41, no. 1, pp. 4–19, 2003.

[18] Y. Bazi, L. Bruzzone, and F. Melgani, "An unsupervised approach based on the generalized Gaussian model to automatic change detection in multitemporal SAR images," *IEEE Transactions on Geoscience and Remote Sensing*, vol. 43, no. 4, pp. 874–887, 2005.

[19] C. Schmullius and D. Evans, "Synthetic aperture radar (SAR) frequency and polarization requirements for applications in ecology, geology, hydrology, and oceanography: A tabular status quo after SIR-C/X-SAR," *International Journal of Remote Sensing*, vol. 18, no. 13, pp. 2713–2722, 1997.

[20] V. Barale, J. Gower, and L. Alberotanza, *Oceanography from Space: Revisited*. Springer Science & Business Media, 2010.

[21] P.-Y. Le Traon, "Satellites and operational oceanography," in *Operational Oceanography in the 21st Century*, pp. 29–54, Springer, 2011.

[22] C. Bentes, D. Velotto, and S. Lehner, "Target classification in oceanographic SAR images with deep neural networks: Architecture and initial results," in *2015 IEEE International Geoscience and Remote Sensing Symposium (IGARSS)*, pp. 3703–3706, IEEE, 2015.

[23] D. K. Hall and J. P. Ormsby, "Use of SEASAT synthetic aperture radar and LANDSAT multispectral scanner subsystem data for Alaskan glaciology studies," *Journal of Geophysical Research: Oceans*, vol. 88, no. C3, pp. 1597–1607, 1983.

[24] J. Gao and Y. Liu, "Applications of remote sensing, GIS and GPS in glaciology: A review," *Progress in Physical Geography*, vol. 25, no. 4, pp. 520–540, 2001.

[25] E. Nezry, M. Leysen, and G. D. de Grandi, "Speckle and scene spatial statistical estimators for SAR image filtering and texture analysis: Some applications to agriculture, forestry, and point targets detection," in *Synthetic Aperture Radar and Passive Microwave Sensing*, vol. 2584, pp. 110–120, International Society for Optics and Photonics, 1995.

[26] T. Mette, K. P. Papathanassiou, I. Hajnsek, and R. Zimmermann, "Forest biomass estimation using polarimetric SAR interferometry," in *IEEE International Geoscience and Remote Sensing Symposium*, vol. 2, pp. 817–819, IEEE, 2002.

[27] G. Peltzer and P. Rosen, "Surface displacement of the 17 May 1993 Eureka Valley, California, earthquake observed by SAR interferometry," *Science*, vol. 268, no. 5215, pp. 1333–1336, 1995.

[28] R. Michel, J.-P. Avouac, and J. Taboury, "Measuring ground displacements from SAR amplitude images: Application to the Landers earthquake," *Geophysical Research Letters*, vol. 26, no. 7, pp. 875–878, 1999.

[29] E. Pathier, E. Fielding, T. Wright, R. Walker, B. Parsons, and S. Hensley, "Displacement field and slip distribution of the 2005 Kashmir earthquake from SAR imagery," *Geophysical Research Letters*, vol. 33, no. 20, 2006.

[30] T. J. Nohara, P. Weber, A. Premji, and C. Livingstone, "SAR-GMTI processing with Canada's Radarsat 2 satellite," in *Proceedings of the IEEE 2000*

Adaptive Systems for Signal Processing, Communications, and Control Symposium (Cat. No. 00EX373), pp. 379–384, IEEE, 2000.

[31] J. J. Sharma, C. H. Gierull, and M. J. Collins, "The influence of target acceleration on velocity estimation in dual-channel SAR-GMTI," *IEEE Transactions on Geoscience and Remote Sensing*, vol. 44, no. 1, pp. 134–147, 2005.

[32] D. Cerutti-Maori, J. Klare, A. R. Brenner, and J. H. Ender, "Wide-area traffic monitoring with the SAR/GMTI system PAMIR," *IEEE Transactions on Geoscience and Remote Sensing*, vol. 46, no. 10, pp. 3019–3030, 2008.

[33] S. V. Venkatakrishnan, C. A. Bouman, and B. Wohlberg, "Plug-and-play priors for model based reconstruction," in *Global Conference on Signal and Information Processing (GlobalSIP), 2013 IEEE*, pp. 945–948, IEEE, 2013.

[34] S. Boyd, N. Parikh, E. Chu, B. Peleato, J. Eckstein, *et al.*, "Distributed optimization and statistical learning via the alternating direction method of multipliers," *Foundations and Trends® in Machine learning*, vol. 3, no. 1, pp. 1–122, 2011.

[35] A. Krizhevsky, I. Sutskever, and G. E. Hinton, "Imagenet classification with deep convolutional neural networks," in *Advances in Neural Information Processing Systems*, pp. 1097–1105, 2012.

[36] K. Simonyan and A. Zisserman, "Very deep convolutional networks for large-scale image recognition," *arXiv preprint arXiv:1409.1556*, 2014.

[37] J. C. Curlander and R. N. McDonough, *Synthetic Aperture Radar*, vol. 11. New York: Wiley, 1991.

[38] R. D. Chaney, A. S. Willsky, and L. M. Novak, "Coherent aspect-dependent SAR image formation," in *Algorithms for Synthetic Aperture Radar Imagery*, vol. 2230, pp. 256–274, International Society for Optics and Photonics, 1994.

[39] A. W. Rihaczek, *Principles of High-Resolution Radar*. Norwood, MA: Artech House, 1996.

[40] A. C. Kak, M. Slaney, and G. Wang, *Principles of Computerized Tomographic Imaging*. Society of Industrial and Applied Mathematics, 2001.

[41] M. Bertero and P. Boccacci, *Introduction to Inverse Problems in Imaging*. CRC Press, 1998.

[42] M. D. Desai and W. K. Jenkins, "Convolution backprojection image reconstruction for spotlight mode synthetic aperture radar," *IEEE Transactions on Image Processing*, vol. 1, no. 4, pp. 505–517, 1992.

[43] W. C. Karl, "Regularization in image restoration and reconstruction," in *Handbook of Image and Video Processing*, pp. 183–V, Elsevier, 2005.

[44] D. L. Phillips, "A technique for the numerical solution of certain integral equations of the first kind," *Journal of the ACM (JACM)*, vol. 9, no. 1, pp. 84–97, 1962.

[45] A. N. Tikhonov, "On the regularization of ill-posed problems," in *Doklady Akademii Nauk*, vol. 153, pp. 49–52, Russian Academy of Sciences, 1963.

[46] B. R. Frieden, "Restoring with maximum likelihood and maximum entropy," *JOSA*, vol. 62, no. 4, pp. 511–518, 1972.

[47] L. I. Rudin, S. Osher, and E. Fatemi, "Nonlinear total variation based noise removal algorithms," *Physica D: nonlinear phenomena*, vol. 60, no. 1-4, pp. 259–268, 1992.

[48] C. R. Vogel and M. E. Oman, "Fast, robust total variation-based reconstruction of noisy, blurred images," *IEEE Transactions on Image Processing*, vol. 7, no. 6, pp. 813–824, 1998.

[49] D. Geman and G. Reynolds, "Constrained restoration and the recovery of discontinuities," *IEEE Transactions on Pattern Analysis & Machine Intelligence*, no. 3, pp. 367–383, 1992.

[50] D. Geman and C. Yang, "Nonlinear image recovery with half-quadratic regularization," *IEEE transactions on Image Processing*, vol. 4, no. 7, pp. 932–946, 1995.

[51] N. Ö. Önhon, *Joint Sparsity-driven Inversion and Model Error Correction for SAR Imaging*. Ph.D. dissertation, Sabancı University, 2012.

[52] N. Ö. Önhon and M. Çetin, "A sparsity-driven approach for joint SAR imaging and phase error correction," *IEEE Transactions on Image Processing*, vol. 21, no. 4, pp. 2075–2088, 2011.

[53] D. W. Warner, D. C. Ghiglia, A. FitzGerrell, and J. Beaver, "Two-dimensional phase gradient autofocus," in *Image Reconstruction from Incomplete Data*, vol. 4123, pp. 162–173, International Society for Optics and Photonics, 2000.

[54] W. D. Brown and D. C. Ghiglia, "Some methods for reducing propagation-induced phase errors in coherent imaging systems. I. Formalism," *JOSA A*, vol. 5, no. 6, pp. 924–941, 1988.

[55] D. C. Ghiglia and W. D. Brown, "Some methods for reducing propagation-induced phase errors in coherent imaging systems. II. Numerical results," *JOSA A*, vol. 5, no. 6, pp. 942–957, 1988.

[56] R. G. Paxman and J. C. Marron, "Aberration correction of speckled imagery with an image-sharpness criterion," in *Statistical Optics*, vol. 976, pp. 37–47, International Society for Optics and Photonics, 1988.

[57] P. H. Eichel, D. C. Ghiglia, and C. Jakowatz, "Speckle processing method for synthetic-aperture-radar phase correction," *Optics Letters*, vol. 14, no. 1, pp. 1–3, 1989.

[58] C. V. Jakowatz and D. E. Wahl, "Eigenvector method for maximum-likelihood estimation of phase errors in synthetic-aperture-radar imagery," *JOSA A*, vol. 10, no. 12, pp. 2539–2546, 1993.

[59] T. M. Calloway and G. W. Donohoe, "Subaperture autofocus for synthetic aperture radar," *IEEE Transactions on Aerospace and Electronic Systems*, vol. 30, no. 2, pp. 617–621, 1994.

[60] D. E. Wahl, C. V. Jakowatz, P. A. Thompson, and D. C. Ghiglia, "New approach to strip-map SAR autofocus," in *Proceedings of IEEE 6th Digital Signal Processing Workshop*, pp. 53–56, IEEE, 1994.

[61] D. E. Wahl, P. H. Eichel, D. C. Ghiglia, and C. V. Jakowatz, "Phase gradient autofocus-a robust tool for high resolution SAR phase correction," *IEEE Transactions on Aerospace and electronic systems*, vol. 30, no. 3, pp. 827–835, 1994.

[62] F. Berizzi and G. Corsini, "Autofocusing of inverse synthetic aperture radar images using contrast optimization," *IEEE Transactions on Aerospace and Electronic Systems*, vol. 32, no. 3, pp. 1185–1191, 1996.

[63] H. L. Chan and T. S. Yeo, "Noniterative quality phase-gradient autofocus (QPGA) algorithm for spotlight SAR imagery," *IEEE Transactions on Geoscience and Remote Sensing*, vol. 36, no. 5, pp. 1531–1539, 1998.

[64] D. G. Thompson, J. S. Bates, and D. V. Arnold, "Extending the phase gradient autofocus algorithm for low-altitude stripmap mode SAR," in *Proceedings of*

the 1999 IEEE Radar Conference. Radar into the Next Millennium (Cat. No. 99CH36249), pp. 36–40, IEEE, 1999.

[65] L. Xi, L. Guosui, and J. Ni, "Autofocusing of ISAR images based on entropy minimization," *IEEE Transactions on Aerospace and Electronic Systems*, vol. 35, no. 4, pp. 1240–1252, 1999.

[66] W. Ye, T. S. Yeo, and Z. Bao, "Weighted least-squares estimation of phase errors for SAR/ISAR autofocus," *IEEE Transactions on Geoscience and Remote Sensing*, vol. 37, no. 5, pp. 2487–2494, 1999.

[67] J. R. Fienup, "Synthetic-aperture radar autofocus by maximizing sharpness," *Optics Letters*, vol. 25, no. 4, pp. 221–223, 2000.

[68] J. R. Fienup and J. J. Miller, "Aberration correction by maximizing generalized sharpness metrics," *JOSA A*, vol. 20, no. 4, pp. 609–620, 2003.

[69] M. P. Hayes and S. A. Fortune, "Recursive phase estimation for image sharpening," in *Image and Vision Computing New Zealand*, 2005.

[70] T. J. Kragh and A. A. Kharbouch, "Monotonic iterative algorithm for minimum-entropy autofocus," in *Adaptive Sensor Array Processing (ASAP) Workshop*, vol. 40, pp. 1147–1159, 2006.

[71] T. J. Schulz, "Optimal sharpness function for SAR autofocus," *IEEE Signal Processing Letters*, vol. 14, no. 1, pp. 27–30, 2006.

[72] R. L. Morrison, M. N. Do, and D. C. Munson, "SAR image autofocus by sharpness optimization: A theoretical study," *IEEE Transactions on Image Processing*, vol. 16, no. 9, pp. 2309–2321, 2007.

[73] X. Qiu, D. Hu, and C. Ding, "An Omega-K algorithm with phase error compensation for bistatic SAR of a translational invariant case," *IEEE Transactions on Geoscience and Remote Sensing*, vol. 46, no. 8, pp. 2224–2232, 2008.

[74] R. L. Morrison, M. N. Do, and D. C. Munson, "MCA: A multichannel approach to SAR autofocus," *IEEE Transactions on Image Processing*, vol. 18, no. 4, pp. 840–853, 2009.

[75] N. Ö. Önhon and M. Çetin, "A nonquadratic regularization-based technique for joint SAR imaging and model error correction," in *Algorithms for Synthetic Aperture Radar Imagery XVI*, vol. 7337, p. 73370C, International Society for Optics and Photonics, 2009.

[76] N. Ö. Önhon and M. Çetin, "Joint sparsity-driven inversion and model error correction for radar imaging," in *2010 IEEE International Conference on Acoustics, Speech and Signal Processing*, pp. 1206–1209, IEEE, 2010.

[77] H. M. J. Cantalloube and C. E. Nahum, "Multiscale local map-drift-driven multilateration SAR autofocus using fast polar format image synthesis," *IEEE Transactions on Geoscience and Remote Sensing*, vol. 49, no. 10, pp. 3730–3736, 2011.

[78] N. Ö. Önhon and M. Çetin, "SAR moving target imaging in a sparsity-driven framework," in *Wavelets and Sparsity XIV*, vol. 8138, p. 813806, International Society for Optics and Photonics, 2011.

[79] N. Ö. Önhon and M. Cetin, "Sparsity-driven image formation and space-variant focusing for sar," in *2011 18th IEEE International Conference on Image Processing*, pp. 173–176, IEEE, 2011.

[80] M. Çetin, Ö. Önhon, and S. Samadi, "Handling phase in sparse reconstruction for SAR: Imaging, autofocusing, and moving targets," in *EUSAR 2012; 9th European Conference on Synthetic Aperture Radar*, pp. 207–210, VDE, 2012.

[81] S. Uğur and O. Arıkan, "SAR image reconstruction and autofocus by compressed sensing," *Digital Signal Processing*, vol. 22, no. 6, pp. 923–932, 2012.

[82] L. Yang, M. Xing, Y. Wang, L. Zhang, and Z. Bao, "Compensation for the NsRCM and phase error after polar format resampling for airborne spotlight sar raw data of high resolution," *IEEE Geoscience and Remote Sensing Letters*, vol. 10, no. 1, pp. 165–169, 2012.

[83] K.-H. Liu, A. Wiesel, and D. C. Munson, "Synthetic aperture radar autofocus via semidefinite relaxation," *IEEE Transactions on Image Processing*, vol. 22, no. 6, pp. 2317–2326, 2013.

[84] N. Ö. Önhon and M. Çetin, "SAR moving target imaging using group sparsity," in *21st European Signal Processing Conference (EUSIPCO 2013)*, pp. 1–5, IEEE, 2013.

[85] V. T. Vu, T. K. Sjogren, and M. I. Pettersson, "Phase error calculation for fast time-domain bistatic SAR algorithms," *IEEE Transactions on Aerospace and Electronic Systems*, vol. 49, no. 1, pp. 631–639, 2013.

[86] T. Zeng, R. Wang, and F. Li, "SAR image autofocus utilizing minimum-entropy criterion," *IEEE Geoscience and Remote Sensing Letters*, vol. 10, no. 6, pp. 1552–1556, 2013.

[87] M. Çetin, I. Stojanovic, N. Ö. Önhon, K. Varshney, S. Samadi, W. C. Karl, and A. S. Willsky, "Sparsity-driven synthetic aperture radar imaging: Reconstruction, autofocusing, moving targets, and compressed sensing," *IEEE Signal Processing Magazine*, vol. 31, no. 4, pp. 27–40, 2014.

[88] A. Güngör, M. Cetin, and H. E. Güven, "An augmented lagrangian method for autofocused compressed SAR imaging," in *2015 3rd International Workshop on Compressed Sensing Theory and its Applications to Radar, Sonar and Remote Sensing (CoSeRa)*, pp. 1–5, IEEE, 2015.

[89] H. E. Güven, A. Güngör, and M. Çetin, "An augmented Lagrangian method for complex-valued compressed SAR imaging," *IEEE Transactions on Computational Imaging*, vol. 2, no. 3, pp. 235–250, 2016.

[90] S. Camlica, A. C. Gurbuz, and O. Arikan, "Autofocused spotlight SAR image reconstruction of off-grid sparse scenes," *IEEE Transactions on Aerospace and Electronic Systems*, vol. 53, no. 4, pp. 1880–1892, 2017.

[91] A. Güngör, M. Çetin, and H. E. Güven, "Autofocused compressive SAR imaging based on the alternating direction method of multipliers," in *2017 IEEE Radar Conference (RadarConf)*, pp. 1573–1576, IEEE, 2017.

[92] M. J. Hasankhan, S. Samadi, and M. Çetin, "Sparse representation-based algorithm for joint SAR image formation and autofocus," *Signal, Image and Video Processing*, vol. 11, no. 4, pp. 589–596, 2017.

[93] N. Ö. Önhon and M. Çetin, "SAR moving object imaging using sparsity imposing priors," *EURASIP Journal on Advances in Signal Processing*, vol. 2017, no. 1, p. 10, 2017.

[94] T. Sanders and T. Scarnati, "Combination of correlated phase error correction and sparsity models for SAR," in *Computational Imaging II*, vol. 10222, p. 102220E, International Society for Optics and Photonics, 2017.

[95] M. Moradikia, S. Samadi, and M. Cetin, "Joint SAR imaging and multi-feature decomposition from 2-D under-sampled data via low-rankness plus sparsity priors," *IEEE Transactions on Computational Imaging*, vol. 5, no. 1, pp. 1–16, 2018.

[96] L. Ran, R. Xie, Z. Liu, L. Zhang, T. Li, and J. Wang, "Simultaneous range and cross-range variant phase error estimation and compensation for highly squinted SAR imaging," *IEEE Transactions on Geoscience and Remote Sensing*, vol. 56, no. 8, pp. 4448–4463, 2018.

[97] T. Scarnati and A. Gelb, "Joint image formation and two-dimensional autofocusing for synthetic aperture radar data," *Journal of Computational Physics*, vol. 374, pp. 803–821, 2018.

[98] O. Zengin, A. S. Khwaja, and M. Çetin, "Sparsity-driven coupled imaging and autofocusing for interferometric SAR," in *Algorithms for Synthetic Aperture Radar Imagery XXV*, vol. 10647, p. 106470G, International Society for Optics and Photonics, 2018.

[99] A. Evers and J. A. Jackson, "A generalized phase gradient autofocus algorithm," *IEEE Transactions on Computational Imaging*, vol. 5, no. 4, pp. 606–619, 2019.

[100] A. Evers and J. A. Jackson, "Generalized phase gradient autofocus using semidefinite relaxation phase estimation," *IEEE Transactions on Computational Imaging*, vol. 6, pp. 291–303, 2019.

[101] J. M. Kantor, "Polar format-based compressive SAR image reconstruction with integrated autofocus," *IEEE Transactions on Geoscience and Remote Sensing*, vol. 58, no. 5, pp. 3458–3468, 2019.

[102] A. S. Khwaja, N. Ö. Önhon, and M. Çetin, "Compressed sensing methods for radar imaging in the presence of phase errors and moving objects," in *Compressed Sensing in Radar Signal Processing*, ch. 11, pp. 321–354, Cambridge University Press, October 2019.

[103] Y. Yang, X. Zhang, G. Gui, and Q. Wan, "Clustered sparsity-driven SAR imaging and autofocus algorithm in structured phase-noisy environments," *IEEE Access*, vol. 7, pp. 70200–70211, 2019.

[104] S. Zhang, Y. Liu, and X. Li, "Computationally efficient sparse aperture ISAR autofocusing and imaging based on fast ADMM," *IEEE Transactions on Geoscience and Remote Sensing*, 2020.

[105] M. A. Herman and T. Strohmer, "General deviants: An analysis of perturbations in compressed sensing," *IEEE Journal of Selected topics in signal processing*, vol. 4, no. 2, pp. 342–349, 2010.

[106] L. M. Novak, S. D. Halversen, G. Owirka, and M. Hiett, "Effects of polarization and resolution on SAR ATR," *IEEE Transactions on Aerospace and Electronic Systems*, vol. 33, no. 1, pp. 102–116, 1997.

[107] L. C. Potter and R. L. Moses, "Attributed scattering centers for SAR ATR," *IEEE Transactions on Image Processing*, vol. 6, no. 1, pp. 79–91, 1997.

[108] J. C. Mossing and T. D. Ross, "Evaluation of SAR ATR algorithm performance sensitivity to MSTAR extended operating conditions," in *Algorithms for Synthetic Aperture Radar Imagery V*, vol. 3370, pp. 554–565, International Society for Optics and Photonics, 1998.

[109] T. D. Ross, S. W. Worrell, V. J. Velten, J. C. Mossing, and M. L. Bryant, "Standard SAR ATR evaluation experiments using the MSTAR public release data set," in *Algorithms for Synthetic Aperture Radar Imagery V*, vol. 3370, pp. 566–573, International Society for Optics and Photonics, 1998.

[110] T. D. Ross, J. J. Bradley, L. J. Hudson, and M. P. O'Connor, "SAR ATR: so what's the problem? an MSTAR perspective," in *Algorithms for Synthetic Aperture Radar Imagery VI*, vol. 3721, pp. 662–672, International Society for Optics and Photonics, 1999.

[111] L. I. Voicu, R. Patton, and H. R. Myler, "Multicriterion vehicle pose estimation for SAR ATR," in *Algorithms for Synthetic Aperture Radar Imagery VI*, vol. 3721, pp. 497–506, International Society for Optics and Photonics, 1999.

[112] L. M. Kaplan, "Analysis of multiplicative speckle models for template-based SAR ATR," *IEEE Transactions on Aerospace and Electronic Systems*, vol. 37, no. 4, pp. 1424–1432, 2001.

[113] J. A. O'Sullivan, M. D. DeVore, V. Kedia, and M. I. Miller, "SAR ATR performance using a conditionally gaussian model," *IEEE Transactions on Aerospace and Electronic Systems*, vol. 37, no. 1, pp. 91–108, 2001.

[114] P. Han, R. Wu, Y. Wang, and Z. Wang, "An efficient SAR ATR approach," in *2003 IEEE International Conference on Acoustics, Speech, and Signal Processing, 2003. Proceedings.(ICASSP'03).*, vol. 2, pp. II–429, IEEE, 2003.

[115] Y. Wang, P. Han, X. Lu, R. Wu, and J. Huang, "The performance comparison of Adaboost and SVM applied to SAR ATR," in *2006 CIE International Conference on Radar*, pp. 1–4, IEEE, 2006.

[116] A. K. Mishra and B. Mulgrew, "Bistatic SAR ATR," *IET Radar, Sonar & Navigation*, vol. 1, no. 6, pp. 459–469, 2007.

[117] S. Chen and H. Wang, "SAR target recognition based on deep learning," in *2014 International Conference on Data Science and Advanced Analytics (DSAA)*, pp. 541–547, IEEE, 2014.

[118] Y. Huang, J. Peia, J. Yanga, B. Wang, and X. Liu, "Neighborhood geometric center scaling embedding for SAR ATR," *IEEE Transactions on Aerospace and Electronic Systems*, vol. 50, no. 1, pp. 180–192, 2014.

[119] S. Song, B. Xu, and J. Yang, "SAR target recognition via supervised discriminative dictionary learning and sparse representation of the SAR-HOG feature," *Remote Sensing*, vol. 8, no. 8, p. 683, 2016.

[120] Y. Sun, L. Du, Y. Wang, Y. Wang, and J. Hu, "SAR automatic target recognition based on dictionary learning and joint dynamic sparse representation," *IEEE Geoscience and Remote Sensing Letters*, vol. 13, no. 12, pp. 1777–1781, 2016.

[121] S. A. Wagner, "SAR ATR by a combination of convolutional neural network and support vector machines," *IEEE transactions on Aerospace and Electronic Systems*, vol. 52, no. 6, pp. 2861–2872, 2016.

[122] M. Wilmanski, C. Kreucher, and J. Lauer, "Modern approaches in deep learning for SAR ATR," in *Algorithms for synthetic aperture radar imagery XXIII*, vol. 9843, p. 98430N, International Society for Optics and Photonics, 2016.

[123] S.-Q. Chen, R.-H. Zhan, J.-M. Hu, and J. Zhang, "Feature fusion based on convolutional neural network for SAR ATR," in *ITM Web of Conferences*, vol. 12, p. 05001, EDP Sciences, 2017.

[124] B. Ding, G. Wen, J. Zhong, C. Ma, and X. Yang, "A robust similarity measure for attributed scattering center sets with application to SAR ATR," *Neurocomputing*, vol. 219, pp. 130–143, 2017.

[125] A. El Housseini, A. Toumi, and A. Khenchaf, "Deep learning for target recognition from SAR images," in *Seminar on Detection Systems Architectures and Technologies (DAT)*, pp. 1–5, IEEE, 2017.

[126] S. Wagner, K. Barth, and S. Brüggenwirth, "A deep learning SAR ATR system using regularization and prioritized classes," in *2017 IEEE Radar Conference (RadarConf)*, pp. 0772–0777, IEEE, 2017.

[127] I. Goodfellow, Y. Bengio, and A. Courville, *Deep Learning*, vol. 1. MIT Press Cambridge, 2016.

[128] I. ibn al-Razzāz al Jazarī and D. R. Hill, *The Book of Knowledge of Ingenious Mechanical Devices: (Kitāb fī ma'rifat al-hiyal al-handasiyya)*. D. Reidel, 1974.

[129] M. E. Moran, "The da Vinci robot," *Journal of Endourology*, vol. 20, no. 12, pp. 986–990, 2006.

[130] F. Rosenblatt, "The perceptron: A probabilistic model for information storage and organization in the brain.," *Psychological Review*, vol. 65, no. 6, p. 386, 1958.

[131] K. Fukushima and S. Miyake, "Neocognitron: A self-organizing neural network model for a mechanism of visual pattern recognition," in *Competition and Cooperation in Neural Nets*, pp. 267–285, Springer, 1982.

[132] D. E. Rumelhart, G. E. Hinton, and R. J. Williams, "Learning representations by back-propagating errors," *Nature*, vol. 323, no. 6088, pp. 533–536, 1986.

[133] M. Miljanovic, "Comparative analysis of recurrent and finite impulse response neural networks in time series prediction," *Indian Journal of Computer Science and Engineering*, vol. 3, no. 1, pp. 180–191, 2012.

[134] S. Hochreiter and J. Schmidhuber, "Long short-term memory," *Neural Computation*, vol. 9, no. 8, pp. 1735–1780, 1997.

[135] J. Chung, C. Gulcehre, K. Cho, and Y. Bengio, "Empirical evaluation of gated recurrent neural networks on sequence modeling," *arXiv preprint arXiv:1412.3555*, 2014.

[136] G. E. Hinton, S. Osindero, and Y.-W. Teh, "A fast learning algorithm for deep belief nets," *Neural Computation*, vol. 18, no. 7, pp. 1527–1554, 2006.

[137] Z. Sun, L. Xue, and Y. Xu, "Recognition of SAR target based on multilayer auto-encoder and SNN," *International Journal of Innovative Computing, Information and Control*, vol. 9, no. 11, pp. 4331–4341, 2013.

[138] D. A. Morgan, "Deep convolutional neural networks for ATR from SAR imagery," in *Algorithms for Synthetic Aperture Radar Imagery XXII*, vol. 9475, p. 94750F, International Society for Optics and Photonics, 2015.

[139] H. Wang, S. Chen, F. Xu, and Y.-Q. Jin, "Application of deep-learning algorithms to MSTAR data," in *2015 IEEE International Geoscience and Remote Sensing Symposium (IGARSS)*, pp. 3743–3745, IEEE, 2015.

[140] Y. Xu, K. Liu, Z. Ying, L. Shang, J. Liu, Y. Zhai, V. Piuri, and F. Scotti, "SAR automatic target recognition based on deep convolutional neural network," in *International Conference on Image and Graphics*, pp. 656–667, Springer, 2017.

[141] H. Xie, S. Wang, K. Liu, S. Lin, and B. Hou, "Multilayer feature learning for polarimetric synthetic radar data classification," in *2014 IEEE Geoscience and Remote Sensing Symposium*, pp. 2818–2821, IEEE, 2014.

[142] X. Huang and X. Wang, "The classification of synthetic aperture radar oil spill images based on the texture features and deep belief network," in *Computer Engineering and Networking*, pp. 661–669, Springer, 2014.

[143] Q. Lv, Y. Dou, X. Niu, J. Xu, and B. Li, "Classification of land cover based on deep belief networks using polarimetric RADARSAT-2 data," in *2014 IEEE Geoscience and Remote Sensing Symposium*, pp. 4679–4682, IEEE, 2014.

[144] J. Geng, J. Fan, H. Wang, X. Ma, B. Li, and F. Chen, "High-resolution SAR image classification via deep convolutional autoencoders," *IEEE Geoscience and Remote Sensing Letters*, vol. 12, no. 11, pp. 2351–2355, 2015.

[145] Q. Lv, Y. Dou, X. Niu, J. Xu, J. Xu, and F. Xia, "Urban land use and land cover classification using remotely sensed SAR data through deep belief networks," *Journal of Sensors*, vol. 2015, 2015.

[146] E. Mason, B. Yönel, and B. Yazıcı, "Deep learning for radar," in *2017 IEEE Radar Conference (RadarConf)*, pp. 1703–1708, IEEE, 2017.

[147] E. Mason, B. Yönel, and B. Yazici, "Deep learning for SAR image formation," in *Algorithms for Synthetic Aperture Radar Imagery XXIV*, vol. 10201, p. 1020104, International Society for Optics and Photonics, 2017.

[148] B. Yönel, E. Mason, and B. Yazıcı, "Deep learning for passive synthetic aperture radar," *IEEE Journal of Selected Topics in Signal Processing*, vol. 12, no. 1, pp. 90–103, 2017.

[149] H. Shi, J. Zhang, E.-F. Gao, T. Yang, and J. Guo, "Deep convolutional neural network for P-band spaceborne synthetic aperture radar imaging through the ionosphere," *Journal of Applied Remote Sensing*, vol. 14, no. 4, p. 046507, 2020.

[150] A. Ribes and F. Schmitt, "Linear inverse problems in imaging," *IEEE Signal Processing Magazine*, vol. 25, no. 4, 2008.

[151] U. S. Kamilov, H. Mansour, and B. Wohlberg, "A plug-and-play priors approach for solving nonlinear imaging inverse problems," *IEEE Signal Processing Letters*, vol. 24, no. 12, pp. 1872–1876, 2017.

[152] S. Samadi, M. Çetin, and M. A. Masnadi-Shirazi, "Multiple feature-enhanced synthetic aperture radar imaging," in *Algorithms for Synthetic Aperture Radar Imagery XVI*, vol. 7337, p. 73370I, International Society for Optics and Photonics, 2009.

[153] S. Samadi, M. Çetin, and M. A. Masnadi-Shirazi, "Sparse representation-based synthetic aperture radar imaging," *IET radar, sonar & navigation*, vol. 5, no. 2, pp. 182–193, 2011.

[154] J. Zeng, J. Fang, and Z. Xu, "Sparse SAR imaging based on $L_{1/2}$ regularization," *Science China Information Sciences*, vol. 55, no. 8, pp. 1755–1775, 2012.

[155] H. H. Bauschke, P. L. Combettes, *et al.*, *Convex Analysis and Monotone Operator Theory in Hilbert Spaces*, vol. 408. Springer, 2011.

[156] I. Daubechies, M. Defrise, and C. De Mol, "An iterative thresholding algorithm for linear inverse problems with a sparsity constraint," *Communications on Pure and Applied Mathematics: A Journal Issued by the Courant Institute of Mathematical Sciences*, vol. 57, no. 11, pp. 1413–1457, 2004.

[157] J. Eckstein and D. P. Bertsekas, "On the Douglas-Rachford splitting method and the proximal point algorithm for maximal monotone operators," *Mathematical Programming*, vol. 55, no. 1-3, pp. 293–318, 1992.

[158] H. Woo and S. Yun, "Alternating minimization algorithm for speckle reduction with a shifting technique," *IEEE Transactions on Image Processing*, vol. 21, no. 4, pp. 1701–1714, 2012.

[159] H. E. Güven and M. Çetin, "An augmented Lagrangian method for sparse SAR imaging," in *EUSAR 2014; 10th European Conference on Synthetic Aperture Radar; Proceedings of*, pp. 1–4, VDE, 2014.

[160] E. Mason, I. Bayram, and B. Yazici, "Optimization methods for synthetic aperture radar imaging," in *Handbook of Convex Optimization Methods in Imaging Science*, pp. 71–103, Springer, 2017.

[161] A. Brifman, Y. Romano, and M. Elad, "Turning a denoiser into a super-resolver using plug and play priors," in *2016 IEEE International Conference on Image Processing (ICIP)*, pp. 1404–1408, IEEE, 2016.

[162] S. H. Chan, X. Wang, and O. A. Elgendy, "Plug-and-play ADMM for image restoration: Fixed-point convergence and applications," *IEEE Transactions on Computational Imaging*, vol. 3, no. 1, pp. 84–98, 2016.

[163] C. A. Metzler, A. Maleki, and R. G. Baraniuk, "BM3D-PRGAMP: Compressive phase retrieval based on BM3D denoising," in *2016 IEEE International Conference on Image Processing (ICIP)*, pp. 2504–2508, IEEE, 2016.

[164] S. Sreehari, S. V. Venkatakrishnan, B. Wohlberg, G. T. Buzzard, L. F. Drummy, J. P. Simmons, and C. A. Bouman, "Plug-and-play priors for bright field electron tomography and sparse interpolation," *IEEE Transactions on Computational Imaging*, vol. 2, no. 4, pp. 408–423, 2016.

[165] A. M. Teodoro, J. M. Bioucas-Dias, and M. A. Figueiredo, "Image restoration and reconstruction using variable splitting and class-adapted image priors," in *2016 IEEE International Conference on Image Processing (ICIP)*, pp. 3518–3522, IEEE, 2016.

[166] T. Meinhardt, M. Moller, C. Hazirbas, and D. Cremers, "Learning proximal operators: Using denoising networks for regularizing inverse imaging problems," in *Proceedings of the IEEE International Conference on Computer Vision*, pp. 1781–1790, 2017.

[167] S. Ono, "Primal-dual plug-and-play image restoration," *IEEE Signal Processing Letters*, vol. 24, no. 8, pp. 1108–1112, 2017.

[168] C. J. Pellizzari, R. Trahan, H. Zhou, S. Williams, S. E. Williams, B. Nemati, M. Shao, and C. A. Bouman, "Optically coherent image formation and denoising using a plug and play inversion framework," *Applied optics*, vol. 56, no. 16, pp. 4735–4744, 2017.

[169] A. M. Teodoro, J. M. Bioucas-Dias, and M. A. Figueiredo, "Scene-adapted plug-and-play algorithm with convergence guarantees," in *2017 IEEE 27th International Workshop on Machine Learning for Signal Processing (MLSP)*, pp. 1–6, IEEE, 2017.

[170] X. Wang and S. H. Chan, "Parameter-free plug-and-play ADMM for image restoration," in *2017 IEEE International Conference on Acoustics, Speech and Signal Processing (ICASSP)*, pp. 1323–1327, IEEE, 2017.

[171] G. T. Buzzard, S. H. Chan, S. Sreehari, and C. A. Bouman, "Plug-and-play unplugged: Optimization-free reconstruction using consensus equilibrium," *SIAM Journal on Imaging Sciences*, vol. 11, no. 3, pp. 2001–2020, 2018.

[172] M. Shi and L. Feng, "Plug-and-play prior based on Gaussian mixture model learning for image restoration in sensor network," *IEEE Access*, vol. 6, pp. 78113–78122, 2018.

[173] V. Unni, S. Ghosh, and K. N. Chaudhury, "Linearized ADMM and fast nonlocal denoising for efficient plug-and-play restoration," in *2018 IEEE Global Conference on Signal and Information Processing (GlobalSIP)*, pp. 11–15, IEEE, 2018.

[174] D. H. Ye, S. Srivastava, J.-B. Thibault, K. Sauer, and C. Bouman, "Deep residual learning for model-based iterative CT reconstruction using plug-and-play framework," in *2018 IEEE International Conference on Acoustics, Speech and Signal Processing (ICASSP)*, pp. 6668–6672, IEEE, 2018.

[175] M. B. Alver, A. Saleem, and M. Çetin, "A novel plug-and-play SAR reconstruction framework using deep priors," in *2019 IEEE Radar Conference (RadarConf)*, pp. 1–6, IEEE, 2019.

[176] S. H. Chan, "Performance analysis of plug-and-play ADMM: A graph signal processing perspective," *IEEE Transactions on Computational Imaging*, vol. 5, no. 2, pp. 274–286, 2019.

[177] R. G. Gavaskar and K. N. Chaudhury, "On the proof of fixed-point convergence for plug-and-play ADMM," *IEEE Signal Processing Letters*, vol. 26, no. 12, pp. 1817–1821, 2019.

[178] E. Ryu, J. Liu, S. Wang, X. Chen, Z. Wang, and W. Yin, "Plug-and-play methods provably converge with properly trained denoisers," in *International Conference on Machine Learning*, pp. 5546–5557, 2019.

[179] Y. Sun, B. Wohlberg, and U. S. Kamilov, "An online plug-and-play algorithm for regularized image reconstruction," *IEEE Transactions on Computational Imaging*, vol. 5, no. 3, pp. 395–408, 2019.

[180] M. U. Ghani and W. C. Karl, "Integrating data and image domain deep learning for limited angle tomography using consensus equilibrium," in *Proceedings of the IEEE International Conference on Computer Vision Workshops*, pp. 0–0, 2019.

[181] K. Zhang, W. Zuo, and L. Zhang, "Deep plug-and-play super-resolution for arbitrary blur kernels," in *Proceedings of the IEEE Conference on Computer Vision and Pattern Recognition*, pp. 1671–1681, 2019.

[182] R. G. Gavaskar and K. N. Chaudhury, "Plug-and-play ISTA converges with kernel denoisers," *arXiv preprint arXiv:2004.03145*, 2020.

[183] G. Song, Y. Sun, J. Liu, Z. Wang, and U. S. Kamilov, "A new recurrent plug-and-play prior based on the multiple self-similarity network," *IEEE Signal Processing Letters*, vol. 27, pp. 451–455, 2020.

[184] Y. Sun, Z. Wu, B. Wohlberg, and U. S. Kamilov, "Scalable plug-and-play ADMM with convergence guarantees," *arXiv preprint arXiv:2006.03224*, 2020.

[185] K. Wei, A. Aviles-Rivero, J. Liang, Y. Fu, C.-B. Schnlieb, and H. Huang, "Tuning-free plug-and-play proximal algorithm for inverse imaging problems," *arXiv preprint arXiv:2002.09611*, 2020.

[186] K. Dabov, A. Foi, V. Katkovnik, and K. Egiazarian, "Image denoising by sparse 3-D transform-domain collaborative filtering," *IEEE Transactions on Image Processing*, vol. 16, no. 8, pp. 2080–2095, 2007.

[187] W. Dong, L. Zhang, G. Shi, and X. Li, "Nonlocally centralized sparse representation for image restoration," *IEEE Transactions on Image Processing*, vol. 22, no. 4, pp. 1620–1630, 2012.

[188] D. L. Donoho, A. Maleki, and A. Montanari, "Message passing algorithms for compressed sensing: I. motivation and construction," in *2010 IEEE information theory workshop on information theory (ITW 2010, Cairo)*, pp. 1–5, IEEE, 2010.

[189] A. Chambolle and T. Pock, "A first-order primal-dual algorithm for convex problems with applications to imaging," *Journal of mathematical imaging and vision*, vol. 40, no. 1, pp. 120–145, 2011.

[190] K. Zhang, W. Zuo, S. Gu, and L. Zhang, "Learning deep CNN denoiser prior for image restoration," in *Proceedings of the IEEE Conference on Computer Vision and Pattern Recognition*, pp. 3929–3938, 2017.

[191] A. E. Brito, S. H. Chan, and S. D. Cabrera, "SAR image formation using 2D reweighted minimum norm extrapolation," in *Algorithms for Synthetic Aperture Radar Imagery VI*, vol. 3721, pp. 78–92, International Society for Optics and Photonics, 1999.

[192] O. Ronneberger, P. Fischer, and T. Brox, "U-net: Convolutional networks for biomedical image segmentation," in *International Conference on Medical Image Computing and Computer-Assisted Intervention*, pp. 234–241, Springer, 2015.

[193] T. Tieleman and G. Hinton, "Lecture 6.5-RMSProp: Divide the gradient by a running average of its recent magnitude," *COURSERA: Neural Networks for Machine Learning*, vol. 4, no. 2, pp. 26–31, 2012.

[194] Z. Wang, A. C. Bovik, H. R. Sheikh, and E. P. Simoncelli, "Image quality assessment: from error visibility to structural similarity," *IEEE Transactions on Image Processing*, vol. 13, no. 4, pp. 600–612, 2004.

[195] R. Werninghaus, "TerraSAR-X mission," in *SAR Image Analysis, Modeling, and Techniques VI*, vol. 5236, pp. 9–16, International Society for Optics and Photonics, 2004.

[196] J. Gao, B. Deng, Y. Qin, H. Wang, and X. Li, "Complex-valued convolutional neural network enhanced radar imaging," *arXiv preprint arXiv:1712.10096*, 2017.